



**Manchester  
Metropolitan  
University**

# **Numerical Modelling of Wave Run-up and Overtopping using Depth Integrated Equations**

**Jonathan Ben Shiach**

February 2008

*A thesis submitted in partial fulfilment of the requirements for the  
degree of Doctor of Philosophy*

Centre for Mathematical Modelling and Flow Analysis  
Department of Computing and Mathematics  
Manchester Metropolitan University

# **Declaration**

No portion of the work referred to in this thesis has been submitted in support of an application for any other degree or qualification at this or any other institute of learning.

Apart from those parts of this thesis which contain citations to the work of the others and apart from the assistance mentioned in the acknowledgements, this thesis is my own work.

Jonathan Ben Shiach

# Abstract

Wave run-up and overtopping of coastal structures have been extensively studied over the last 30 years to provide guidance for the construction of sea defences. Numerical models based on fluid flow equations can provide a useful aid in the design of these coastal defences. Computers have now advanced sufficiently to enable programs written to solve the flow equations to run on hardware that is readily available (e.g., desktop or laptop computers), thus giving engineers the ability to conduct multiple runs of an experiment, reconfigure the bathymetry, change the wave conditions and collect data from anywhere in the solution domain.

An existing numerical model, AMAZON, based on the non-linear Shallow Water Equations (SWE) was used to give wave height and overtopping discharges for a series of violent overtopping experiments. A second-order accurate high-resolution finite-volume method was used to solve the SWE. The source terms that model the bed topography were treated using the Surface Gradient Method (SGM). The numerical model gave overtopping predictions to within 20% of the experimental overtopping discharges for cases where the wave conditions at the sea wall were not severely impacting. However, wave height comparisons showed that the SWE could not model wave propagation in intermediate depth water.

The Boussinesq class of equations was chosen to extend the numerical modelling of wave propagation, run-up and overtopping into intermediate depth water. A hybrid finite-volume/finite-difference solver was used to solve two different extended Boussinesq formulations, one of which was chosen to model a range of run-up and overtopping experiments. It was found that the numerical model was able to model wave propagation where the typical depth to wavelength ratio was less than 0.35 for both regular and irregular waves. However, the numerical model was not able to accurately model breaking waves. Comparisons between overtopping discharges from the physical experiments and the numerical model showed that, in the majority of cases, the numerical model was able to provide predictions to within an absolute relative error of 3. It was found that as the gradient of the seawall increased, so did the accuracy of the numerical overtopping predictions.

# Acknowledgements

In the preparation of this document, and perhaps more importantly over the course of my post graduate studies, I have drawn on the help and support of many people to whom I would like to express my gratitude and acknowledge their contribution.

Principally my supervisory team, Clive Mingham of the Manchester Metropolitan University and Dr. David Ingram of the University of Edinburgh (formally of the Manchester Metropolitan University). I thank them for their guidance and patience. Dr. Stephen Richardson and William Allsop of HR Wallingford Ltd., Dr. Jonathan Pearson and Tom Bruce of the University of Edinburgh who have all aided me in this study by providing experimental data and engineering expertise. The overtopping data for the Kansai experiments was kindly provided by Professor Hajime Mase of Kyoto University and processed by Dr. Maria Teresa Reis of the Laboratório Nacional de Engenharia Civil (LNEC), Lisbon.

I would also like to acknowledge the contribution of my family and friends, most notably my partner Hayley Jackson who has been extremely patient and supportive over the course of my post-graduate studies. Finally, Darren Dancey, Timothy Jackson and Naresh Subramaniam have provided peer support and advice that has been invaluable.

The VOWS project was funded by the EPSRC under two linked grants, numbers GR/M 42312 and GR/M 42428. The CLASH project was a EU Framework-V funded project, contract number EVK3-CT-2001-00058.

# Table of Contents

<b>1</b>	<b>Introduction</b>	<b>1</b>
1.1	Wave Theory . . . . .	8
1.1.1	Definition of terms . . . . .	9
1.1.2	Particle motion . . . . .	9
1.1.3	Relative depth ratio . . . . .	11
1.1.4	Dispersion relation . . . . .	12
1.1.5	The Froude number . . . . .	14
1.2	Physical Modelling . . . . .	15
1.2.1	Wave generation . . . . .	17
1.2.1.1	The JONSWAP spectrum . . . . .	19
1.2.2	European Projects . . . . .	20
1.2.2.1	VOWS project . . . . .	20
1.2.2.2	CLASH project . . . . .	21
1.3	Thesis Outline . . . . .	22
<b>2</b>	<b>The Shallow Water Flow Solver</b>	<b>23</b>
2.1	The Shallow Water Equations . . . . .	24
2.2	The Finite-Volume Method . . . . .	24
2.2.1	The Hancock scheme . . . . .	25
2.2.2	MUSCL Reconstruction . . . . .	26
2.2.3	The HLL Riemann Solver . . . . .	28
2.2.3.1	Wave speed estimates . . . . .	29
2.2.4	Boundary conditions . . . . .	30
2.2.5	Time step calculation . . . . .	31
2.2.6	Minimum wet depth parameter . . . . .	31
2.3	Numerical Results . . . . .	32
2.3.1	One-dimensional dam break problem: Wet bed . . . . .	32
2.3.2	One-dimensional dam break problem: Dry bed . . . . .	35
2.4	The Surface Gradient Method . . . . .	38

2.4.1	Data reconstruction . . . . .	39
2.4.2	Discretisation of source terms . . . . .	40
2.4.3	Implementation within a Godunov-type method . . . . .	40
2.4.4	Boundary conditions . . . . .	41
2.5	Numerical Results . . . . .	41
2.5.1	Tidal wave flow . . . . .	41
2.5.2	Tidal wave flow over an irregular bed . . . . .	42
2.5.3	Steady flow over a bump . . . . .	44
2.5.3.1	Transcritical flow without a shock . . . . .	46
2.5.3.2	Transcritical flow with a shock . . . . .	46
2.5.3.3	Subcritical flow . . . . .	47
2.5.4	Quasi-stationary case . . . . .	47
2.5.5	Surge crossing a step . . . . .	47
2.6	Chapter Summary . . . . .	53
<b>3</b>	<b>Shallow Water Modelling of Wave Overtopping</b>	<b>54</b>
3.1	Wave and Overtopping Statistics . . . . .	55
3.1.1	Significant wave height and mean wave period . . . . .	55
3.1.2	Rayleigh Wave Height Distribution . . . . .	56
3.1.3	Wave run-up and overtopping . . . . .	56
3.2	Violent Wave Overtopping . . . . .	57
3.2.1	Previous Work on Violent Wave Overtopping . . . . .	58
3.2.2	The $h^*$ Parameter . . . . .	59
3.2.3	Besley Formula . . . . .	60
3.3	The Edinburgh Wave Flume Experiments . . . . .	60
3.4	Numerical Modelling of Violent Wave Overtopping . . . . .	62
3.5	Results . . . . .	63
3.6	Chapter Summary . . . . .	76
<b>4</b>	<b>The Boussinesq Equations</b>	<b>77</b>
4.1	Nwogu's Boussinesq Equation system . . . . .	78
4.1.1	Dispersive properties of Nwogu's Boussinesq Equations . . . . .	79
4.2	Finite Difference Methods . . . . .	81
4.2.1	Time differencing . . . . .	82
4.3	Finite Difference Solver for the Boussinesq Equations . . . . .	83
4.3.1	Spatial differencing . . . . .	85
4.3.2	The Thomas algorithm . . . . .	86
4.3.3	Time step calculation and stability . . . . .	88
4.4	Boundary conditions . . . . .	88

4.4.1	Incident wave boundary condition . . . . .	89
4.4.2	Radiation boundary condition . . . . .	89
4.4.3	Solid wall boundary condition . . . . .	90
4.5	Internal wave generation . . . . .	90
4.6	Sponge layers . . . . .	92
4.7	Numerical Results . . . . .	93
4.7.1	Solitary wave propagation . . . . .	93
4.7.2	Solitary wave interaction . . . . .	96
4.7.3	Monochromatic wave propagation . . . . .	97
4.7.3.1	Single period monochromatic wave . . . . .	97
4.7.3.2	Multiple period monochromatic wave . . . . .	98
4.7.4	Monochromatic wave reflection . . . . .	99
4.7.5	Regular wave propagation over a submerged bar . . . . .	101
4.8	Chapter Summary . . . . .	108
<b>5</b>	<b>Hybrid Finite-Volume/ Finite-Difference Solver</b>	<b>110</b>
5.1	Hybrid Numerical Solver: Nwogu's Formulation . . . . .	111
5.2	Numerical Scheme . . . . .	112
5.2.1	Spatial Discretisation . . . . .	113
5.2.2	MUSCL Reconstruction . . . . .	114
5.2.3	Time integration . . . . .	115
5.3	Madsen and Sørensen's Boussinesq Formulation . . . . .	116
5.3.1	Wave breaking . . . . .	117
5.4	Numerical Results . . . . .	117
5.4.1	Solitary wave propagation . . . . .	118
5.4.2	Regular wave propagation over a submerged bar . . . . .	119
5.4.3	Solitary wave run-up on a sloping beach . . . . .	124
5.4.4	Numerical simulation of the Edinburgh wave flume experiments . . . . .	127
5.4.5	Random wave overtopping . . . . .	130
5.5	Chapter Summary . . . . .	136
<b>6</b>	<b>Conclusions</b>	<b>137</b>
6.1	Further Work . . . . .	144
<b>Bibliography</b>		<b>148</b>
<b>A Validation of the Hyperbolic Nature of the SWE</b>		<b>158</b>

---

<b>B Derivation of difference formulae</b>	<b>159</b>
B.1 Derivation of Fourth- Order Finite Difference Schemes . . . . .	160
<b>C Wave Statistics, Run-up and Overtopping Tables</b>	<b>163</b>
C.1 Solitary Wave Run-up on a Sloping Beach . . . . .	163
C.2 Edinburgh Wave Flume Experiments: wave statistics . . . . .	163
C.3 Random Wave Overtopping Results . . . . .	164
<b>D Published Papers</b>	<b>175</b>

# List of Figures

1.1	Wave overtopping of a harbour wall. . . . .	4
1.2	Wave theory definitions. . . . .	9
1.3	Motion of a particle in a water wave. . . . .	10
1.4	Relative depth ratio and classification of water depth. . . . .	12
1.5	Subcritical to supercritical flow. . . . .	15
1.6	Supercritical to subcritical flow. . . . .	15
1.7	The University of Edinburgh wave flume. . . . .	16
1.8	Simplified shallow water piston-type wave maker. . . . .	18
1.9	$H/S$ ratio for piston-type and flap-type wave makers. . . . .	19
1.10	The JONSWAP spectrum. . . . .	21
2.1	Finite-volume cell. . . . .	25
2.2	Piecewise continuous MUSCL reconstruction. . . . .	27
2.3	Simple Riemann Fan. . . . .	28
2.4	A diagram of a one-dimensional boundary. . . . .	30
2.5	One-dimensional dam break solution ( $h$ ). . . . .	33
2.6	One-dimensional dam break solution ( $u$ ). . . . .	34
2.7	One-dimensional dam break solution with dry bed ( $h$ ). . . . .	36
2.8	One-dimensional dam break solution with dry bed ( $u$ ). . . . .	37
2.9	Definition sketch of bed topography. . . . .	39
2.10	Tidal wave flow. . . . .	43
2.11	Tidal wave flow over an irregular bed $t = 10800$ seconds. . . . .	45
2.12	Tidal wave flow over an irregular bed $t = 32400$ seconds. . . . .	46
2.13	Transcritical flow over a bump without a shock. . . . .	48
2.14	Transcritical flow over a bump with a shock. . . . .	48
2.15	Subcritical flow over a bump. . . . .	49
2.16	Water surface elevation with small perturbation. . . . .	50
2.17	Surge wave crossing a step. . . . .	52
3.1	Definitions of run-up, $R$ , and crest freeboard, $R_c$ . . . . .	57

3.2	Video images of a breaking wave impacting on a structure. . . . .	58
3.3	Edinburgh wave flume: side elevation. . . . .	61
3.4	Edinburgh wave flume: experimental setup. . . . .	61
3.5	Edinburgh experiments: comparison of water surfaces. . . . .	64
3.6	Edinburgh experiments: comparison of discharges (runs 1 – 3). . . .	65
3.7	Edinburgh experiments: comparison of discharges (runs 4 – 6). . . .	66
3.8	Edinburgh experiments: comparison of discharges (runs 7 – 9). . . .	67
3.9	Edinburgh experiments: comparison of discharges (runs 10 – 12). .	68
3.10	Edinburgh experiments: comparison of discharges (runs 13 – 15). .	69
3.11	Edinburgh experiments: experimental Rayleigh distribution. . . . .	70
3.12	Edinburgh experiments: numerical Rayleigh distribution. . . . .	71
3.13	Edinburgh experiments: dimensionless discharge comparisons. . . .	74
3.14	Edinburgh experiments: $N_{ow}/N_w$ (%) comparisons. . . . .	75
3.15	Edinburgh experiments: absolute error comparisons. . . . .	75
4.1	Dispersive properties of Nwogu's Boussinesq equations ( $C/C_{\text{Airy}}$ ). .	80
4.2	Dispersive properties of Nwogu's Boussinesq equations ( $C/C_g$ Airy). .	81
4.3	Finite difference discretisation. . . . .	82
4.4	Node numbering convention for boundary conditions. . . . .	88
4.5	Internal wave generation using source function method. . . . .	91
4.6	Solitary wave propagation. . . . .	95
4.7	Analytical solitary wave solution compared with numerical solution.	95
4.8	Solitary wave interaction. . . . .	96
4.9	Monochromatic wave propagation flume. . . . .	97
4.10	Internally generated monochromatic wave. . . . .	98
4.11	Internally generated multiple period monochromatic wave. . . . .	99
4.12	Monochromatic wave reflection: sketch of wave flume. . . . .	100
4.13	Monochromatic wave reflection. . . . .	100
4.14	Standing waves created by monochromatic wave reflection. . . . .	101
4.15	Sketch of wave flume of the Delft Hydraulics experiments. . . . .	102
4.16	Regular wave propagation over a submerged bar solution. . . . .	104
4.17	Regular wave propagation over a submerged bar: configuration (a).	105
4.18	Regular wave propagation over a submerged bar: configuration (b).	106
4.19	Regular wave propagation over a submerged bar: configuration (c).	107
5.1	Solitary wave propagation using the van Leer limiter. . . . .	119
5.2	Solitary wave propagation using the minmod limiter. . . . .	120
5.3	Regular wave propagation over a submerged bar: configuration (a).	121
5.4	Regular wave propagation over a submerged bar: configuration (a).	122

5.5	Regular wave propagation over a submerged bar: configuration (a).	123
5.6	Solitary wave run-up on a sloping beach: diagram of wave flume.	124
5.7	Solitary wave run-up comparisons.	126
5.8	Solitary wave run-up relative errors.	127
5.9	Edinburgh experiments: comparison of water surfaces.	129
5.10	Edinburgh experiments: significant wave heights.	130
5.11	Diagram of the Kansai University wave flume.	131
5.12	Kansai experiments: overtopping discharges for 1:10 and 1:7 slopes.	133
5.13	Kansai experiments: overtopping discharges for 1:5 and 1:3 slopes.	134
5.14	Kansai experiments: overtopping discharges for a 1:4/3 slope.	135
5.15	Kansai experiments: absolute relative errors for dimensionless dis- charges.	135

# List of Tables

1.1	Classification of wave phenomena and their generating force. . . . .	9
1.2	Linear Wave theory: definition of terms. . . . .	10
1.3	Relative depth ratio and the classification of water depth. . . . .	11
1.4	Classification of subcritical, critical and supercritical flow . . . . .	14
2.1	Tidal flow over an irregular bed: Bed elevation . . . . .	44
3.1	Edinburgh wave flume experiment parameters . . . . .	62
3.2	Edinburgh wave flume experiments: experimental observations . . .	72
3.3	Edinburgh wave flume experiments: numerical results . . . . .	72
4.1	Wave configurations of submerged bar test. . . . .	103
5.1	Random wave overtopping: experimental values . . . . .	131
C.1	Solitary wave run-up on a sloping beach: run-up values. . . . .	165
C.2	Solitary wave run-up on a sloping beach: run-up values. . . . .	166
C.3	Edinburgh wave flume experiments: experimental $H_s$ . . . . .	167
C.4	Edinburgh wave flume experiments: experimental $T_m$ . . . . .	167
C.5	Edinburgh wave flume experiments: Hybrid $H_s$ . . . . .	168
C.6	Edinburgh wave flume experiments: Hybrid $T_m$ . . . . .	168
C.7	Random wave overtopping: experimental setup. . . . .	169
C.8	Random wave overtopping: experimental setup. . . . .	170
C.9	Random wave overtopping: experimental setup. . . . .	171
C.10	Random wave overtopping: overtopping values. . . . .	172
C.11	Random wave overtopping: overtopping values. . . . .	173
C.12	Random wave overtopping: overtopping values. . . . .	174

# Nomenclature

---

$A$	area of finite-volume cell or empirical model coefficient
$B$	empirical model coefficient
$a$	wave amplitude (m)
$C$	wave celerity ( $\text{ms}^{-1}$ )
$\mathcal{C}, \mathcal{Z}$	conservative properties
$C_f$	friction coefficient
$C_g$	group wave celerity ( $\text{ms}^{-1}$ )
$D$	magnitude of source function
$d$	water depth between the bed surface and the SWL (m)
$d_{toe}$	water depth at toe of structure (m)
$\mathbf{F}$	flux vector
$F_r$	Froude number
$F_{sponge}$	sponge layer component
$f$	frequency or arbitrary function
$G(a, b)$	slope limiter function
$g$	acceleration due to gravity ( $\text{ms}^{-2}$ )
$g(x)$	Gaussian shape function
$H$	wave height or partial depth between bed surface and arbitrary datum (m)
$H_{rms}$	root mean square of the wave heights (m)
$H_s$	significant wave height (m)
$h$	water depth (m)
$h^*$	impulsive/impacting wave parameter
$i, j$	spatial indices (subscript)
$k$	wave number
$L$	wavelength (m)
$n$	time step counter (superscript)
$Q$	overtopping volumes ( $\text{m}^3$ )

---

$Q^*$	dimensionless discharge (sloping seawalls)
$Q_h$	dimensionless discharge (vertical seawalls)
$q$	discharge ( $\text{m}^2\text{s}^{-1}$ )
$R_{err}$	global relative error
$R$	run-up distance (m)
$R_c$	crest freeboard (m)
$R^*$	dimensionless freeboard (sloping seawalls)
$R_h$	dimensionless freeboard (vertical seawalls)
$r(z)$	radius of particle motion orbits (m)
$\mathbf{S}$	source term vector
$S$	wave maker stroke (m)
$S(f)$	spectral density
SWL	still water level (m)
$s_L, s_R$	slowest and fastest travelling wavespeeds ( $\text{ms}^{-1}$ )
$T$	wave period (s)
$T_m$	mean wave period (s)
$T_s$	significant wave period (s)
$t$	time (s)
$\mathbf{U}$	vector of conserved variables
$u, v$	horizontal velocities ( $\text{ms}^{-1}$ )
$F_{sponge}$	sponge layer component
$u_\alpha$	horizontal velocity at an arbitrary depth ( $\text{ms}^{-1}$ )
$x, y$	Cartesian coordinates
$x_s$	centre of wave generation function
$z$	vertical elevation (m)
$z_b$	bed surface elevation (m)

## Greek symbols

---

$\alpha, \beta$	Boussinesq constants or JONSWAP spectrum parameters
$\gamma$	peak enhancement parameter or wave breaking parameter
$\Delta$	difference operator
$\delta$	slope limited gradients or minimum wet depth parameter
$\zeta$	water surface elevation above the bottom datum (m)
$\eta$	water surface elevation above the SWL (m)
$\nu$	Courant number
$\pi$	ratio of circumference to diameter of a circle
$\rho$	density
$\sigma$	JONSWAP spectrum parameter
$\tau$	shear stress
$\phi$	geopotential
$\psi$	dispersion terms
$\omega$	wave frequency
$\nabla$	gradient operator
$\sum$	summation operator

# Chapter 1

## Introduction

Advances in digital computing technology in the twentieth century has given rise to a new branch of mathematics – Computational Fluid Dynamics (CFD). CFD is concerned with the use of computers to approximate the solutions of mathematical equations describing fluid flow. These mathematical equations are generally in the form of a system of partial differential equations (PDE). It is rare that an exact analytical solution to a system of PDEs exists except in special circumstances, hence the need for a method of approximation. The solution process required to solve these governing equations usually takes the form of an algorithm, a series of recursive steps that will eventually lead to a solution. CFD algorithms often require thousands of calculations to achieve a solution, therefore are dependent upon the computational power available.

The equations that describe the behaviour of fluids have been known for centuries. It was the Dutch mathematician Daniel Bernoulli (1700–1782) who was the first to study the motion of a fluid utilising the principle of conservation of mass. Bernoulli's work on fluid dynamics titled *Hydrodynamica* (Bernoulli, 1738) gave rise to the modern term *Hydrodynamics* to describe the study of liquids. Leonard Euler (1707–1783) who was a contemporary of Bernoulli, derived a set of equations directly from Newton's laws of motion and the conservation of mass, momentum and energy. Euler's equations, whilst a good model of water flow, describe incompressible flow, i.e., they assume a constant density. Claude Navier (1785–1836) extended the Euler equations to model compressible flow by taking into account the forces acting between the molecules of a fluid (O'Connor and Robertson, 2000). The resulting system of equations have become known as the Navier-Stokes equations. The reason for this was that Navier did not fully understand the inclusion of shear stresses in his formulation, despite his formulation being correct and it was later in 1845 that George Stokes (1819–1903) also de-

---

rived Navier's system of equations taking into account internal friction between fluids. It should be noted that although Stokes provided a correct derivation for Navier's equations for which he is credited, the French mathematician Jean Claude Saint-Venant (1797–1886) published a correct derivation two years before Stokes. However, Saint-Venant received no such accreditation (Anderson, 1997).

Although Saint-Venant's name is omitted from the Navier-Stokes formulation, he does lend his name to another system of equations that model shallow water flows. The Saint-Venant equations, which are also commonly known as the one-dimensional Shallow Water Equations (SWE), are a simplified form of the full Navier-Stokes system. By assuming a constant velocity profile in the vertical direction, the SWE are derived by integrating the Navier-Stokes equations in the vertical direction. Therefore the SWE represent a depth-averaged form of the Navier-Stokes equations. The SWE are significantly easier than the full Navier-Stokes formulation to solve in both the complexity of the solution algorithm and the computational resources required. A property of the SWE is that they are hyperbolic in nature and therefore can admit discontinuities into the solution (Hirsch, 1988). This means that the SWE can model wave propagation where wave breaking is likely to occur without compromising the stability of the numerical solution.

The assumption of a vertical velocity profile used in the simplification of the Navier-Stokes equations means that the SWE are only really applicable for shallow water flows (the formal definition of what constitutes shallow water is given in Section 1.1.3). From an maritime engineering standpoint, this means that the usefulness of the SWE is limited to near shore wave propagation cases only. In order to model wave propagation in deeper water a number of models have been suggested. Among these are the Boussinesq-type models (Peregrine, 1967; Witting, 1984; Madsen *et al.*, 1991; Nwogu, 1993) and the Green-Naghdi equations (Green and Naghdi, 1976). Both of these models include additional terms that introduce dispersion into the mass and momentum equations so that the properties of wave propagation in deeper water are retained. Of these two models that include dispersion, it is the Boussinesq-type models that has received the most attention. In general, Boussinesq-type models require a higher order accurate numerical solver than the SWE but still represent a significant improvement over the Navier-Stokes equations when considering the computational effort required to solve the governing equations.

It was inevitable that mathematical models would lend themselves as a tool for applications in coastal engineering. Research in the field of coastal engineer-

ing is primarily focused on the design and construction of structures that protect inland areas and harbours. These structures can be located offshore, e.g., breakwaters and harbour walls whose function is to protect the near shore region, or onshore, e.g., seawalls and dikes that protect inland areas from damage caused by wave overtopping and flooding (Fig. 1.1). Traditionally the knowledge base on flow in coastal regions has been gathered by field observations and laboratory experiments. Information gathered by field observations tends to be very time consuming and expensive to collate. This process usually consists of placing measuring instruments at the point of interest and recording the sea state and overtopping over time. However, coastal engineers are generally only interested in the ‘worst case scenarios’ that occur when conditions are at their most extreme, i.e., during a storm. As storm predictions can often be unreliable, the instrumentation has either got to be installed over a long period of time which in itself leads to the problems of maintenance, or installed immediately prior to a storm occurring which can limit the size of the area under study. The disadvantages of relying upon field observations can be overcome by use of physical experiments conducted in the controlled environment of a laboratory. The physical experiments are a small scale representation of a coastal region constructed in a wave tank. Experiments of this type can allow a particular configuration to be run repeatedly thus providing enough data for meaningful analysis. However, small scale physical models are expensive and inflexible. The costs associated with constructing the model and performing the experiments can become substantial. In addition, once constructed a change in the configuration, for example the bathymetry, is not a trivial matter.

A numerical model based on the equations of fluid flow has several advantages over a physical modelling approach. Firstly the cost of running a numerical model is significantly less than that of a physical model. Once the software has been developed, multiple experiments can be performed and data collected at almost no additional cost. Also a numerical model provides the flexibility to change an experimental configuration instantly, e.g., wave conditions, instrument location, bathymetry, coastal structures and water depth. Finally, numerical models are portable, that is they can be installed on a desktop computer, a laptop or sent *via* electronic communications. It is highly unlikely that numerical models will ever totally replace the need for physical experimentation, but they do provide an important tool for engineers when considering experimental design and design of coastal structures. Before numerical models can be applied in this way with a degree of confidence, they have to be developed and extensively validated against



Figure 1.1: Wave overtopping of a harbour wall. Whitby, United Kingdom. (Photograph by the author)

the physical models to ensure that the predictions provided by the numerical model closely match those of the physical model.

The origin of numerical methods for solving mathematical equations, in particular PDEs is attributed by Roache (1972) to a paper by Richardson (1910). Richardson presented an arithmetic solution to a number of PDEs including Laplace's equation, distinguished between hyperbolic and elliptic problems, described a treatment for the boundary conditions, introduced the idea of error analysis and comparisons between calculated solutions and exact solutions. Finally, Richardson applied his numerical method to a real world problem of determining the stresses action on a masonry dam. This methodology that Richardson used in his 1910 paper is the basic methodology adopted by subsequent researchers. The method that Richardson applied to solve PDEs was the finite-difference method. This is one of the simplest and widely used numerical methods. The solution domain is discretised into a number of solution points, or computational nodes, that contain the current solution of the system at a point in time. Finite-differences, derived from a series approximation of a function, are used to approximate partial derivatives in the governing equations by using the values of the neighbouring nodes (see Section 4.2). Richardson only used values from the previous time step for the calculation of the values for the next time step. Liepmann (1918) showed that the general method of finite-differences can be greatly improved in terms of the convergence rate by using the values at the nodes for the next time step where available (these type of method have become known as Successive Over Relaxation

---

methods or SOR methods). The improvement made by Liepmann set the tone for what was to follow in the discipline of CFD, i.e., that a relatively minor alteration in an existing method could significantly reduce the effort required to achieve a solution (Roache, 1972).

One of the most important publications in the field of CFD was that of Courant, Friedrichs and Lewy (1928) which was later translated into English in Courant *et al.* (1967). In their paper, Courant *et al.* proved the existence and uniqueness of solutions to hyperbolic PDEs and as a result also provided what is now known as the CFL condition. The CFL condition states that in order for a numerical PDE solver to converge to a solution, the time step used must be less than the time taken for a wave to travel to adjacent grid points. A parameter called the Courant number is introduced (denoted by  $\nu$  here) that assumes a value such that the CFL condition is always satisfied. Therefore, given the spatial step lengths, the fluid velocities and  $\nu$ , the maximum time step can be calculated that ensures the numerical scheme remains stable.

The first use of the digital computer for a hydrodynamic application was made in the late 1960s by Cunge *et al.* (Cunge, 1987; Hu, 2000) where a four point implicit box scheme (also known as a Preissmann scheme) was used to solve the one-dimensional shallow water (Saint-Venant) equations. Extension to two-dimensions was achieved by Leendertse (1967) and Abbot *et al.* (1973) where an Alternation Direction Implicit (ADI) method was used to solve the two-dimensional SWE. ADI methods split the two-dimensional governing equations into two one-dimensional equations that are solved using a one-dimensional solver. This development lead to an increased interest in using ADI methods for modelling flow in rivers, estuaries and near shore coastal regions (Falconer, 1976; Weare, 1976; Stelling, 1984).

There are two major disadvantages of using the finite-difference method to solve PDEs such as the SWE. The first is that finite-difference methods are generally not suitable for solving hyperbolic systems of equations near discontinuities, i.e., bore wave representation of a breaking wave (Fagherazzi *et al.*, 2004), as spurious oscillations tend to contaminate the solution. The second is that when applied to a Cartesian coordinate system, the finite-difference stencil provides a poor representation of irregular boundaries. This deficiency has been previously overcome by use of a boundary fitted coordinate system where the governing equations are transformed for the new coordinate system (Johnson and Thompson, 1978; Barber, 1992; Borthwick and Kaar, 1993). Another approach for modelling irregular boundaries is to use a numerical method that does not require an orthogonal mesh. Finite-volume methods is one such example where the solution domain is

---

constructed using arbitrary shaped solution cells so that irregular topographies can be modelled. Finite-volume methods solve the integral form of the governing equations, which are valid in both discontinuous and smooth regions, averaging the solution across the finite-volume cell.

Finite-volume methods have been used extensively to solve the SWE. Mingham and Causon (1998), Zhao *et al.* (1994), Zhao *et al.* (1996), Alcrudo and García-Navarro (1993), Hu *et al.* (1998), Zhou *et al.* (2001) and Shiach *et al.* (2004) all apply a finite-volume method where there exists a discontinuity at the cell boundaries, also known as Riemann problems. In its simplest terms a Riemann problem consists of an initial value problem where two constant states are separated by a discontinuity. Godunov (1959) in his seminal paper presented a numerical scheme for hyperbolic equations that required the solution of a Riemann problem, and thereafter, methods that utilise Riemann solvers are known as Godunov-type methods (Toro, 1997). Various approximate and exact Riemann solvers exist and have been used in Godunov-type schemes. The HLL (Harten, Lax and van Leer, 1983) approximate Riemann solver was used in Mingham and Causon (1998), Hu *et al.* (1998) and Zhou *et al.* (2001) and was found to be accurate and robust in practice. The approximate Riemann solver of Roe (1981) was used in Dodd (1998), Hubbard and Dodd (2002) and Alcrudo and García-Navarro (1993) and a Weighted Average Flux (WAF) method was used by Toro (1989, 1992) (Fagherazzi *et al.*, 2004).

A treatment of the source terms in the SWE that model bed topography, bed friction and shear stresses is needed in order to apply the SWE to model flow in estuaries and coastal regions. Several approaches have been suggested for use in conjunction with finite-volume methods. Bermudez and Vázquez-Cendón (1994), Vázquez-Cendón (1999) and Castro *et al.* (2004) all apply an upwind approach for their treatment of the source terms. This upwind approach entails a complicated treatment where the source terms are projected onto the basis of eigenvectors of the Jacobian matrix when using Roe's scheme (García-Navarro and Vázquez-Cendón, 2000). Leveque (1998) treated the source terms by introducing a Riemann problem in the centre of each grid cell whose flux difference exactly cancels the source terms. Leveque's method performs well for quasi-steady problems but is reported to be less successful for transcritical flow with a shock (Zhou *et al.*, 2001). The method of fractional steps is another method that has been used for the treatment of source terms. The governing equations are split so that a finite-volume method is used to solve the homogeneous inviscid terms, and a simple Ordinary Differential Equation (ODE) solver is used to solve the source terms. Hu *et al.* (2000) demonstrated that

---

using a first order implicit Euler method for the source terms and a symmetric operator sequence provides an accurate treatment, although it was noted that this approach provides an extra constraint on the maximum allowable time step. A different approach entirely from the approaches listed above was one suggested by Zhou *et al.* (2001). They suggested using the water surface elevation, i.e., the height of the water above an arbitrary datum, as the basis of monotonic reconstruction as opposed to the water depth used previously in Godunov-type schemes. Therefore, any perturbations between the treatments of the inviscid terms and the bed terms in the balancing approaches of Leveque (1998) and Hu *et al.* (2000) do not affect the solution. This treatment, labelled the Surface Gradient Method (SGM), is a simple extension of a Godunov-type scheme and the additional computational cost is negligible.

Recently, various models have been developed that utilise the SWE to model water flow in near shore coastal regions. Kobayashi *et al.* (1987) and Kobayashi and Wurjanto (1989) are perhaps the first to use the SWE to model run-up and reflection on impermeable rough slopes. Van Gent (1994, 1995) developed their model called ODIFLOCS based upon the concepts of Hibberd and Peregrine (1979) and it has been used to model wave overtopping of sea dikes (Niemeyer *et al.*, 2002). ANENOME OTT developed by Dodd (1998) and Hubbard and Dodd (2002) and AMAZON by Hu *et al.* (2000) have both used similar finite-volume schemes to model run-up and overtopping of shallow sloping structures (Richardson *et al.*, 2002). Richardson *et al.* (2001) and Shiach *et al.* (2004) focused on overtopping of near vertical structures caused by violent interaction of the waves breaking against the structure. Violent wave overtopping provides a tougher challenge for a numerical model than wave overtopping of gentle sloping structures modelled previously. It was found that whilst the SWE can provide good predictions of overtopping volumes for violent wave overtopping, the absence of dispersion terms resulted in poor predictions for the wave heights in the intermediate depth water and thus provides a restriction upon the applicability of the SWE (Shiach *et al.*, 2004).

Attempts at extending the range of applicability of depth-averaged numerical models of run-up and overtopping to model flow in deeper water have mainly centred around the use of Boussinesq-type models. Peregrine (1967) used his new formulation to model solitary wave propagation on a sloping beach. An analysis of the dispersion properties of Peregrine's formulation suggests that his equations do not represent a significant improvement over the SWE when considering modelling the transition between deep and shallow water (Nwogu, 1993). Madsen *et al.*

(1997a,b) and Sørensen *et al.* (1998) produced a series of papers examining surf zone dynamics by introducing a wave breaking model to their existing Boussinesq equation system (Madsen *et al.*, 1991; Madsen and Sørensen, 1992). Lynett *et al.* (2002) used the extended formulation of the Boussinesq equations by Liu (1994) to which to apply their moving boundary algorithm for use in wave run-up cases. Shiach *et al.* (2005) suggested a hybrid model where the extended Boussinesq equations of Nwogu (1993) are used in the intermediate zone and the SWE are used to model shallow water and run-up and violent overtopping of a near vertical seawall. This approach required a careful treatment of a boundary matching procedure combining two different governing equations with two different solution methods. A more elegant approach to producing a hybrid model was suggested almost simultaneously by Erduran *et al.* (2005) and Borthwick *et al.* (2005). Both papers propose a hybrid scheme to solve Madsen and Sørensen's extended Boussinesq equations where a finite-volume solver is used for the inviscid (SWE) terms and a finite-difference solver for the dispersion and bed source terms. Borthwick *et al.* (2005) used a second-order treatment of the time derivatives whilst Erduran *et al.* (2005) favoured the fourth-order scheme used by Wei and Kirby (1995) to integrate the equations through time.

## 1.1 Wave Theory

There are many different forms of waves that occur in many different media but for the purposes of this study, only waves that significantly affect coastal regions are discussed here. Water waves occur when the water is disturbed by some external force causing a disturbance in the free surface that propagates due to the fluid properties of water. The classification of waves is made on the basis of the physical parameters which characterise the waves: the wave height  $H$ , the wavelength  $L$ , the wave period  $T$  and the water depth  $d$  (for a formal definition of these parameters see Section 1.1.1). Various types of wave phenomena are listed with the associated wave period and the generating force in Table 1.1 (Koutitas, 1988). For the purposes of this study, wind generated waves of the type that are typically seen in coastal zones are of most interest although it should be noted that the numerical models presented here have been previously validated for tsunamis (Richardson *et al.*, 2002; Watts *et al.*, 2005) and tidal waves (Zhou *et al.*, 2001).

It is fundamental to the design of coastal structures to understand the propagation and formation of waves from deep to shallow water. Linear wave theory (sometimes called Airy wave theory after English mathematician George Airy)

Table 1.1: Classification of wave phenomena and their generating force.

Phenomena	Period ( $T$ )	Generating force
Wind generated waves	0–15 s	Pressure of wind on water surface
Swell	0–30 s	Long distance wind waves
Surf beats	1–5 mins	Grouping of breaking waves
Tsunami	5–60 mins	Seismic activity
Tide	12–24 hours	Moon/sun influence on earth gravity

provides an understanding of these processes and formal definition of terms used to describe surface waves. In the following sections these definitions are given as well as descriptions of wave evolution and the dispersion relation.

### 1.1.1 Definition of terms

The terms used in linear wave theory are defined in Fig. 1.2 and Table 1.2.

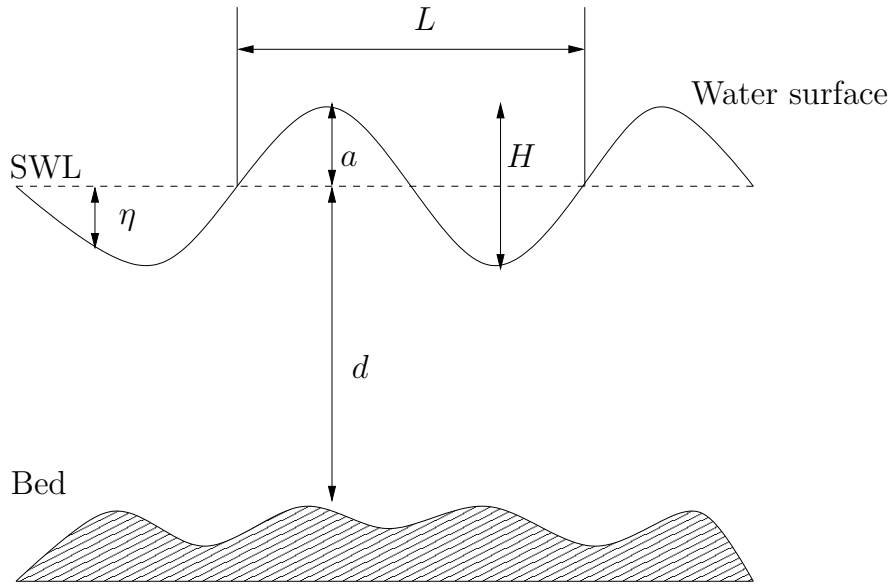


Figure 1.2: Diagram of a one-dimensional wave showing the definitions used in linear wave theory.

### 1.1.2 Particle motion

There are two ways in which to visualise the motion of individual fluid particles (Silvester, 1974): the first is to concentrate on a fixed point in space and observe

Table 1.2: Linear Wave theory: definition of terms.

Term	Definition
SWL	Still Water Level: the surface elevation of still water.
$a$	Wave amplitude: the height of the wave crest above SWL;
$d$	Water depth between the bed surface and the SWL;
$\eta$	Water surface elevation: distance between the water surface and the SWL;
$H$	Wave height: distance between the crest and trough of a wave
$L$	Wavelength: distance between two corresponding points on successive wave forms
$T$	Wave period: the time that elapses during the period of one wavelength;
$C = L/T$	Wave celerity: the phase velocity of the crest of a wave.

the changes that occur in time (known as *Eulerian* presentation) and the second is to observe the path of an arbitrary fluid particle in time (known as *Lagrangian* presentation). Here, the Lagrangian presentation is used to describe particle motion as it shows more clearly the transition between deep, intermediate and shallow water that are defined later.

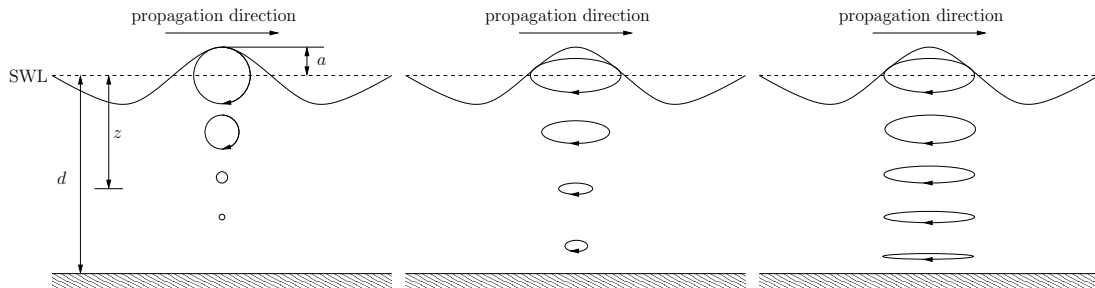


Figure 1.3: Lagrangian presentation of the orbital motion of a fluid particle: deep water (left), intermediate depth water (middle) and shallow water (right) (Silvester, 1974).

Consider a regular, sinusoidal wave propagating in a one-dimensional channel (Fig. 1.3). In deep water, a fluid particle at the free surface moves in a circular orbit with a radius equal to that of the wave amplitude  $a$ . As the depth,  $z$ , of the fluid particle in question increases, the radii of the circular orbits decrease exponentially. The radii of the motion orbits are given by the function (Sørensen, 1993)

$$r(z) = a \exp\left(-\frac{2\pi z}{L}\right), \quad (1.1)$$

where  $L$  is the wavelength of the free surface wave. Using Eq. (1.1) to calculate the radius of a motion orbit when  $z = L/2$  gives

$$r \left( \frac{L}{2} \right) = a \exp(-\pi) \approx 0.043a. \quad (1.2)$$

Therefore when the depth of the fluid particle is half of that of the wavelength, the radius of the motion orbits are less than 1/20th that of the radius at the free surface. This leads to the classification of the deep water limit discussed in Section 1.1.3.

The motion of a fluid particle in intermediate depth water follows an elliptical orbit where the major axis decreases as  $z$  increases. This leads to the particle motion in shallow water where the orbits are also elliptical. However, the major axis remains constant between the free surface and the bed whilst the minor axis decreases when the particle in question is near the bed.

### 1.1.3 Relative depth ratio

When discussing wave theory and the formation and propagation of waves it is common to classify the depth of the water using three different terms: deep water, transitionary or intermediate water and shallow water. The formal classification for these three terms is given in terms of the relative depth ratio which is given by

$$\text{Relative depth ratio} = \frac{d}{L}, \quad (1.3)$$

and the classification of water depth is given in Table 1.3.

Table 1.3: Relative depth ratio and the classification of water depth.

Relative depth	Category
$d/L > 1/2$	Deep water
$1/2 \leq d/L \leq 1/20$	Intermediate depth water
$d/L < 1/20$	Shallow water

The equations describing fluid flow in intermediate and shallow water are likely to be more complex than those for deep water conditions (Silvester, 1974). When waves approach shallow water, the transition from deep water causes the waves to shoal when  $d/L < 1/2$  (Fig. 1.4). The wave period remains constant whilst the wavelength decreases and the wave height increases. This causes an asymmetry in

the wave profile. In shallow water, the wave height becomes too large to sustain the shape of the wave and breaking occurs. McCowan (1894) defined the point at which a wave breaks using the ratio of wave height to water depth, where a value of  $H/d > 0.78$  indicates breaking. However, this ratio does not take into account that waves can break in deep water as well. Longuet-Higgins (1997) used the value of the wave slope given by  $ak$ , where  $k$  is the wavenumber Eq. (1.4). The breaking criterion using the wave slope is given as  $ak > 0.32$ .

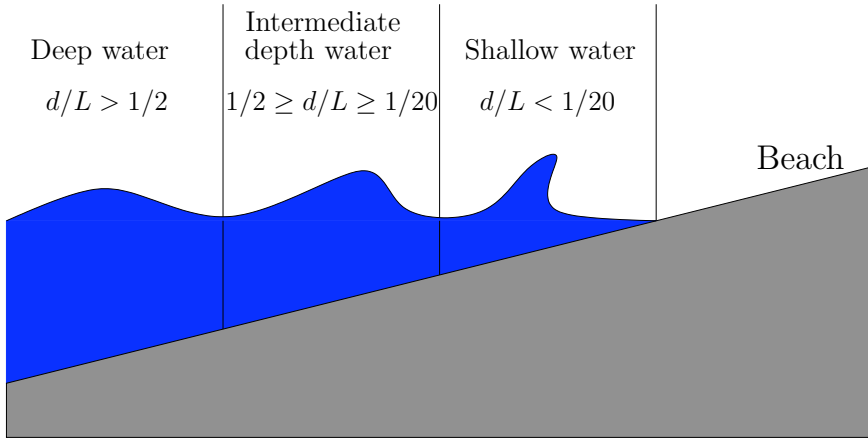


Figure 1.4: Relative depth ratio and classification of water depth.

#### 1.1.4 Dispersion relation

The wavelength and wave frequency of a wave are related by the linear dispersion relation (Krogstad and Arnsten, 2000). In order to determine the wave celerity (i.e., the wave velocity)  $C$ , two new parameters are introduced:

$$k = \frac{2\pi}{L}, \quad (1.4)$$

$$\omega = \frac{2\pi}{T}, \quad (1.5)$$

where  $k$  is known as the wavenumber and  $\omega$  is the wave frequency.

Consider a regular sinusoidal wave of amplitude  $a$ , period  $T$  and wavelength  $L$  (Krogstad and Arnsten, 2000)

$$\eta(x, t) = a \sin \left( \frac{2\pi}{T} t - \frac{2\pi}{L} x \right) = a \sin(\omega t - kx). \quad (1.6)$$

Then the dispersion relation giving  $\omega$  in terms of  $k$  is described by (Lamb, 1945;

Billingham and King, 2000; Stewart, 2004)

$$\omega^2 = gk \tanh(kd). \quad (1.7)$$

Therefore the dispersion relation also restricts the values that the wave period and wavelength can take depending on the value of the other variable.

The wave celerity  $C$  can be written in terms of  $k$  and  $\omega$  giving

$$C = \frac{\omega}{k}. \quad (1.8)$$

Using the dispersion relation given in Eq. (1.7), Eq. (1.8) can be rearranged to give the wave celerity in terms of  $k$  and  $\omega$

$$C = \frac{g}{\omega} \tanh(kd). \quad (1.9)$$

For shallow water the wave celerity is calculated by noting that when  $d \ll L$  then  $kd$  is small meaning that the approximation

$$\tanh(kd) \approx kd \quad (1.10)$$

can be used. This leads to the following expression for  $\omega$

$$\omega = k\sqrt{gd}. \quad (1.11)$$

Therefore, substituting Eq. (1.11) into Eq. (1.8) gives

$$C = \frac{k\sqrt{gd}}{k} = \sqrt{gd}, \quad (1.12)$$

which is the wave celerity for shallow water. Note that in shallow water, only the water depth determines the velocity of waves. A similar process can be applied for deep water. In deep water,  $d \gg L$ , then  $kd$  is large meaning that

$$\tanh(kd) \approx 1, \quad (1.13)$$

and the wave frequency becomes

$$\omega = \sqrt{gk}. \quad (1.14)$$

Along with Eq. (1.8), Eq. (1.14) gives the following expression for the wave celerity

in deep water

$$C = \sqrt{\frac{g}{k}}. \quad (1.15)$$

### 1.1.5 The Froude number

The Froude number is a dimensionless parameter that is used to indicate the influence of gravity on fluid motion. It is defined as the ratio of the inertial force to the gravitational force and for shallow water waves can be written as (Weisstein, 2007)

$$F_r = \frac{u}{\sqrt{gd}}, \quad (1.16)$$

where  $u$  is the velocity of the fluid. The Froude number is used to classify flow as either *supercritical* or *subcritical* (Table 1.4). Supercritical flow occurs when the flow velocity is greater than the free surface velocity and surface waves are unable to propagate against the main direction of flow. Flow of this form occurs when the current is strong and the water is shallow, for example, flow in fast moving streams or wave run-up on a beach. Subcritical flow occurs when the flow velocity is less than the free surface velocity and surface waves are able to propagate against the main direction of flow. Water in a subcritical flow region appears calmer than that of a supercritical flow region.

Table 1.4: Classification of subcritical, critical and supercritical flow

Froude number	Classification of flow
$F_r < 1$	Subcritical
$F_r = 1$	Critical
$F_r > 1$	Supercritical

Transition from subcritical flow to supercritical flow can only occur due to a change in the bathymetry, e.g., a bump in the bed topography (Fig. 1.5) or the narrowing of the channel. This causes the wave celerity to decrease and as a result the Froude number to increase. Where supercritical flow encounters a subcritical flow region, an upstream travelling hydraulic jump forms resembling a step in the free surface (Fig. 1.6).

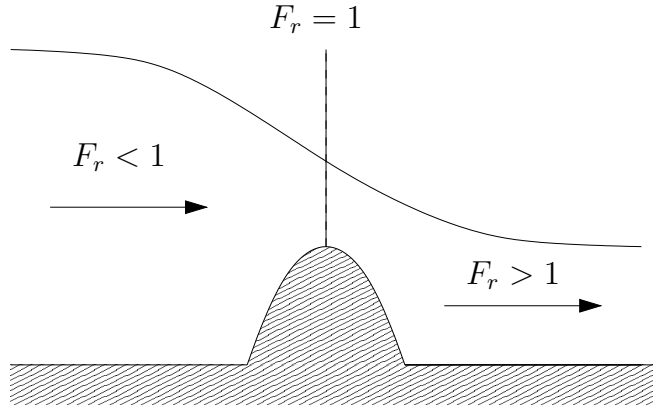


Figure 1.5: Subcritical to supercritical flow transition caused by a bump in the bed topography.

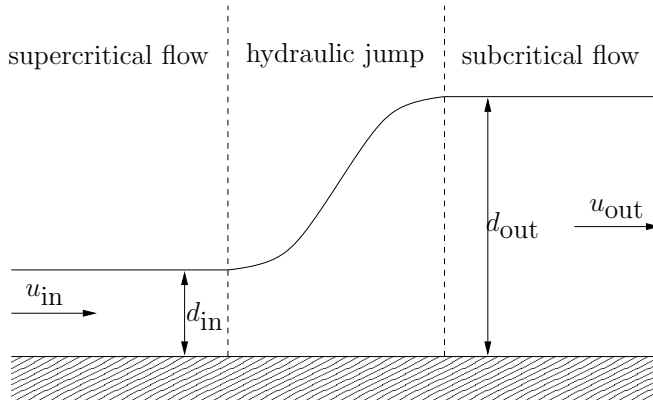


Figure 1.6: Supercritical to subcritical flow transition with hydraulic jump.

## 1.2 Physical Modelling

In order to study the interaction between waves and structures it is convenient to conduct physical experiments in a laboratory environment. These experiments are typically conducted in a wave tank, in which is constructed a small scale representation of the coastal zone under study (Fig. 1.7). Waves are generated in the water to simulate regular waves of a constant period or random waves that are sampled from a given spectrum (Section 1.2.1). The water surface elevation is measured by gauges, placed throughout the wave tank and connected to a computer, that record the water depth over time. For experiments where the velocities of individual fluid particles are required, neutrally buoyant particles may be added to the water to allow a Particle Image Velocimetry (PIV) system to detect and calculate the movement vectors of the fluid. Overtopping volumes are recorded by placing a container that collects any water that has overtapped

and then they are weighed by a load cell to calculate the volume of water. These experiments can either be conducted to examine one-dimensional flow in a wave flume or two-dimensional flow in a wave basin (the convention of referring to flow as one or two-dimensions used here refers to the dimension of the computational mesh applied to discretise the solution domain).



Figure 1.7: Typical example of a one-dimensional wave flume. The University of Edinburgh (photograph courtesy of Tom Bruce).

Over the last 30 years, small scale physical experiments have been used to study wave overtopping of coastal structures. The physical parameters of the experiments are expressed in dimensionless form so as to allow for comparison between differing configurations. Guidance on mean overtopping discharge volumes are given through empirical formulae derived by a regression analysis of the dimensionless overtopping volumes and physical parameters. Typically, experiments are conducted for approximately 1000 wave periods to ensure that enough data is collected for a meaningful comparison and analysis (Besley, 1999).

Goda *et al.* (1975) were the first to provide empirical formulae for mean overtopping discharge rate using laboratory measurements. Guidance for tolerable discharge rates for pedestrians, vehicles and buildings resulting from the overtopping of seawalls was provided by Owen (1980) following a series of experiments conducted at HR Wallingford. Besley (1999) concentrated on overtopping of near vertical seawalls, in particular, violent overtopping resulting from incident wave breaking on the structure. Typically, empirical models follow an exponential func-

tion of the form

$$Q^* = A \exp(-BR^*), \quad (1.17)$$

where  $Q^*$  is the dimensionless discharge,  $R^*$  is the dimensionless freeboard and  $A$  and  $B$  are empirical coefficients. The values of  $A$  and  $B$  are found by a maximum likelihood analysis based on the experimental values. Hedges and Reis (1998) based their semi-empirical H&R model on the formula for discharge over a weir where the water level exceeds the seawall crest level. This approach eliminates the problem that fully empirical models have in predicting zero overtopping.

An alternative approach to empirical curve fitting methods is to use Artificial Neural Networks (ANN). ANNs were originally developed as a model of the mammalian brain. They consist of a network of neurons that can be ‘trained’ to produce any function mapping. Once the ANN is trained using experimental data, overtopping predictions can be made using the neural network. The trained ANN is in essence a generalised regression function but has the advantage over the empirical models as not being limited to the choice of any particular mathematical function (Wedge, 2006).

### 1.2.1 Wave generation

Wave generation in physical model experiments is achieved by disturbing the water at one end of the wave flume allowing the resulting waves to propagate into the flume. The two most common types of wave generators are piston-type wave makers where a vertical plane is oscillated in the horizontal direction thus displacing a mass of water that creates the waves; and flap-type wave makers where the vertical plane is hinged at the bottom of the flume so that vertical profile of the motion of the plane more closely resembles that of the velocity field. In order for a wave maker to generate waves of a desired wavelength and period the extent of the horizontal movement of the plane (the stroke  $S$ ) needs to be defined.

The calculation of  $S$  begins by first considering a simplified shallow water case for a piston-type wave maker (Dean and Dalrymple, 1991). Galvin (1964) reasoned that the volume of water displaced by a vertical plane oscillating in the horizontal direction with a stroke  $S$  is equal to the volume of water contained in the crest of a propagating wave (cf., the two shaded regions in Fig. 1.8). It can be easily seen that the volume of water displaced by one stroke of the wave maker is  $dS$  and that the volume of water contained in the wave crest can be found by the definite

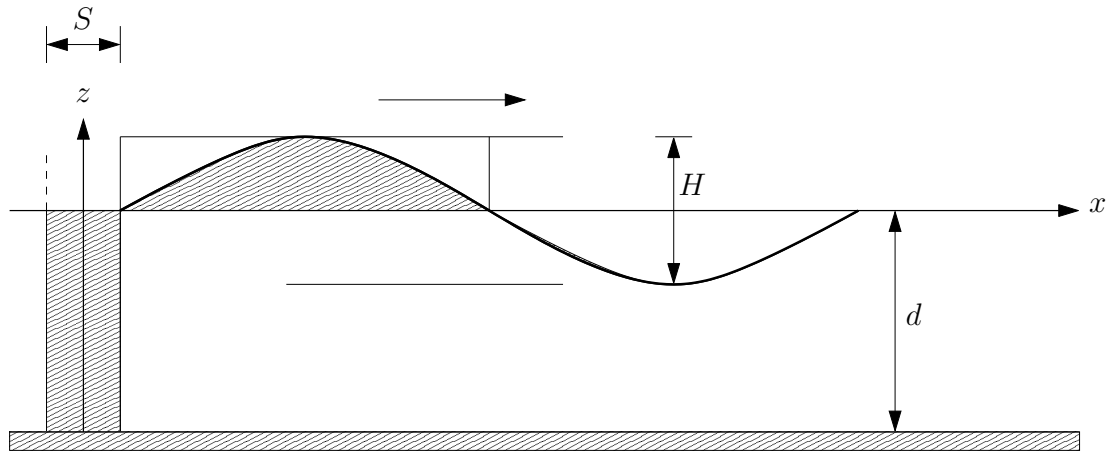


Figure 1.8: Simplified shallow water piston-type wave maker.

integral

$$\int_0^{L/2} \frac{H}{2} \sin\left(\frac{2\pi}{L}x\right) dx \quad (1.18)$$

Evaluating the integral and equating the two volumes gives

$$dS = \frac{HL}{2\pi} \quad (1.19)$$

which can be rearranged to give the height to stroke ratio for a piston-type wave maker

$$\left(\frac{H}{S}\right)_{\text{piston}} = kd. \quad (1.20)$$

If the vertical plane is hinged at the bottom, then the volume of water displaced by the wave maker is halved and therefore the height to stroke ratio becomes

$$\left(\frac{H}{S}\right)_{\text{flap}} = \frac{kd}{2}. \quad (1.21)$$

These two relationships will only be applicable in shallow water. For deeper water it can be shown that using Laplace's equation with treatments for the boundaries at the bed surface, the free surface and the wave maker, the first-order solution for a piston-type wave maker is (Hughes, 1993)

$$\left(\frac{H}{S}\right)_{\text{piston}} = \frac{4 \sinh^2(kd)}{\sinh(2kd) + 2kd}, \quad (1.22)$$

and for a flap-type wave maker

$$\left(\frac{H}{S}\right)_{\text{flap}} = \frac{4 \sinh(kd)}{\sinh(2kd) + 2kd} \left[ \sinh(kd) + \frac{1 - \cosh(kd)}{kd} \right]. \quad (1.23)$$

The first-order solutions for the height to stroke ratio of a piston-type and flap-type wave maker are plotted against values of  $kd$  in Fig. 1.9. The shallow water ratios derived above are also displayed on the same axis and show that they provide a good approximation up to the shallow water limit  $kd \leq 0.3$ .

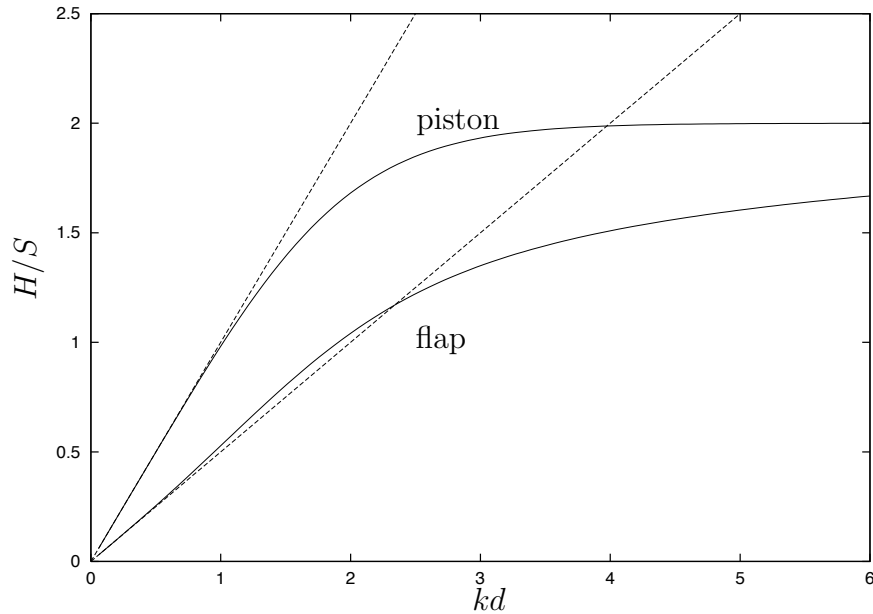


Figure 1.9: The first-order solutions for the  $H/S$  ratio for piston-type and flap-type wave makers.

The wave flume facility at the University of Edinburgh for which the flow solvers in this study have been applied to replicate experiments (see Chapters 3 and 5) uses an absorbing flap-type wave maker. The motion of the oscillating plane is controlled so that any reflected waves propagating towards the wave maker do not affect the incident waves generated.

### 1.2.1.1 The JONSWAP spectrum

Random waves in a typical sea state may appear to be random, but can be analysed assuming that they consist of the sum of an infinite number of sinusoids with differing frequencies, amplitudes and direction (Goda, 2000). A plot of the energy against the frequency for each of these wavelets gives a frequency spectrum that can be used as a description for the sea state. Given a frequency spectrum, it

is possible to take a random sample of  $n$  wavelets and using the principle of superposition, composite a random sea state with the same characteristics as the sea used to generate the frequency spectrum.

Hasselmann *et al.* (1973) developed a spectrum that describes surface waves by analysing the data collected by the JOInt North Sea WAve observation Project (JONSWAP). The JONSWAP spectrum is given in terms of the significant wave height and peak wave period by Goda (1988) as

$$S(f) = \alpha H_s^2 f_p^4 f^{-5} \gamma^\beta \exp \left[ -\frac{5}{4} \left( \frac{f_p}{f} \right)^4 \right], \quad (1.24)$$

$$\alpha = \frac{0.0624}{0.230 + 0.0336\gamma - [0.185/(1.9 + \gamma)]}, \quad (1.25)$$

$$\beta = \exp \left[ -\frac{(f - f_p)^2}{2\sigma^2 f_p^2} \right], \quad (1.26)$$

$$\sigma \approx \begin{cases} 0.07 & f \leq f_p \\ 0.09 & f > f_p \end{cases}, \quad (1.27)$$

where  $S(f)$  is the spectral density,  $H_s$  is the significant wave height (mean of the top 1/3 wave heights),  $f$  is the frequency of each wavelet,  $f_p = 1/T_p$  is the peak frequency,  $T_p$  is the peak wave period, and  $\gamma$  is the peak enhancement parameter that determines the sharpness of the spectral peak. Hasselmann *et al.* (1973) determined a value of  $\gamma = 3.3$  based on the wave conditions of the North Sea. A plot of the JONSWAP spectrum is shown in Fig. 1.10 for  $H_s = 1.0$  over a range of values for  $\gamma$ .

## 1.2.2 European Projects

Some of the work produced in this study was performed in collaborations with other research institutes during funded projects examining the effects of wave overtopping of coastal structures. These projects are summarised here for the purpose of acknowledgement and to provide an understanding in the current research focus in using CFD to model coastal processes.

### 1.2.2.1 VOWS project

The VOWS (Violent Overtopping by Waves at Seawalls) project is an EPSRC (Engineering and Physical Sciences Research Council) funded study to examine and provide a better understanding of violent overtopping processes. Investigators included Tom Bruce, Dr. Jonathan Pearson from the University of Edinburgh

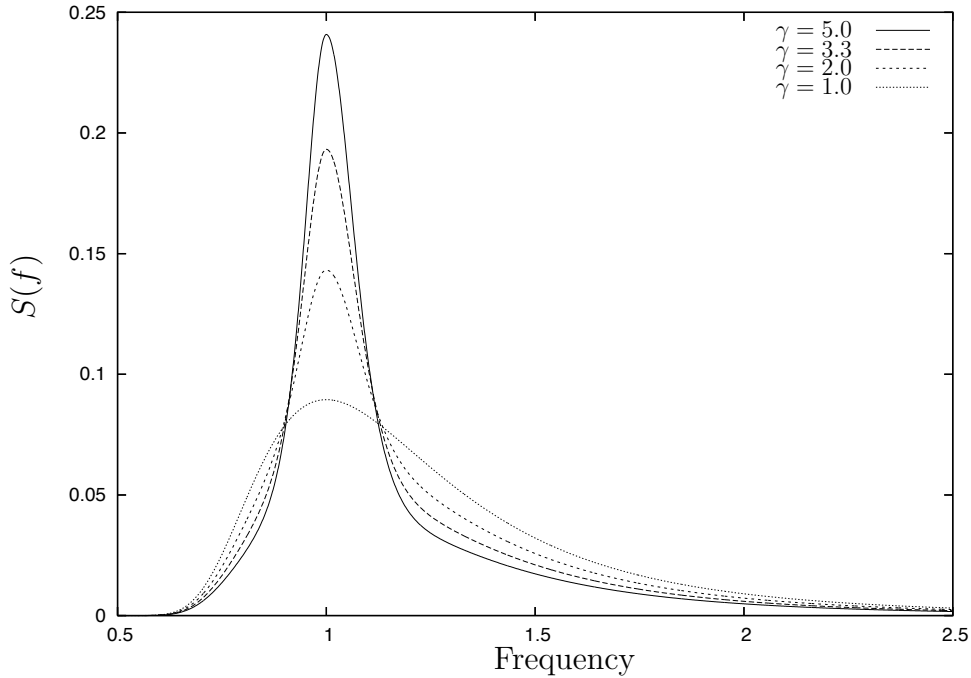


Figure 1.10: A plot of the JONSWAP spectrum for various values of the peak enhancement parameter  $\gamma$

and Professor William Allsop from HR Wallingford who conducted the small scale physical modelling of violent wave overtopping at the University of Edinburgh's wave flume facility for one-dimensional experiments and HR Wallingford's wave basin for two-dimensional experiments. Numerical modelling of violent wave overtopping was carried out at the Centre for Mathematical Modelling and Flow Analysis (CMMFA) at the Manchester Metropolitan University.

### 1.2.2.2 CLASH project

The CLASH (Crest Level Assessment of coastal Structures by full scale monitoring, neural network prediction and Hazard analysis on permissible wave overtopping) project is a European Union funded study examining the effects that scale has on overtopping predictions and to provide a generic prediction method for the crest height in the design of coastal structures. In addition gathering overtopping data from multiple test sites and wave tank experiments, the numerical predictions included applications of CFD and Artificial Neural Networks (ANN). A full list of the collaborators can be found on the CLASH website.

## 1.3 Thesis Outline

It was the aim of this study to extend the SWE based AMAZON model to be able to model wave propagation in deeper water ( $d/L > 1/20$ ), in addition to providing predictions of wave run-up and overtopping of coastal structures. The numerical models are compared and validated against physical experiments. The research is presented in six chapters. An overview of the field of coastal engineering and numerical models, introduction to linear wave theory and current prediction methods is given in Chapter 1. An existing numerical model based on the SWE is discussed and validated against standard test cases in Chapter 2. This model is then applied to model a series of wave flume experiments focusing on violent wave overtopping in Chapter 3. The use of a SWE based model of this type to provide predictions for violent wave overtopping has never previously been examined. The statistical analysis and comparisons with an empirical model are also presented in Chapter 3.

The extended Boussinesq equations, along with their dispersion properties and a numerical solver are presented in Chapter 4 and are tested against standard test cases. A hybrid numerical scheme that can use either a SWE or a Boussinesq based model for modelling flow in shallow or intermediate depth water where appropriate is discussed in Chapter 5. This is the first time that this scheme has been used to solve Nwogu's extended Boussinesq formulation. The hybrid scheme is applied to Madsen and Sørensen's Boussinesq equations to model a range of run-up and overtopping experiments.

The conclusions made as a result of the research conducted are given in Chapter 6 along with further work that has been highlighted as a result of this study. The appendices are located at the back of this thesis and include two published papers that resulted from this work.

# Chapter 2

## The Shallow Water Flow Solver

Ideally, a numerical model of wave motion and interaction with solid structures would be based on the full Navier-Stokes equations. However, due to their complexity the solution methods applied to solve these equations require extensive computational resources. Until the computing power available to engineers allow for Navier-Stokes based models to be used, a common alternative is to use the shallow water equations (SWE). The SWE are a simplified depth averaged form of the Navier-Stokes equations. The depth averaging process works under the assumption that particle velocity is negligible in the vertical direction as represented in Fig. 1.3. The result of this simplifying assumption is a set of equations that are much simpler than the Navier-Stokes equations and as a result require significantly less computational effort to solve. The simplifying assumption does mean that the SWE are only applicable in shallow water where the depth to wavelength ratio is in the range  $d/L \leq 1/20$ .

This chapter is concerned with the numerical solution to the SWE both for the homogeneous form and the inclusion of source terms for modelling bed topography. The SWE are given in vector form and the finite-volume method is summarised in Sections 2.1 and 2.2. The numerical solver used here to solve the inviscid form is then presented in Sections 2.2.1–2.2.5. A comparison of the basic solver is made against a one-dimension dam break with both a wet and dry bed (Section 2.3). The treatment for the source terms is discussed in Section 2.4 and validated against various standard test cases examining the numerical scheme's ability to cope with tidal, subcritical, supercritical, transcritical flow and discontinuities in the bed topography (Section 2.5).

## 2.1 The Shallow Water Equations

The SWE written in vector notation are

$$\frac{\partial}{\partial t} \mathbf{U} + \nabla \cdot \mathbf{F}(\mathbf{U}) = \mathbf{S}_b + \mathbf{S}_f, \quad (2.1)$$

where  $\mathbf{U}$  is the vector of conserved variables,  $\mathbf{F}(\mathbf{U})$  is the flux vector function,  $\mathbf{S}_b$  and  $\mathbf{S}_f$  represents the vector of sources terms that model bed topography and bed friction and  $\nabla = \mathbf{i} \frac{\partial}{\partial x} + \mathbf{j} \frac{\partial}{\partial y}$  is the gradient operator.  $\mathbf{U}$ ,  $\mathbf{F}(\mathbf{U})$ ,  $\mathbf{S}_b$  and  $\mathbf{S}_f$  are given by

$$\mathbf{U} = \begin{pmatrix} \phi \\ \phi u \\ \phi v \end{pmatrix}, \quad \mathbf{F}(\mathbf{U}) = \begin{pmatrix} \phi \mathbf{q} \\ \phi u \mathbf{q} + \frac{1}{2} \phi^2 \mathbf{i} \\ \phi v \mathbf{q} + \frac{1}{2} \phi^2 \mathbf{j} \end{pmatrix}, \quad (2.2)$$

$$\mathbf{S}_b = \begin{pmatrix} 0 \\ g \phi \frac{\partial H}{\partial x} \\ g \phi \frac{\partial H}{\partial y} \end{pmatrix}, \quad \mathbf{S}_f = \begin{pmatrix} 0 \\ -\frac{g}{\rho} \tau_{fx} \\ -\frac{g}{\rho} \tau_{fy} \end{pmatrix}, \quad (2.3)$$

where  $\phi = gh$  is the geopotential;  $g = 9.81 \text{ ms}^{-2}$  is the acceleration due to gravity;  $h$  is the water depth;  $u$  and  $v$  are the depth averaged velocities in the  $x$ - and  $y$ -directions respectively;  $\mathbf{q} = u\mathbf{i} + v\mathbf{j}$  is the velocity vector;  $H$  is the partial depth between the bed surface and a fixed datum and  $\tau_{fx}$ ,  $\tau_{fy}$  are the bed shear stress terms given by

$$\tau_{fx} = \rho C_f u \sqrt{u^2 + v^2}, \quad \tau_{fy} = \rho C_f v \sqrt{u^2 + v^2}, \quad (2.4)$$

where  $C_f$  is the bed friction coefficient which can be estimated from  $C_f = g/C_z^2$  where  $C_z$  is the Chezy coefficient (Zhou *et al.*, 2001).

The SWE are hyperbolic in nature meaning that discontinuities can be admitted into the solution (Appendix A). This is important for modelling shallow water flows as breaking waves are likely to occur when the ratio of wave height to water depth increases.

## 2.2 The Finite-Volume Method

The finite-volume method solves partial differential equations (PDEs) by calculating the values of the conserved variables averaged across a finite-volume cell (Fig. 2.1). The one major advantage that finite-volume methods have over finite-difference methods is that a non-uniform grid can be used to model complex

solution domains. An additional advantage of finite-volume methods has over alternative methods such as the finite-difference method is that because the conservative variables are contained within the volume element and not at nodes or surfaces, boundary conditions can be applied without specifically changing the values of the conserved variables.

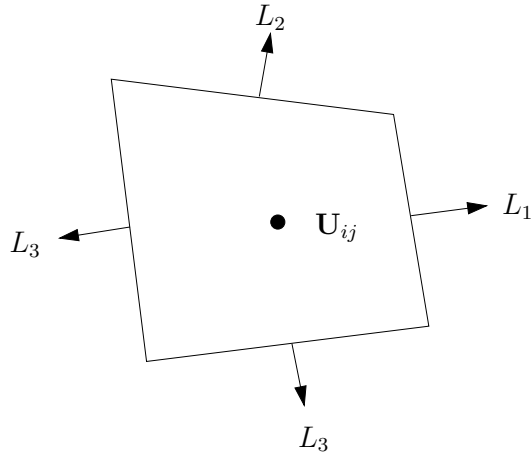


Figure 2.1: Finite-volume cell.

An integral form of the SWE is achieved by integrating the homogeneous form of Eq. (2.1) over a volume element of area  $A_0$  as in Fig. 2.1 (Mingham and Causon, 1998)

$$\frac{\partial}{\partial t} \iint_{A_0} \mathbf{U} dA_0 + \iint_{A_0} \nabla \cdot \mathbf{F}(\mathbf{U}) dA_0 = 0. \quad (2.5)$$

Applying Gauss's divergence theorem to the second term of Eq. (2.5) leads to a semi-discrete finite-volume discretisation for the cell centre mean value of the conserved variables

$$\frac{\partial}{\partial t} \mathbf{U}_0 = -\frac{1}{A_0} \sum_{m=1}^M \mathbf{F}(\mathbf{U}_m) \cdot \mathbf{L}_m. \quad (2.6)$$

where  $\mathbf{F}(\mathbf{U}_m) \cdot \mathbf{L}_m$  are the fluxes normal to each cell face  $m$  and  $M$  is the number of cell faces.

### 2.2.1 The Hancock scheme

The finite-volume scheme used here is a Godunov-type, two-stage scheme attributed to Hancock by van Leer (1985). The values of the conserved variables that are required for the fluxes at the cell interfaces are calculated using a piecewise linear reconstruction method that ensures that no spurious oscillations affect the solution.

The predictor stage is given by

$$\mathbf{U}_{ij}^{n+1/2} = \mathbf{U}_{ij}^n - \frac{\Delta t}{2A_{ij}} \left( \sum_{m=1}^M \mathbf{F}(\mathbf{U}_m) \cdot \mathbf{L}_m \right), \quad (2.7)$$

where  $n$  is the time step counter,  $ij$  is the cell index,  $\Delta t$  is the time step,  $A_{ij}$  is the cell area,  $\mathbf{L}_m$  is the cell side vector defined as the cell side multiplied by the outward pointing unit normal vector and  $M$  is the number of sides of the cell  $ij$ . The fluxes at the cell interfaces are calculated using slope limited gradients based upon neighbouring cell data as explained in Section 2.2.2.

The corrector stage provides a fully conservative solution over one time step and is given by

$$\mathbf{U}_{ij}^{n+1} = \mathbf{U}_{ij}^n - \frac{\Delta t}{A_{ij}} \left( \sum_{m=1}^M \mathbf{F}(\mathbf{U}_m^L, \mathbf{U}_m^R)^{n+1/2} \cdot \mathbf{L}_m \right), \quad (2.8)$$

where the values of the flux vector  $\mathbf{F}(\mathbf{U}_m^L, \mathbf{U}_m^R)$  are solutions to local Riemann problems at each cell interface (Section 2.2.3) calculated using slope limited gradients applied to the predictor values  $\mathbf{U}_{ij}^{n+1/2}$ .

### 2.2.2 MUSCL Reconstruction

It is well known that second-order scheme exhibits spurious oscillations when resolving discontinuities within the solution domain. Various methods have been applied to numerical schemes to either dampen or remove these oscillations from the solution. Harten *et al.* (1983) proposed a scheme based upon the principle of Total Variation (TV). TV is basically defined as the sum of the differences of the conserved variables between neighbouring cells. Total Variation Diminishing (TVD) schemes are designed to insure that the TV for a successive time step is less than the TV for the previous time step. This condition is preserved by using a non-oscillatory first-order scheme where oscillations are likely to occur and a higher order scheme is used elsewhere. This creates a scheme that is not fully second-order and can experience difficulties in resolving shocks. Instead, in this study, a monotonic preservation scheme is used.

Monotonic Upwind Schemes for Conservation Laws (MUSCL schemes) use the values of the conserved variables of the cells immediately adjacent to the cell  $i$  to calculate a slope limited gradient that ensure no spurious oscillations enter the solution (Fig.2.2). The values of the conserved variables that the cell interfaces

require in the predictor and corrector stages of the Hancock scheme, Eqs. (2.7) and (2.8), are then calculated using piecewise continuous linear reconstruction methods based upon the slope limited gradients.

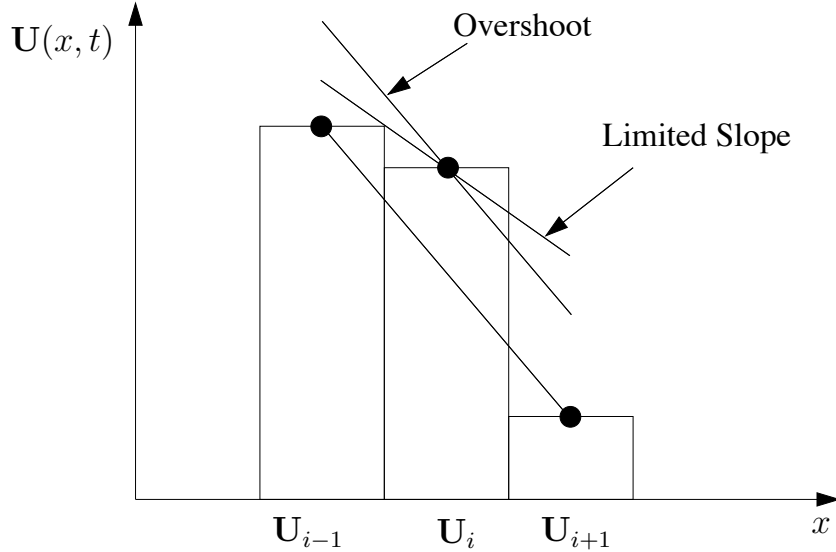


Figure 2.2: Piecewise continuous MUSCL reconstruction.

Therefore for cell  $i$ , the values of the conserved variables at the interfaces ( $i \pm 1/2$ ) are

$$\mathbf{U}_{i\pm 1/2} = \mathbf{U}_i \pm \frac{1}{2} \Delta x_i \delta \mathbf{U}_i, \quad (2.9)$$

where  $\delta \mathbf{U}_i$  are slope limited gradients across cell  $i$  and

$$\Delta x_i = x_{i+1/2} - x_{i-1/2}. \quad (2.10)$$

The calculation of these slope limited gradients is performed to ensure that overshoots and undershoots at the cell interfaces are minimised.

Three of the most common slope limiter functions are given below:

- minmod Limiter

$$G(a, b) = \max[0, \min(a, b)]. \quad (2.11)$$

- superbee Limiter

$$G(a, b) = s \max[0, \min(2|b|, sa), \min(|b|, 2sa)]. \quad (2.12)$$

- van Leer Limiter

$$G(a, b) = \frac{a|b| + |a|b}{|a| + |b|}. \quad (2.13)$$

where

$$G(a, b) = G \left( \frac{\mathbf{U}_{i+1} - \mathbf{U}_i}{x_{i+1} - x_i}, \frac{\mathbf{U}_i - \mathbf{U}_{i-1}}{x_i - x_{i-1}} \right), \quad (2.14)$$

and  $s = \text{sign}(b)$ . The choice of slope limiting function will have a subtle effect on the solution obtained from the Godunov-type scheme. Therefore, a numerical investigation is advised in order to select the most suitable slope limiting function. A comparison of the slope limiter functions given in Eqs. (2.11)–(2.13) can be found in Sections 2.3.1 and 2.3.2.

### 2.2.3 The HLL Riemann Solver

The calculation of the corrector step of the Hancock scheme, Eq. (2.8), requires the solution to local Riemann problems at each cell interface. In this study, an approximate Riemann solver developed by Harten, Lax and van Leer (Harten *et al.*, 1983) (HLL) is used. The HLL Riemann solver has been extensively tested (Mingham and Causon, 1998; Hu *et al.*, 2000) and is found to be accurate and robust in practice.

Consider the simple Riemann fan consisting of three constant states separated by the fastest and slowest acoustic waves,  $s_L$  and  $s_R$  respectively, between which is a constant region as shown in Fig. 2.3.

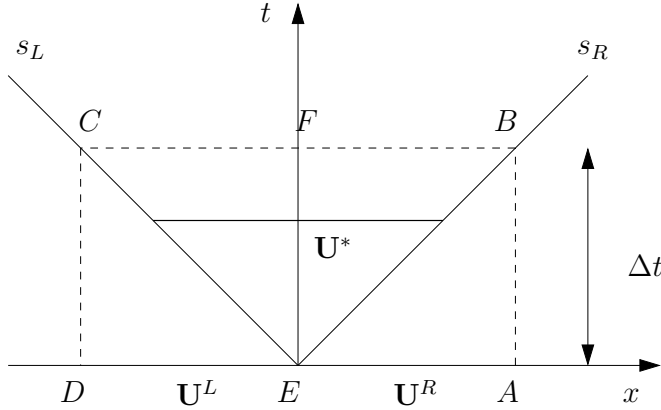


Figure 2.3: Simple Riemann Fan.

Integrating round the contour  $ABCD$  obtains

$$\mathbf{F}(\mathbf{U}^R)\Delta t - \mathbf{U}^*(s_R\Delta t - s_L\Delta t) - \mathbf{F}(\mathbf{U}^L)\Delta t + \mathbf{U}^L s_L + \mathbf{U}^R s_R \Delta t = 0. \quad (2.15)$$

Rearranging to make  $\mathbf{U}^*$  the subject gives

$$\mathbf{U}^* = \frac{\mathbf{F}(\mathbf{U}^R) - \mathbf{F}(\mathbf{U}^L) - s_L \mathbf{U}^L + s_R \mathbf{U}^R}{s_R - s_L}. \quad (2.16)$$

It follows that

$$\mathbf{F}(\mathbf{U}^*) = \frac{s_R \mathbf{F}(\mathbf{U}^L) - s_L \mathbf{F}(\mathbf{U}^R) + s_L s_R (\mathbf{U}^R - \mathbf{U}^L)}{s_R - s_L}. \quad (2.17)$$

For supercritical flow ( $s_L \geq 0$ ) and subcritical flow ( $s_R \leq 0$ ) the Riemann fluxes are defined by the interface fluxes using the relation

$$\mathbf{F}(\mathbf{U}^L, \mathbf{U}^R) = \begin{cases} \mathbf{F}(\mathbf{U}^L) & \text{if } s_L \geq 0 \\ \mathbf{F}(\mathbf{U}^L, \mathbf{U}^R) & \text{if } s_L < 0 < s_R \\ \mathbf{F}(\mathbf{U}^R) & \text{if } s_R \leq 0 \end{cases}. \quad (2.18)$$

### 2.2.3.1 Wave speed estimates

The wave speed estimates of the slowest and fastest travelling waves  $s_L$  and  $s_R$  are defined by

$$s_L = \min \left( \mathbf{q}_L \cdot \mathbf{n}_m - \sqrt{\phi_L}, u_s - \sqrt{\phi_s} \right), \quad (2.19)$$

$$s_R = \max \left( \mathbf{q}_R \cdot \mathbf{n}_m + \sqrt{\phi_R}, u_s + \sqrt{\phi_s} \right), \quad (2.20)$$

where

$$u_s = \frac{(\mathbf{q}_L + \mathbf{q}_R) \cdot \mathbf{n}_m}{2} + \sqrt{\phi_L} - \sqrt{\phi_R}, \quad (2.21)$$

$$\sqrt{\phi_s} = \frac{\sqrt{\phi_L} + \sqrt{\phi_R}}{2} - \frac{(\mathbf{q}_L - \mathbf{q}_R) \cdot \mathbf{n}_m}{4}, \quad (2.22)$$

and  $\mathbf{n}_m$  is the normalised cell side vector for face  $m$  (Toro, 1992).

Alternatively, when there exists a dry bed (see Section 2.2.6 for definition of a dry bed), the following estimates are used (Fraccarollo and Toro, 1995)

- right dry bed:

$$s_L = \mathbf{q}_L \cdot \mathbf{n}_m - \sqrt{\phi_L}, \quad s_R = \mathbf{q}_L \cdot \mathbf{n}_m + 2\sqrt{\phi_L}. \quad (2.23)$$

- left dry bed:

$$s_L = \mathbf{q}_R \cdot \mathbf{n}_m - 2\sqrt{\phi_R}, \quad s_R = \mathbf{q}_R \cdot \mathbf{n}_m + \sqrt{\phi_R}. \quad (2.24)$$

## 2.2.4 Boundary conditions

As discussed in Section 2.2.2, the calculation of the conserved variables at the cell interfaces are dependent upon cell centre values from the neighbouring cells. This does not present a problem for the cells in the middle of the solution domain. However, for those cells that have interfaces on the boundary, the gradient across the cell interface normal to the boundary requires data from cells that do not exist. This is overcome by creating ‘ghost’ cells outside of the boundary (Fig. 2.4). The values of the ghost cells can be specified to influence the behaviour of the fluid within the computational domain.

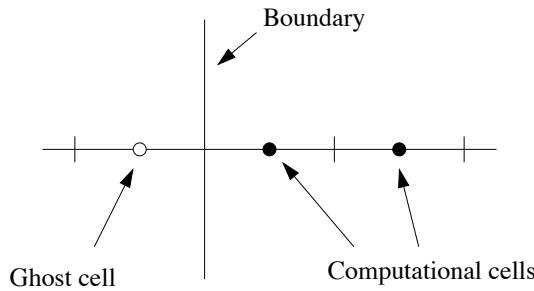


Figure 2.4: A diagram of a one-dimensional boundary.

In this section, two main boundary conditions are discussed: the transient flow boundary condition and the solid wall boundary condition. Transient flow boundary conditions are mainly used where a semi-infinite solution domain is required and allows waves to propagate out of the solution domain without reflection. The values of the geopotential and velocity of the ghost cells are given by (for a one-dimensional mesh)

$$\begin{aligned}\phi_0 &= \phi_1, & \phi_{n+1} &= \phi_n, \\ u_0 &= u_1, & u_{n+1} &= u_n,\end{aligned}\tag{2.25}$$

where the cell indices 0 and  $n + 1$  represent the ghost cells, and the cell indices 1 and  $n$  denote the first computational cells in from the boundary.

Solid wall boundaries are applied where flow out of the solution domain is zero, i.e.,  $\nabla q \cdot \mathbf{n} = 0$ . Simple linear interpolation gives an expression for the velocity at the ghost cells as

$$\begin{aligned}\phi_0 &= \phi_1, & \phi_{n+1} &= \phi_n, \\ u_0 &= -u_1, & u_{n+1} &= -u_n.\end{aligned}\tag{2.26}$$

### 2.2.5 Time step calculation

For any time marching scheme, it is preferable for the value of the time step  $\Delta t$  to be as large as possible to decrease the overall computation time. However, unless the scheme that is being used is unconditionally stable, there will exist a limit to how large the value of  $\Delta t$  can be so that the scheme remains stable. Courant, Friedrichs and Lewy (Morton and Mayers, 1994) derived a relationship that expresses the maximum allowable time step as a function of the spatial step,  $\Delta x$ , the wave speeds and a free parameter  $\nu$ .

$$\Delta t = \nu \min(\Delta t_x, \Delta t_y), \quad (2.27)$$

where

$$\Delta t_x = \min_i \left( \frac{\Delta x_i}{|\mathbf{q}_{ij}| + \sqrt{\phi_{ij}}} \right), \quad (2.28)$$

$$\Delta t_y = \min_j \left( \frac{\Delta y_i}{|\mathbf{q}_{ij}| + \sqrt{\phi_{ij}}} \right). \quad (2.29)$$

This relationship is commonly known as the CFL condition (Courant *et al.*, 1928, 1967) and the  $\nu$  parameter is called the Courant number. For the Hancock scheme to remain stable, it can be shown that the Courant number can take a value in the region  $0 < \nu \leq 1$  although, in practice, it is better to specify a value of  $\nu$  that is less than unity to ensure against computational rounding errors. In this study, all calculations performed using the Hancock scheme have used a Courant number of  $\nu = 0.9$ .

### 2.2.6 Minimum wet depth parameter

Although the numerical solver discussed in the previous sections will remain stable as long as the CFL condition is not violated, modelling cases where wetting and drying occurs will cause instabilities in the solver unless some form of special treatment is used. These instabilities occur when a negative value for the mass of water, of depth  $h$ , is calculated. Not only is this not physically possible in a modelling sense, it also causes the solver to attempt to find the square root of a negative number either in the calculation of the wave speeds or the time step. In order to prevent this from occurring, a minimum wet depth parameter,  $\delta$ , is introduced where if the water depth is calculated as being less than  $\delta$  a dry cell is assumed. Typically the value of  $\delta$  should be as close to zero as possible whilst

retaining the stability of the numerical scheme. In all calculations performed in this study a value of  $\delta = 10^{-4}$  metres is used.

## 2.3 Numerical Results

The MUSCL-Hancock scheme described in Section 2.2 is applied to solve the one-dimensional dam break problem. This is a common test of any numerical solver of hyperbolic conservation equations as the solution can include the resolution of a bore wave that, without proper treatment, will cause a poorly designed numerical solver to become unstable. In addition, there is an exact solution (Wu *et al.*, 1999) which can be used for comparison with the computed solution.

The one-dimensional dam break is an initial value problem (IVP) consisting of two still bodies of water of different heights. The upstream body (the reservoir) is separated from the downstream body of water by a partition that is instantaneously removed at time  $t = 0$  seconds. The two bodies of water are allowed to interact under the force of gravity.

### 2.3.1 One-dimensional dam break problem: Wet bed

A solution domain of length  $L = 1.0$  metres is discretised into 100 computational cells ( $\Delta x = 0.01$  m) with the partition located exactly half way along the flume ( $x = 0.5$  m). The initial water depths to the left- and right-hand side of the partition are given by

$$h(x) = \begin{cases} 1.0 \text{ m} & x \leq L/2 \\ 0.1 \text{ m} & x > L/2, \end{cases}, \quad (2.30)$$

and the solution is iterated until time  $t = 0.1$  seconds. The computed solutions for the water depth and horizontal velocity using the three slope limiting functions described in Section 2.2.2 are compared against the exact solution in Figs. 2.5 and 2.6.

The solution of the wet bed one-dimensional dam break problem takes the form of two waves. A bore wave is formed propagating downstream as gravity acts on the upstream body of water. The mass of water displaced from the upstream body of water creates an upstream travelling rarefaction wave. Comparisons between the analytical solution and the numerical solution (Figs. 2.5 and 2.6) shows that the numerical scheme accurately solves the SWE and the discontinuity formed by the bore wave is resolved. The choice of slope limiter function has a subtle

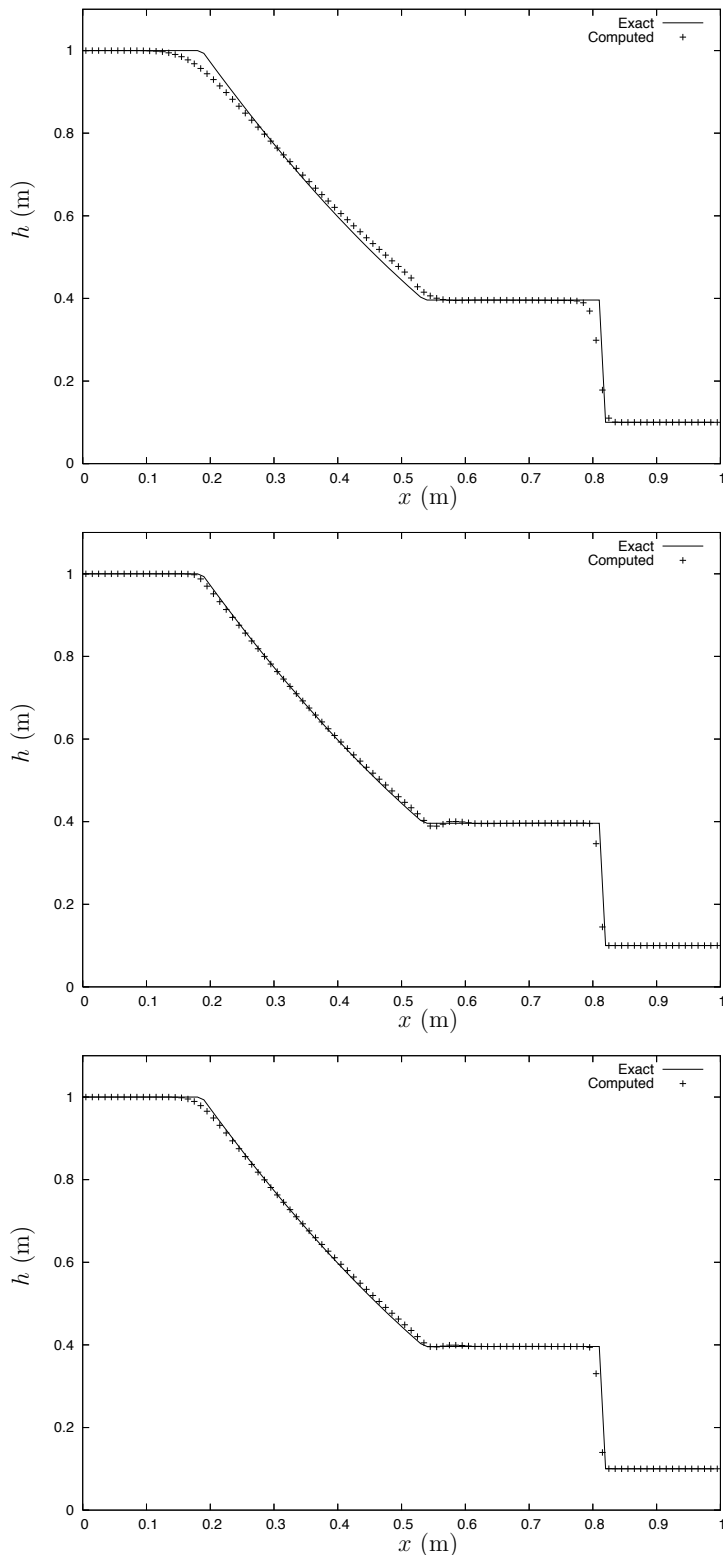


Figure 2.5: One-dimensional dam break solution: solution of the water height using the minmod limiter (top), the superbee limiter (middle) and the van Leer limiter (bottom).

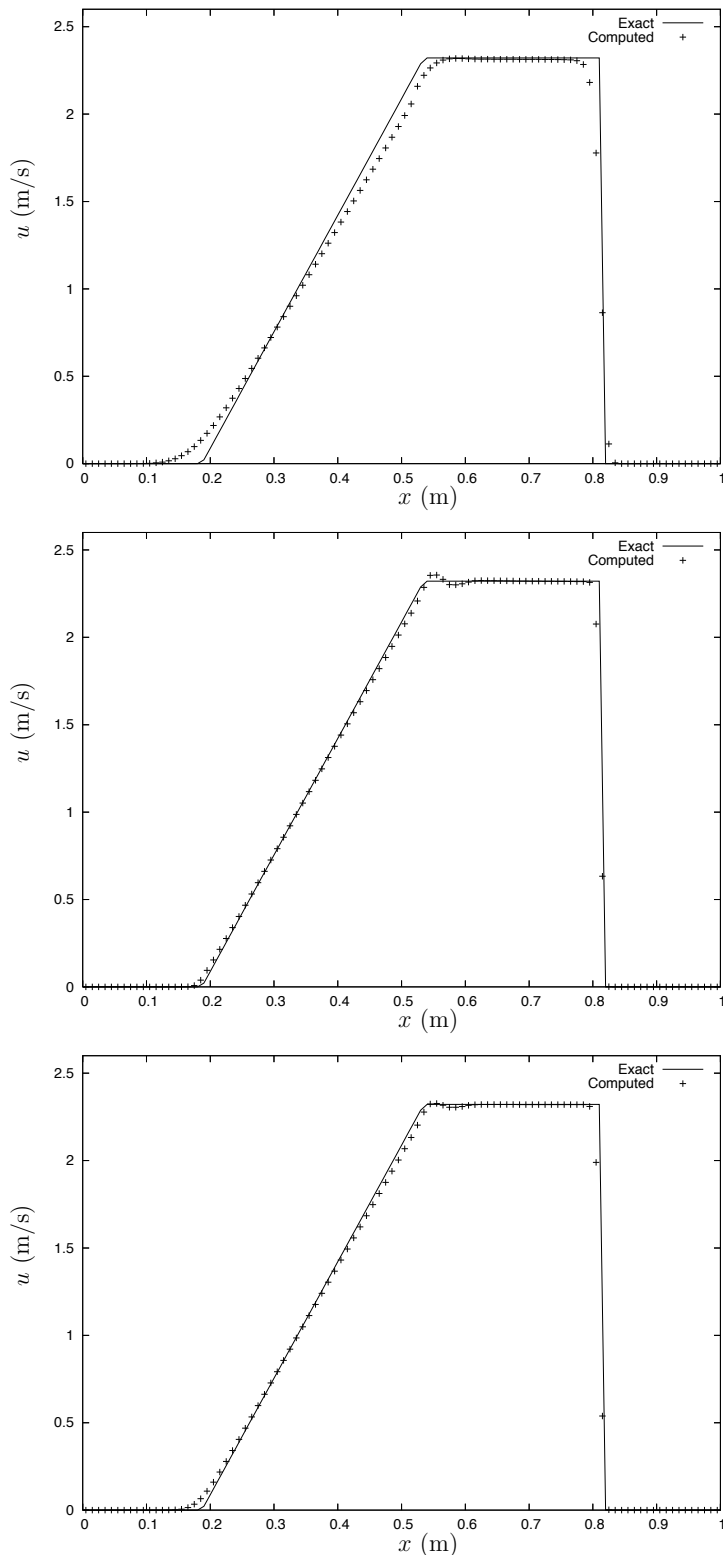


Figure 2.6: One-dimensional dam break: solution of the horizontal velocity using the minmod limiter (top), the superbee limiter (middle) and the van Leer limiter (bottom).

influence on the solution and therefore the most suitable limiter function should be chosen for all subsequent calculations. The minmod limiter tends to smooth out the solution where an abrupt change in gradient occurs, most notably at the leading edge of the bore wave. The solution calculated using the superbee limiter function is more accurate than the minmod solution. However, it does have a tendency to create over- and under-shoots at points in the solution domain where there is an abrupt change of gradient. This is most evident in the plot of the depth-averaged velocity. The van Leer slope limiter function neither smooths out the solution or creates over- and under-shoots and it appears to be the most suitable choice of slope limiting function in this case.

### 2.3.2 One-dimensional dam break problem: Dry bed

The dry bed dam break problem is a difficult test of the numerical scheme's ability to resolve the horizontal velocity where the water is very shallow. This test is also useful for validating a numerical scheme's treatment of the interface between wet and dry regions necessary for modelling wave run-up on a dry slope. The length of the solution domain remains at  $L = 1.0$  metres with the partition located half-way along the flume at  $x = 0.5$  metres. The water depths to the left- and right-hand sides of the partition are given by

$$h(x) = \begin{cases} 1.0\text{m} & x \leq L/2 \\ 0.0\text{m} & x > L/2 \end{cases}. \quad (2.31)$$

The computational domain is discretised into 100 computational cells giving  $\Delta x = 0.01$  metres. The solution is iterated until  $t = 0.07$  seconds. The computed solutions for the water depth and horizontal velocity using the three slope limiting functions described in Section 2.2.2 are compared against the exact solutions in Figs. 2.7 and 2.8.

The solution of the depth-averaged velocity in the dry bed dam break problem is of most interest here (Fig. 2.8) as it shows more clearly the difference between the analytical solution (Wu *et al.*, 1999) and the computed solution. As gravity acts on the upstream body of water, a wave front propagates downstream without the formation of a bore wave. The velocity of the rarefaction wave steadily increases in an almost linear fashion until it reaches its peak at the wave front where water depth is at a minimum. The velocity drops abruptly to zero where there is no water present. Both the minmod and superbee slope limiting functions fail to replicate the abrupt change in gradient at the leading edge of the upstream trav-

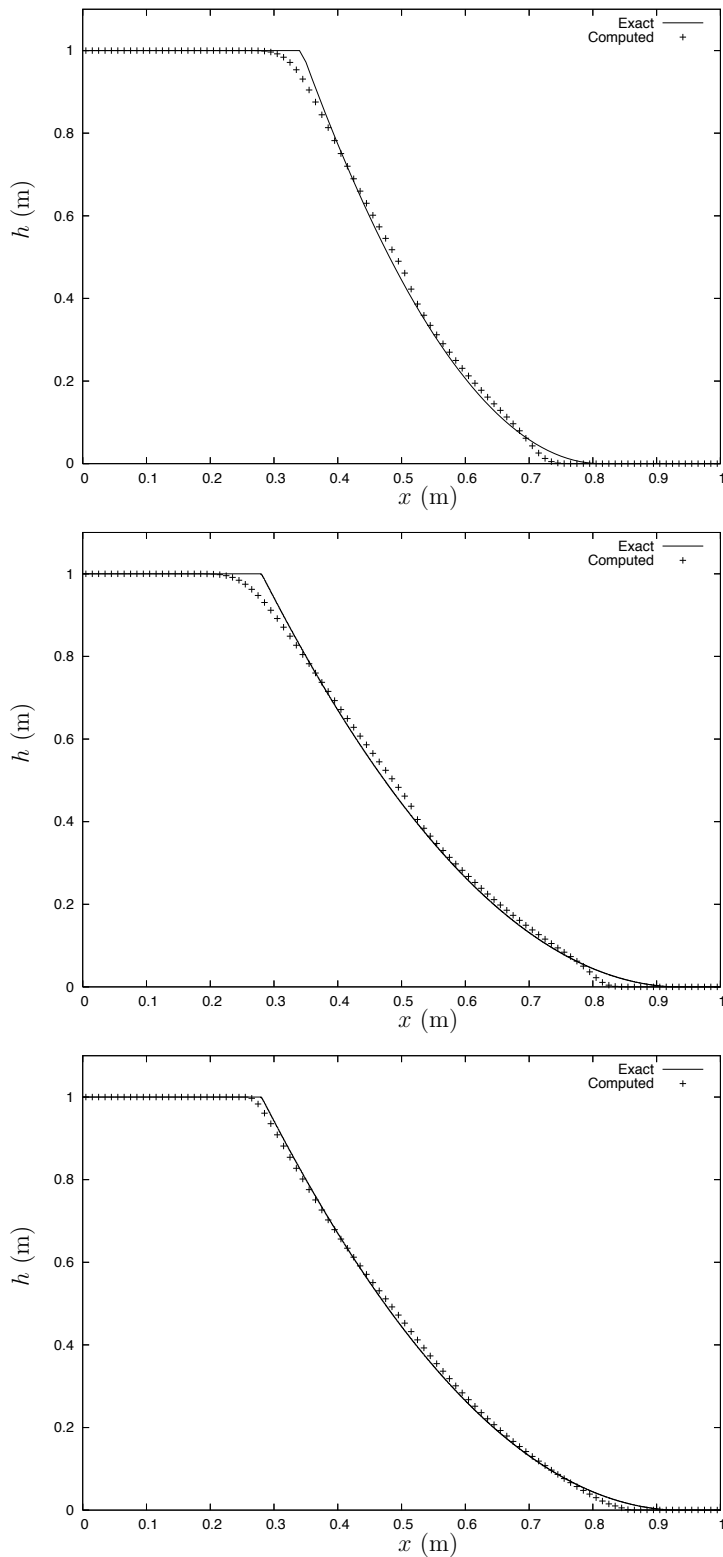


Figure 2.7: One-dimensional dam break with dry bed: solution of the water depth using the minmod limiter (top), the superbee limiter (middle) and the van Leer limiter (bottom).

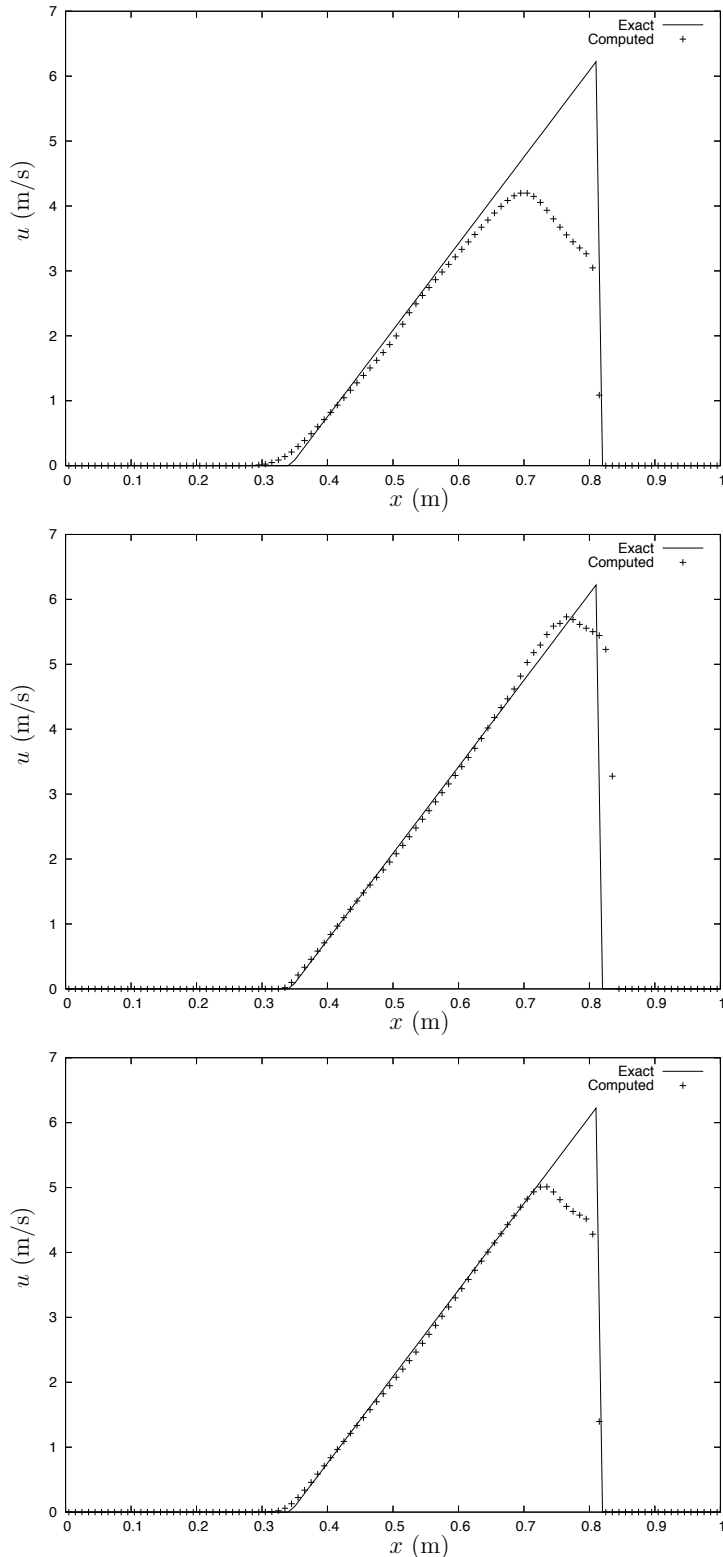


Figure 2.8: One-dimensional dam break with dry bed: solution of the horizontal velocity using the minmod limiter (top), the superbee limiter (middle) and the van Leer limiter (bottom).

elling rarefaction wave. All three limiter functions fail to model the peak velocity. However, the superbee limiter provides the best solution in this case.

In this study, all subsequent computations using the MUSCL-Hancock scheme have been performed using the van Leer limiter. The analysis performed in this section indicates that the van Leer limiter is superior to both the minmod and superbee slope limiting functions. Although the superbee limiter was better at modelling the depth-averaged velocity in the dry bed dam break problem, use of the superbee limiter can allow negative values for the water depth to enter the solution and the numerical scheme crashes at the next time step.

## 2.4 The Surface Gradient Method

The MUSCL-Hancock scheme presented in Section 2.2 solves the homogeneous form of the SWE, i.e., the left-hand side of Eq. (2.1) that contains the terms that model advection only ( $\mathbf{S}_b + \mathbf{S}_f = \mathbf{0}$ ). The applications of this inviscid form of the SWE are limited to flat bed shock and bore wave propagation problems. Therefore, the inclusion of source terms that model bed topography are necessary to ensure more realistic formulations applicable to problems such as wave run-up and overtopping of coastal structures and tidal flows in coastal water regions. Care needs to be taken when solving the SWE, including source terms, as a naïve treatment of the source terms will lead to non-physical behaviour of the fluid (Leveque, 1998).

The numerical treatment of source terms has received particular attention in the last few years with a variety of different methods proposed. Garcia-Navarro and Váquez-Cendón (2000) proposed an upwind scheme which utilises an extension of the formulation of Roe's scheme (Roe, 1981). Another approach was proposed by Hu *et al.* (2000), in which the authors split the SWE into two parts: the inviscid terms and the source terms. The scheme described in Section 2.2 was used to solve the inviscid terms whilst a simple implicit Euler formulation was used to solve the source terms. This method has the disadvantage of using a finite-difference based solver for the source terms and additional constraints are placed on the time step calculation. Leveque (1998) proposed a method that balances the source terms and the flux gradients. The method works well for quasi-steady problems but encounters problems modelling transcritical flow with a shock.

The Surface Gradient Method (SGM) developed by Zhou *et al.* (2001) provides an accurate treatment of the source terms that requires very few alterations to the MUSCL-Hancock scheme. The SGM uses the water surface elevation as the

bases of the MUSCL reconstruction for the mass conservation equation and not the water depth as described in Section 2.2.2 (Fig. 2.9). This approach ensures that any errors that are caused by the difference between the gradient of the water height,  $h$ , and the gradient of the bed slope,  $z_b$ , do not affect the solution. The SGM was proven to be fully conservative and satisfies both the exact- $\mathcal{C}$  and  $\mathcal{Z}$  properties (García-Navarro and Vázquez-Cendón, 2000). A numerical scheme satisfies the exact- $\mathcal{C}$  property if it can replicate the exact solution to the stationary flow problem

$$h \equiv H, \quad u \equiv 0. \quad (2.32)$$

The definition of the exact- $\mathcal{Z}$  property is that a numerical scheme provides the exact values of a variable in the flow domain to the stationary flow case, Eq. (2.32), when using a centred discretisation for the treatment of the source terms.

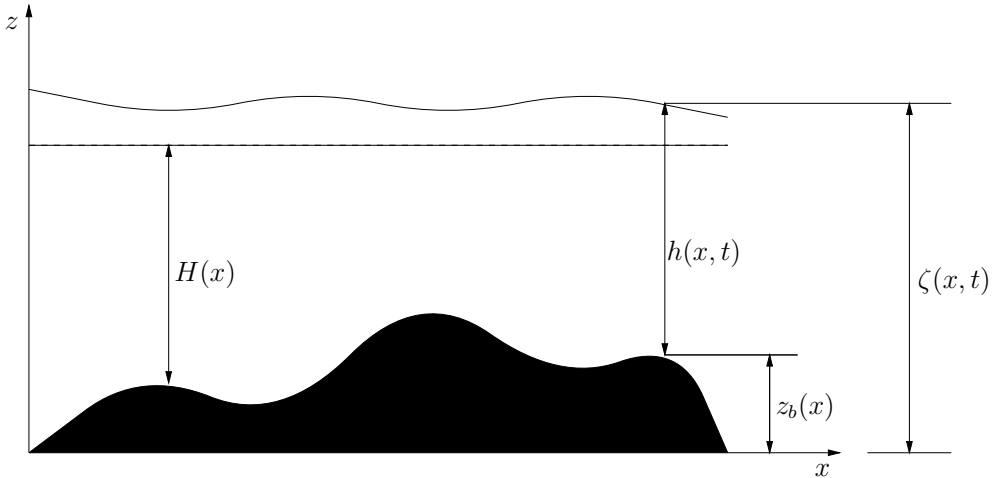


Figure 2.9: Definition sketch of bed topography.

#### 2.4.1 Data reconstruction

The SGM uses the water surface elevation as the basis for the MUSCL reconstruction as opposed to the water depth as used in the method presented in Section 2.2.2, hereafter referred to as the Depth Gradient Method (DGM). The water surface elevation,  $\zeta_i$ , is defined by (Fig. 2.9)

$$\zeta_i = h_i + z_{bi}, \quad (2.33)$$

where  $h$  is the water depth and  $z_b$  is the bed surface elevation (Fig. 2.9). It follows from the definition in Eq. (2.33) that the water surface elevations at the

cell interfaces are given by

$$\zeta_{i\pm 1/2} = \zeta_i \pm \frac{1}{2} \Delta x_i \delta \zeta_i. \quad (2.34)$$

The data reconstruction of the depth-averaged velocities are applied using the usual method. Rearrangement of Eq. (2.33) leads to the following expression for the reconstruction of the geopotential,  $\phi$ , at the interfaces ( $i \pm 1/2$ )

$$\phi_{i\pm 1/2} = g \left( \zeta_i \pm \frac{1}{2} \Delta x_i \delta \zeta_i - z_{bi\pm 1/2} \right). \quad (2.35)$$

In the case where there is no bed, i.e.,  $z_b = 0$ , the water surface elevation ( $\zeta$ ) is simply the water depth ( $h$ ) and the SGM returns to a scheme equivalent to the DGM.

#### 2.4.2 Discretisation of source terms

It has been shown that to maintain the conservative property of the SGM (and also satisfy the exact- $\mathcal{Z}$  property), a centred discretisation of the source terms is required (Zhou *et al.*, 2001). For example, for the bed slope term given in Eq. (2.3) the centred discretisation for the  $x$ -direction is

$$g\phi \frac{\partial H}{\partial x} = g\phi_i \left( \frac{H_{i+1/2} - H_{i-1/2}}{\Delta x} \right). \quad (2.36)$$

The bed slope elevations at the cell centres are determined simply by averaging the values at the cell interfaces

$$z_{bi} = \frac{z_{bi+1/2} + z_{bi-1/2}}{2}. \quad (2.37)$$

#### 2.4.3 Implementation within a Godunov-type method

The inclusion of source terms within the SWE that are being treated using the SGM require the following alterations to the Hancock scheme predictor and corrector stages, Eqs.(2.7) and (2.8)

- Predictor stage:

$$\mathbf{U}_{ij}^{n+1/2} = \mathbf{U}_{ij}^n - \frac{\Delta t}{2A} \left( \sum_{m=1}^M \mathbf{F}(\mathbf{U}_m)^n \cdot \mathbf{L}_m - A \mathbf{S}_{ij}^n \right), \quad (2.38)$$

- Corrector stage:

$$\mathbf{U}_{ij}^{n+1} = \mathbf{U}_{ij}^n - \frac{\Delta t}{A} \left( \sum_{m=1}^M \mathbf{F}(\mathbf{U}_m^L, \mathbf{U}_m^R)^{n+1/2} \cdot \mathbf{L}_m - A \mathbf{S}_{ij}^{n+1/2} \right). \quad (2.39)$$

#### 2.4.4 Boundary conditions

In the majority of cases, when using the SGM, the boundaries can be modelled in the same way as the DGM using the relationships discussed in Section 2.2.4. These cases are primarily where the bed level is constant at the boundary, i.e.,  $\nabla \cdot H = 0$ . In the case where the bed level is not constant at the boundary, the value of the water surface elevation at the boundary is assumed to be that of the first cell in from the boundary. Therefore, the value of  $\phi$  at the boundary is given by

$$\phi_0 = g(h_1 + z_{b1} - z_{b0}). \quad (2.40)$$

The value of the depth-averaged velocity is taken as the same as the first cell in from the boundary as in Section 2.2.4.

## 2.5 Numerical Results

The SGM described in the previous section has been validated against a number of test cases. Tidal wave flow over a smooth bed and an irregular bed is examined in Sections 2.5.1 and 2.5.2. The numerical scheme's ability to resolve subcritical, supercritical and transcritical flow with and without shocks is tested using flow over a bump in the bed surface in Section 2.5.3. A quasi-stationary test case used by Leveque (1998) to test his flux balancing scheme is applied to test the SGM for very small perturbations in the water surface in Section 2.5.4. Finally, flow over a submerged step tests the scheme's ability to model a discontinuity in the bed profile in Section 2.5.5.

### 2.5.1 Tidal wave flow

One of the principal applications for the SWE is the modelling of tidal wave flow. Here the SGM have been used to solve a tidal flow problem over a varying bed which Bermudez and Vázquez-Cendón (1994) used to test their upwind discretisation of the source terms.

The length,  $L$ , of the solution domain is 14,000 metres, which has been dis-

cretised using 50 computational cells ( $\Delta x = 280$  metres). The bed topography is defined using

$$z_b = H(0) - H(x), \quad (2.41)$$

where

$$H(x) = 50.5 - \frac{40x}{L} - 10 \sin \left[ \pi \left( \frac{4x}{L} - \frac{1}{2} \right) \right]. \quad (2.42)$$

The initial and boundary conditions are

$$h(x, 0) = H(x), \quad (2.43)$$

$$u(x, 0) = 0, \quad (2.44)$$

and

$$h(0, t) = H(0) + 4 - 4 \sin \left[ \pi \left( \frac{4t}{86,400} + \frac{1}{2} \right) \right], \quad (2.45)$$

$$u(L, t) = 0. \quad (2.46)$$

There exists an asymptotic solution to this tidal flow problem which is was stated by Bermudez and Vázquez-Cendón (1994) as

$$h(x, t) = H(x) + 4 - 4 \sin \left[ \pi \left( \frac{4t}{86,400} + \frac{1}{2} \right) \right], \quad (2.47)$$

$$u(x, t) = \frac{(x - L)\pi}{5,400h(x, t)} \cos \left[ \pi \left( \frac{4t}{86,400} + \frac{1}{2} \right) \right]. \quad (2.48)$$

The top graph in Fig. 2.10 shows a comparison between the numerical water surface and the analytical water surface at time,  $t = 7552.13$  seconds, where the tidal wave has risen to a water surface elevation of 62.68 metres. There are very few discrepancies between the analytical water surface solution and the numerical water surface solution. The bottom graph in Fig. 2.10 shows a comparison of the depth-averaged velocity between the analytical and numerical results for the same time period. The SGM has slightly underestimated the velocity across the solution domain.

### 2.5.2 Tidal wave flow over an irregular bed

A further test using the tidal wave conditions defined in Eqs.(2.43)–(2.45) was proposed by a workshop on dam break simulation (Goutal and Maurel, 1997) and was also used by Vázquez-Cendón (1999) to test their upwind scheme over an

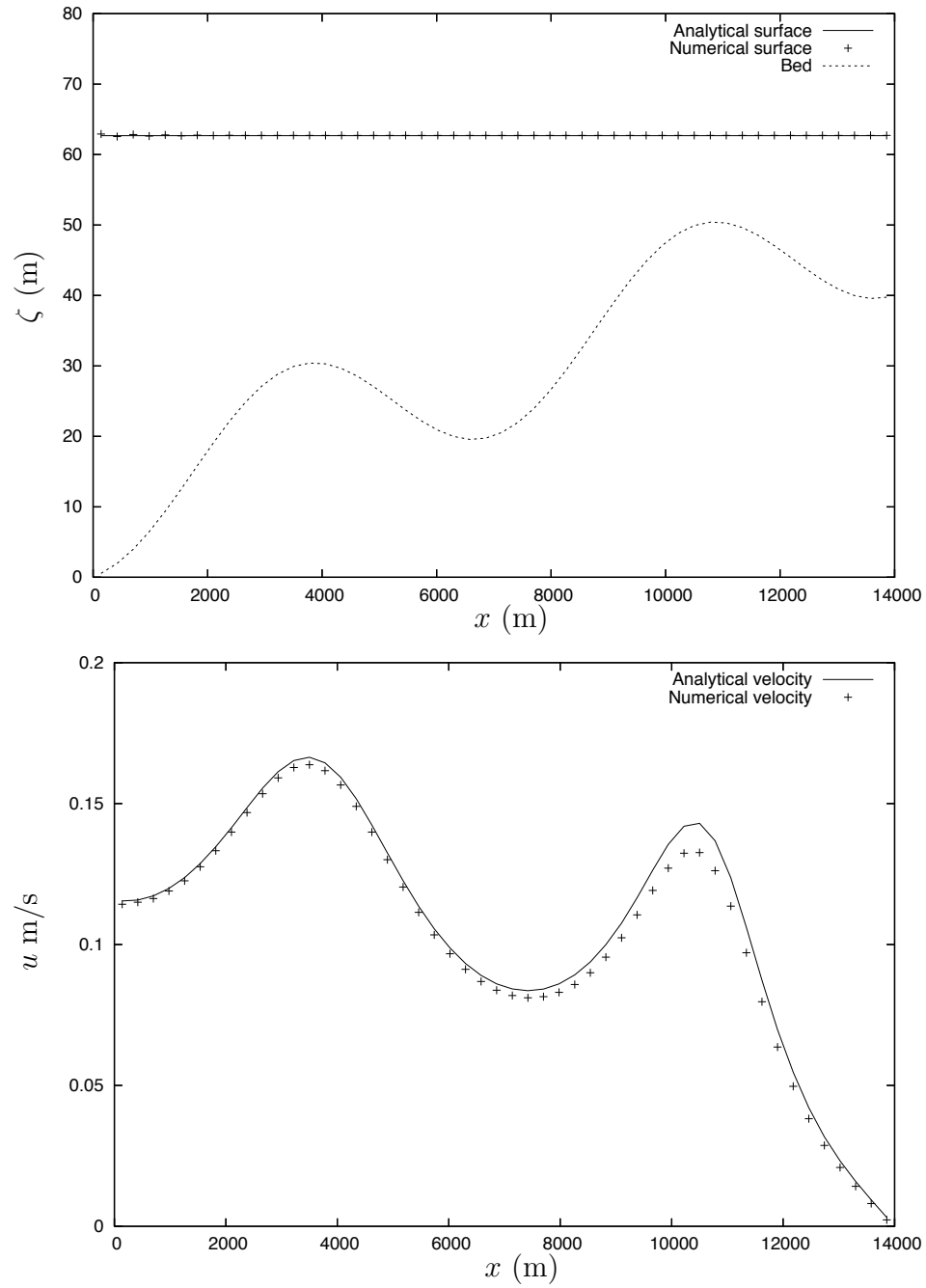


Figure 2.10: Tidal wave flow: comparisons between the numerical results and the analytical solutions at time  $t = 7552.13$  seconds. Water surface elevation (top) and depth-averaged velocity (bottom).

irregular bed. The bed topography is defined in Table. 2.1 and shown in Fig. 2.11. The initial and boundary conditions are similar to those given in Eqs. (2.43) and (2.45) but with the following alterations.

$$H(0) = 16 \text{ m}, \quad L = 1500 \text{ m}, \quad H(x) = H(0) - z_b(x). \quad (2.49)$$

Table 2.1: Tidal flow over an irregular bed: Bed elevation

$x$ (m)	0	50	100	50	250	300	350	400	425	435
$z_b$ (m)	0.0	0.0	2.5	5.0	5.0	3.0	5.0	5.0	7.5	8.0
$x$ (m)	450	475	500	505	530	550	565	575	600	650
$z_b$ (m)	9.0	9.0	9.1	9.0	9.0	6.0	5.5	5.5	5.0	4.0
$x$ (m)	700	750	800	820	900	950	1000	1500		
$z_b$ (m)	3.0	3.0	2.3	2.0	1.2	0.4	0.0	0.0		

The solution to this problem can be found by using Eqs. (2.47) and (2.48).

The solutions to the tidal flow problem over an irregular bed are depicted in Fig. 2.11 for both the water surface elevation and the velocity at time,  $t = 10,800$  seconds, and the velocity at time,  $t = 32,400$  seconds, in Fig. 2.12. The SGM shows excellent agreement between the numerical and analytical solutions for both the water height and velocity and confirms that the SGM is an accurate treatment of the source terms for tidal flow.

### 2.5.3 Steady flow over a bump

Another validation test for treatment of source terms in the SWE was used by Vázquez-Cendón (1999) to test their upwind scheme. The problem consists of a one-dimensional channel with a bump in the bed topography. The flow is subcritical ( $F_r < 1$ ) in the region downstream of the bump until the bed elevation increases, causing the flow to accelerate reaching critical conditions ( $F_r = 1$ ) at the top of the bump. It is at the point where the bed surface is a maximum that transcritical flow can only occur (Alcrudo and Benkhaldoun, 2001; Chow, 1959). The flow downstream of the bump is supercritical ( $F_r > 1$ ), unless boundary conditions are used to force the flow to become subcritical.

For this test case, a flume of 25 metres in length is used with the bed surface elevation defined by

$$z_b(x) = \begin{cases} 0.2 - 0.05(x - 10)^2 & \text{if } 8 < x < 12 \\ 0 & \text{otherwise} \end{cases}. \quad (2.50)$$

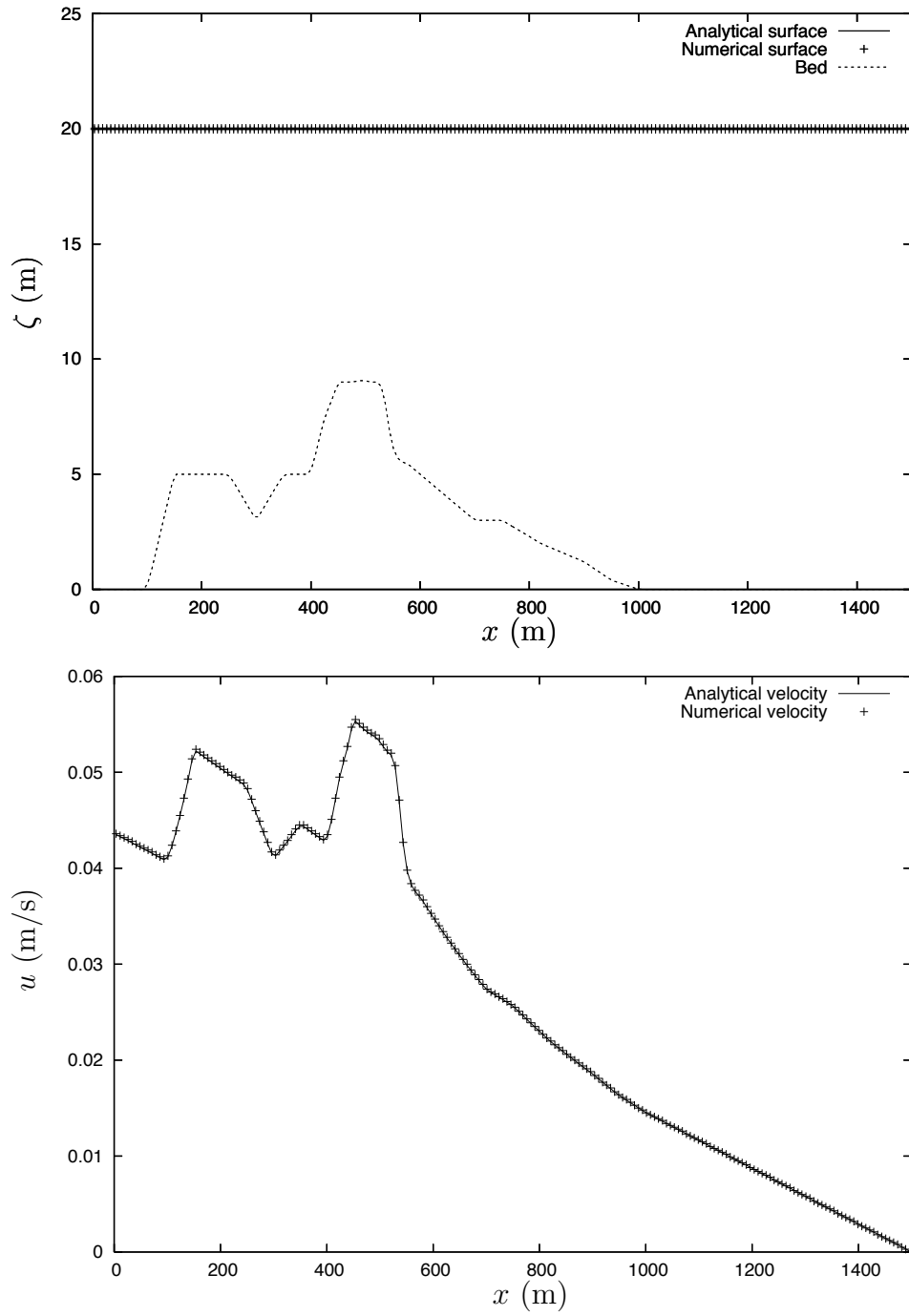


Figure 2.11: Tidal wave flow over an irregular bed: comparisons between the numerical results and the analytical solutions at time  $t = 10800$  seconds. Water surface elevation (top) and depth-averaged velocity (bottom).

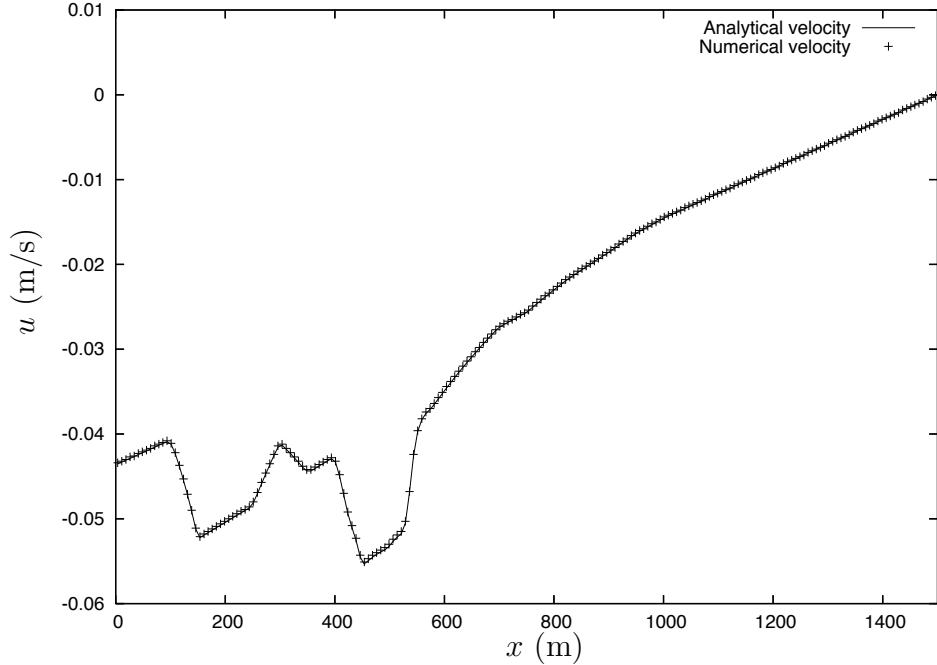


Figure 2.12: Tidal wave flow over an irregular bed: Comparison of the numerical velocity against the analytical velocity,  $t = 32400$  seconds.

The SGM is iterated until global convergence between successive time steps is reached. This condition is met when the global relative error,  $R_{err}$ , satisfies

$$R_{err} = \sqrt{\sum_i \left( \frac{h_i^n - h_i^{n-1}}{h_i^n} \right)^2} < 1 \times 10^{-6}. \quad (2.51)$$

### 2.5.3.1 Transcritical flow without a shock

Transcritical flow without a shock is achieved by imposing a discharge per unit width of  $q = 1.53 \text{ m}^2\text{s}^{-1}$  at the inflow boundary, and a transient flow boundary condition, Eq. (2.25), was used at the outflow boundary. The flume was discretised using 100 computational cells giving a spatial step of  $\Delta x = 0.25$  metres. A comparison between the numerical solution and the analytical solution given by Goutal and Maurel (1997) is made in Fig. 2.13.

### 2.5.3.2 Transcritical flow with a shock

Transcritical flow with a shock is achieved by imposing a discharge per unit width of  $q = hu = 0.18 \text{ m}^2\text{s}^{-1}$  at the inflow boundary, and a depth of  $h = 0.33$  metres at the outflow boundary. The velocity at the outflow boundary remains consistent with that of Eq. (2.25). A comparison between the numerical solution and the

analytical solution is given in Fig. 2.14.

### 2.5.3.3 Subcritical flow

Subcritical flow is created by imposing a discharge per unit width of  $q = 4.42 \text{ m}^2\text{s}^{-1}$  at the inflow boundary and water depth of  $h = 2.0$  metres at the outflow boundary. A comparison between the numerical solution and the analytical solution is given in Fig. 2.15.

### 2.5.4 Quasi-stationary case

Leveque (1998) chose a quasi-stationary test case to test his flux balancing scheme on computations involving small perturbations in the water surface. The problem consists of a channel 1.0 metres in length with a bed topography defined by

$$z_b(x) = \begin{cases} 0.25\{\cos[10\pi(x - 1/2)] + 1\} & \text{if } |x - 1/2| < 1/10 \\ 0 & \text{otherwise} \end{cases}, \quad (2.52)$$

and  $H(0) = 1.0$  metres. For this test case, Leveque specified the acceleration due to gravity of  $g = 1.0 \text{ ms}^{-2}$ . The initial conditions for the water surface elevation consists of a ‘top-hat’ function defined by

$$\zeta(x, 0) = \begin{cases} H(0) + \epsilon & \text{if } 0.1 < x < 0.2 \\ H(0) & \text{otherwise} \end{cases}, \quad (2.53)$$

where  $\epsilon = 0.2$  is the height of the initial top-hat function and  $u = 0 \text{ ms}^{-1}$ .

At time  $t = 0$  seconds, gravity acts on the top-hat function creating two left and right travelling waves, travelling at celerity ( $\pm\sqrt{gd}$ ). The small perturbations present in the water surface are a demanding test for any treatment of the SWE along with bed source terms. Fig. 2.16 shows that the SGM compares favourably with Leveque’s treatment of the source terms.

### 2.5.5 Surge crossing a step

The resolution of a surge crossing a step has been used by Hu *et al.* (2000) to test their split scheme’s ability to model discontinuities in the bed slope. A channel of length,  $L = 10,000$  metres, has a bed slope given by

$$z_b(x) = \begin{cases} 0 & \text{if } x \leq 5000 \\ 2 & \text{otherwise} \end{cases}. \quad (2.54)$$

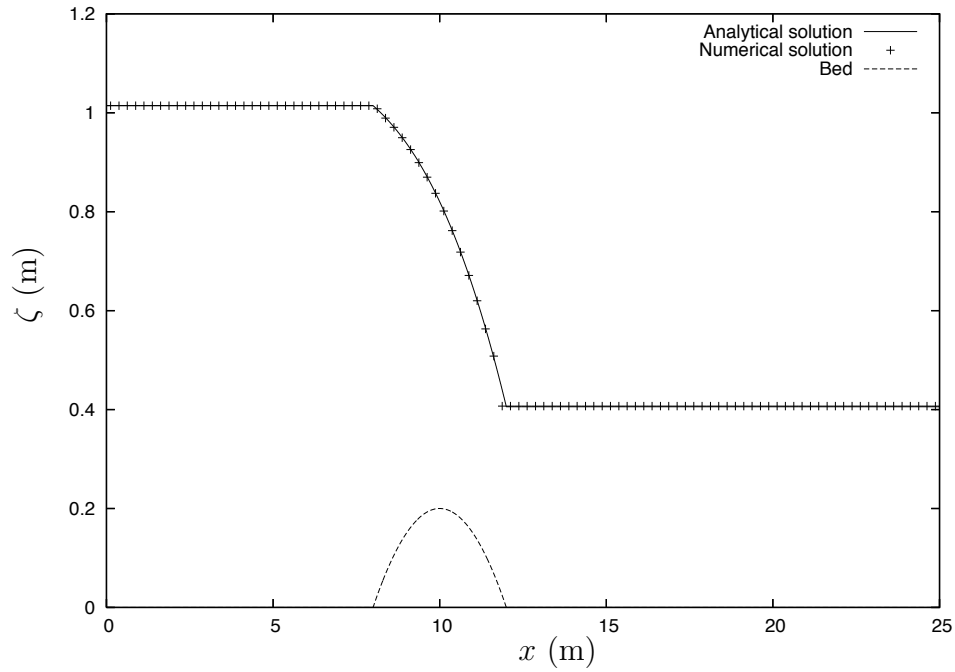


Figure 2.13: Steady transcritical flow over a bump without a shock: comparison of the numerical and analytical solution for a steady state solution.

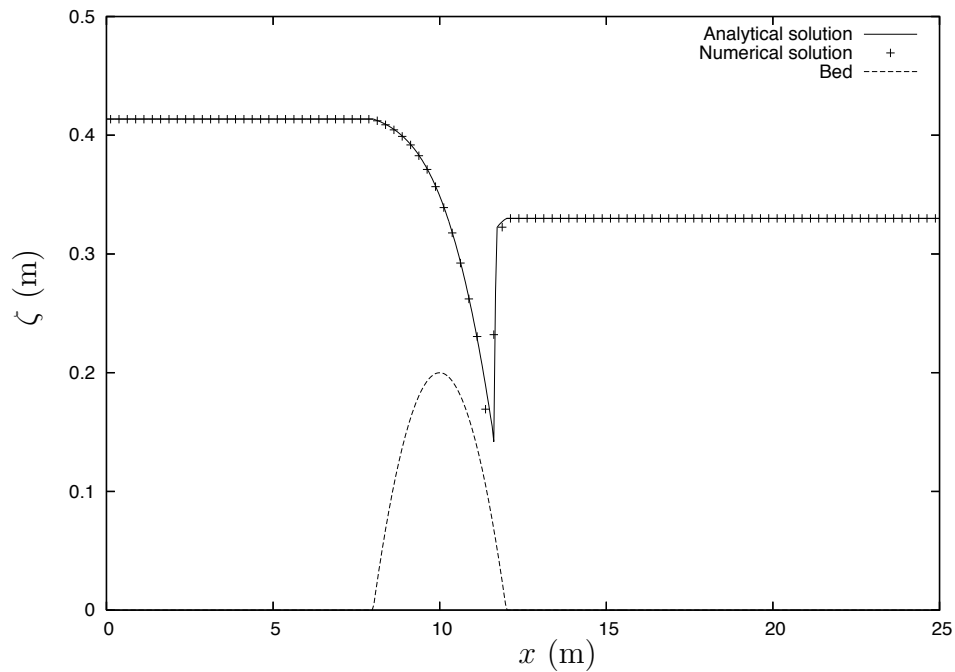


Figure 2.14: Steady transcritical flow over a bump with a shock: comparison of the numerical and analytical solution for a steady state solution.

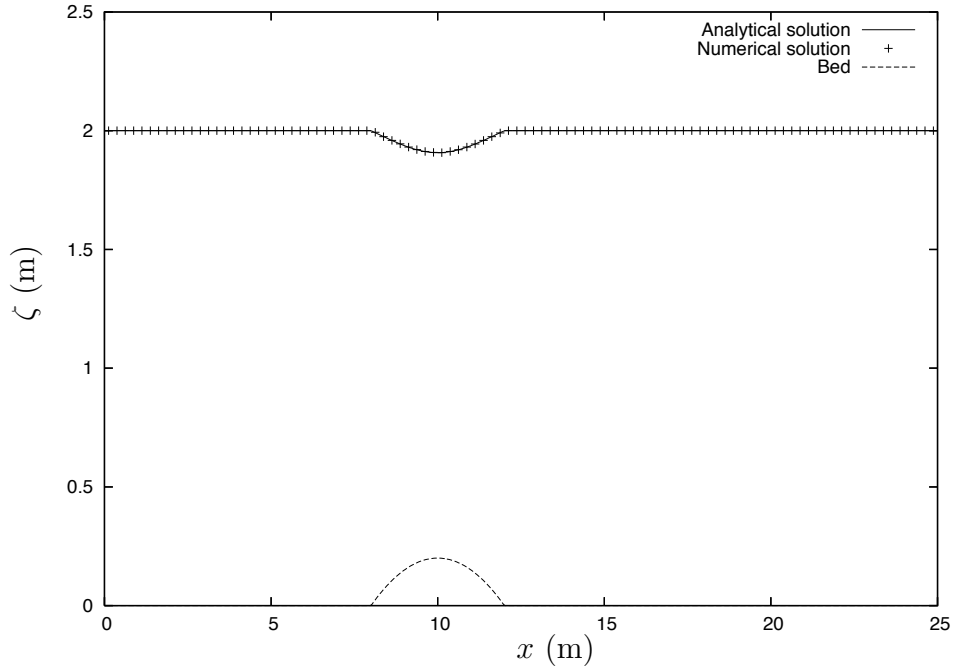


Figure 2.15: Subcritical flow over a bump: comparison of the numerical and analytical solution for a steady state solution.

Initially, the water is at rest and the water surface elevation is 5 metres. A supercritical flow condition is imposed at the left-hand boundary in the form of a surge wave with a depth of 10 metres. A solid wall condition (Eq. 2.26) is employed at the right-hand boundary. The incident velocity,  $u_I$ , can be calculated from the following equation (Chow, 1959)

$$u_I = \frac{c_1(d_1 - d_2)}{d_1}, \quad (2.55)$$

where  $d_1$  and  $d_2$  represent the depths of the surge wave and initial water depth respectively and

$$c_1 = \sqrt{\frac{gd_1(d_1 + d_2)}{2d_2}}. \quad (2.56)$$

When the surge wave hits the step in the bed it creates two new waves, one travelling upstream with a water depth of  $h'_1$  and velocity  $u'_1$ , and the other downstream with a water depth of  $h'_2$  and velocity  $u'_2$ . The analytical solution of the

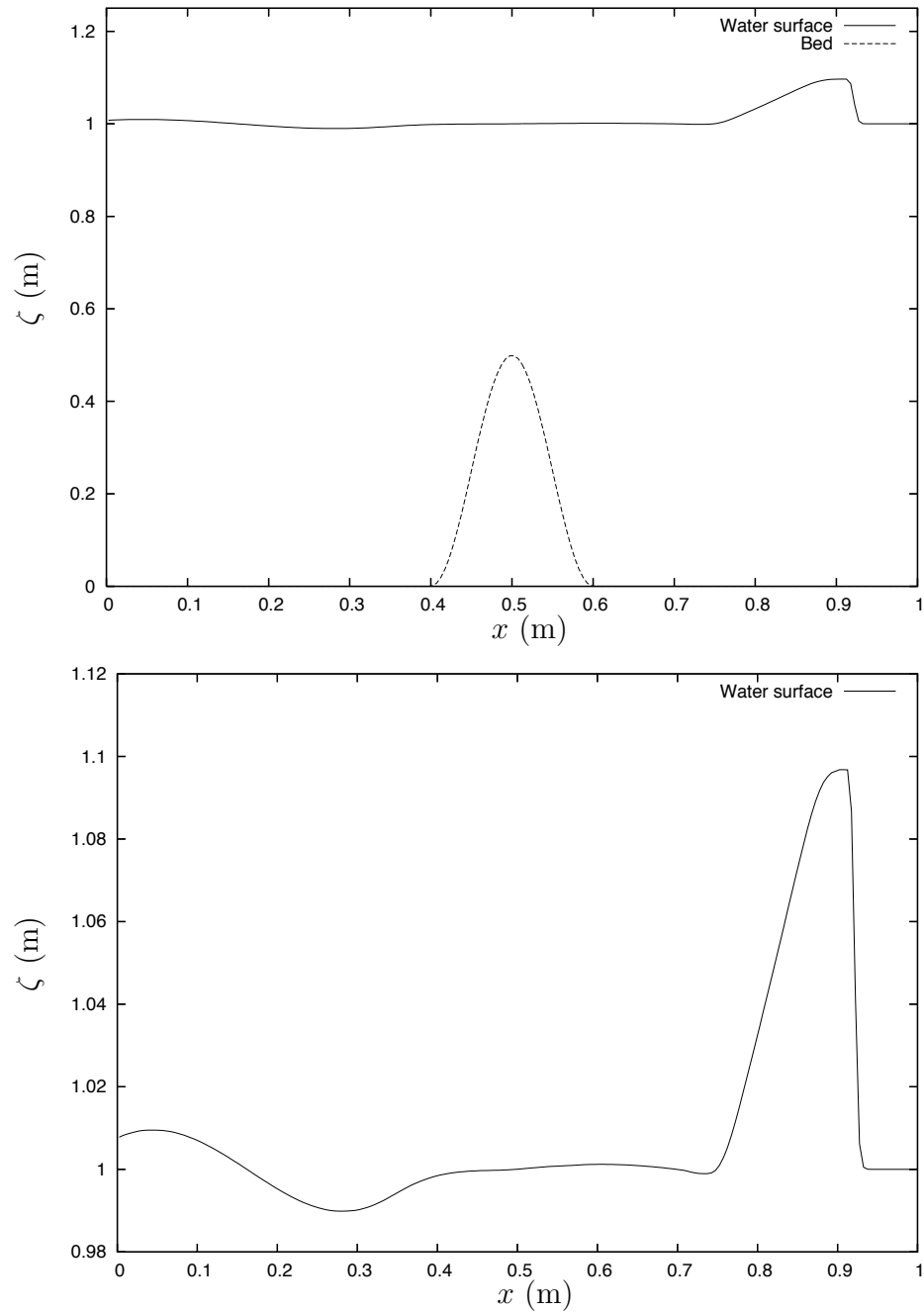


Figure 2.16: Quasi-stationary case: Water surface elevation with small perturbation,  $\epsilon = 0.2$ ,  $t = 0.7$  seconds (top) and magnified view (bottom).

two new surges can be calculated using the following equations (Chow, 1959)

$$(u_1 - u'_1)^2 = (h_1 - h'_1)^2 \frac{(h_1 + h'_1)g}{2h_1 h'_1}, \quad (2.57)$$

$$(u_2 - u'_2)^2 = (h_2 - h'_2)^2 \frac{(h_2 + h'_2)g}{2h_2 h'_2}, \quad (2.58)$$

$$h'_1 = h'_2 + 2 + \frac{(u'_2 - u'_1)^2}{2g}, \quad (2.59)$$

$$h'_2 = \frac{u'_1 h'_1}{u'_2}. \quad (2.60)$$

Fig 2.17 shows a comparison of the numerical water surface and velocity against the analytical solutions. There is excellent agreement between the numerical and analytical results indicating that the SGM can be used to model a discontinuous bed topography or near vertical bed topography.

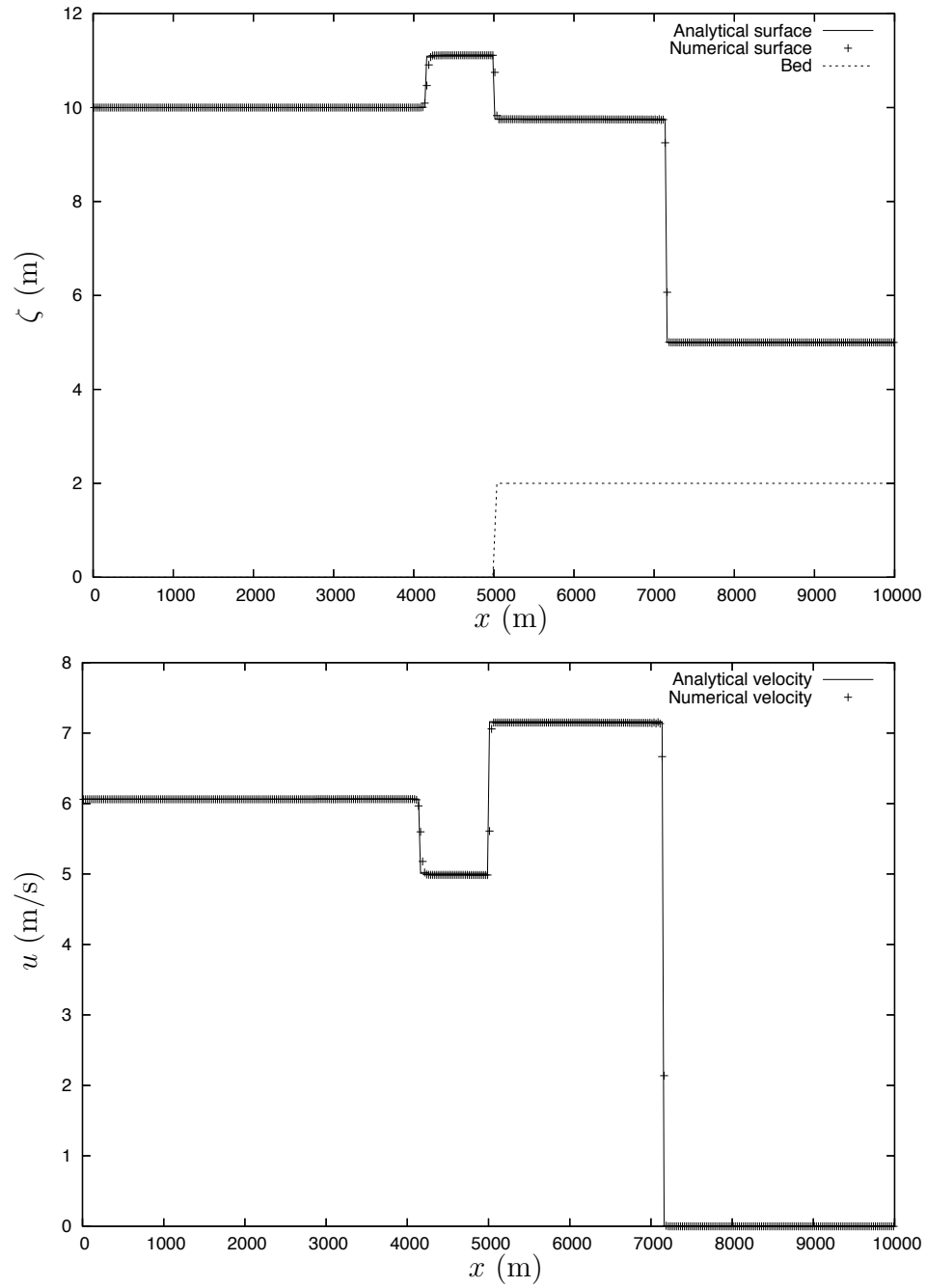


Figure 2.17: Surge crossing a step: comparisons of numerical results and analytical solutions at time  $t = 600$  seconds, water surface elevation (top) and depth-averaged velocity (bottom).

## 2.6 Chapter Summary

The non-linear Shallow Water Equations (SWE) were presented and an overview of the finite-volume method was included in Section 2.2. A Godunov-type high-resolution finite-volume scheme that is used to solve the homogeneous form of the SWE is also presented (Section 2.2.1). The Hancock scheme uses a linear reconstruction technique to obtain values of the conserved variables at the cell interfaces. The values at the cell interfaces are calculated using slope limited gradients to eliminate spurious oscillations. An approximate Riemann solver is used to calculate the solution to local Riemann problems that are required for the Godunov-type solver. The Surface Gradient Method (SGM), a method for the treatment of the source terms for the SWE in a finite-volume method, is given in Section 2.4. The SGM uses the water surface elevation as opposed to the geopotential as a basis for the monotonic reconstruction for the mass conservation equation. This treatment ensures that any differences in the solution of the inviscid terms and the source terms do not affect the solution.

The numerical scheme has been tested over a range of well known test problems. Firstly, the inviscid solver was tested for a one-dimensional dam break problem with both a wet, and dry bed and for different choices of slope limiting functions. The implementation of the SGM within the MUSCL-Hancock scheme has been tested for tidal flow over smooth and irregular bed topography; subcritical, supercritical and transcritical flow over a bump; small perturbation flow and surge wave crossing a step. In all test cases performed, the numerical scheme is shown to be accurate, robust and efficient in practice.

Chapter 3 uses the numerical scheme described in this chapter to model a series of experiments examining wave run-up and, in particular, violent overtopping of a seawall.

# Chapter 3

## Shallow Water Modelling of Wave Overtopping

The shallow water flow solver presented in the previous chapter has been validated against standard test cases with well known analytical solutions. In order to be able to apply a flow solver to provide guidance on the design of coastal structures, it is important that the accuracy and limitations of the solver are known. Comparisons between real world observations and numerical models are difficult to make because the numerical models require wave height data over the whole of the solution domain. Instead it is much more practical to make comparisons with wave flume experiments and the empirical models developed using field and experimental observations.

At present, the most widely used method for the prediction of wave overtopping is the application of empirical models (Reis *et al.*, 2005). Measurements relating to the factors affecting the volume of water that overtops a seawall are collected from wave flume experiments and field observations. These measurements are then used to calibrate an empirical model by utilising curve fitting methods to provide an equation for the given physical configuration of the wave flume/seawall. Empirical methods provide a useful method for estimating the discharge volumes from values of the incident wave parameters.

This chapter discusses the analysis of wave overtopping using statistical methods and the calibration of empirical overtopping formulae. Section 3.1 begins by defining the wave statistics used to describe the type of wave attack on coastal structures and the probability distribution of water waves. The definitions of wave run-up and overtopping are given in Section 3.1.3 along with formulae for dimensionless values and the basic empirical model. Violent wave overtopping is

discussed in Section 3.2 and the shallow water model presented in Chapter 2 is applied to model violent wave overtopping. The results are compared against the experimental observations and empirical formulae in Section 3.5.

## 3.1 Wave and Overtopping Statistics

For the purpose of analysis, ocean waves can be considered to be a random process. Therefore, analysis of wave data can be conducted using statistical methods. The three main statistical methods used are the analysis of mean values, and the calculation of probability density functions (PDFs) and spectral density functions. Mean values provide a single measure of the wave conditions which are used for comparison between observations and also for derivation of empirical formulae. Probability density functions are used to give a probability that a random variable, usually the wave height, will not exceed a given value. PDFs therefore provide a more complete picture of the wave conditions than the mean values. Spectral density functions use Fourier analysis to give an energy distribution in the frequency domain.

### 3.1.1 Significant wave height and mean wave period

When observing the motion of waves, it is natural to use the wave height as a measure to describe the wave conditions. A visual estimation of the average wave height will tend to only use the larger waves in the estimation and disregard the smaller waves. The omission of the smaller waves in the estimation does not invalidate the average wave height as a measure of the wave conditions, rather by only taking into account the larger more significant waves, the visual estimation of the average wave heights can be referred to as the significant wave height. Therefore the definition of the significant wave height, denoted by  $H_s$ , is given by Sverdrup (1947) as the average of the top 1/3 wave heights in a wave record:

$$H_s = \frac{3}{n} \sum_{i=1}^{n/3} H_i, \quad (3.1)$$

where  $H_i$  are the wave heights ordered in descending order and  $n$  is the number of waves in the sequence. The other main wave statistic that describes the incident

wave attack is the mean wave period denoted by  $T_m$

$$T_m = \frac{1}{n} \sum_{i=1}^n T_i, \quad (3.2)$$

where  $T_i$  is the wave period.

### 3.1.2 Rayleigh Wave Height Distribution

Longuet-Higgins (1952) showed that, based upon the linear model of waves with a narrow energy spectrum, wave heights in deep water should follow the Rayleigh distribution (Battjes and Groenendijk, 2000). Goda and Kudaka (2005) recently demonstrated that the applicability of the Rayleigh distribution is not dependent upon the shape of the energy spectrum and that a narrow energy spectrum is not required. The probability of non-exceedence (a random wave having a height less than  $H$ ) given by the Rayleigh distribution is

$$P(\underline{H} < H) = 1 - \exp \left[ - \left( \frac{H}{H_{rms}} \right)^2 \right], \quad (3.3)$$

where  $\underline{H}$  is a random variable,  $H_{rms} = H_s / 1.416$  is the root mean square (rms) of the wave heights.

Comparison between the observed probability distribution and the theoretical Rayleigh distribution corresponding with the observed  $H_s$  will indicate whether the waves that are being generated either in a wave tank or by a numerical model are consistent with those that occur in the real world. The observed probability distribution can be calculated by using

$$P(\underline{H} < H) = 1 - \frac{i}{n+1} \quad (3.4)$$

where  $i$  is the  $i$ th largest recorded wave height and  $n$  is the number of waves recorded.

### 3.1.3 Wave run-up and overtopping

When non-breaking waves propagate towards and interact with sloping structures, the wave will run-up the face of the slope until either the wave loses energy and is reflected seaward, or the wave reaches the top of the structure and continues to flow inland. The vertical distance that the wave travels up a slope from the

SWL is defined as run-up and is denoted here by  $R$  (Fig. 3.1). If the wave run-up distance is higher than that of the crest freeboard (the vertical distance between the SWL and the top of the structure),  $R_c$ , the water will overtop the structure in a continuous sheet of water. Overtopping of this kind is known as ‘green water’ overtopping Besley (1999).

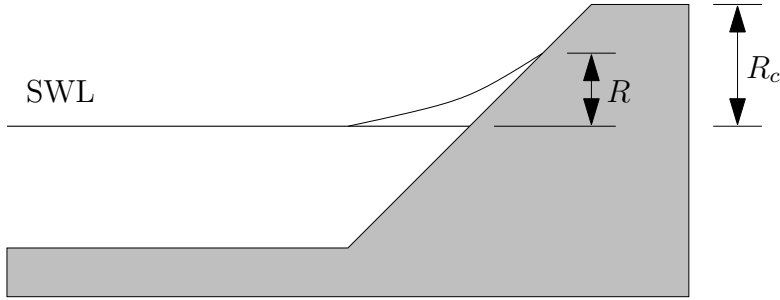


Figure 3.1: Definitions of run-up,  $R$ , and crest freeboard,  $R_c$ .

Overtopping is measured as the mean volume of water overtopping a structure per second per metre of seawall and is denoted by  $Q$ . For comparisons between different wave conditions and bathymetry, dimensionless values of the overtopping discharge volumes and freeboard are calculated. For example, Owen (1980) used the following relationships to determine dimensionless values for his model

$$Q^* = \frac{Q}{T_m g H_s} \quad (3.5)$$

$$R^* = \frac{R_c}{T_m \sqrt{g H_s}} \quad (3.6)$$

where  $Q^*$  and  $R^*$  denote the dimensionless values of the overtopping and freeboard respectively for non-impacting waves.

In general, empirical models that describe the relationship between dimensionless overtopping discharge and the dimensionless crest freeboard take the form of an exponential equation

$$Q^* = A \exp(-B R^*) \quad (3.7)$$

where  $A$  and  $B$  are dimensionless empirical coefficients. The values of the empirical coefficients are determined by utilising a maximum likelihood approach.

## 3.2 Violent Wave Overtopping

Violent wave overtopping occurs when waves break upon steep sloping structures which causes pressures and velocities much larger than normally associated under

gravity (Peregrine, 2003). This phenomena can be seen in Fig. 3.2 that shows three frames of a video recording of a wave flume experiment.



Figure 3.2: Video images of a breaking wave impacting on a structure.

The image on the left shows a wave that has propagated up a sloping beach and has formed a plunging breaker that is about to impact on the vertical structure to the right of the image. The centre image shows the breaking wave impacting on the structure. The combination of the air trapped by the breaking wave and the force of the wave impacting against the structure causes the violent explosion of water in the vertical direction as seen in the image on the right. In real life situations, the jet of water that is propelled into the air is often blown landwards by the force of the wind.

Due to the simplifying assumptions, the SWE and other depth-averaged models cannot model the multiply connected region of the air trapped by the breaking waves, but as discussed previously, the numerical models that can model such phenomena are very computationally expensive. The SWE can, however, represent the breaking waves as discontinuities due to the hyperbolic nature of the system, and thus can provide a model of the wave breaking against a structure.

### 3.2.1 Previous Work on Violent Wave Overtopping

Water wave overtopping had been studied extensively over the past 30 years. Goda *et al.* (1975), Owen (1982) and Franco *et al.* (1994) all present data and guidance on overtopping volumes for a variety of sloping and vertical structures. Owen and Franco *et al.* focus primarily upon cases where waves do not break (pulsating or non-impulsive conditions). While Goda's data includes violent or impulsive conditions, these are not treated separately. Besley *et al.* (1998) and Pearson *et al.* (2001) have used observations from either physical models or field data to gain greater understanding of violent, impulsive overtopping. Guidance on mean and wave-by-wave overtopping volumes under violent conditions is now established, but for simple structures and standard sea spectra only.

Violent overtopping events are difficult to model using current numerical methods. Ideally, the use of the Navier-Stokes equations would provide a good model of overtopping events. However, the computational resources needed to solve a Navier-Stokes formulation would negate the advantages of using a mathematical model over small-scale physical models. Until computing power has advanced sufficiently to enable the Navier-Stokes equations to be solved within a practical time frame, alternative methods are required.

The Shallow Water Equations (SWE) given in Eqs. (2.1)–(2.3) provide a good model of water flow under certain conditions. They represent a depth-averaged formulation of the Navier-Stokes equations and as a result, vertical velocity is neglected. The SWE in theory may not be suitable as a basis for a numerical model for violent wave overtopping where vertical velocities are a major feature (Section 3.2). However, it has been shown that solvers exists, such as the one discussed in Chapter 2, that are easy to implement and computationally efficient. Therefore, it is necessary to establish whether the SWE are applicable for modelling overtopping events.

Existing numerical models of overtopping based on the shallow water equations include HR Wallingford’s ANENOME OTT model developed by Dodd (1998) and ODIFLOCS developed by van Gent (1994, 1995) at Delft Hydraulics. ANENOME OTT and ODIFLOCS have been used to model run-up and overtopping on mild sloping structures (Richardson *et al.*, 2002; Clarke and Damgaard, 2002). So far, to the author’s knowledge, neither model has been used to model overtopping of near vertical structures. Richardson *et al.* (2001) and Shiach *et al.* (2004) have both examined the use of the SWE based AMAZON model for violent wave overtopping resulting from a range of impulsive wave conditions. Most of the analysis in this chapter is taken from Shiach *et al.* (2004) (Appendix D).

### 3.2.2 The $h^*$ Parameter

When examining violent wave overtopping, it is important to be able to quantify the impacting wave interaction on the structure. Allsop *et al.* (1995) developed a parameter,  $h^*$ , that gives a measure to the type of wave that dominates at a seawall. The value that  $h^*$  takes determines whether it is the inshore propagating incident waves or the reflected waves that dominate at the structure. Of course, for violent overtopping events to occur, incident waves must dominate to enable

waves to break against the structure. The  $h^*$  parameter is calculated using

$$h^* = \frac{d_{toe}}{H_s} \left( \frac{2\pi h}{gT_m^2} \right), \quad (3.8)$$

where  $d_{toe}$  is the water depth measured at the toe of the structure,  $H_s$  is the significant wave height defined in Eq. (3.1),  $g = 9.81 \text{ ms}^{-2}$  is the acceleration due to gravity and  $T_m$  is the mean wave period defined in Eq. (3.2). Allsop *et al.* (1995) showed that for values of  $h^* < 0.3$  incident waves dominate, and for values of  $h^* \geq 0.3$  it is the reflected waves that dominate. Therefore violent wave overtopping is likely to occur when  $h^* < 0.3$ .

### 3.2.3 Besley Formula

Besley (1999) used the  $h^*$  parameter in his model to derive empirical formulae that provide predictions of the dimensionless discharges and the proportion of waves that overtop a vertical structure. For conditions conducive to violent wave overtopping, the dimensionless discharge and percentage of waves that overtop according to the Besley model are:

$$Q_h = \left( \frac{Q}{\sqrt{gH_s^3}} \right) / h^{*2}, \quad (3.9)$$

$$R_h = \left( \frac{R_c}{H_s} \right) h^*, \quad (3.10)$$

$$N_{ow}/N_w = 0.031 R_h^{-0.99}, \quad (3.11)$$

where  $Q_h$  and  $R_h$  are dimensionless values for the discharge and crest freeboard for impacting waves and vertical seawalls,  $N_{ow}$  and  $N_w$  are the number of waves that cause overtopping of the seawall and the number of waves that are recorded over the observed time scale respectively.

## 3.3 The Edinburgh Wave Flume Experiments

A series of experiments was carried out by Jon Pearson and Tom Bruce at Edinburgh University to study violent wave overtopping as part of the VOWS project (Violent Overtopping by Waves at Seawalls). These experiments have been modelled using the shallow-water equations in Shiach *et al.* (2004).

The Edinburgh wave flume experiments consisted of a wave flume 20 metres in length by 0.4 metres wide. An absorbing flap-type wave generator was located

at one end of the flume (Fig. 3.3). The operating water depth was 0.7 metres, which provided intermediate depth conditions at the wave generator. The basic bathymetry of the wave flume consisted of a 1:10 sloping beach on which was placed a 10:1 battered wall, so that the water depth at the toe of the wall was 0.09 metres. The crest freeboard was 0.15 metres.

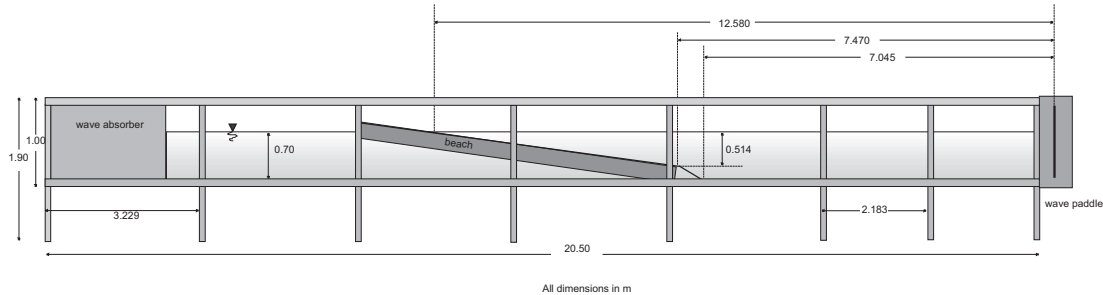


Figure 3.3: Edinburgh wave flume: side elevation.

Eight depth gauges that record water surface elevation were placed at locations 1.0, 2.0, 3.0, 4.25, 5.5, 6.75, 8.0 and 11.21 metres from the battered wall and record at a rate of 100 Hz (Fig. 3.4). The wave generator produced waves sampled from the JONSWAP spectrum with a peak enhancement parameter of  $\gamma = 3.3$ . 15 runs of the experiment were carried out for 1000 waves over 1024 seconds and 6 runs were carried out over a reduced time of 160 seconds. All of the runs of the experiment were carried out for  $h^*$  values between 0.03 and 0.1, so that impacting waves would dominate at the structure and violent wave overtopping would occur.

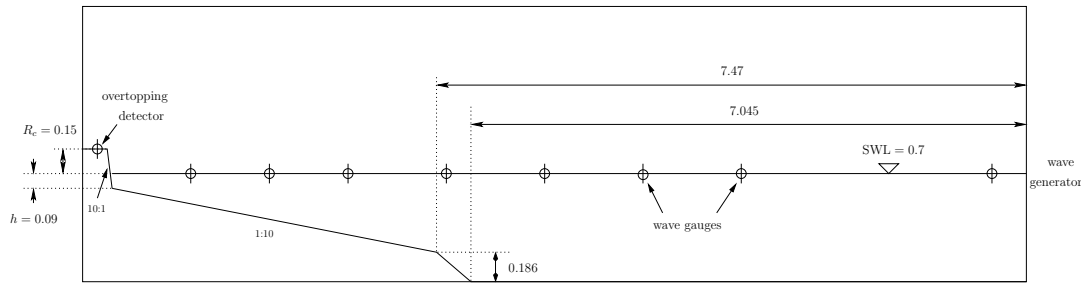


Figure 3.4: Edinburgh wave flume: experimental setup.

Table 3.1 contains the significant wave heights ( $H_s$ ) measured at the toe of the battered wall, the mean wave period ( $T_m$ ), the  $h^*$  parameter and the dimensionless freeboard ( $R_h$ ) for the 15 runs of the experiment.

Table 3.1: Edinburgh wave flume experiment parameters

Run	$H_s$ †	$T_m$ †	$h^*$	$R_h$
1	0.063	1.23	0.0544	0.1296
2	0.074	1.27	0.0435	0.0881
3	0.069	1.25	0.0481	0.1046
4	0.059	1.25	0.0563	0.1431
5	0.062	1.25	0.0536	0.1296
6	0.071	1.50	0.0325	0.0686
7	0.078	1.48	0.0304	0.0584
8	0.063	1.52	0.0356	0.0849
9	0.050	1.52	0.0449	0.1347
10	0.075	1.50	0.0307	0.0615
11	0.062	0.97	0.0889	0.2152
12	0.059	0.95	0.0974	0.2477
13	0.066	0.98	0.0818	0.1860
14	0.068	1.00	0.0763	0.1683
15	0.064	0.98	0.0844	0.1978

† Measured at the toe of the battered wall.

## 3.4 Numerical Modelling of Violent Wave Overtopping

The shallow water flow solver presented in Chapter 2 has been applied to model the violent wave overtopping observed in the Edinburgh experiments. A reduced solution domain starting at 2.0 metres away from the battered wall was used to minimise the discrepancies between the physical waves and the shallow water model of wave propagation in intermediate depth water. The total length of the numerical flume was 2.1 metres which was discretised into 100 computational cells ( $\Delta x = 0.021$  metres). The water surface elevation recorded at the gauge placed 2.0 metres away from the battered wall served as the boundary condition for the water depth at the left-hand boundary, whilst the velocity was assumed to be the same as that of the first computational cell in front of the left-hand boundary. This boundary condition takes into account both incident waves and waves reflecting from the structure. A study carried out by Richardson *et al.* (2001) showed that this boundary condition provides values of the water surface and velocity that are 99% and 85% accurate, respectively, when compared to a moving boundary model. A transmissive boundary condition was used at the right-hand boundary

to allow water to pass out of the solution domain.

Data was collected from two points within the solution domain. At  $x = 1.0$  metres, the water surface elevation was recorded which corresponds with the gauge placed 1.0 metres from the battered wall. At  $x = 2.03$  metres, the overtopping discharge  $Q$  was calculated from the water depth and positive velocity by using the equation

$$Q = hu\Delta t. \quad (3.12)$$

An overtopping event is considered to have occurred if a positive water depth is recorded at the gauge placed at the top of the battered wall and the velocity recorded at the same gauge is landward.

## 3.5 Results

A plot of the numerical and experimental water surface at the gauge placed 1.0 metres from the battered wall over two separate time intervals can be seen in Fig. 3.5. A comparison between the water surface elevation for the physical model and the numerical model suggests that the numerical surface over-predicts the wave heights at the gauge placed 1.0 metres from the battered wall. This is because the numerical model is being applied to model wave propagation outside of the range of applicability for the SWE ( $d/L > 1/20$ ). Therefore, it causes the waves to shoal prematurely. As the wave steepens, the wave height increases, thus over-predicting the height of the wave crests. The crests of the numerical waves occur at the same time as the physical waves.

Plots showing the cumulative overtopping discharge,  $q$ , over time 0–1200 seconds for all 15 runs of the numerical model and the physical model can be seen in Figs. 3.6–3.10. An overtopping event can be identified by a steep upward turn in the discharge plot. Runs 3, 13 and 14 show agreement to within 12% between the numerical and physical discharge. However, runs 7, 9 and 10 show that the agreement is poor for these cases. For all 15 runs of the experiment, the numerical discharge replicates some of the major overtopping events demonstrating an advantage that numerical models have over empirical formulae in that they may be used to model individual overtopping events.

The individual wave heights observed from both the Edinburgh experiments and the numerical model have been compared to the corresponding Rayleigh probability function in Figs. 3.11 and 3.12 for selected runs. The comparisons have

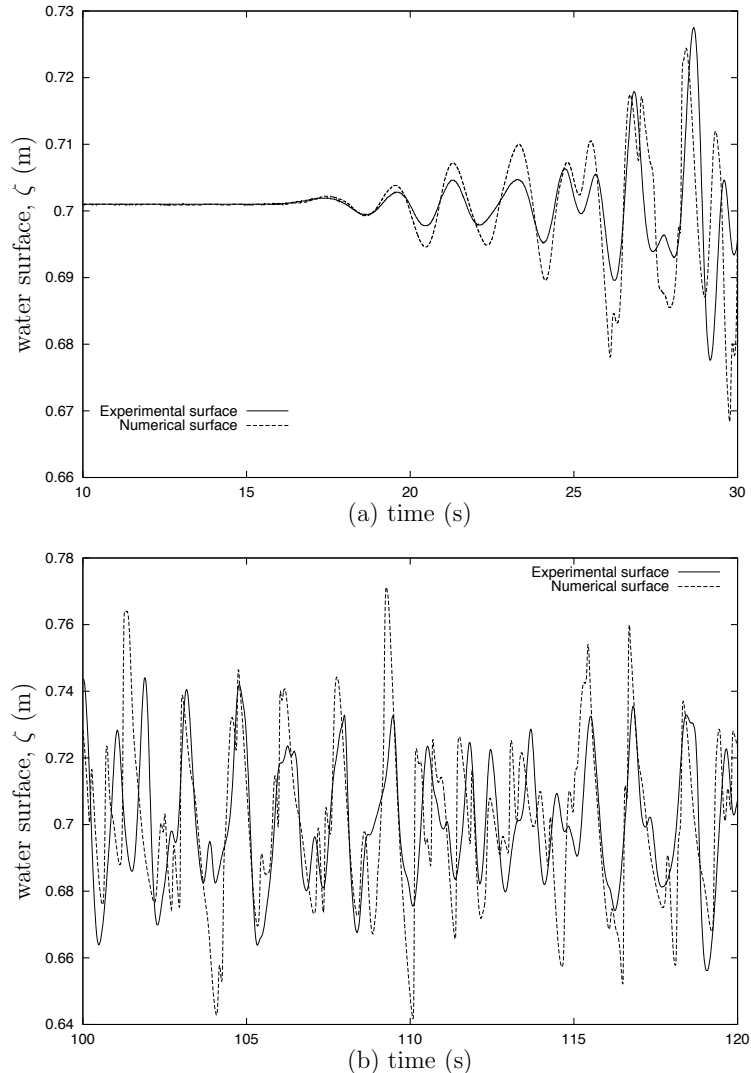


Figure 3.5: Numerical simulation of the Edinburgh wave flume experiments: Comparison of the experimental (solid line) and the numerical (dotted line) water surface at gauge placed 1.0 metres from the battered wall over time intervals of  $t = [10, 30]$  (a) and  $t = [100, 120]$  (b).

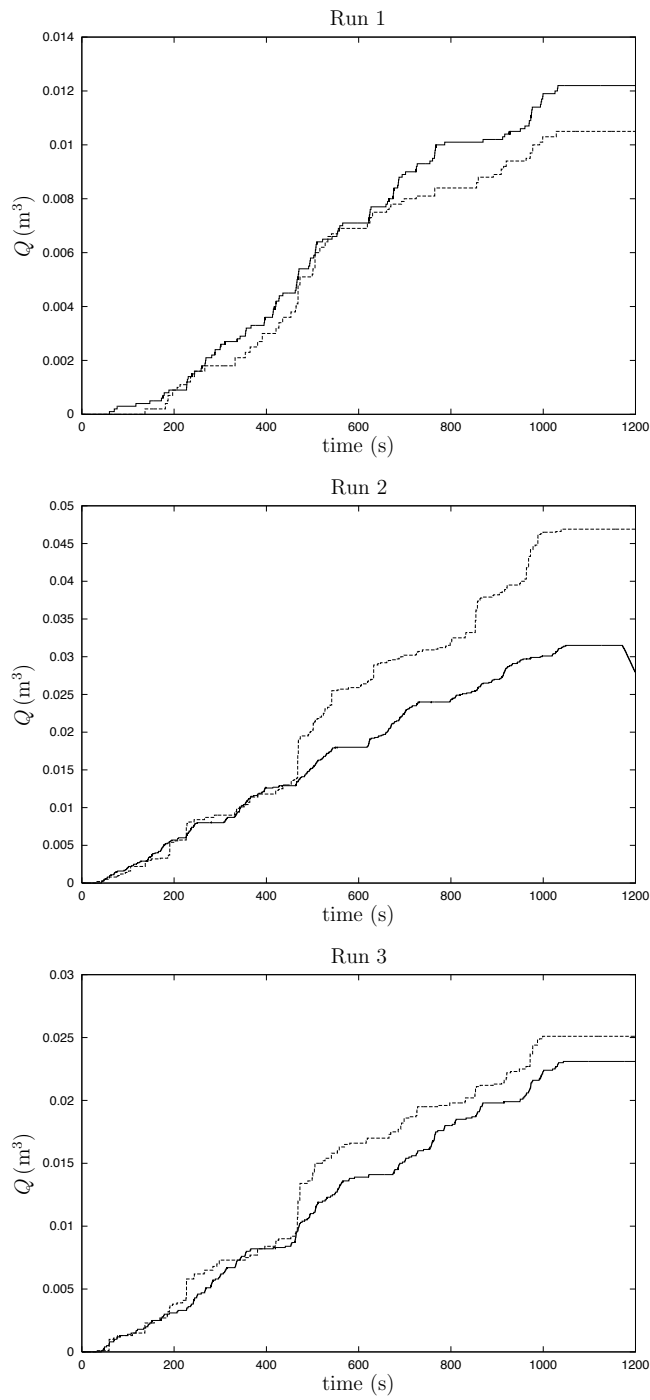


Figure 3.6: Numerical modelling of the Edinburgh experiments: comparison of the numerical discharge (dotted line) against the experimental discharge (solid line) for runs 1 – 3.

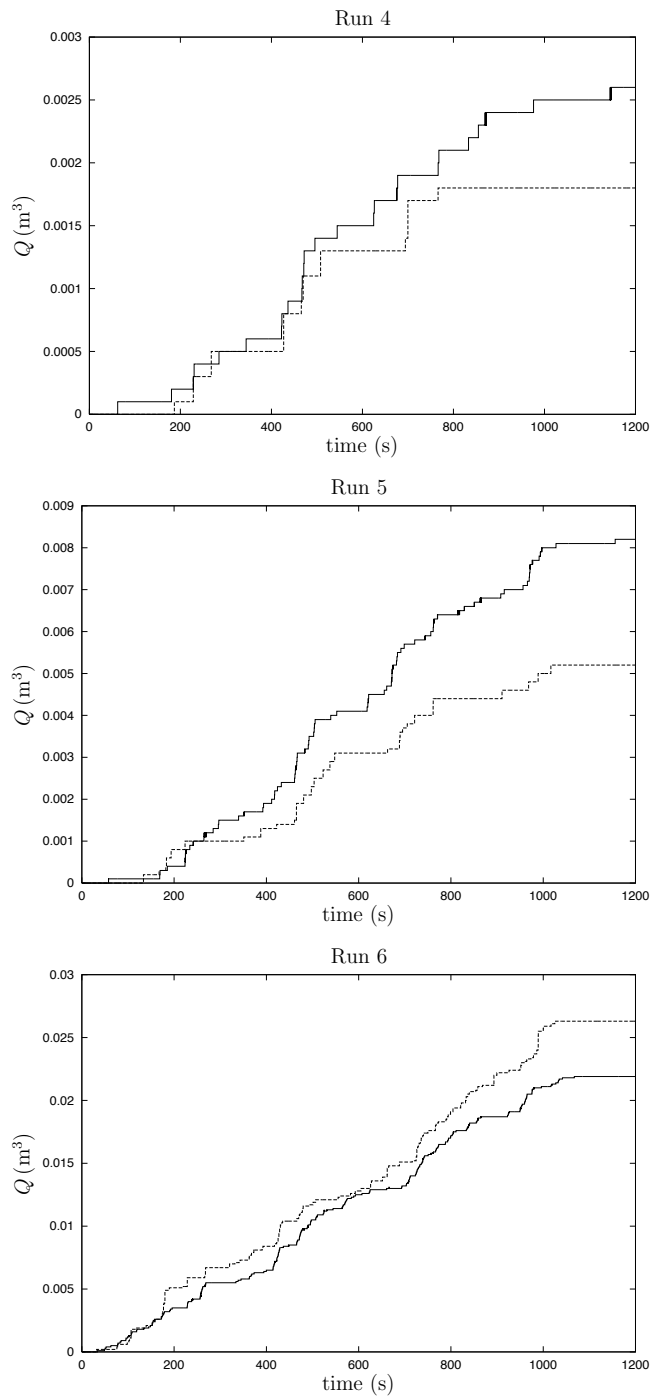


Figure 3.7: Numerical modelling of the Edinburgh experiments: comparison of the numerical discharge (dotted line) against the experimental discharge (solid line) for runs 4 – 6.

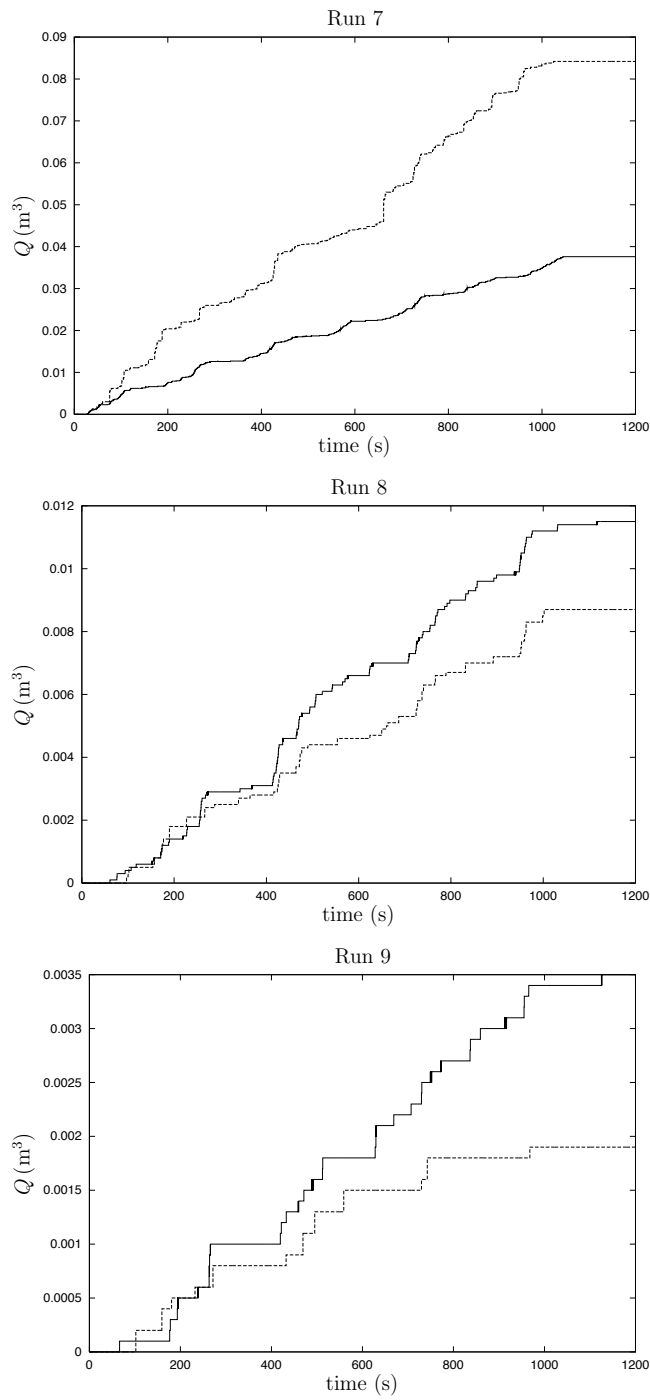


Figure 3.8: Numerical modelling of the Edinburgh experiments: comparison of the numerical discharge (dotted line) against the experimental discharge (solid line) for runs 7 – 9.

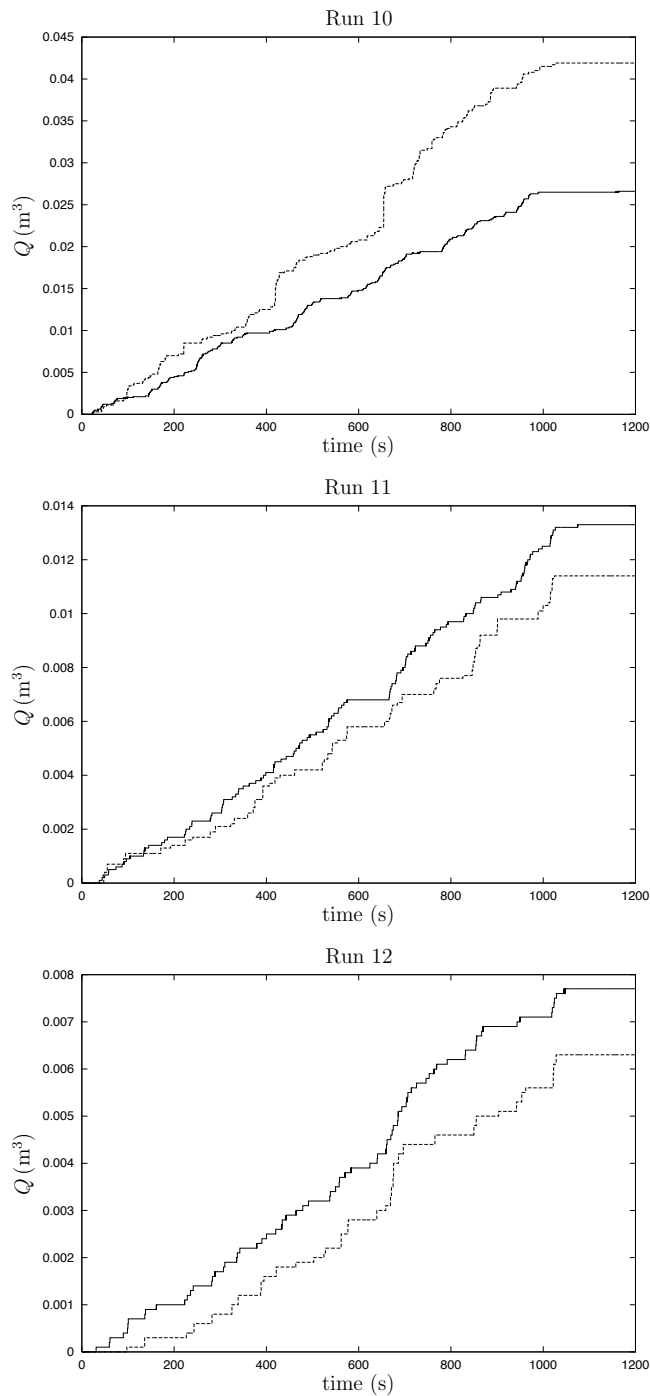


Figure 3.9: Numerical modelling of the Edinburgh experiments: comparison of the numerical discharge (dotted line) against the experimental discharge (solid line) for runs 10 – 12.

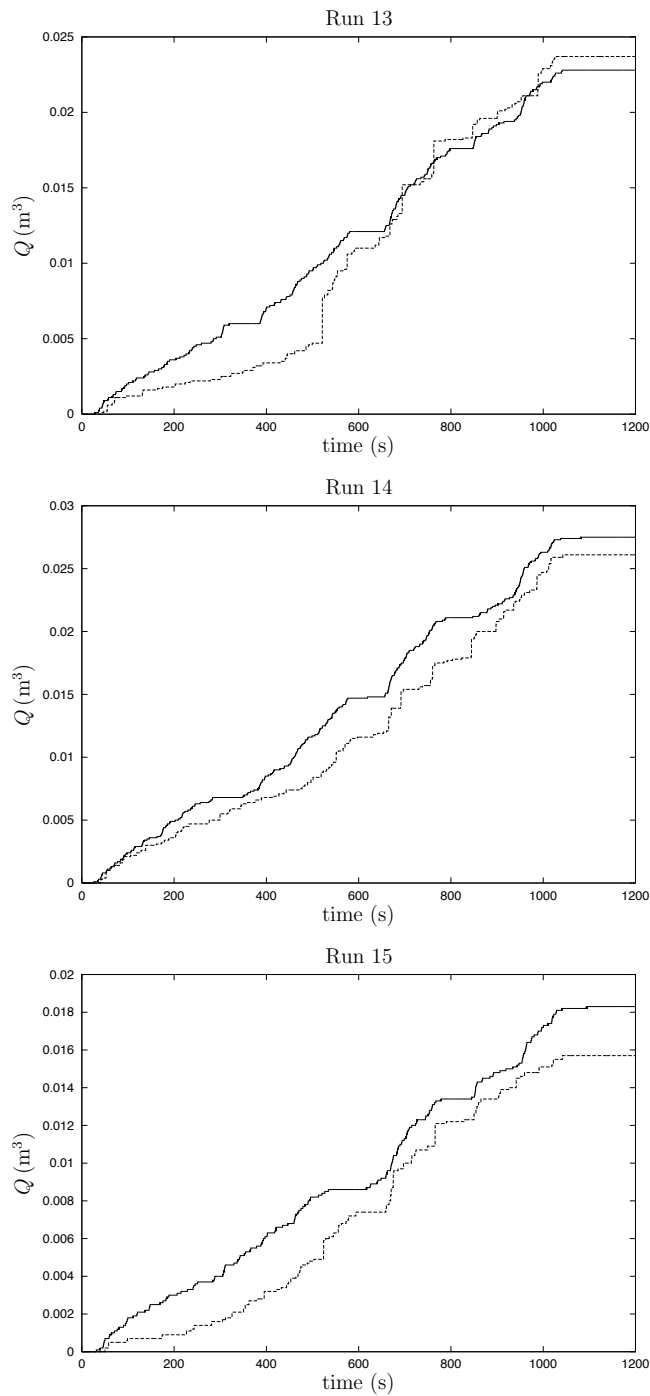


Figure 3.10: Numerical modelling of the Edinburgh experiments: comparison of the numerical discharge (dotted line) against the experimental discharge (solid line) for runs 13 – 15.

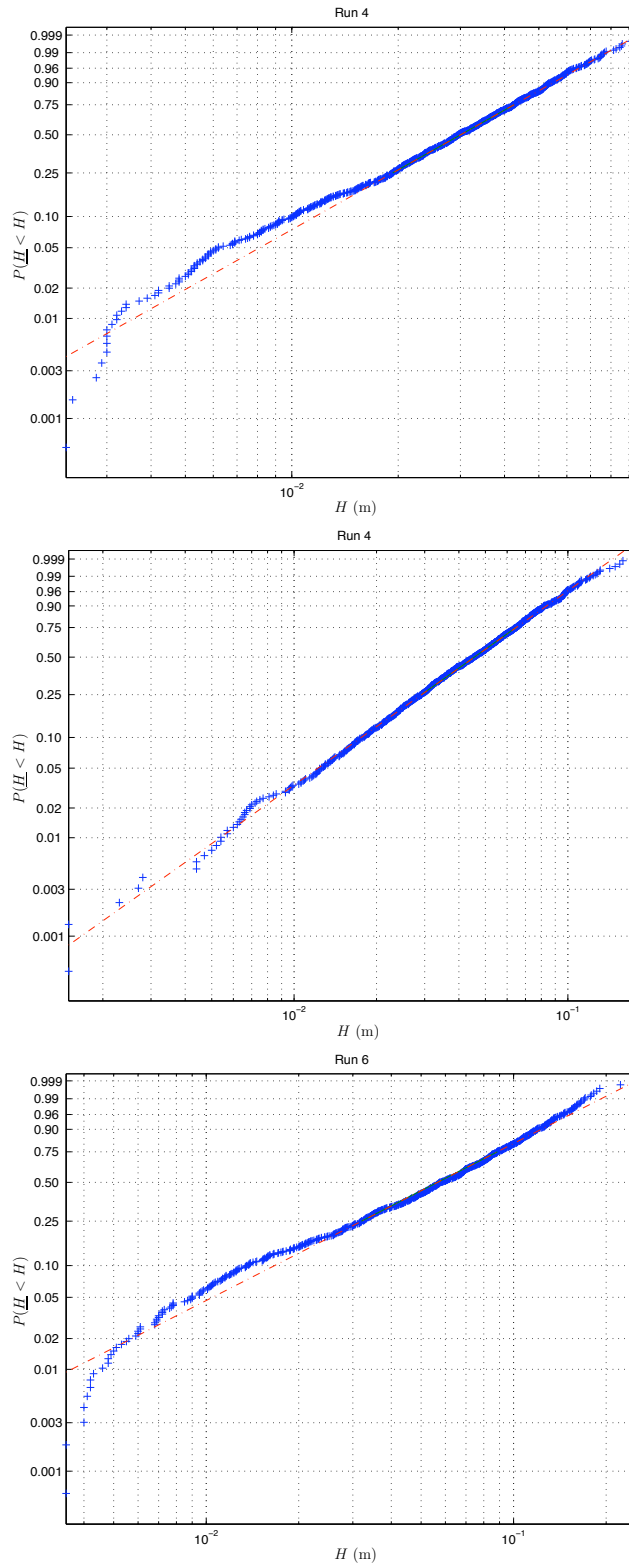


Figure 3.11: Numerical modelling of the Edinburgh experiments: experimental wave heights (+) compared to the Rayleigh distribution (dashed line) for runs 4, 6 and 9.

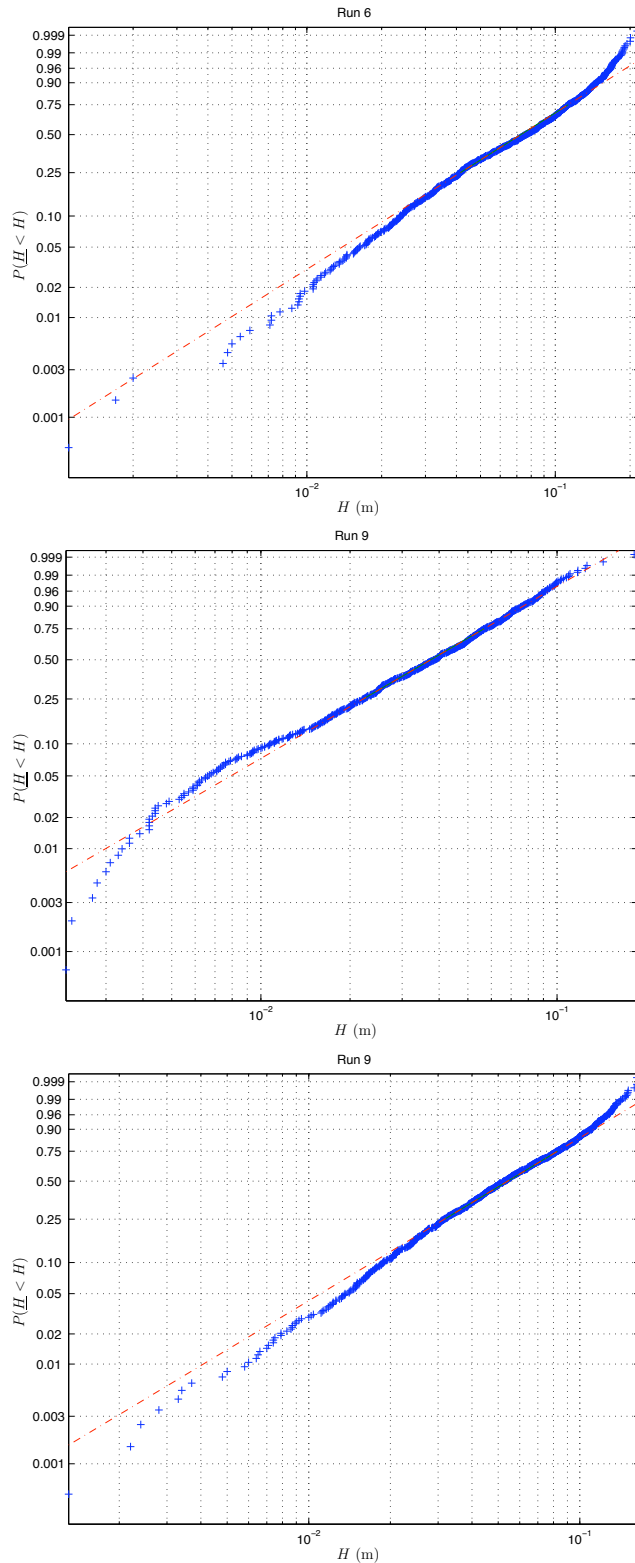


Figure 3.12: Numerical modelling of the Edinburgh experiments: numerical wave heights (+) compared to the Rayleigh distribution (dashed line) for runs 4, 6 and 9.

Table 3.2: Edinburgh wave flume experiments: experimental observations

Run	$h^*$	$Q$	$Q_h$	$N_{ow}$	$N_w$	$N_{ow}/N_w(\%)$
1	0.0544	1.26E-05	0.0502	175	863	20
2	0.0435	3.25E-05	0.2033	479	888	54
3	0.0481	2.38E-05	0.1216	299	900	33
4	0.0563	2.68E-06	0.0100	39	850	5
5	0.0536	8.45E-06	0.0349	132	898	15
6	0.0325	2.26E-05	0.2531	329	719	46
7	0.0304	3.88E-05	0.4971	535	712	75
8	0.0356	1.19E-05	0.1104	173	682	25
9	0.0449	3.61E-06	0.0212	76	658	12
10	0.0307	2.74E-05	0.3431	410	719	57
11	0.0889	1.37E-05	0.0205	204	1000	20
12	0.0974	7.94E-06	0.0099	125	1017	12
13	0.0818	2.35E-05	0.0415	394	985	40
14	0.0763	2.84E-05	0.0576	357	1000	36
15	0.0844	1.89E-05	0.0313	278	985	28

Table 3.3: Edinburgh wave flume experiments: numerical results

Run	$h^*$	$Q$	$Q_h$	$N_{ow}$	$N_w$	$N_{ow}/N_w(\%)$
1	0.0544	1.09E-05	0.0436	84	1037	8
2	0.0435	5.02E-05	0.3142	290	967	30
3	0.0481	2.70E-05	0.1379	196	1017	19
4	0.0563	1.24E-06	0.0046	13	1038	1
5	0.0536	6.19E-06	0.0255	44	1042	4
6	0.0325	2.40E-05	0.2693	203	854	24
7	0.0304	8.83E-05	1.1317	541	847	64
8	0.0356	9.49E-06	0.0883	61	861	7
9	0.0449	2.17E-06	0.0127	14	849	2
10	0.0307	4.87E-05	0.6088	292	864	34
11	0.0889	1.11E-05	0.0167	89	1252	7
12	0.0974	6.91E-06	0.0086	47	1239	4
13	0.0818	2.61E-05	0.0460	150	1233	12
14	0.0763	2.63E-05	0.0534	214	1225	17
15	0.0844	1.63E-05	0.0270	121	1239	10

been plotted on Rayleigh distributed axes so that the Rayleigh distribution appears to be a straight line. In all cases, the distribution of the measured wave heights closely follow that of the Rayleigh distribution for the larger waves. As the wave height decreases, i.e., for the less significant waves, the wave heights for both the experiment and numerical model deviate from the Rayleigh distribution. This analysis shows that the waves that were recorded 2.0 metres from the seawall were similar to those expected in a typical sea state.

The values of the  $h^*$  parameter, dimensionless discharges and the number of waves overtapped observed in the Edinburgh experiments, and calculated using the numerical model are presented in Tables 3.2 and 3.3 respectively. The dimensionless discharge volumes collected from both the wave flume experiments and the numerical model are compared to the empirical model of Besley in Fig. 3.13. The values of  $H_s$  from the experimental observations were used in the calculation of  $Q_h$  for the numerical discharges. It can be seen that both the experimental and numerical values follow the general Besley curve for  $R_h$  in the range [0.05,0.25]. For values of  $0.15 \leq R_h \leq 0.25$ , there is excellent agreement between the computed values, the experimental values and the empirical model. For the values of the crest freeboard,  $R_h \leq 0.1$ , the model over-predicts the dimensionless discharge volumes by up to a factor of 3. The Besley model over-predicts the experimental discharges in this range. It was noted in Besley (1999) that overtopping predictions using empirically derived models of wave overtopping should only be considered accurate to within a factor of 3 over the actual overtopping rate. Values of the dimensionless freeboard,  $R_h$ , and the ratio of overtopping waves,  $N_{ow}/N_w$ , for the Edinburgh experiments and the numerical model are compared to the Besley curve in Fig. 3.14. For all 15 runs of the experiment modelled, the numerical model under-predicts the number of overtopping waves. The numerical prediction improves slightly where the waves are not severely impacting ( $h^* > 0.15$ ).

The absolute relative errors between the numerical and experimental values of significant wave heights and dimensionless discharge volumes are plotted in Fig. 3.15. The absolute relative error is calculated here using

$$\text{Absolute relative error (\%)} = 100 \left( \frac{|f_{exp} - f_{num}|}{f_{exp}} \right), \quad (3.13)$$

where  $f_{exp}$  and  $f_{num}$  are the experimental and numerical values respectively. For values of  $h^* > 0.075$ , there is good agreement between the numerical and experimental dimensionless discharges with the numerical model providing overtopping predictions to within 20% of the experimental dimensionless discharges. For values

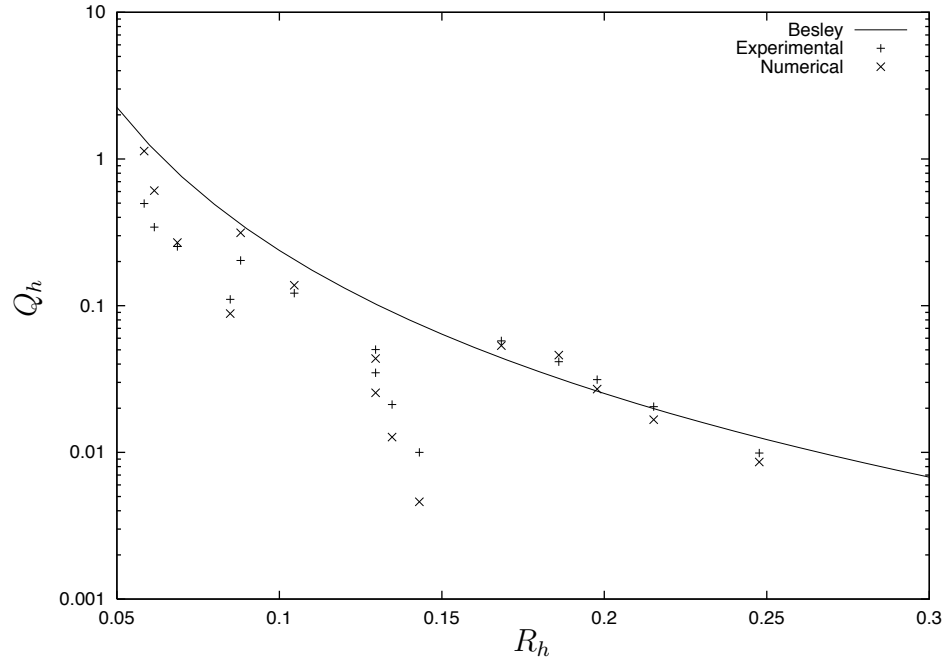


Figure 3.13: Edinburgh wave flume experiments: values of the experimental and numerical dimensionless discharge ( $Q_h$ ) plotted against the Besley empirical model.

of  $h^* < 0.06$ , there is a marked decrease in accuracy in the numerical predictions of both the overtopping dimensionless discharges and wave heights. There were no runs of the Edinburgh experiments conducted for values of  $h^* = [0.055, 0.075]$ .

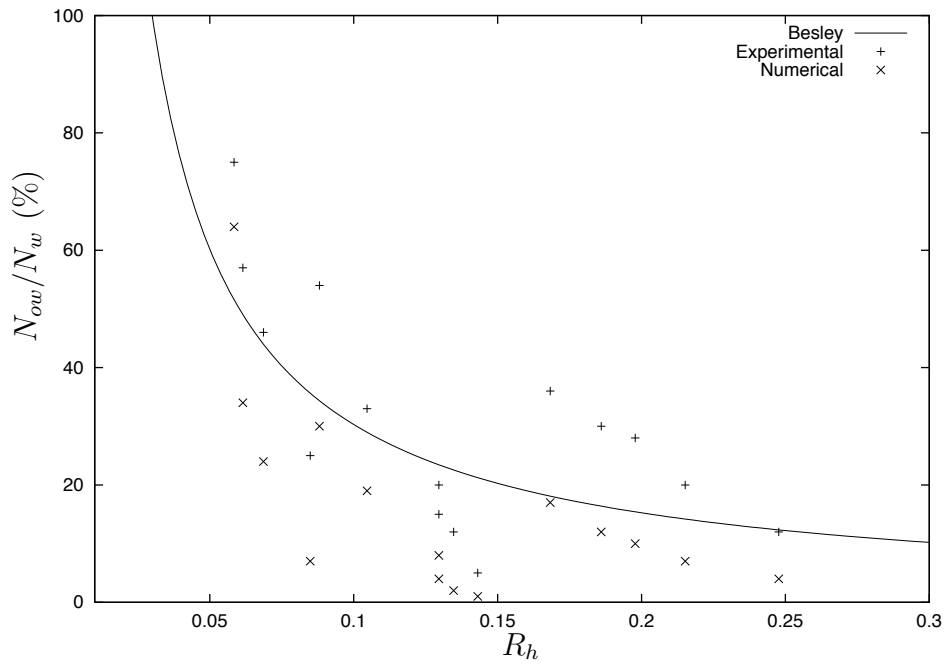


Figure 3.14: Edinburgh wave flume experiments: the ratio of overtopping waves to total number of waves ( $N_{ow}/N_w \%$ ) plotted against the Besley empirical model.

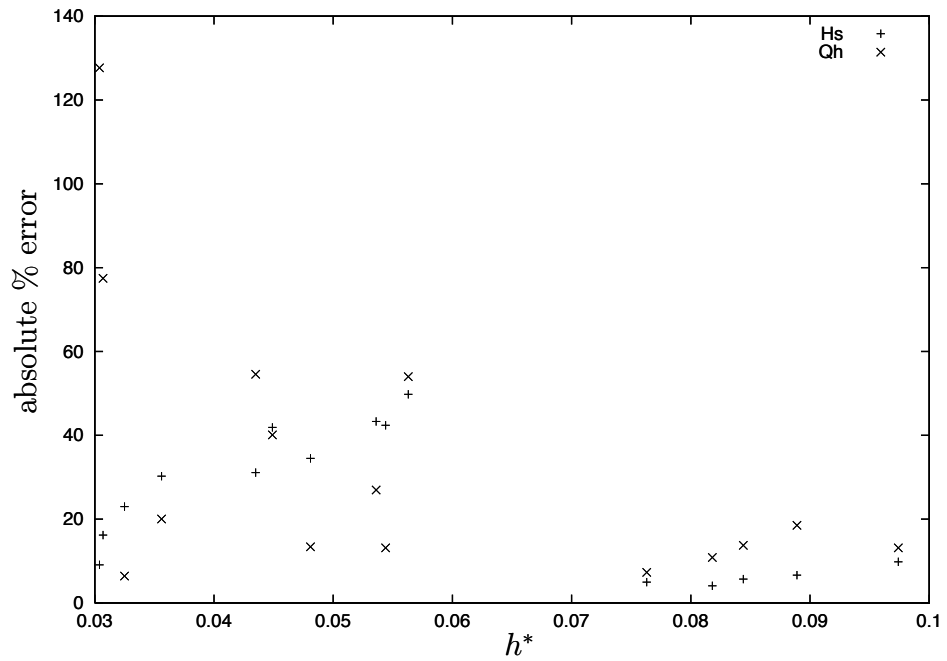


Figure 3.15: Edinburgh wave flume experiments: the absolute error between the numerical and experimental values of  $Q_h$  and  $H_s$  for varying values of  $h^*$ .

## 3.6 Chapter Summary

This chapter was concerned with the application of the shallow water flow solver presented in Chapter 2 to model violent wave overtopping. The wave statistics that are commonly used to analyse the propagation of water waves, the significant wave heights ( $H_s$ ) and mean wave periods ( $T_m$ ), are defined in Section 3.1.1. The Rayleigh distribution that gives the probability of non-exceedence of wave heights in deep water is presented in Section 3.1.2. A description of the basic empirical model for the prediction of overtopping volumes is given in Section 3.1.3. The physical phenomenon of violent wave overtopping is explained in Section 3.2 along with a review of previous studies. The  $h^*$  parameter that determines whether impacting or impulsive waves dominate at the seawall is defined in Eq. (3.8) and the empirical model of Besley that gives overtopping volumes of violent wave interaction with vertical seawalls is explained (Section 3.2.3).

A set of experiments that was conducted to examine violent wave overtopping is presented in Section 3.3, and was modelled using the shallow water flow solver in Section 3.4. An analysis of the wave heights showed that the numerical waves were larger than the experimental waves measured at a depth gauge located 1.0 metres from the seawall. This over-prediction can be attributed to the absence of terms that model dispersion in the governing equations, preventing the modelling of wave propagation in intermediate depth water. An analysis of the overtopping predictions has been conducted using both a comparison of the individual overtopping events and mean values. It was found that the numerical model was able to replicate some of the major overtopping events at the same time as they occurred in the experiments. The experimental and numerical observations were compared to the empirical model derived by Besley. It was found that for less impacting waves ( $h^* > 0.06$ ) the shallow water model gave wave height and overtopping predictions to within 20% of the experimental values. For more impacting waves there is a notable decrease in accuracy.

The next chapter examines a form of the Boussinesq equations which are a depth-averaged system of governing equations with terms that model dispersion allowing for intermediate depth water to be modelled.

# Chapter 4

## The Boussinesq Equations

Peregrine (1967) derived a set of flow equations for small amplitude waves over varying depth based upon the work of French mathematician Joseph Boussinesq (1842–1929). Now known as the standard Boussinesq equations, this system used the water surface elevation above the still water level (SWL) and the horizontal depth-averaged velocity as the conserved variables. The standard Boussinesq equations are:

$$\frac{\partial \eta}{\partial t} + \frac{\partial}{\partial x}[(d + \eta)u] = 0 \quad (4.1)$$

$$\frac{\partial u}{\partial t} + g \frac{\partial \eta}{\partial x} + u \frac{\partial u}{\partial x} + \frac{d^2}{6} \frac{\partial^3 u}{\partial x^2 \partial t} - \frac{d}{2} \frac{\partial^2}{\partial x^2} \left( d \frac{\partial u}{\partial t} \right) = 0 \quad (4.2)$$

where  $\eta$  is the water surface elevation above the SWL,  $u$  is the depth-averaged velocity and  $d$  is the water depth (the distance between the SWL and the bed surface). Peregrine used his formulation to model the propagation of a solitary wave on a beach of uniform slope.

Peregrine's work, along with advances in digital computing, has since sparked a renewed interest in Boussinesq-type models. Although the standard Boussinesq equations include terms that model dispersion, the range of applicability of these equations are not significantly greater than the shallow water equations (SWE), i.e., that the depth to wavelength ratio has to be less than 1/20. Witting (1984), Murray (1989), Madsen *et al.* (1991) and Nwogu (1993) have all extended the standard Boussinesq equations to be able to model flow in intermediate depth water ( $0 < d/L \leq 1/2$ ). Witting (1984) expressed the exact depth-integrated momentum equations in terms of the velocity at the surface using coefficients of a fourth-order Taylor series expansion to obtain the best dispersion characteristics. However, Witting's equations are only applicable for propagation over a constant

depth and a two-dimensional formulation cannot easily be derived. Murray (1989) and Madsen *et al.* (1991) both introduced additional third-order terms into the standard Boussinesq equations to obtain a system of equations with a dispersion relation closely relating to that obtained by linear theory.

Nwogu (1993) used a different approach to extend the range of the standard Boussinesq equations. By assuming a quadratic velocity profile in the vertical direction, Nwogu derived a system of equations where the horizontal velocity is calculated at an arbitrary depth. This leads to a formulation where the dispersion characteristics of the equations are dependent upon this depth of the assumed velocity. By minimising the error between linear wave theory and that of the governing equations, the optimum depth for where the velocity is determined can be found (Section 4.1.1). This chapter presents a numerical solution method for the extended Boussinesq equations of Nwogu.

This chapter is structured as follows: the extended Boussinesq equations of Nwogu are presented and their dispersion properties compared with those of other Boussinesq models as well as linear theory (Section 4.1). The finite difference method is introduced (Section 4.2) and the numerical scheme used to solve Nwogu's equation is presented (Section 4.3). Methods of treating the boundaries and wave generation are discussed (Sections 4.4 and 4.5) before the numerical solver is validated against a number of common test cases (Section 4.7).

## 4.1 Nwogu's Boussinesq Equation system

Nwogu's extended Boussinesq equation system is given by

$$\frac{\partial \eta}{\partial t} + \nabla \cdot [(d + \eta)\mathbf{u}_\alpha] + \nabla \cdot \left\{ \left( \frac{z_\alpha^2}{2} - \frac{d^2}{6} \right) d \nabla (\nabla \cdot \mathbf{u}_\alpha) + \left( z_\alpha + \frac{d}{2} \right) d \nabla [\nabla \cdot (d \mathbf{u}_\alpha)] \right\} = 0 \quad (4.3)$$

$$\frac{\partial \mathbf{u}_\alpha}{\partial t} + g \nabla \eta + (\mathbf{u}_\alpha \cdot \nabla) \mathbf{u}_\alpha + z_\alpha \left\{ \frac{z_\alpha}{2} \nabla \left( \nabla \cdot \frac{\partial \mathbf{u}_\alpha}{\partial t} \right) + \nabla \left[ \nabla \cdot \left( d \frac{\partial \mathbf{u}_\alpha}{\partial t} \right) \right] \right\} = 0 \quad (4.4)$$

where  $\eta$  is the water surface elevation,  $d$  is the local water depth,  $\mathbf{u}_\alpha = (u_\alpha, v_\alpha)$  is the horizontal velocity at depth  $z_\alpha$ ,  $\nabla = (\partial/\partial x, \partial/\partial y)$  is the horizontal gradient operator and  $g = 9.81 \text{ ms}^{-2}$  is the acceleration due to gravity.

### 4.1.1 Dispersive properties of Nwogu's Boussinesq Equations

Nwogu (1993), in the formulation of his Boussinesq system, used a velocity at an arbitrary depth,  $z_\alpha$ , as a parameter in its derivation. This allows it to use the values for the horizontal velocity at the seabed, the still water level or anywhere in between. The choice of depth where the horizontal velocity is calculated is made in order to minimise the error between the dispersion present in the current formulation and that given by linear dispersion theory. For this analysis, the linearised version of the full Nwogu Boussinesq system is used and a constant depth is assumed, i.e.,

$$\frac{\partial \eta}{\partial t} + d \frac{\partial u_\alpha}{\partial x} + \left( \alpha + \frac{1}{3} \right) d^3 \frac{\partial^3 u_\alpha}{\partial x^3} = 0 \quad (4.5)$$

$$\frac{\partial u_\alpha}{\partial t} + g \frac{\partial \eta}{\partial x} + \alpha d^2 \frac{\partial^3 u_\alpha}{\partial x^2 \partial t} = 0 \quad (4.6)$$

where  $\alpha$  is related to  $z_\alpha$  and  $d$  by the quadratic equation

$$\alpha = \frac{1}{2} \left( \frac{z_\alpha}{d} \right)^2 + \frac{z_\alpha}{d}. \quad (4.7)$$

The value of  $\alpha$  can be chosen from any value in the interval  $-1/2 \leq \alpha \leq 0$  depending upon the depth where the velocity is calculated. For example, the velocity at the seabed corresponds to a value of  $\alpha = -1/2$ . Alternatively, if the velocity at the still water level is required, then this corresponds to a value of  $\alpha = 0$ .

Assuming a periodic sinusoidal wave of amplitude  $a$ , period  $T = 2\pi/\omega$  and wavelength  $L = 2\pi/k$  (where  $\omega$  is the wave frequency and  $k$  is the wavenumber), i.e.,

$$\eta = a \sin(kx - \omega t) \quad (4.8)$$

$$u = b \sin(kx - \omega t) \quad (4.9)$$

leads to the following expression for the dispersion relation (Nwogu, 1993; Walkley and Berzins, 1999b)

$$C^2 = \frac{\omega^2}{k^2} = gd \left[ \frac{1 - (\alpha + 1/3)(kd)^2}{1 - \alpha(kd)^2} \right]. \quad (4.10)$$

where  $C$  is the phase speed. The linear dispersion relation for Airy waves is given

by

$$C^2 = gd \frac{\tanh(kd)}{kd}. \quad (4.11)$$

The group velocity,  $C_g$ , that governs the wave energy in a wave train is also important when considering the dispersion properties of the governing equations. Nwogu (1993) derived the group velocity for his equation system and it is given by

$$C_g = \frac{d\omega}{dk} = C \left\{ 1 - \frac{(kd)^2/3}{[1 - \alpha(kd)^2][1 - (\alpha + 1/3)(kd)^2]} \right\}. \quad (4.12)$$

The normalised phase speeds and group velocities for Nwogu's Boussinesq equations for different values of  $\alpha$  have been plotted in Figs. 4.1 and 4.2 against the water depth to wavelength ratio  $d/L$  in the interval  $0 < d/L \leq 1/2$  (replicating two figures from Nwogu (1993)). Recall the shallow water limit is considered to be  $d/L < 1/20$ , the intermediate depth is considered to be  $1/20 \leq d/L \leq 1/2$  and the deep water limit is  $d/L > 1/2$ .

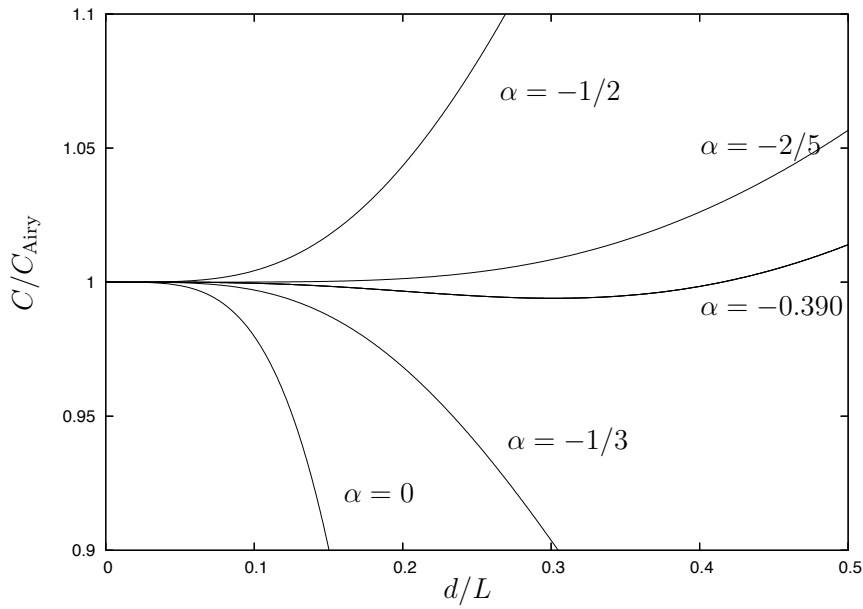


Figure 4.1: Dispersive properties of Nwogu's Boussinesq equations: comparison of the normalised phase speeds for different values of  $\alpha$ .

Fig. 4.1 shows that at the shallow water limit the dispersion relations are all equivalent to the exact dispersion relation given by Eq. (4.11). However, as the depth to wavelength ratio increases, it is clear that the choice of  $\alpha$  will considerably alter the dispersive properties of the governing equations. Values of  $\alpha = -1/3$  and  $\alpha = -2/5$  correspond to the system of equations derived by Peregrine (1967) and Witting (1984) respectively. It is clear that Peregrine's system of equations

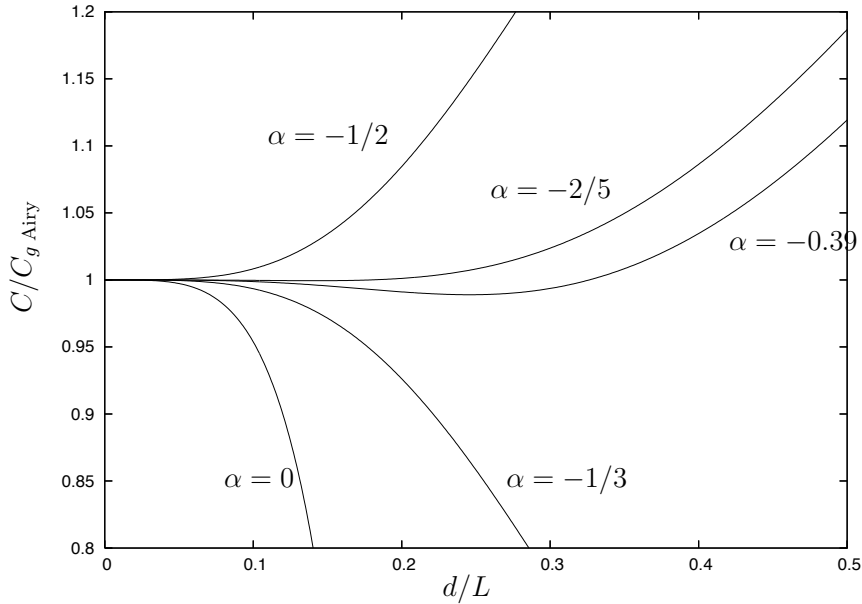


Figure 4.2: Dispersive properties of Nwogu's Boussinesq equations: comparison of the normalised group velocities for different values of  $\alpha$ .

are only applicable up to  $d/L = 0.1$  and will be insufficient for modelling wave propagation in intermediate depth water. The dispersion of the system using the velocity at the seabed ( $\alpha = 0$ ) gives the poorest comparison to linear dispersion theory. This is, of course, to be expected as the particle motion near the seabed is minimal. The value of  $\alpha = -0.390$ , which corresponds to a water depth of  $z_\alpha = 0.531d$ , was obtained by minimising the error between Eqs. (4.10) and (4.11). The comparison of the group velocities in Fig. 4.2 shows that the value of  $\alpha = -0.390$  gives a reasonable approximation of the exact dispersion relation. It is evident from Figs. 4.1 and 4.2 that this value provides the best dispersion properties for the governing equations, when compared to linear wave theory, and is used for all subsequent calculations.

## 4.2 Finite Difference Methods

A common approach in the numerical solution of differential equations or systems of differential equations is to discretise the solution domain into a number of solution points (or nodes). The solution of the system at each of these nodes is then calculated by way of finite differences that are derived *via* a rearrangement of the Taylor series expansion.

A finite difference discretisation is represented in Fig 4.3. Here, a one-dimensional solution domain is discretised into five solution nodes. The spatial step

between each of the nodes is constant in this case and is denoted by  $\Delta x$ . The values at these nodes over time are denoted by  $n - 1$ ,  $n$  and  $n + 1$  where  $n$  are the current known values,  $n - 1$  are the previous values and  $n + 1$  are the next values to be calculated. The time step is denoted by  $\Delta t$ . For an arbitrary variable  $a$ , the value of node  $i$  at time step  $n$  is given by the notation  $a_i^n$ .

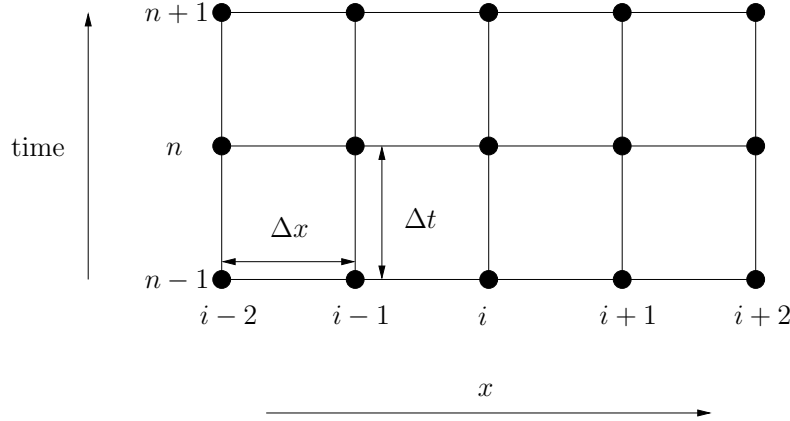


Figure 4.3: Finite difference discretisation.

The Taylor series provides an approximation of a function at a given point. For example, consider a function  $f(x)$  at the point  $x + \Delta x$ . The Taylor series expansion is (using the subscript notation  $f_{i+1} = f(x + \Delta x)$ )

$$f_{i+1} = f_i + \frac{\Delta x f'_i}{1!} + \frac{\Delta x^2 f''_i}{2!} + \frac{\Delta x^3 f^{(3)}_i}{3!} + \dots + \frac{\Delta x^n f^{(n)}_i}{n!} \quad (4.13)$$

where  $f'_i, f''_i, \dots, f^{(n)}_i(x)$  denote the derivatives of  $f(x)$  and  $n!$  denotes the factorial of  $n$ . The accuracy of the series expansion of a function is dependent upon the number of terms included in the series. For an  $n$ th-order accurate expansion of the function  $f(x)$ , only the terms up to and including  $f^{(n)}(x)$  are retained. For example,

$$f_{i+1} = f_i + \Delta x f'_i + \dots + \Delta x^n f^{(n)}_i + \mathcal{O}(\Delta x^{n+1}) \quad (4.14)$$

where  $\mathcal{O}(\Delta x^{n+1})$  denotes the truncation error due to the absence of the higher-order terms. The method of undetermined coefficients has been used to derive the finite-differences, details of which can be found in Appendix B.

### 4.2.1 Time differencing

The finite difference approximations derived in Appendix B approximate the spatial derivatives (i.e.,  $\partial y / \partial x$ ). A similar approach can be used to derive approxima-

tions of the time derivative  $\partial y / \partial t$ . However, using central or forward differences in time, the calculation at the next time step  $n + 1$  will require knowledge of the values at future time steps  $n + 2, n + 3, \dots$ . It is common to use a backward treatment for the time derivatives so that the values at  $n + 1$  are only dependent upon previously calculated values at  $n, n - 1, n - 2, \dots$ . The Adams-Basforth and Adams-Moulton time marching methods are used in Section 4.3 to advance the solution of the extended Boussinesq equations through time. Adams' methods are an example of a backwards treatment of the time derivative.

## 4.3 Finite Difference Solver for the Boussinesq Equations

Previous methods for solving Boussinesq-type models have mainly utilised finite difference methods. Peregrine (1967) and Abbot *et al.* (1978) both used finite difference methods to solve the standard Boussinesq equations, and Nwogu (1993) used a third-order Crank-Nicholson formulation to solve his system of extended Boussinesq equations. Other numerical methods that have been used to solve Boussinesq equations include a finite-element implementation by Walkley and Berzins (1999a, 2002) for Nwogu's system and a hybrid finite volume/finite difference implementation by Ilic *et al.* (2005) for the equations of Madsen and Sørensen (1992). The numerical solver for an extended Boussinesq formulation that has received the most interest is a finite difference method by Wei and Kirby (1995).

Wei and Kirby (1995) in their scheme approximated the first-order spatial derivatives to fourth-order accuracy, and second-order spatial derivatives to second-order accuracy. Coupled with a fourth-order accurate in time predictor/corrector scheme, this treatment ensures that the truncation errors in the numerical approximations are smaller than that of the dispersive terms retained by the governing equations. Here, Wei and Kirby's scheme has been applied to solve Nwogu's Boussinesq system. In this section only one spatial dimension is considered, Eqs. (4.15) and (4.16). A complete description of the full two-dimensional scheme

can be found in (Wei and Kirby, 1995).

$$\frac{\partial \eta}{\partial t} + \frac{\partial}{\partial x}[(d + \eta)u_\alpha] + \frac{\partial}{\partial x} \left[ \left( \frac{z_\alpha^2}{2} - \frac{d^2}{6} \right) d \frac{\partial^2 u_\alpha}{\partial x^2} + \left( z_\alpha + \frac{d}{2} \right) d \frac{\partial^2}{\partial x^2}(du_\alpha) \right] = 0, \quad (4.15)$$

$$\frac{\partial u_\alpha}{\partial t} + g \frac{\partial \eta}{\partial x} + u \frac{\partial u_\alpha}{\partial x} + z_\alpha \left[ \frac{z_\alpha}{2} \frac{\partial^3 u_\alpha}{\partial x^2 \partial t} + \frac{\partial^2}{\partial x^2} \left( d \frac{\partial u_\alpha}{\partial t} \right) \right] = 0. \quad (4.16)$$

Rearranging Eqs. (4.15) and (4.16) so that all terms involving a time derivative are on the left-hand side gives

$$\frac{\partial \eta}{\partial t} = E, \quad (4.17)$$

$$\frac{\partial U}{\partial t} = F, \quad (4.18)$$

where

$$E = -\frac{\partial}{\partial x}[(d + \eta)u_\alpha] - \frac{\partial}{\partial x} \left[ \left( \frac{z_\alpha^2}{2} - \frac{d^2}{6} \right) d \frac{\partial^2 u_\alpha}{\partial x^2} + \left( z_\alpha + \frac{d}{2} \right) d \frac{\partial^2}{\partial x^2}(du_\alpha) \right], \quad (4.19)$$

$$F = -g \frac{\partial \eta}{\partial x} - u_\alpha \frac{\partial u_\alpha}{\partial x}, \quad (4.20)$$

and

$$U = u_\alpha + z_\alpha \left[ \frac{z_\alpha}{2} \frac{\partial^2 u_\alpha}{\partial x^2} + \frac{\partial^2}{\partial x^2}(du_\alpha) \right]. \quad (4.21)$$

The rewritten form of the governing equations, Eqs. (4.17) and (4.18), results in a purely tri-diagonal system for the horizontal velocities in Eq. (4.21) when a second-order central difference stencil is used. Time differencing is achieved through a fourth-order predictor/corrector method. The predictor values for  $\eta$  and  $U$  are calculated using a third-order Adams-Bashforth explicit scheme given by

$$\eta_i^{n+1/2} = \eta_i^n + \frac{\Delta t}{12} [23E_i^n - 16E_i^{n-1} + 5E_i^{n-2}], \quad (4.22)$$

$$U_i^{n+1/2} = U_i^n + \frac{\Delta t}{12} [23F_i^n - 16F_i^{n-1} + 5F_i^{n-2}], \quad (4.23)$$

where the superscripts  $n$ ,  $n - 1$  and  $n - 2$  denote the known values at the previous and current time step,  $n + 1/2$  denotes the predicted values and  $\Delta t$  is the time step. For the first iteration of the predictor/corrector scheme the values of the previous time steps are unknown. In this study, these values were initialised by setting them

equal to the initial conditions. The evaluation of the horizontal velocities is then achieved through the solution of a tri-diagonal system given by Eq. (4.21). The coefficient matrices are constant and therefore can be inverted and stored for use at each time level. However, it was found that the implementation of the Thomas algorithm (Thomas, 1949) at each time step provided significant improvement on the overall computation time (Section 4.3.2).

The corrector stage used to calculate the values for the next time step  $n + 1$  is a fourth-order Adams-Moulton method given by

$$\eta_i^{n+1} = \eta_i^n + \frac{\Delta t}{24} [9E_i^{n+1/2} + 19E_i^n - 5E_i^{n-1} + E_i^{n-2}], \quad (4.24)$$

$$U_i^{n+1} = U_i^n + \frac{\Delta t}{24} [9F_i^{n+1/2} + 19F_i^n - 5F_i^{n-1} + F_i^{n-2}]. \quad (4.25)$$

The corrector stage is iterated until convergence between two successive iterations is achieved. The difference between two successive iterations of the corrector stage is calculated using

$$\text{Difference} = \max_i \left( \frac{\sum_i |\eta_i^{n+1} - \eta_i^{(n+1)*}|}{\sum_i |\eta_i^{n+1}|}, \frac{\sum_i |U_i^{n+1} - U_i^{(n+1)*}|}{\sum_i |U_i^{n+1}|} \right), \quad (4.26)$$

where  $(*)$  denotes the estimate from the previous iteration. The tolerance used in all computations was set at  $1 \times 10^{-4}$  and typically required just one iteration of the corrector to reach convergence.

### 4.3.1 Spatial differencing

As discussed in the previous section, first and second-order spatial derivatives are evaluated to fourth-order and second-order accuracy respectively. The method of undetermined coefficients was used to derive the appropriate difference schemes.

For first-order derivatives, the following fourth-order stencil was applied

$$\left( \frac{\partial f}{\partial x} \right)_i = \frac{f_{i-2} - 8f_{i-1} + 8f_{i+1} - f_{i+2}}{12\Delta x}, \quad (4.27)$$

where  $f = \{\eta, u\}$  and  $i$  is the spatial index.

For most of the solution domain a centred discretisation is applicable. However, for the first computational nodes in from the boundary ( $f_2, f_{n-1}$ ) and those nodes

on the boundary ( $f_1, f_n$ ) the following skewed difference schemes are used

$$\left( \frac{\partial f}{\partial x} \right)_1 = \frac{-25f_1 + 48f_2 - 36f_3 + 16f_4 - 3f_5}{12\Delta x}, \quad (4.28)$$

$$\left( \frac{\partial f}{\partial x} \right)_2 = \frac{-3f_1 - 10f_2 + 18f_3 - 6f_4 + f_5}{12\Delta x}, \quad (4.29)$$

$$\left( \frac{\partial f}{\partial x} \right)_{n-1} = \frac{3f_n + 10f_{n-1} - 18f_{n-2} + 6f_{n-3} - f_{n-4}}{12\Delta x}, \quad (4.30)$$

$$\left( \frac{\partial f}{\partial x} \right)_n = \frac{25f_n - 48f_{n-1} + 36f_{n-2} - 16f_{n-3} + 3f_{n-4}}{12\Delta x}. \quad (4.31)$$

The second-order spatial derivatives are approximated to second-order accuracy using the finite difference stencil

$$\left( \frac{\partial^2 f}{\partial x^2} \right)_i = \frac{f_{i-1} - 2f_i + f_{i+1}}{\Delta x^2}. \quad (4.32)$$

The second-order derivatives are either specified at the boundary or are not required in the solution procedure depending upon the problem specification.

### 4.3.2 The Thomas algorithm

Applying the finite difference stencil Eq. (4.32) to Eq. (4.21) results in the following finite difference scheme

$$\begin{aligned} U_i &= \left( \frac{z_\alpha^2}{2\Delta x^2} + \frac{z_\alpha d_{i-1}}{\Delta x^2} \right) u_{\alpha,i-1} + \left( 1 - \frac{z_\alpha^2}{\Delta x^2} - \frac{2z_\alpha d_i}{\Delta x^2} \right) u_{\alpha,i} \\ &\quad + \left( \frac{z_\alpha^2}{2\Delta x^2} + \frac{z_\alpha d_{i+1}}{\Delta x^2} \right) u_{\alpha,i+1}. \end{aligned} \quad (4.33)$$

Eq. (4.33) can be written as a matrix equation giving the tri-diagonal system

$$\begin{pmatrix} U_1 \\ U_2 \\ \vdots \\ U_{n-1} \\ U_n \end{pmatrix} = \begin{pmatrix} b_1 & c_1 & & & \\ a_2 & b_2 & c_2 & & \\ & \ddots & \ddots & \ddots & \\ & & a_{n-1} & b_{n-1} & c_{n-1} \\ & & & a_n & b_n \end{pmatrix} \begin{pmatrix} u_{\alpha,1} \\ u_{\alpha,2} \\ \vdots \\ u_{\alpha,n-1} \\ u_{\alpha,n} \end{pmatrix}, \quad (4.34)$$

where

$$a_i = \frac{z_\alpha^2}{2\Delta x^2} + \frac{z_\alpha d_{i-1}}{\Delta x^2}, \quad (4.35)$$

$$b_i = 1 - \frac{z_\alpha^2}{\Delta x^2} - \frac{2z_\alpha d_i}{\Delta x^2}, \quad (4.36)$$

$$c_i = \frac{z_\alpha^2}{2\Delta x^2} + \frac{z_\alpha d_{i+1}}{\Delta x^2}. \quad (4.37)$$

The Thomas algorithm is employed to solve the tri-diagonal matrix system given in Eqs. (4.34)–(4.37). The algorithm is a well known algorithm that is more computationally efficient than Gaussian elimination for solving tri-diagonal matrix equations. The algorithm is thought to have been developed by Thomas (1949) although the first full description appeared in an article by Bruce *et al.* (1953) (Ames, 1977).

The algorithm is described in two stages. The first stage is a forward sweep of the matrix to eliminate the lower diagonal terms,  $a_i$ . The new terms in the main diagonal,  $b'_i$ , are then given by

$$b'_i = b_i - c'_{i-1} \frac{a_i}{b'_{i-1}} \quad (4.38)$$

and the new left-hand side vector terms,  $U'_i$ , are given by

$$U'_i = U_i - U'_{i-1} \frac{a_i}{b'_{i-1}}. \quad (4.39)$$

The second stage consists of a backwards sweep to obtain the solution. First the  $n^{\text{th}}$  term is calculated using

$$u_{\alpha,n} = \frac{U'_n}{b'_n} \quad (4.40)$$

and then the remaining terms,  $u_{\alpha,n-1}, u_{\alpha,n-2}, \dots, u_{\alpha,1}$  are found by

$$u_{\alpha,i} = \frac{U'_i - c'_i u_{\alpha,i+1}}{b'_i}. \quad (4.41)$$

The Thomas algorithm is called at each iteration after the predictor/corrector stages have been calculated.

### 4.3.3 Time step calculation and stability

The predictor/corrector scheme described in Section 4.3 is not fully implicit in nature, therefore there exists a constraint on the size of time step required to ensure stability. Numerical experiments have indicated that for the numerical scheme to remain stable, the values that the Courant number can take are in the interval  $0 < \nu \leq 1$ . The calculation of the maximum allowable time step,  $\Delta t$ , is analogous to that used for the MUSCL-Hancock scheme in Section 2.2.5, i.e.,

$$\Delta t = \nu \min_i \left( \frac{\Delta x}{|\mathbf{u}_{\alpha,i}| + \sqrt{g(d_i + \eta_i)}} \right). \quad (4.42)$$

## 4.4 Boundary conditions

Without special treatment for the flow of mass across the solution boundaries, problems that use the extended Boussinesq equations are limited to initial value problems only. It is for this reason that three different types of boundary conditions are discussed here. These are:

- Incident wave boundary conditions,
- Absorbing boundary conditions,
- Solid wall boundary conditions.

As only the one-dimensional form of the governing equations has been presented here, the boundary conditions are specified for the one-dimensional case only. For the remainder of this section it is assumed that the computational nodes are indexed  $1, 2, \dots, n$  where the index 1 represents the values at the left-hand boundary and an index of  $n$  represents the values at the right-hand boundary (Fig. 4.4).

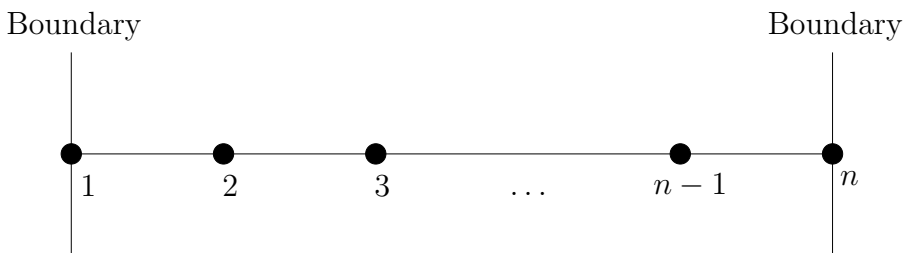


Figure 4.4: Node numbering convention for boundary conditions.

#### 4.4.1 Incident wave boundary condition

To allow the extended Boussinesq equations to be applied to model wave propagation (either single period or random waves), a boundary condition is required that can introduce a wave profile into the solution domain. Values for the conserved variables,  $\eta$  and  $u_\alpha$ , are specified at the boundary. Nwogu (1993) derived the following relationship between the water surface of the incident wave at the boundary  $\eta_I$  and the velocity  $u_{\alpha,I}$  using linear wave theory

$$u_{\alpha,I} = \frac{\omega}{kd_0[1 - (\alpha + 1/3)(kd_0)^2]} \eta_I \quad (4.43)$$

where  $u_1$  is the horizontal velocity at the boundary,  $\omega = 2\pi/T$  is the wave frequency of the incident wave,  $k$  the wave number and  $d_0$  is the depth at the boundary.

In practice, it was found that this treatment of the boundary condition tended to cause spurious oscillations in the solution domain unless the wave profile, and therefore the time derivative, is known *a priori*. In addition to the fact that this treatment does not allow for waves to propagate out of the boundary where it is applied, the incident wave boundary is given here for completeness, although it has not been used in the calculations performed in this study.

#### 4.4.2 Radiation boundary condition

Radiation boundary conditions are used where a boundary is required that allows waves to pass out of the solution domain without reflection. In order to satisfy this condition, it can be shown the the mass governing equation Eq. (4.15) at the boundary is written as (Nwogu, 1993)

$$\frac{\partial \eta}{\partial t} + C \frac{\partial \eta}{\partial x} = 0 \quad (4.44)$$

where  $C = \omega/k$  is the phase speed,  $\omega = 2\pi/T$  is the wave frequency,  $T$  is the wave period and  $k$  is the wave number.

The application of the boundary condition, Eq. (4.44), in the current model causes some reflection at the boundary due to the fact that no single phase speed exists for the system (Wei and Kirby, 1995). Without further treatment, the reflected energy causes oscillations near the boundary and eventually the scheme becomes unstable. To overcome this, it is common to use sponge layers at absorbing boundaries to dampen the wave energy as the waves approach the boundary

(Section 4.6).

#### 4.4.3 Solid wall boundary condition

A method of simulating a solid wall boundary condition is necessary for modelling wave reflection. Here it is assumed that the gradient of the water surface and the velocity across the boundary are zero where the solid wall boundary condition is applied. For example, when this treatment is applied to the right-hand boundary

$$u_{\alpha,n} = 0, \quad (4.45)$$

$$\left(\frac{\partial \eta}{\partial x}\right)_n = 0. \quad (4.46)$$

### 4.5 Internal wave generation

For cases where there are going to be reflective waves propagating back past the incident wave boundary, the treatment of the boundary conditions given in Section 4.4.1 would be insufficient. Specifying the variables at the boundary will not allow for waves to pass out of the solution domain, and oscillations will occur at the boundary contaminating the solution.

To overcome this problem, Larsen and Dancy (1983) proposed a method where a volume of fluid is added to the mass governing equation, Eq. (4.3), at a single grid point to create a wave propagating in both directions. Sponge layers (see Section 4.6) were used at absorbing boundaries to dampen the waves that are absorbed by the radiation boundary condition, Eq. (4.44). This approach was extended by Lee *et al.* (2001) who found that using energy transport as opposed to mass transport provided more accurate wave amplitudes in the wave train. However both approaches used a single grid point to oscillate on a staggered finite difference grid. If the same approach was employed on an un-staggered grid, oscillations are formed that soon cause the numerical scheme to become unstable. To allow internal generation of waves using their fourth-order finite difference method, Wei *et al.* (1999) extended the basic idea where mass is added to the momentum equation over a range of grid points in the form of a Gaussian curve instead of a single grid point. This approach enabled a scheme using an un-staggered grid to employ a source function method to generate waves in the solution domain. In keeping with the other sections in this chapter, only the one-dimensional case is considered.

A source function,  $f(x, t)$ , is added to Eq. (4.15) at every iteration of the solver (Fig. 4.5).

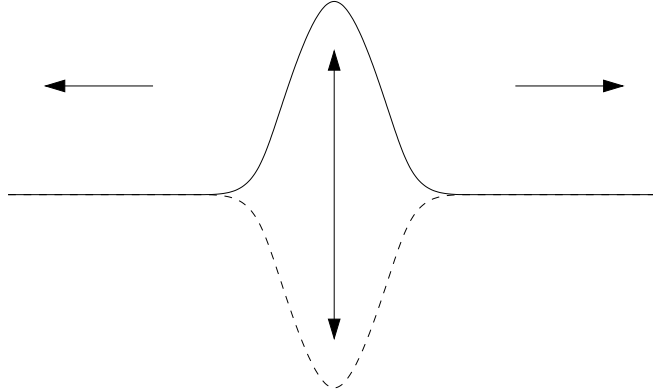


Figure 4.5: Internal wave generation using source function method.

$$\frac{\partial \eta}{\partial t} + \frac{\partial}{\partial x}[(d + \eta)u_\alpha] + \frac{\partial}{\partial x} \left[ \left( \frac{z_\alpha}{2} - \frac{d^2}{6} \right) d \frac{\partial^2 u_\alpha}{\partial x^2} + \left( z_\alpha + \frac{d}{2} \right) d \frac{\partial^2}{\partial x^2}(du_\alpha) \right] = f(x, t) \quad (4.47)$$

The source function itself consists of a product of two functions  $g(x)$  and  $s(t)$ , where  $g(x)$  is a Gaussian shape function and  $s(t)$  is a time dependent input signal.

$$f(x, t) = g(x)s(t). \quad (4.48)$$

The Gaussian shape function is defined by

$$g(x) = \exp[-\beta(x - x_s)^2] \quad (4.49)$$

where  $x_s$  is the centre of the Gaussian curve and  $\beta$  is a parameter that determines the width of the source function. The larger the value of  $\beta$ , the narrower the source function will be. However, if the source function is too narrow, spurious oscillations can enter the solution. If the source function is too wide, the extra grid points that are used in the source function can cause the solver to slow down. For the best results, it was found that the width of the source function,  $W$ , is half the wavelength  $L$ . It can be shown that

$$W = 2\sqrt{\frac{5}{\beta}}. \quad (4.50)$$

If the source function is assumed to be one half of the wavelength, i.e.,  $W = L/2$ ,

then Eq. (4.50) becomes

$$\frac{L}{2} = 2\sqrt{\frac{5}{\beta}}. \quad (4.51)$$

Therefore, the parameter  $\beta$  can be given by

$$\beta = \frac{80}{L^2}. \quad (4.52)$$

For random waves,  $\beta$  is determined by the peak frequency of the wave train ( $T_p$ ). The time dependent input signal is defined by

$$s(x) = D \sin(-\omega t) \quad (4.53)$$

where  $D$  is the magnitude of the source function,  $\omega = 2\pi/T$  is the wave frequency,  $T$  is the wave period and  $t$  is the time. Wei *et al.* (1999) derived the following expression for  $D$

$$D = \frac{2a_0(\omega^2 - \alpha_1 g k^4 d^3)}{\omega I k [1 - \alpha(kd^2)]} \quad (4.54)$$

where  $a_0$  is the required wave amplitude,  $\alpha_1 = \alpha + 1/3$  and  $I$  is an integral given by

$$I = \int_{-\infty}^{\infty} \exp(-\beta x^2) \exp(-iLx) dx = \sqrt{\frac{\pi}{\beta}} \exp\left(-\frac{L^2}{4\beta}\right). \quad (4.55)$$

## 4.6 Sponge layers

Sponge layers are used in conjunction with the radiation boundary condition Eq. (4.44) to model absorbing boundaries. The sponge layer consists of a function of the horizontal velocity that is added to the momentum equation Eq. (4.16) to dampen the wave energy approaching the boundary, i.e.,

$$\frac{\partial u_\alpha}{\partial t} + g \frac{\partial \eta}{\partial x} + u \frac{\partial u_\alpha}{\partial x} + z_\alpha \left[ \frac{z_\alpha}{2} \frac{\partial^3 u_\alpha}{\partial x^2 \partial t} + \frac{\partial x}{\partial x^2} \left( d \frac{\partial u_\alpha}{\partial t} \right) \right] = F_{\text{sponge}}(u_\alpha). \quad (4.56)$$

The dampening function  $F_{\text{sponge}}(u_\alpha)$  is defined by

$$F_{\text{sponge}}(u_\alpha) = \alpha_1 \omega f(x) u_\alpha, \quad (4.57)$$

where  $\alpha_1$  is a free parameter to be determined for each individual run,  $\omega = 2\pi/T$  is the frequency of the wave to be damped,  $T$  is the period of the wave to be damped and  $f(x)$  is a monotonic function that increases from 0 to 1 as it nears the boundary. For random waves, the value of  $T$  and therefore  $\omega$  is not known

at the present time step. Therefore, in practice, the peak wave period is used to calculate  $\omega$ , resulting in a sponge layer of constant width.  $f(x)$  is defined by

$$f(x) = \frac{\exp[(x - x_s)/(x_e - x_s)]^2 - 1}{\exp(1) - 1} \quad (4.58)$$

where  $x_s$  and  $x_e$  are the start and end points of the sponge layer respectively. It was found that a sponge layer of approximately three times the typical wavelength was sufficient to dampen the wave energy whilst ensuring that no more grid points than necessary were used.

## 4.7 Numerical Results

Before the extended Boussinesq equations are applied to model wave run-up and overtopping, it is necessary to validate the numerical solver to ensure that the scheme provides solutions to the required accuracy. A number of standard test cases have been applied to the numerical solver presented in Sections 4.3–4.6 to validate, in particular, the boundary conditions and the source function method for generating waves.

### 4.7.1 Solitary wave propagation

Solitary wave propagation provides a good test for governing equations that include dispersive terms. A solitary wave (often referred to as a soliton) propagating down a flat-bedded channel will experience no loss of amplitude or velocity. This is due to an exact balance between the dispersion, which acts on the wave to spread it out into a series of waves, and non-linear effects which tend to steepen the wave.

Here, the numerical scheme described in Section 4.3 is applied to a solitary wave propagation problem used by Wei and Kirby (1995). The water surface,  $\eta$ , and velocity,  $u_\alpha$ , are given by

$$\eta = A_1 \operatorname{sech}^2[B(x - Ct)] + A_2 \operatorname{sech}^4[B(x - Ct)] \quad (4.59)$$

$$u_\alpha = A \operatorname{sech}^2[B(x - Ct)] \quad (4.60)$$

where  $A$ ,  $B$ ,  $A_1$  and  $A_2$  are constants defined by

$$A = \frac{C^2 - gd}{C} \quad (4.61)$$

$$B = \left( \frac{C^2 - gd}{4d^2[(\alpha + 1/3)gd - \alpha C^2]} \right)^{1/2} \quad (4.62)$$

$$A_1 = \frac{C^2 - gd}{3[(\alpha + 1/3)gd - \alpha C^2]} d \quad (4.63)$$

$$A_2 = -\frac{(C^2 - gd)^2}{2gdC^2} \frac{[(\alpha + 1/3)gd + 2\alpha C^2]}{[(\alpha + 1/3)gd - \alpha C^2]} d \quad (4.64)$$

where  $C$  is the phase speed dependent upon the  $\alpha$  parameter and the wave amplitude to water depth ratio ( $a/d$ ) by the following relation

$$2\alpha \left( \frac{C^2}{gd} \right)^3 - \left( 3\alpha + \frac{1}{3} + 2\alpha \frac{a}{d} \right) \left( \frac{C^2}{gd} \right)^2 + 2\frac{a}{d} \left( \alpha + \frac{1}{3} \right) \left( \frac{C^2}{gd} \right) + \alpha + \frac{1}{3} = 0. \quad (4.65)$$

The roots of Eq. (4.65) are calculated using the Newton-Raphson method and converge to a solution with little computational effort.

The numerical scheme has been tested on the solution of a solitary wave propagating down a channel 450 metres in length with constant depth,  $d = 0.45$  metres. The channel is discretised into 4501 solution nodes given a spatial step of  $\Delta x = 0.1$  metres. The solitary wave has an amplitude of  $a = 0.045$  metres, giving a phase speed of  $C = 2.203\text{ms}^{-1}$ . The solitary wave is created at the left-hand boundary by explicitly stating values for  $\eta$  and  $u$  from Eqs. (4.59)–(4.65). The numerical solution to this problem at times,  $t = 40, 80, 120, 160$  and 200 seconds can be seen in Fig. 4.6. A comparison between the numerical solution and the analytical solution at time  $t = 160$  seconds can be seen in Fig. 4.7. The values of the water surfaces in Fig. 4.6 have been deliberately offset to best show the computed water surface over the course of the simulation.

Fig 4.6 shows that the solitary wave propagates down the channel with no loss of amplitude or velocity. Very small high frequency oscillations are present behind the propagating solitary wave which are a feature of higher-order finite difference schemes. These oscillations although present, do not significantly affect the solution. Fig 4.7 shows a magnified plot of the analytical and numerical solutions at time  $t = 100$  seconds. There is excellent agreement between the two sets of values indicating that a fourth-order solver is sufficient for calculating the dispersion terms in Nwogu's Boussinesq formulation.

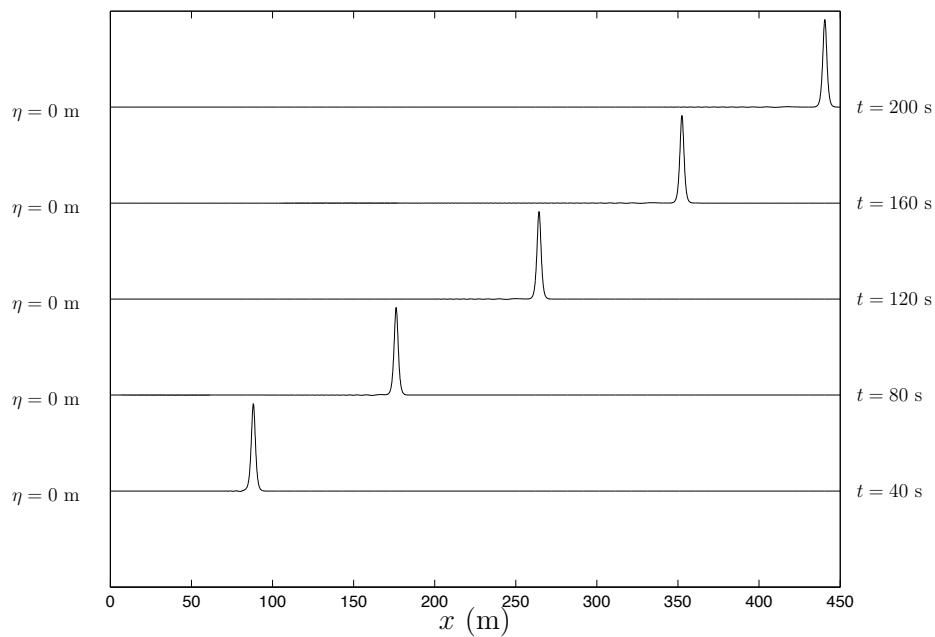


Figure 4.6: Solitary wave propagation: plots of the water surface elevation for times,  $t = 40, 80, 120, 160$  and  $200$  seconds.

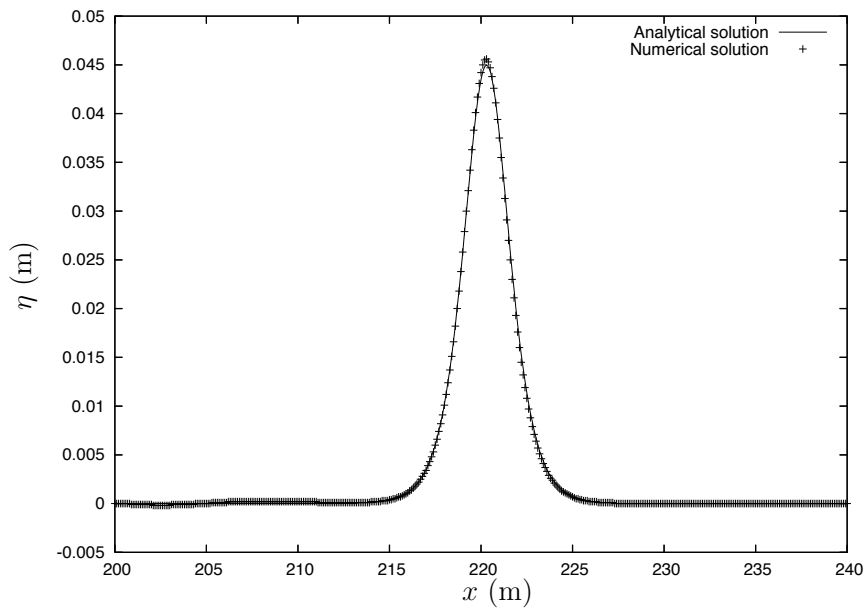


Figure 4.7: Solitary wave propagation: a comparison of the numerical water surface and the analytical water surface at time  $t = 100$  seconds.

### 4.7.2 Solitary wave interaction

Here the numerical scheme described in Section 4.3 has been applied to solve the problem of solitary wave interaction. Another property of solitary waves is that due to the dispersion being perfectly balanced with the steepening exhibited by the velocity of the wave, a solitary wave is able to pass through another solitary wave without loss of shape or amplitude.

The problem specification is similar to that described in Section 4.7.1, with the exception that another upstream travelling solitary wave is specified at the right-hand boundary using Eqs. (4.59)–(4.65). With a water depth of  $d = 0.45$  metres and an amplitude of  $a = 0.045$  metres, the corresponding phase speed is calculated as  $C = 2.203\text{ms}^{-1}$  meaning that the two waves cross at  $t = 102.13$  seconds. Fig. 4.8 shows water surface plots at time  $t = 40, 80, 120, 160$  and  $200$  seconds.

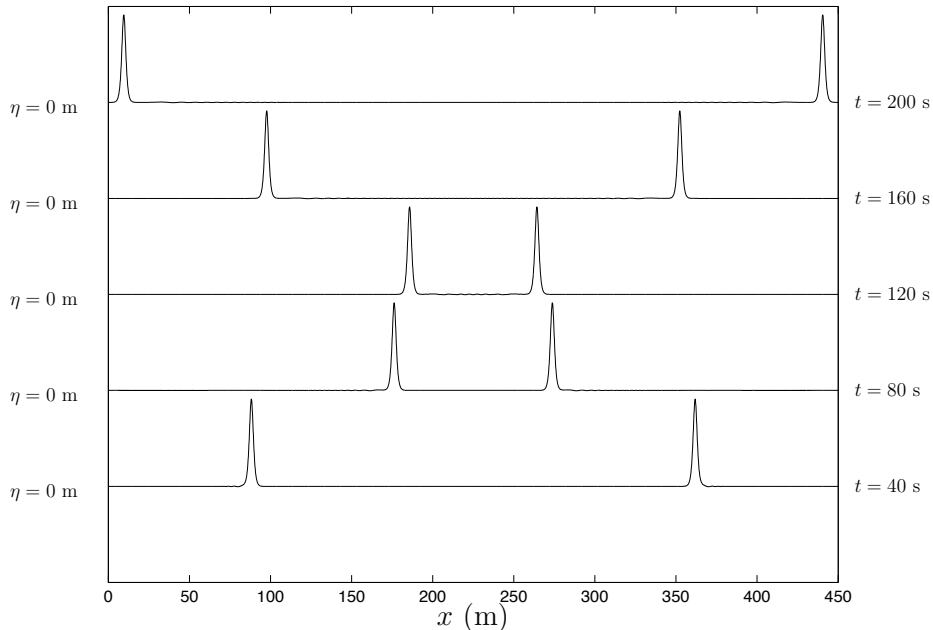


Figure 4.8: Solitary wave interaction: plots of the water surface elevation for times,  $t = 40, 80, 120, 160$  and  $200$  seconds.

The plots of the solution to the solitary wave interaction problem in Fig. 4.8 show that both of the solitary waves maintain their shape after the interaction has taken place. It is also worth noting that the interaction did not have any effect on the velocity of the travelling waves.

### 4.7.3 Monochromatic wave propagation

The internal generation of monochromatic waves using the source function method given in Section 4.5 has been tested using the numerical scheme described in Section 4.3. Firstly, wave generation was tested using a single wave period in order to test the source function method and to ensure that the absorbing boundaries perform satisfactorily. Secondly, the source function method was tested over a range of different wave periods.

For both of the tests, the dimensions of the channel were set at 50 metres with a water depth of  $d = 0.5$  metres. The centre of the source function was located half way along the channel, at  $x_s = 25$  metres, and the sponge layers were located within the 50 metre channel (Fig. 4.9).

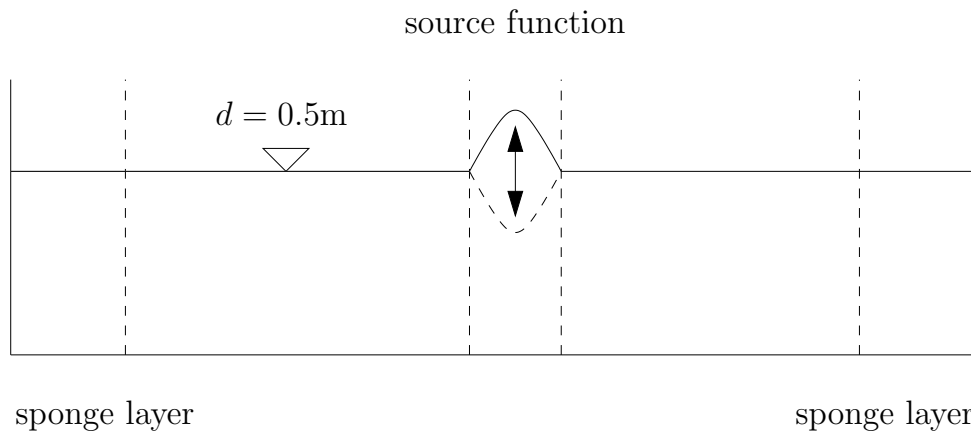


Figure 4.9: Monochromatic wave propagation flume.

#### 4.7.3.1 Single period monochromatic wave

A monochromatic wave with period  $T = 1.0$  seconds was generated using the source function method. The amplitude of the wave was set at  $a = 0.05$  metres giving a wavelength of  $L = 1.513$  metres and a relative depth ratio of  $d/L = 0.33$ . The width of the sponge layers was set at three times the wavelength, i.e.,  $x_e - x_s = 4.539$  metres and a value of  $\alpha_1 = 0.2$  was used for the free parameter. Plots of the normalised water surface at times  $t = 10, 20, 40$  and  $100$  seconds are shown in Fig. 4.10.

Fig. 4.10 shows that the method of generating monochromatic waves by use of the internal source function works well with the numerical scheme. The waves created all have the desired amplitude, period and wavelength. At  $t = 40$  seconds, the waves have propagated past the absorbing boundaries showing that the use

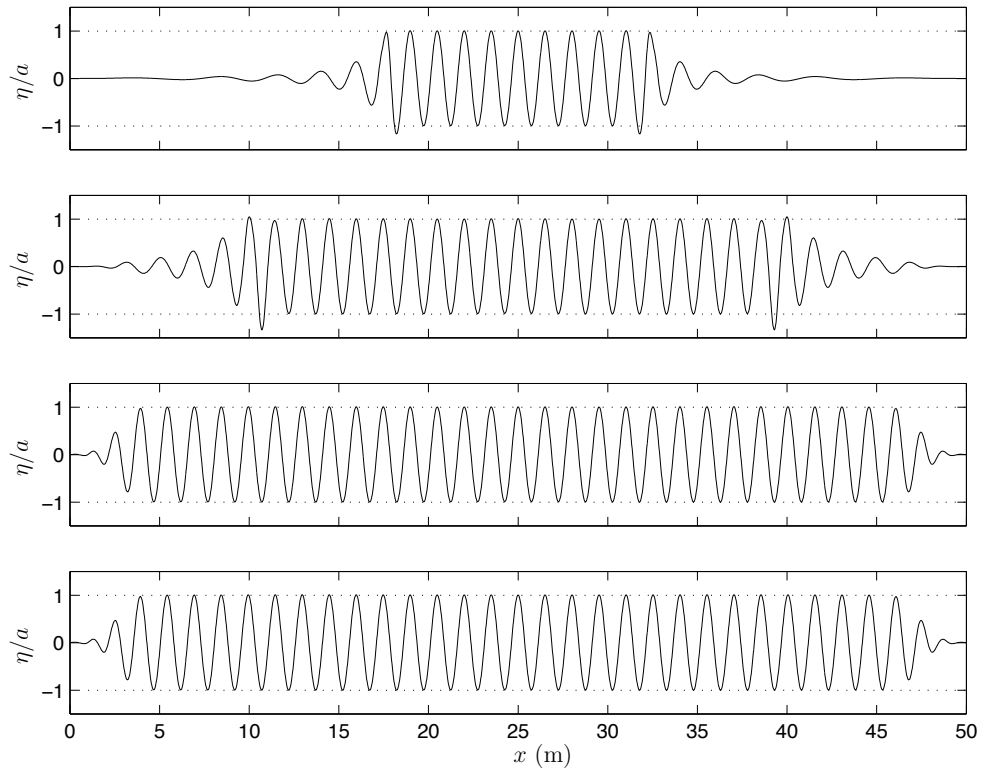


Figure 4.10: Internally generated monochromatic wave: plots of the normalised water surface elevation ( $T = 1$  s) at time (from top to bottom)  $t = 10, 20, 40, 100$  s. The source function is centred at  $x_s = 25$  metres.

of the radiation boundary condition and sponge layer combination satisfy the conditions for an absorbing boundary. The solution of the problem at  $t = 100$  seconds is very similar to that at  $t = 40$  seconds indicating that a quasi-steady state is reached.

#### 4.7.3.2 Multiple period monochromatic wave

Monochromatic waves with amplitude,  $a = 0.05$  metres, and periods,  $T = 1, 1.5$  and  $2.0$  seconds, have been created using the source function method. The corresponding wavelengths are  $L = 2.827$  and  $L = 4.056$  metres giving depth to wavelength ratios of  $0.177$  and  $0.123$  for periods  $T = 1.5$  and  $2.0$  seconds respectively. The length of the sponge layers are three times the wavelength in each case and  $\alpha_1 = 0.2$ . Fig. 4.11 shows the normalised water surface at time  $t = 100$  seconds.

The plots of the normalised water surface in Fig. 4.11 show that the source function method can create monochromatic waves over a range of wave periods.

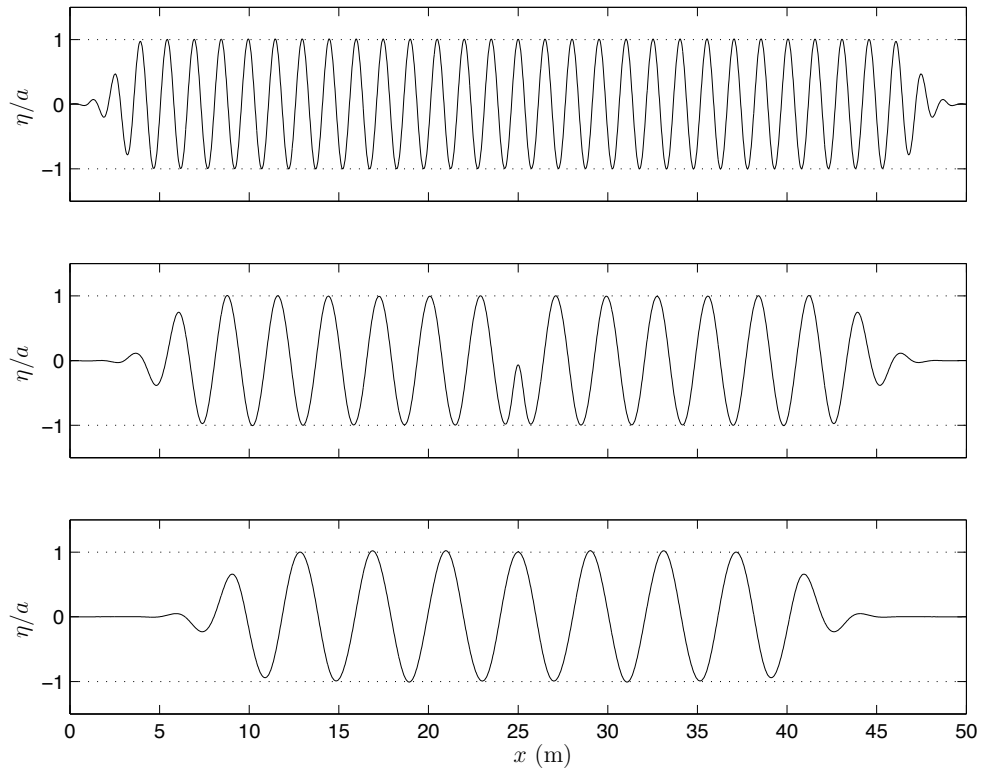


Figure 4.11: Internally generated monochromatic wave: plots of the normalised water surface elevation at time  $t = 100$  seconds for periods (from top to bottom)  $T = 1.0, 1.5, 2.0$  seconds. The source function is centred at  $x_s = 25$  metres.

#### 4.7.4 Monochromatic wave reflection

The internal generation of waves only real application is to provide a method of inducing waves into the solution domain that also permits the outflow of waves through the incident wave boundary. If a method of this kind is unable to allow waves to pass out through the computational domain then problems will be limited to propagation in one direction only.

In order to test the source function method's ability to allow reflected waves to pass out of the computational domain, monochromatic wave reflection was used. The problem consisted of a channel 25 metres in length with a constant depth of 0.4 metres. Waves were induced into the channel by the source function method that was centred at the left-hand boundary (Fig. 4.12). A sponge layer was used to dampen the left-hand travelling waves propagating from the source function. At the right-hand boundary, a solid wall boundary condition was used (Section 4.4.3).

The source function generated a monochromatic wave in the same way that was observed in Sections 4.7.3.1 and 4.7.3.2. The left-hand travelling waves were damped by the sponge layer and absorbed by the radiation boundary conditions.

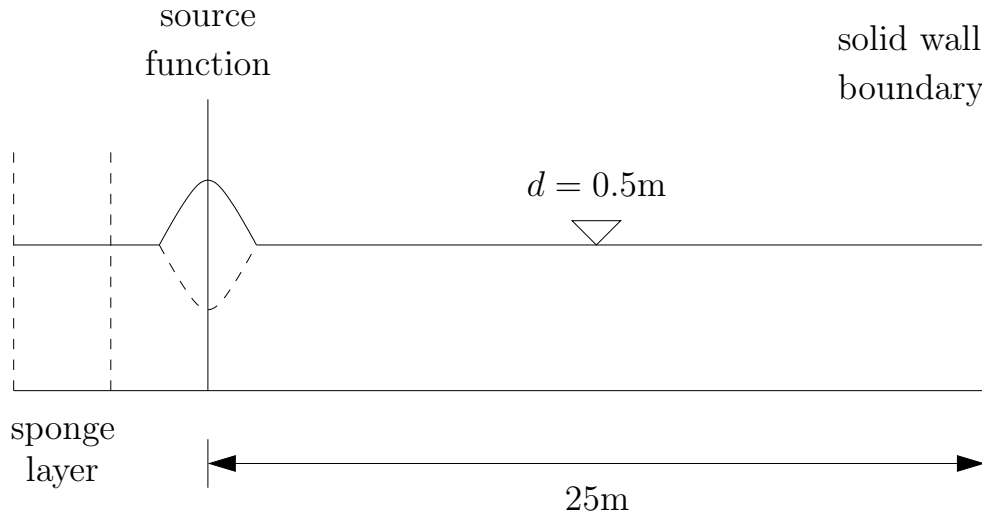


Figure 4.12: Monochromatic wave reflection: sketch of wave flume.

The right-hand travelling waves propagated up to the right-hand boundary at which point they were reflected back into the computational domain by the solid wall boundary condition at double the amplitude. Eventually the reflected waves passed through the source function and were absorbed by the sponge layer.

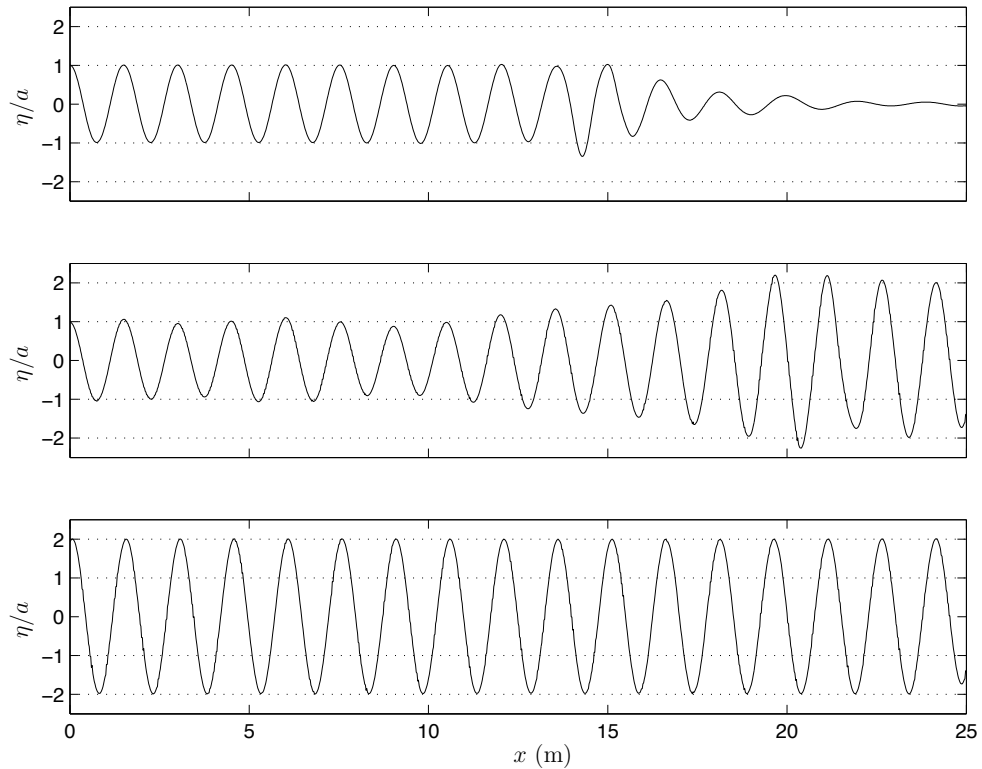


Figure 4.13: Monochromatic wave reflection: plots of the normalised water surface ( $T = 1\text{s}$ ) at time (from top to bottom)  $t = 20, 40$  and  $80$  seconds.

Fig. 4.13 shows the normalised water surface for times,  $t = 20, 40$  and  $80$  seconds. At time  $t = 20$  seconds, the waves generated by the source function have propagated into the flume. At time  $t = 40$  seconds, the waves have propagated up to the solid wall boundary and wave reflection has occurred producing waves at double the amplitude of the incident waves. The plot of the water surface at time  $t = 80$  seconds shows that the reflected waves have propagated back to the incident boundary and have been allowed to pass out of the solution domain.

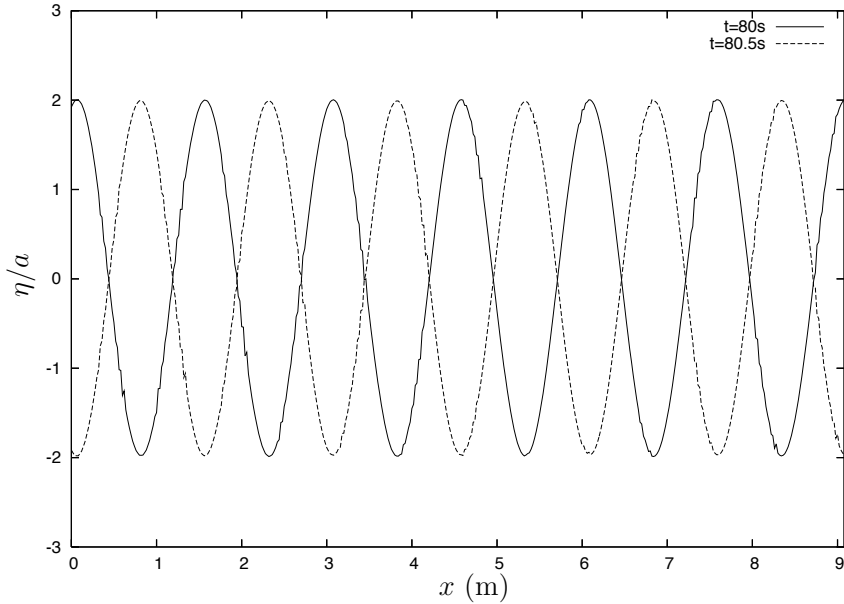


Figure 4.14: Standing wave created by monochromatic waves reflection: plots of the normalised water surface ( $T = 1\text{s}$ ) at time  $t = 80$  and  $80.5$  seconds.

Fig. 4.14 shows a plot of the normalised water surface at times  $t = 80$  and  $t = 80.5$  seconds, i.e., half a wave period apart. Provided that the source function method allows waves to pass out of the solution domain without any reflection at all, standing waves should occur. It is clear from Fig. 4.14 that each anti-node oscillates between  $2a$  and  $-2a$  (where  $a$  denotes the wave amplitude), thus indicating that standing waves has indeed occurred. This, along with Fig. 4.13, shows that the source function method is an appropriate method with which to generate waves at a boundary that also allows waves to pass out of the solution domain.

#### 4.7.5 Regular wave propagation over a submerged bar

Regular wave propagation over a submerged bar has been widely used as a test case for comparisons between various numerical models and experimental measure-

ments. Dingemans (1987) was the first to use the trapezoidal bar to verify Delft Hydraulics' numerical model HISWA for wave propagation over a submerged bar. This experiment has been repeated since, most notably by Beji and Battjes (1993) and Luth *et al.* (1994), the latter of which was performed with a length scale twice as large as the flume presented here. Dingemans (1994) provided comparisons between various Boussinesq-type models and experimental measurements performed by a number of different experimentalists using the same basic bathymetry and, more recently, Gobbi and Kirby (1999) used it as a validation exercise for their higher-order Boussinesq formulation.

The wave evolution occurs as follows (Gobbi and Kirby, 1999): as the wave propagates along the front slope, nonlinear interactions cause a steepening of the wave. When the wave begins to travel along the back slope the coupling of the higher frequency waves to the fundamental wave becomes weaker and eventually the fundamental wave breaks up into the Fourier components which form free waves which travel at different speeds. Modelling this nonlinear behaviour represents a tough test for Boussinesq-type models.

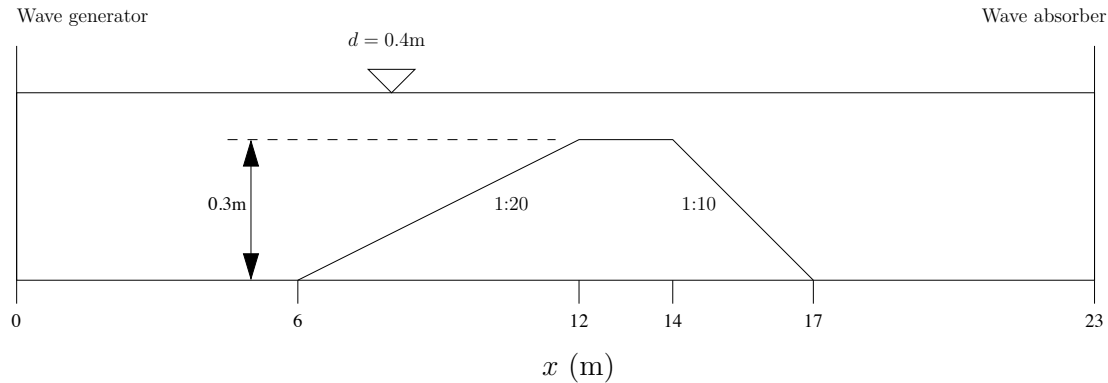


Figure 4.15: Sketch of wave flume of the Delft Hydraulics experiments.

For the purposes of the comparison performed here, the numerical solver has been tested against the experiments performed by Beji and Battjes (1993). The bathymetry of the bar consisted of a 1:20 front slope and a 1:10 back slope separated by a level plateau of 2.0 metres in length. The water depth was 0.4 metres measured from the bottom of the flume, decreasing to 0.1 metres on top of the submerged bar (Fig. 4.15). Regular waves were generated by a wave generator placed at one end of the flume and a wave absorber served to dampen all energy and remove any reflected waves that propagated back into the flume. Beji and Battjes (1993) performed their experiments for three different wave conditions listed in Table 4.1. Configuration (a) ensures that none of the waves break as they

propagate up the front slope, configuration (b) provides spilling breakers that were visually observed and configuration (c) provides non-breaking waves with a small period.

Table 4.1: Wave configurations for the experiments performed by Beji and Battjes (1993)

Configuration	Wave height (m)	Wave period (s)	Comments
(a)	0.020	2.020	non-breaking waves
(b)	0.029	2.525	spilling breakers ( $13.3\text{m} \leq x \leq 15.3\text{m}$ )
(c)	0.041	1.010	non-breaking waves

The numerical model of the submerged bar test used the source function method to generate the regular waves for the values of wave height and period, corresponding to the test configurations (a), (b) and (c). A sponge layer was placed at the opposite end of the numerical flume starting at  $x = 23$  metres to act as a numerical analogy to the wave absorber used in the physical experiments. Six depth gauges were placed along the length of the flume to record the water surface elevations. The locations of the depth gauges used for comparison purposes here were  $x = 2.0, 5.7, 10.5, 13.5, 15.7$  and  $19.0$  metres, corresponding to the locations used in the first run of the experiments performed by Beji and Battjes (1993). It should be noted that in the experiment, the location of the second gauge was inaccurate and subsequent analysis has shown that the actual gauge location should be  $x = 5.2$  metres. The comparisons made here are made against the uncorrected gauge location.

The solution profile for configuration (b) is given in Fig. 4.16 and clearly shows the regular waves propagating from the source function and beginning to steepen as they approach the plateau. From the latter part of the plateau the disintegration of the fundamental waves and the propagation of the free waves can be seen.

The water surface elevations at each of the six depth gauges over the time interval  $40 \leq t \leq 50$  seconds for configurations (a), (b) and (c) are given in Figs. 4.17, 4.18 and 4.19 respectively. The comparisons given in Fig. 4.17 for test configuration (a) show good agreement between the numerical solver and the experimental water surface. Regular waves are observed for the plots showing the gauges placed before the bar and on the front slope. A phase error is evident for the gauge placed at  $x = 5.7$  metres caused by the error in the gauge location, as noted earlier. The gauges located on the top of the bar, the 1:10 back slope and after the bar show that the higher-frequency waves have separated and are travelling at their own speeds and exhibit periodic behaviour.

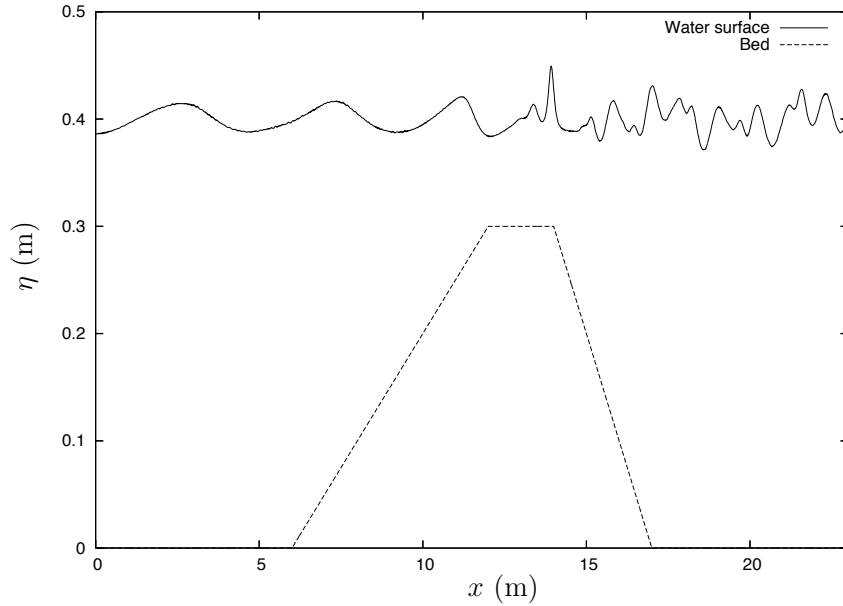


Figure 4.16: Regular wave propagation over a submerged bar: solution profile at time  $t = 50$  seconds for configuration (b).

For the test configurations (b) and (c) (Figs. 4.18 and 4.19) the numerical scheme shows poorer agreement than for configuration (a). For the gauges placed on the front side of the bar, the numerical scheme under-predicts the heights of the periodic wave. Configuration (b) exhibited some breaking waves in the range  $13.3 \leq x \leq 15.3$  metres, and whilst the gauge placed at  $x = 13.5$  metres shows reasonable agreement with the experimental data, the gauge placed at  $x = 15.7$  metres shows a clear overshoot of the water surface. Configuration (c) consisted of a non-breaking wave conditions. For all six depth gauges the numerical scheme over-predicts the wave heights observed in the physical experiments.

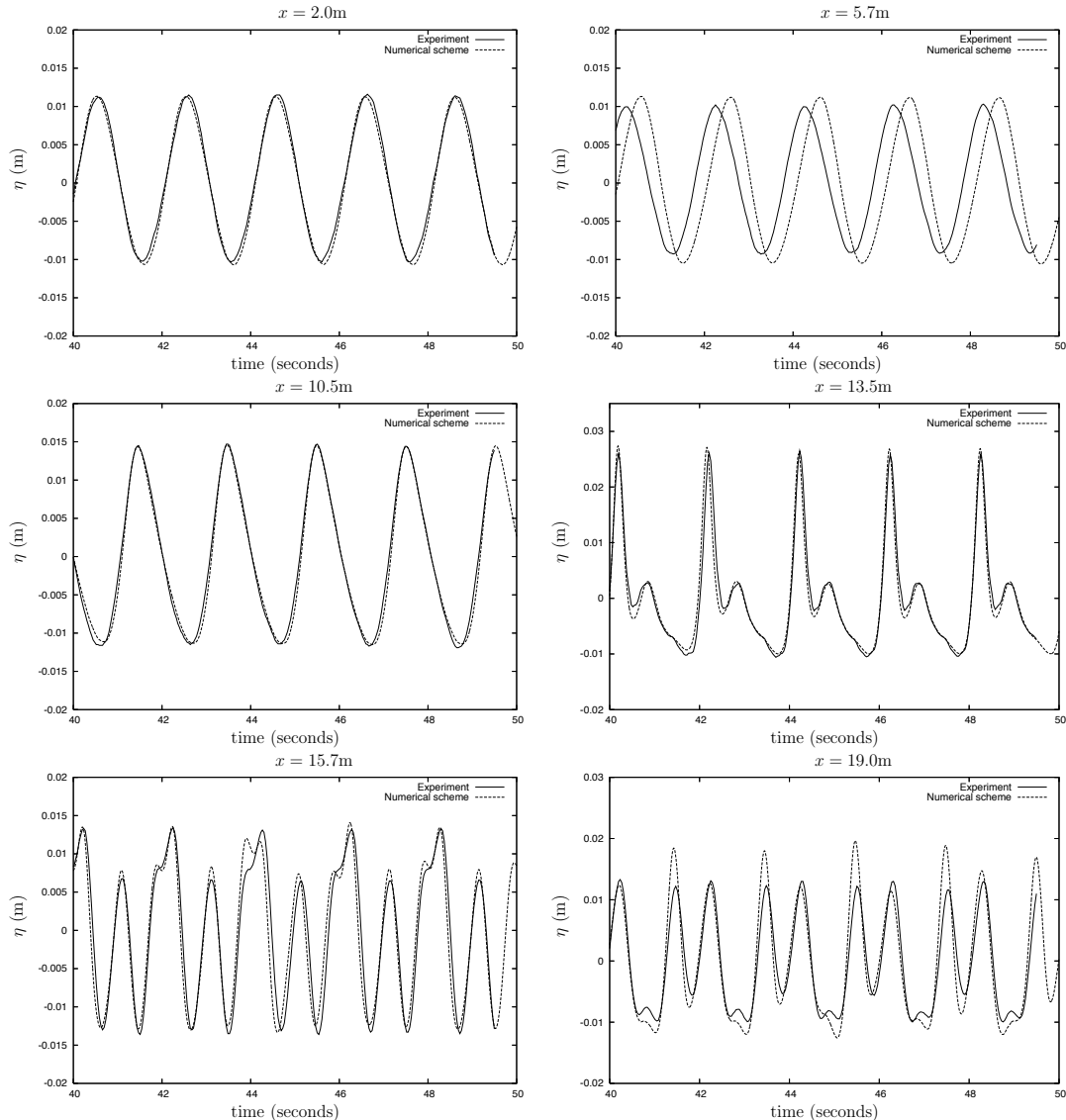


Figure 4.17: Regular wave propagation over a submerged bar: water surface elevations from gauges placed at  $x = 2.0, 5.7, 10.5, 13.5, 15.7, 19.0\text{m}$  from the wave paddle for test configuration (a).

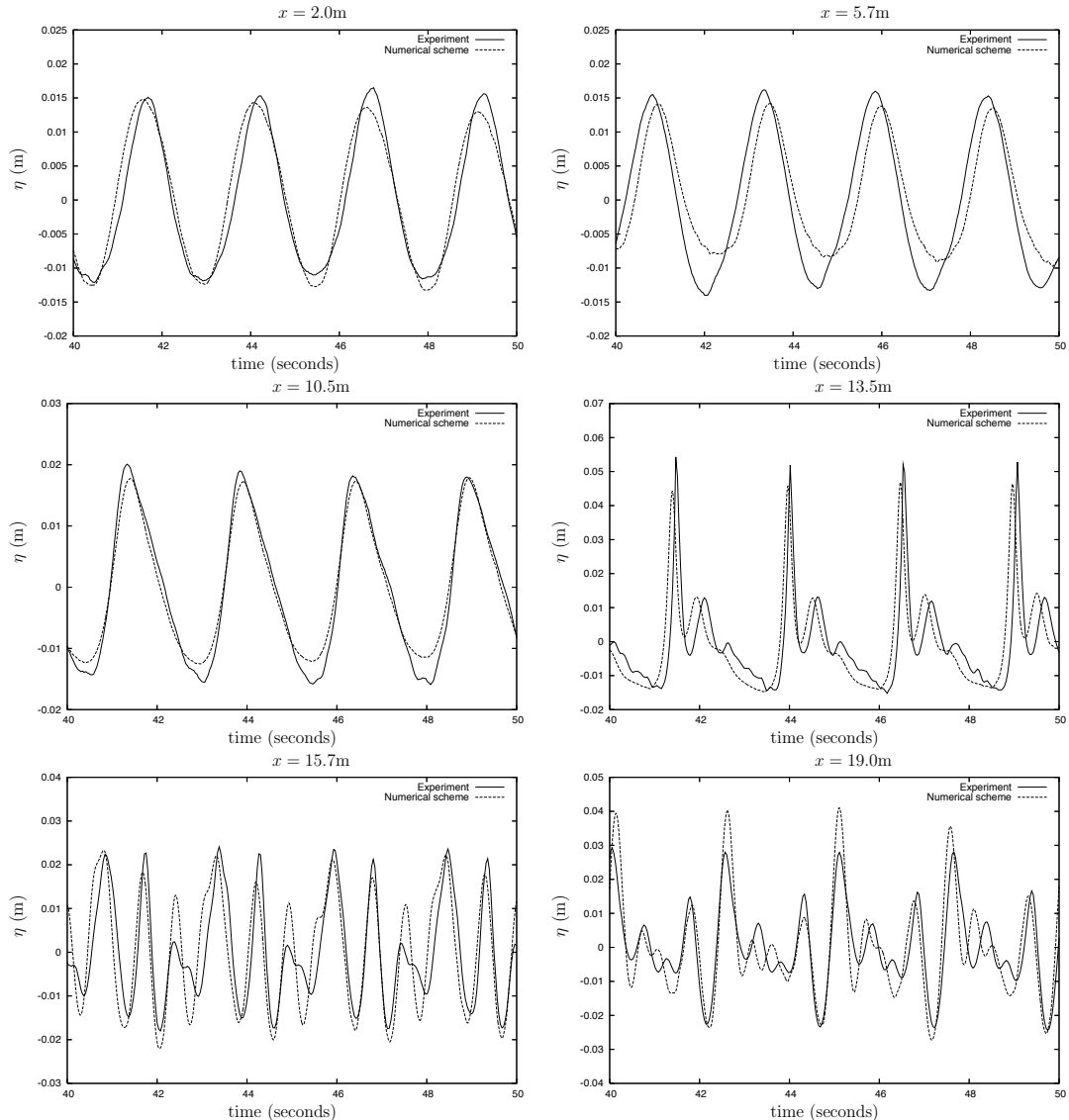


Figure 4.18: Regular wave propagation over a submerged bar: water surface elevations from gauges placed at  $x = 2.0, 5.7, 10.5, 13.5, 15.7, 19.0\text{m}$  from the wave paddle for test configuration (b).

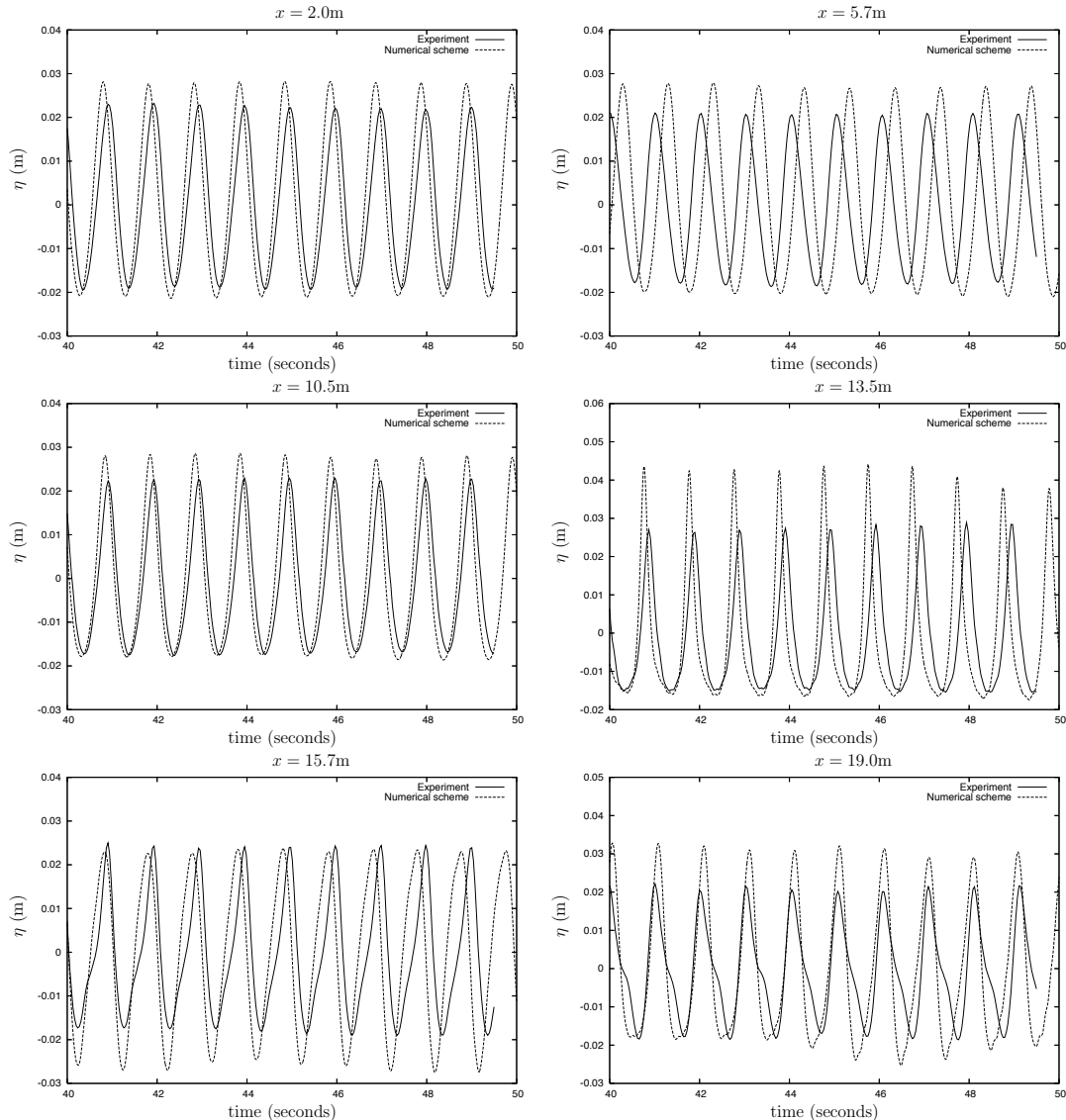


Figure 4.19: Regular wave propagation over a submerged bar: water surface elevations from gauges placed at  $x = 2.0, 5.7, 10.5, 13.5, 15.7, 19.0\text{m}$  from the wave paddle for test configuration (c).

## 4.8 Chapter Summary

An extended form of the Boussinesq equations derived by Nwogu (1993) was presented. Nwogu used the horizontal velocity at an arbitrary depth as a basis of the derivation of his equations. This approach leads to a free parameter that determines the dispersive properties of the system. A comparison against linear wave theory for both the phase velocity and the group velocity suggests that a value of  $\alpha = -0.390$  provides the optimum dispersive properties, indicating that the extended Boussinesq equations are applicable in the range  $d/L < 0.35$ .

A finite difference method first suggested by Wei and Kirby (1995) was described and implemented. The numerical method integrates through time using a third-order predictor, fourth-order corrector Adams method. Spatial differencing is achieved *via* a fourth-order finite difference approximation for first-order derivatives, and a second-order accurate finite difference approximation for second-order derivatives, ensuring that the truncation error in the solver is less than that of the governing equations. The second-order finite difference stencil in the momentum equation provides a tri-diagonal system that is solved using the Thomas algorithm at each time step. The boundary conditions for reflected and absorbing boundaries were explained, with the latter being achieved using a sponge layer analogy. Wave generation within the solution domain was also discussed.

The numerical scheme for solving the extended Boussinesq equations was tested against a number of standard test cases. To begin with, a solitary wave propagation problem was used to show that the numerical scheme accurately solves the extended Boussinesq equations. Also, the dispersion terms within the governing equations ensure that the soliton retains its shape as it propagates along the flume. The interaction between two solitary waves propagating in opposite directions was also tested and it was shown that two solitons pass through each other with no loss of amplitude or velocity.

Wave generation by the internal source function method and the use of absorbing boundary conditions has been tested for problems involving both single period and variable period monochromatic wave propagation. It was shown that the source function method is capable of generating regular waves, and that the sponge layers dampen the energy to allow waves to pass out of the solution domain without reflection. The treatment of a solid wall boundary was tested, showing that the reflecting waves caused the incident amplitude to double and a standing wave quasi-steady state solution was reached. Finally, the numerical scheme was used to model regular wave propagation over a submerged trapezoidal bar.

A common test case for Boussinesq models, the numerical results showed good agreement with the experimental data, and that the non-linear behaviour of the fluid is retained by the model.

# Chapter 5

## Hybrid Finite-Volume/ Finite-Difference Solver

The class of extended Boussinesq equations allow intermediate depth water to be modelled and therefore provide a more useful alternative than the shallow water equations (SWE) when considering near shore wave propagation and interaction with coastal structures. In the previous chapter, the extended Boussinesq equations derived by Nwogu (1993) and a solution method using a fourth-order finite-difference method were discussed. It was noted by Wei and Kirby (1995) that in order to retain the higher order terms in the extended Boussinesq equations, the numerical scheme needs to be at least fourth-order accurate for the first-order space and time derivatives.

Finite-difference models are limited to structured discretisations of the solution domain which greatly limits the shape of the seawall structures that can be modelled. Recent attempts at using a boundary fitting method for solving the extended Boussinesq equations have showed promise. Walkley and Berzins (1999b,a) used a finite-element solver to solve Nwogu's formulation. Erduran *et al.* (2005), Ilic *et al.* (2005) and Borthwick *et al.* (2005) have all used a finite-volume scheme similar to that described in Chapter 2 to approximate the spatial advection terms in the extended Boussinesq equations of Madsen and Sørensen (1992). The former used a second-order MUSCL reconstruction with the Hancock predictor/corrector scheme described in Section 2.2.1 to integrate the governing equations through time. The latter used a fourth-order MUSCL reconstruction with the time integration performed by the fourth-order Adams method suggested by Wei and Kirby (1995) (Section 4.3). The method used by Erduran *et al.* has since been applied to solve the extended Boussinesq equations derived by Beji and Nadaoka in Erduran

(2007).

This chapter presents the scheme used by Erduran *et al.* and has been applied to solve both Madsen and Sørensen's and Nwogu's Boussinesq formulations. The use of this hybrid scheme to solve Nwogu's equations has not previously been examined. Nwogu's Boussinesq equations were rewritten following the approach used by Erduran *et al.* (2005), which produces of form similar to that of the SWE plus additional dispersion terms. The two Boussinesq formulations were compared using standard test cases, and Madsen and Sørensen's equations were used to model three different sets of experiments examining wave run-up and overtopping.

## 5.1 Hybrid Numerical Solver: Nwogu's Formulation

The extended Boussinesq equations derived by Nwogu are given in Eqs. (4.3) and (4.4). Considering flow only in the  $x$ -direction, these equations can be expressed as

$$\frac{\partial \eta}{\partial t} + \frac{\partial}{\partial x} [(d + \eta) u_\alpha] + \frac{\partial}{\partial x} \left[ \left( \frac{z_\alpha^2}{2} - \frac{d^2}{6} \right) d \frac{\partial^2 u_\alpha}{\partial x^2} + \left( z_\alpha + \frac{d}{2} \right) d \frac{\partial^2}{\partial x^2} (du_\alpha) \right] = 0, \quad (5.1)$$

$$\frac{\partial u_\alpha}{\partial t} + g \frac{\partial \eta}{\partial x} + u \frac{\partial u_\alpha}{\partial x} + z_\alpha \left[ \frac{z_\alpha}{2} \frac{\partial^3 u_\alpha}{\partial x^2 \partial t} + \frac{\partial^3}{\partial x^2 \partial t} (du_\alpha) \right] = 0. \quad (5.2)$$

All variables are defined in Section 4.1. By following the approach used by Erduran *et al.* (2005) for the equations of Madsen and Sørensen of assuming that the bed surface elevation remains constant through time, Eqs. (5.1) and (5.2) can be written in the form similar to that used for the SWE as follows.

First, a local water depth parameter  $h$  is introduced defined by

$$h = \eta + d, \quad (5.3)$$

where  $d$  is the distance between the SWL and the bed surface elevation. Assuming the bed surface remains constant in time this leads to

$$\frac{\partial \eta}{\partial t} = \frac{\partial}{\partial t} (h - d) = \frac{\partial h}{\partial t} - \frac{\partial d}{\partial t} = \frac{\partial h}{\partial t}. \quad (5.4)$$

Using the redefined local water depth Nwogu's Boussinesq equations can be written in the form

$$\frac{\partial}{\partial t}\mathbf{U} + \frac{\partial}{\partial x}\mathbf{F}(\mathbf{U}) = \mathbf{S}_b + \mathbf{S}_d, \quad (5.5)$$

where  $\mathbf{U}$  and  $\mathbf{F}(\mathbf{U})$  are the vectors of conserved variables and flux vector function respectively, given by

$$\mathbf{U} = \begin{pmatrix} h \\ U \end{pmatrix}, \quad \mathbf{F}(\mathbf{U}) = \begin{pmatrix} hu_\alpha \\ gh + \frac{1}{2}u_\alpha^2 \end{pmatrix}, \quad (5.6)$$

and

$$U = u_\alpha + z_\alpha \left[ \frac{z_\alpha}{2} \frac{\partial^2 u_\alpha}{\partial x^2} + \frac{\partial^2}{\partial x^2}(du_\alpha) \right]. \quad (5.7)$$

$\mathbf{S}_b$  and  $\mathbf{S}_d$  are vectors containing the terms that model bed topography and dispersion respectively, and are given by

$$\mathbf{S}_b = \begin{bmatrix} 0 & g \frac{\partial d}{\partial x} \end{bmatrix}^T, \quad (5.8)$$

$$\mathbf{S}_d = -\frac{\partial}{\partial x} \left[ \left( \frac{z_\alpha^2}{2} - \frac{d^2}{6} \right) d \frac{\partial^2 u_\alpha}{\partial x^2} + \left( z_\alpha + \frac{d}{2} \right) d \frac{\partial^2}{\partial x^2}(du_\alpha) \quad 0 \right]^T. \quad (5.9)$$

In this form, Nwogu's Boussinesq equations resemble the SWE in that there are the hyperbolic inviscid terms on the left-hand side of Eq. (5.5) and the source terms and dispersion terms on the right-hand side. Using this approach will allow for a hybrid finite-volume/finite-difference scheme to solve the extended Boussinesq equations of Nwogu, where the finite-volume method with MUSCL reconstruction used in Chapter 2 can solve the inviscid terms, and a fourth-order finite-difference scheme can be used to treat the source and dispersion terms. This approach was used by Erduran *et al.* (2005) for Madsen and Sørensen's Boussinesq formulation.

## 5.2 Numerical Scheme

The hybrid numerical scheme which is used to solve the extended Boussinesq equations is based on the fourth-order accurate finite-difference scheme developed by Wei and Kirby (1995) and presented in Chapter 4. The governing equations are written so that all of the time derivative terms are on one side of the equation, i.e.,

$$\frac{\partial}{\partial t}\mathbf{U} = E, \quad (5.10)$$

where

$$E = -\frac{\partial}{\partial x} \mathbf{F}(\mathbf{U}) + \mathbf{S}_b + \mathbf{S}_d. \quad (5.11)$$

In this form, the governing equations can be solved using the Adams-Moulton/Adams-Bashforth predictor/corrector method used in Chapter 4. The flux vector function is discretised using finite-volumes with a fourth-order MUSCL reconstruction. The source terms representing bed topography and dispersion terms are discretised using finite-difference approximations. Therefore, the numerical solver is a hybrid of finite-volume and finite-difference methods, hereafter referred to as the hybrid Boussinesq solver.

### 5.2.1 Spatial Discretisation

The flux vector terms,  $\mathbf{F}(\mathbf{U})$ , are discretised using the finite-volume method discussed in Section 2.2 resulting in

$$\frac{\partial}{\partial x} \mathbf{F}(\mathbf{U}) = \frac{1}{A} \sum_{m=1}^M \mathbf{F}(\mathbf{U}_m^L, \mathbf{U}_m^R) \cdot \mathbf{L}_m, \quad (5.12)$$

where  $A$  is the area of the finite-volume cell,  $M$  is the number of cell sides,  $\mathbf{L}_m$  is the length of the side  $m$  multiplied by the outward pointing normal vector,  $\mathbf{F}(\mathbf{U}_m^L, \mathbf{U}_m^R)$  are the solutions to local Riemann problems that occur at each cell interface as a result of the MUSCL reconstruction process (Section 5.2.2).

The source terms and dispersion terms are discretised using centred finite-difference schemes. The first-order derivatives are approximated to fourth-order accuracy and the second-order derivatives to second-order accuracy

$$\mathbf{S}_{b,i} = \frac{g}{2\Delta x} (d_{i+1} - d_{i-1}), \quad (5.13)$$

$$\mathbf{S}_{d,i} = \frac{d_i}{12\Delta x^3} (f_{i-2} + 8f_{i-1} - 8f_{i+1} + f_{i+2}), \quad (5.14)$$

where

$$\begin{aligned} f_i &= \left( \frac{z_{\alpha,i}^2}{2} - \frac{d_i^2}{6} \right) (u_{\alpha,i-1} - 2u_{\alpha,i} + u_{\alpha,i+1}) + \\ &\quad \left( z_{\alpha,i} + \frac{d_i}{2} \right) [(du_{\alpha})_{i-1} - 2(du_{\alpha})_i + (du_{\alpha})_{i+1}]. \end{aligned} \quad (5.15)$$

### 5.2.2 MUSCL Reconstruction

The values of the conserved variables at the cell interfaces that are used in the finite-volume discretisation of the flux terms are calculated using a fourth-order MUSCL reconstruction (Section 2.2.2). Following from Yamamoto *et al.* (1998), the fourth-order reconstruction is achieved *via* a van Leer limiter applied to values calculated using a third-order minmod limiter. The interface values are calculated using

$$\mathbf{U}_{i+1/2}^L = \mathbf{U}_i + \left[ \phi(r_1) \Delta^* \mathbf{U}_{i-1/2} + 2\phi\left(\frac{1}{r_1}\right) \Delta^* \mathbf{U}_{i+1/2} \right] / 6, \quad (5.16)$$

$$\mathbf{U}_{i+1/2}^R = \mathbf{U}_{i+1} - \left[ 2\phi(r_2) \Delta^* \mathbf{U}_{i+1/2} + \phi\left(\frac{1}{r_2}\right) \Delta^* \mathbf{U}_{i+3/2} \right] / 6, \quad (5.17)$$

where the function  $\phi(r_i)$  is the van Leer slope limiting function

$$\phi(r_1) = \frac{r_1 + |r_1|}{1 + r_1}, \quad (5.18)$$

where

$$r_1 = \frac{\Delta^* \mathbf{U}_{i+1/2}}{\Delta^* \mathbf{U}_{i-1/2}}, \quad r_2 = \frac{\Delta^* \mathbf{U}_{i+3/2}}{\Delta^* \mathbf{U}_{i+1/2}}. \quad (5.19)$$

The values of  $\Delta^* \mathbf{U}$  are calculated using a third-order minmod limiter approach

$$\Delta^* \mathbf{U}_{i+1/2} = \Delta \mathbf{U}_{i+1/2} - (\Delta \bar{\mathbf{U}}_{i+3/2} - 2\Delta \bar{\mathbf{U}}_{i+1/2} + \Delta \bar{\mathbf{U}}_{i-1/2}) / 6, \quad (5.20)$$

where

$$\Delta \bar{\mathbf{U}}_{i-1/2} = \text{minmod}(\Delta \mathbf{U}_{i-1/2}, \Delta \mathbf{U}_{i+1/2}, \Delta \mathbf{U}_{i+3/2}), \quad (5.21)$$

$$\Delta \bar{\mathbf{U}}_{i+1/2} = \text{minmod}(\Delta \mathbf{U}_{i+1/2}, \Delta \mathbf{U}_{i+3/2}, \Delta \mathbf{U}_{i-1/2}), \quad (5.22)$$

$$\Delta \bar{\mathbf{U}}_{i+3/2} = \text{minmod}(\Delta \mathbf{U}_{i+3/2}, \Delta \mathbf{U}_{i-1/2}, \Delta \mathbf{U}_{i+1/2}), \quad (5.23)$$

and

$$\Delta \mathbf{U}_{i+1/2} = \mathbf{U}_{i+1} - \mathbf{U}_i. \quad (5.24)$$

The minmod limiter is given by

$$\text{minmod}(a, b, c) = s \max[0, \min(|a|, 2sb, 2sc)] \quad (5.25)$$

where  $s = \text{sign}(b)$ . Yamamoto *et al.* (1998) used the minmod limiter for both the first- and third-order MUSCL reconstruction in their application to the Navier-

Stokes equations. It was found by Erduran *et al.* (2005) that the use of the van Leer limiter for the first-order reconstruction preserved the fourth-order terms. Numerical experiments performed for this study also reinforced this conclusion (Section 5.4.1).

Using the SGM approach presented in Section 2.4 the data reconstruction described in Eqs. (5.16)–(5.25) is applied to the water surface elevation,  $\eta$ , as opposed to the local water depth,  $h$ . Therefore, before the MUSCL reconstruction is applied, the vector of conserved variables  $\mathbf{U}$  is calculated using

$$\mathbf{U} = \begin{pmatrix} h + z_b \\ u_\alpha \end{pmatrix} \quad (5.26)$$

where  $z_b$  is the bed surface elevation. After the MUSCL reconstruction has been applied, the values of the conserved variables at the cell interfaces are recovered by a simple rearrangement of Eq. (5.26).

### 5.2.3 Time integration

The integration of the governing equations in time is achieved with the third-order Adams-Bashforth predictor and fourth-order Adams-Moulton corrector method suggested by Wei and Kirby (1995) and presented in Section 4.3. For the rewritten form of Nwogu's Boussinesq equations used here, the scheme is

$$\mathbf{U}^{n+1/2} = \mathbf{U}^n + \frac{\Delta t}{12} (23E^n - 16E^{n-1} + 5E^{n-2}), \quad (5.27)$$

$$\mathbf{U}^{n+1} = \mathbf{U}^n + \frac{\Delta t}{24} (9E^{n+1/2} + 19E^n - 5E^{n-1} + E^{n-2}). \quad (5.28)$$

The superscripts  $n + 1/2$  and  $n + 1$  denote the solution at the predictor and corrector stages respectively and  $n$ ,  $n - 1$  and  $n - 2$  are the values for the current and previous time steps. The corrector stage is iterated until the values of the conserved variables have converged to a given tolerance. For the numerical experiments conducted here, the tolerance was given as  $1 \times 10^{-4}$  using Eq. (4.26) to calculate the difference between successive iterations.

As discussed in Section 4.3, the solution for the velocities,  $u_\alpha$ , after the predictor and corrector stage requires the solution of a tri-diagonal system of linear equations. This is performed using an efficient tri-diagonal solution algorithm given in Section 4.3.2.

### 5.3 Madsen and Sørensen's Boussinesq Formulation

In addition to Nwogu's Boussinesq formulation, the extended Boussinesq formulation by Madsen and Sørensen has also been used to model wave propagation, run-up and overtopping. The solution method for Madsen and Sørensen's equations has been developed by Erduran *et al.* (2005) and is similar to that described in Section 5.1. The governing equations derived by Madsen and Sørensen (1992) are

$$\frac{\partial \eta}{\partial t} + \frac{\partial P}{\partial x} = 0, \quad (5.29)$$

$$\frac{\partial P}{\partial t} + \frac{\partial}{\partial x} \left( \frac{P^2}{h} \right) + gh \frac{\partial \eta}{\partial x} + \psi_x = 0, \quad (5.30)$$

where  $P = hu$  is the volume flux,  $u$  is the depth-averaged velocity (note that this is different from the velocity  $u_\alpha$  used in the Nwogu Boussinesq formulation which is the velocity at an arbitrary depth),  $h$  is the water depth, and  $\psi_x$  denotes the higher order Boussinesq terms (i.e., the dispersion terms) given as

$$\psi_x = - \left( B + \frac{1}{3} \right) d^2 \frac{\partial^3 P}{\partial x^2 \partial t} - Bgd^3 \frac{\partial^3 \eta}{\partial x^3} - d \frac{\partial d}{\partial x} \left( \frac{1}{3} \frac{\partial^2 P}{\partial x \partial t} + 2Bgd \frac{\partial^2 \eta}{\partial x^2} \right). \quad (5.31)$$

Madsen and Sørensen suggested a value of  $B = 1/15$  for optimum dispersion properties when compared to linear wave theory.

Using the assumption that the bed surface elevation does not change over time ( $\partial d / \partial t = 0$ ), Eqs. (5.29) and (5.30) can be rewritten as follows

$$\frac{\partial}{\partial t} \mathbf{U} + \frac{\partial}{\partial x} \mathbf{F}(\mathbf{U}) = \mathbf{S}_b + \mathbf{S}_d, \quad (5.32)$$

where

$$\mathbf{U} = \begin{pmatrix} h \\ U \end{pmatrix}, \quad \mathbf{F}(\mathbf{U}) = \begin{pmatrix} hu \\ hu^2 + \frac{1}{2}gh^2 \end{pmatrix}, \quad (5.33)$$

and

$$U = hu - \left( B + \frac{1}{3} \right) d^2 \frac{\partial^2}{\partial x^2} (hu) - \frac{d}{3} \frac{\partial d}{\partial x} \frac{\partial}{\partial x} (hu). \quad (5.34)$$

$\mathbf{S}_b$  and  $\mathbf{S}_d$  are vectors containing the terms that model bed topography and dis-

persion respectively and are given by

$$\mathbf{S}_b = \begin{bmatrix} 0 & gh \frac{\partial d}{\partial x} \end{bmatrix}^T, \quad (5.35)$$

$$\mathbf{S}_d = \begin{bmatrix} 0 & Bgd^2 \left( \frac{\partial^3 h}{\partial x^3} + 2 \frac{\partial d}{\partial x} \frac{\partial^2 h}{\partial x^2} \right) \end{bmatrix}^T. \quad (5.36)$$

The rewritten form of the Madsen and Sørensen formulation results in the Boussinesq equations written as the SWE plus the higher order Boussinesq terms. The numerical scheme described for the solution of the rewritten form of the Nwogu Boussinesq equations is used to solve Eqs. (5.33)–(5.36). Where the additional dispersion terms are not required in the solution, the vector of conserved variables in Eq. (5.34) reverts to that of the SWE,  $\mathbf{U} = (h \ hu)^T$ , and the tri-diagonal matrix for use in the solution of the velocities in the intermediate steps is replaced by the identity matrix for the required rows.

### 5.3.1 Wave breaking

The rearrangement of the governing equations leading to Eqs. (5.5)–(5.9) allows for the dispersion terms to be discarded and removed from the solution if required. This means that discontinuities can be admitted into the solution because the absence of source terms reverts the governing equations back to a hyperbolic system (see Appendix A). Therefore, in cases where wave breaking is likely to occur, the dispersion terms are removed and the breaking wave is modelled as a discontinuity.

To determine which finite-volume cells require the inclusion of the dispersion terms, Borthwick *et al.* (2005) used the following condition

$$-\frac{\partial}{\partial x}(hu) > \gamma \sqrt{gd} \quad (5.37)$$

where  $\gamma$  is an empirical constant that determines when wave breaking occurs depending on the shallow water wave celerity.

## 5.4 Numerical Results

The hybrid Boussinesq solver has been applied to model two standard test cases similar to those used in the testing of the finite-difference solver in Chapter 4, namely the propagation of a solitary wave along a channel and regular wave propagation over a submerged bar. In the submerged bar test case, both the Nwogu

and the Madsen and Sørensen Boussinesq formulations were compared against the experimental observations made by Dingemans (1994). In addition, the hybrid solver has been used to model three sets of wave flume experiments testing wave run-up and overtopping.

The first set of experiments modelled were conducted by Synolakis (1987) who ran an extensive range of experiments looking at run-up on a sloping beach of a solitary wave. The second set of experiments modelled were the Edinburgh wave flume experiments described in Section 3.3, where the wave conditions tested were such that impacting waves dominated at the seawall structure. Finally, the hybrid solver was used to model a series of experiments conducted at Kansai University, Japan (Mase *et al.*, 2003) that measured overtopping volumes resulting from overtopping of a seawall for a range of differing variables such as the crest freeboard and water depth.

### 5.4.1 Solitary wave propagation

This solitary wave propagation test is a standard test of a numerical scheme to accurately solve the dispersion terms within the governing equations. The solitary wave retains its shape, amplitude and velocity because of an exact balance between the dispersion that tends to flatten the wave and the non-linear effects that tend to cause the wave to steepen and eventually break. This case was used to test the fourth-order finite-difference solver presented in Chapter 4 and a detailed description of the test conditions is given there.

For this test, the hybrid Boussinesq solver was used to solve Nwogu's formulation of the Boussinesq equations. The mesh consisted of the 450 metre channel discretised into cells of width  $\Delta x = 0.1$  metres. The solitary wave was created by explicitly stating values of  $\eta$  and  $u_\alpha$  at the left-hand boundary using values calculated from Eqs. (4.59)–(4.65). The test was conducted for both the van Leer and minmod limiters for the MUSCL reconstruction in Eqs. (5.16) and (5.17) to test the observation made by Erduran *et al.* (2005) that the minmod limiter was unsuitable for accurately resolving the fourth-order terms.

The solutions of water surface elevation at times,  $t = 40, 80, 120, 160$  and  $200$  seconds, are given in Figs. 5.1 and 5.2 for the van Leer and minmod slope limiting functions respectively. It is clear that the hybrid scheme using the van Leer limiter produces solutions comparable with those of the fourth-order finite-difference method used in Chapter 4. A closer examination of the solution shows that the non-oscillatory behaviour of the MUSCL scheme reduces the high frequency os-

cillations in the tail of the solitary wave that were present in the finite-difference solution. The solution using the minmod limiter, however, clearly shows that the solitary wave solution is asymmetric and that the balance between the dispersion and non-linear effects has not been retained by the numerical solver.

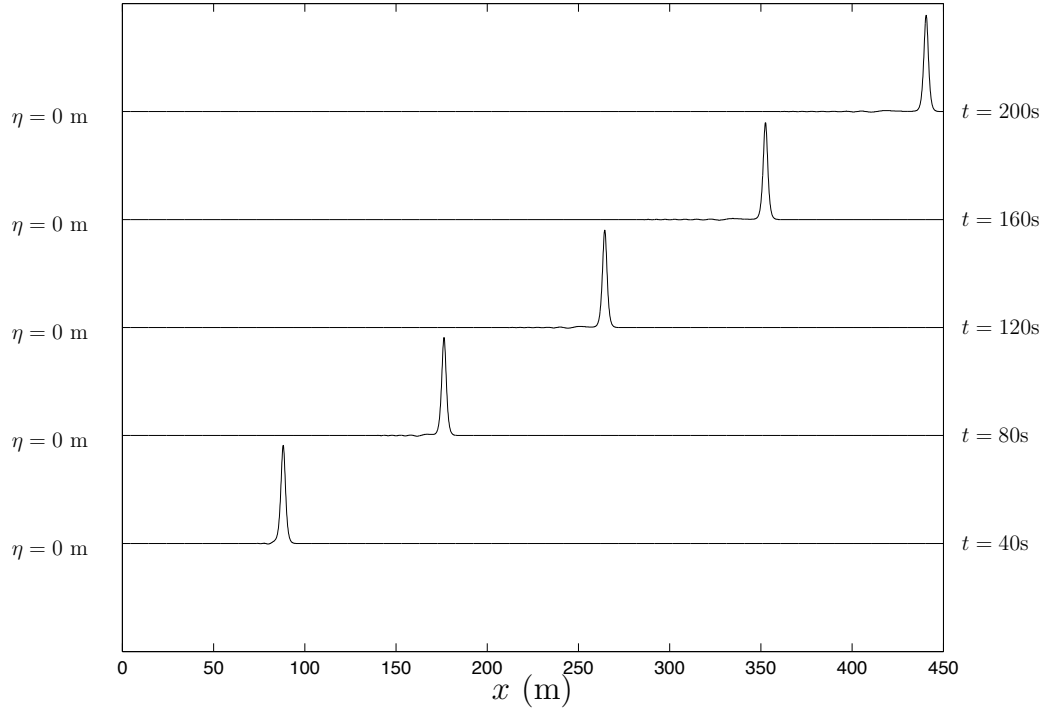


Figure 5.1: Solitary wave propagation: solution plots of the water surface for times,  $t = 40, 80, 120, 160$  and  $200$  seconds using the van Leer limiter.

### 5.4.2 Regular wave propagation over a submerged bar

The hybrid scheme was used to solve both Nwogu's and Madsen and Sørensen's Boussinesq formulations for the regular wave propagation over a submerged bar test used in Section 4.7.5 for the finite-difference solver. As the waves propagate up the 1:20 front slope they begin to steepen due to the effects of the varying bed topography. The 1:10 back slope causes a breaking up into higher frequency waves which travel at different speeds. A more detailed description can be found in Section 4.7.5 or (Dingemans, 1987).

For the purpose of comparison, both the Nwogu and Madsen and Sørensen Boussinesq formulations were used over identical configurations. The 23 metre wave flume (see Fig. 4.15) was discretised into finite-volume cells with  $\Delta x = 0.02$  metres. Regular waves were generated using the source function method described in Section 4.5 with sponge layers at both the left- and right-hand boundaries to

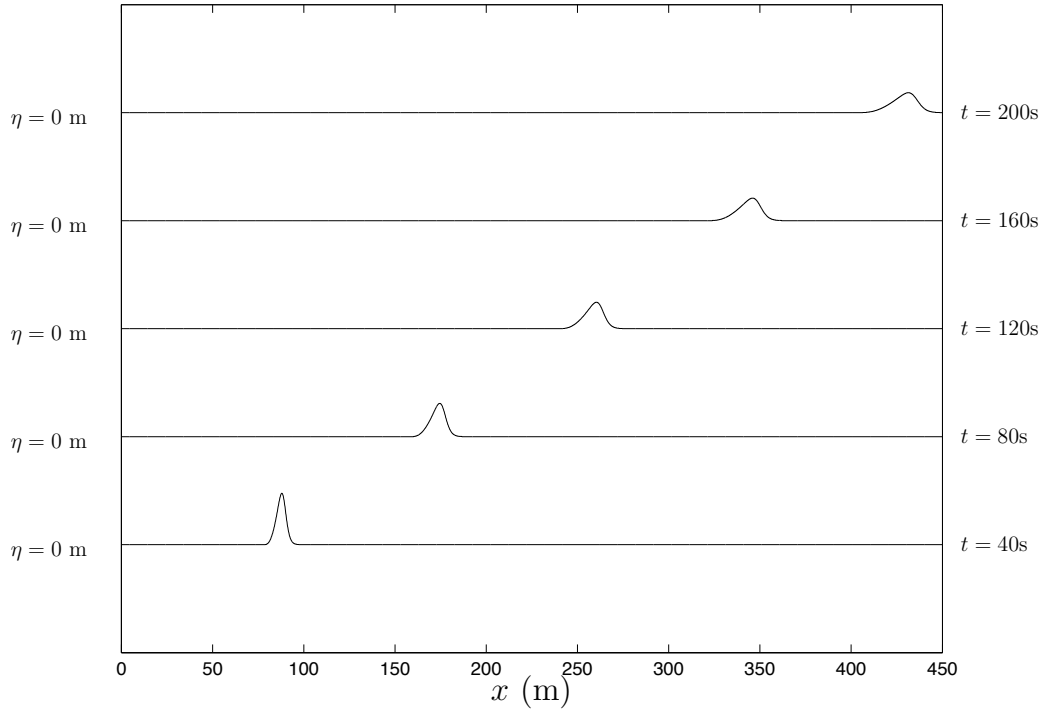


Figure 5.2: Solitary wave propagation: solution plots of the water surface for times,  $t = 40, 80, 120, 160$  and  $200$  seconds using the minmod limiter.

absorb all energy from the outward propagating waves (see Section 4.6). The test case was conducted for all three wave configurations given in Table. 4.1.

The water surface elevations recorded at depth gauges placed 2.0, 5.7, 10.5, 13.5, 15.7 and 19.0 metres from the wave maker boundary are presented in Figs. 5.3 – 5.5 for wave configurations (a) through (c) respectively. For all three configurations, the wave gauges prior to the breakup into higher frequency waves show good agreement with the experimental water surface (recall that the location of the second gauge was mistakenly specified at 5.7 metres from the wave maker boundary causing the phase error). The gauges at 15.7 and 19.0 metres show that the Madsen and Sørensen formulation performs better than Nwogu's formulation for this hybrid solver when compared to the experimental results. For wave configuration (b) where waves form spilling breakers on the plateau, neither formulation manages to accurately resolve the water surface elevation after the breakup of the wave train.

The submerged bar test has demonstrated that the Madsen and Sørensen formulation of the Boussinesq equations is more conducive to the hybrid finite-difference/finite-volume scheme suggested by Erduran *et al.* (2005) than the Nwogu formulation. In addition, the Madsen and Sørensen formulation uses a depth averaged velocity as opposed to a velocity specified at an arbitrary depth in Nwogu's

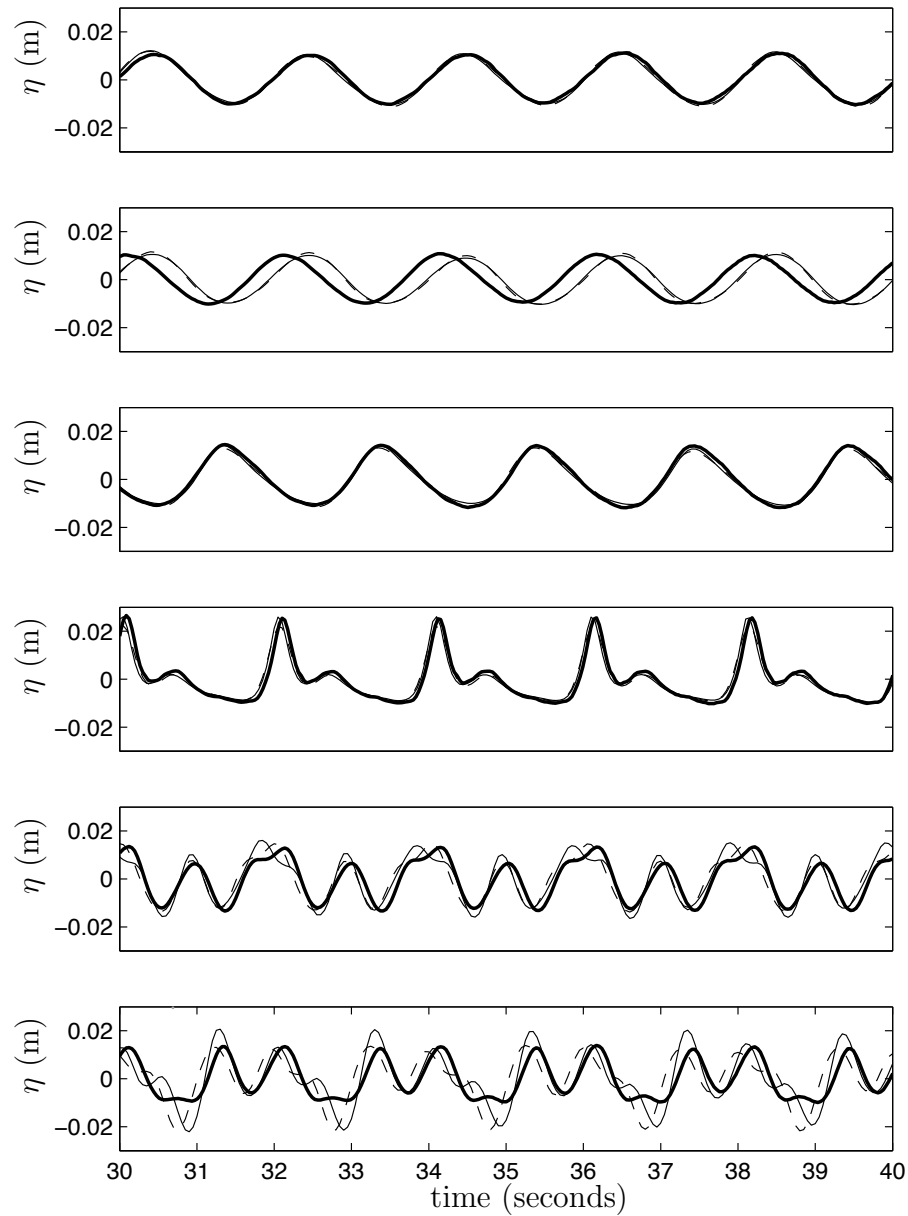


Figure 5.3: Regular wave propagation over a submerged bar: comparisons between the water surface elevations for the experiment (thick line), Nwogu's formulation (thin line) and Madsen and Sørensen's formulation (dashed line) for gauges placed at (top to bottom)  $x = 2.0, 5.7, 10.5, 13.5, 15.7, 19.0$  metres from the wave paddle for test configuration (a).

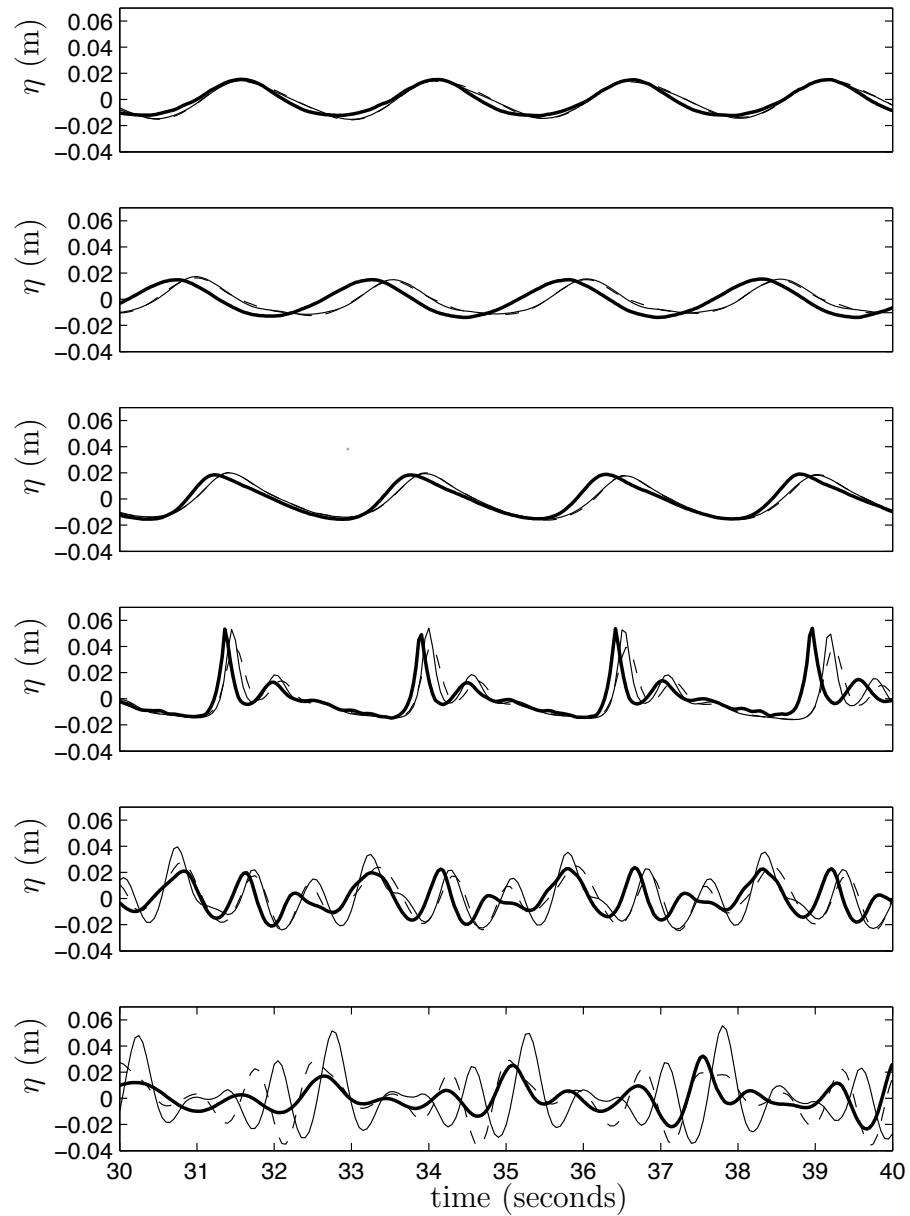


Figure 5.4: Regular wave propagation over a submerged bar: comparisons between the water surface elevations for the experiment (thick line), Nwogu's formulation (thin line) and Madsen and Sørensen's formulation (dashed line) for gauges placed at (top to bottom)  $x = 2.0, 5.7, 10.5, 13.5, 15.7, 19.0$  metres from the wave paddle for test configuration (b).

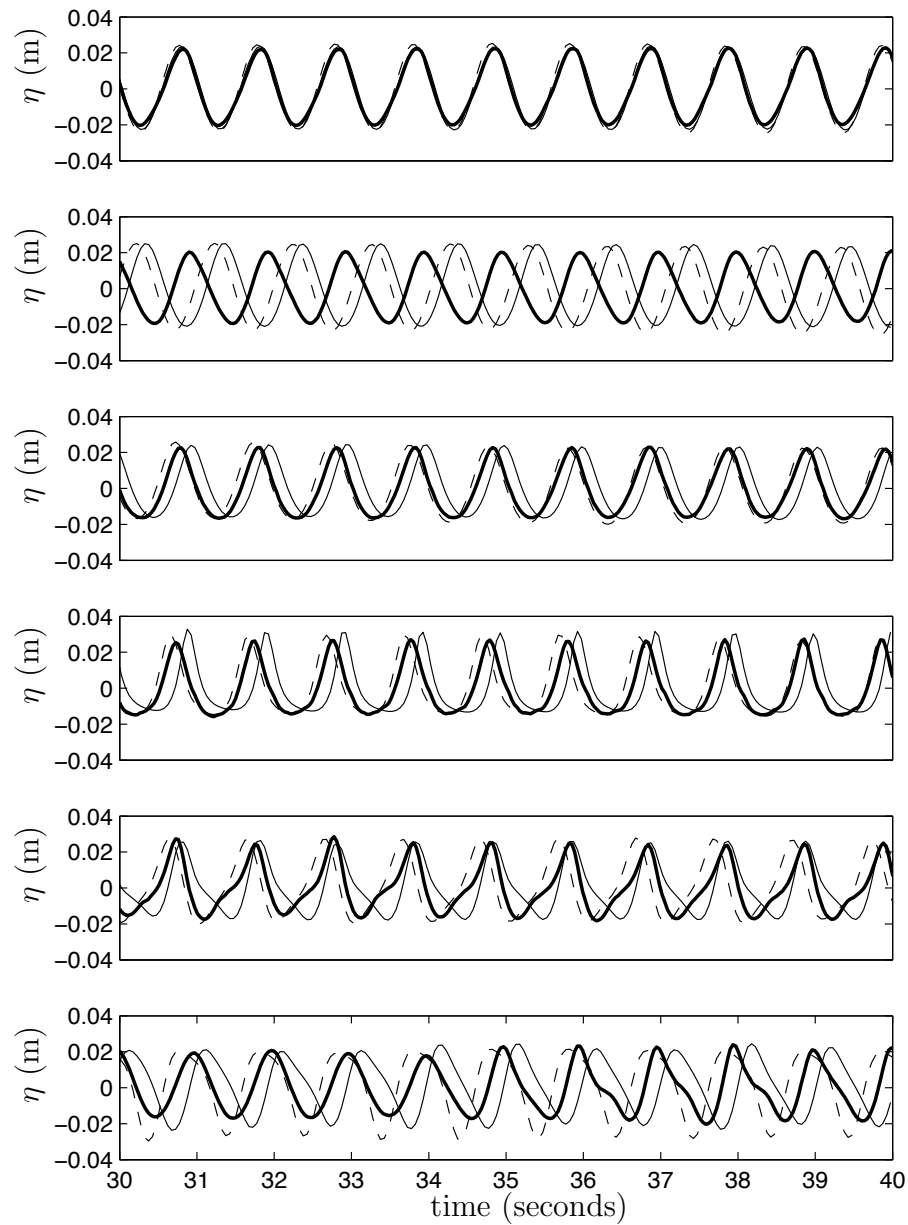


Figure 5.5: Regular wave propagation over a submerged bar: comparisons between the water surface elevations for the experiment (thick line), Nwogu's formulation (thin line) and Madsen and Sørensen's formulation (dashed line) for gauges placed at (top to bottom)  $x = 2.0, 5.7, 10.5, 13.5, 15.7, 19.0$  metres from the wave paddle for test configuration (c).

formation, meaning that the dispersion terms within the governing equations can be disregarded where the need arise. For example, this is the case when wave breaking is likely to occur, or where the bed surface elevation is greater than the water surface elevation ( $d < 0$ ). Numerical experience showed that the hybrid solver when applied to the Nwogu formulation exhibited spurious oscillations at the boundary where the dispersion terms were removed, and whilst the scheme remained stable, it is unsuitable for use when there is an abrupt change between a velocity at an arbitrary depth and a depth-averaged velocity. It is for these reasons that for all following test cases and experiments conducted in this study, the Madsen and Sørensen Boussinesq formulation was used.

### 5.4.3 Solitary wave run-up on a sloping beach

Solitary wave run-up is used to help provide predictions of run-up and inundation resulting from tsunami events. Tsunamis are long waves that are caused by impulsive geophysical events. Synolakis (1987) conducted an extensive study into solitary wave run-up including wave flume experiments using a range of different values for the water depth and amplitude. Borthwick *et al.* (2005) used the data provided by Synolakis' experiments to test their second-order finite-volume based Boussinesq solver. The fourth-order hybrid Boussinesq solver has been applied to model Synolakis' experiments and the the run-up values compared against the experimental values to assess the applicability of the hybrid Boussinesq solver for modelling wave run-up.

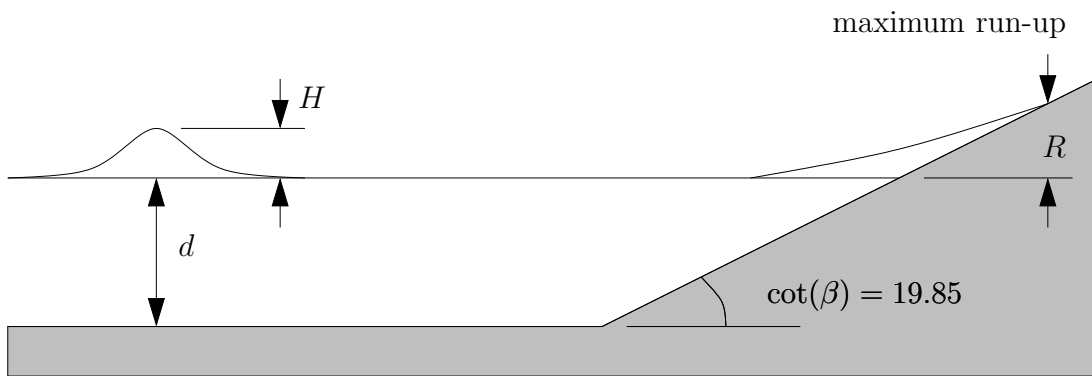


Figure 5.6: Solitary wave run-up on a sloping beach: diagram of wave flume.

The numerical wave flume used here consisted of a flat bed channel with a 1:19.85 sloping beach (Fig. 5.6) placed such that the toe of the slope is 10 metres from the left-hand boundary. The solitary waves were created as an initial value

problem within the domain using the definitions of  $\eta$  and  $u$  given by

$$\eta(x, 0) = H \operatorname{sech}^2 \left[ \sqrt{\frac{3H}{4d^3}}(x - x_s) \right], \quad (5.38)$$

$$u(x, 0) = \eta(x, 0) \sqrt{\frac{g}{d}}, \quad (5.39)$$

where  $H$  is the height of the solitary wave above the SWL,  $d$  is the water depth,  $x_s$  is the centre of the solitary wave and  $g = 9.81 \text{ ms}^{-2}$  is the acceleration due to gravity. The run-up,  $R$ , is defined by the maximum vertical elevation above the SWL reached by the water on the beach. The solitary waves were generated for values of  $H/d$  in the range  $0.009 \leq H/d \leq 0.462$ . The solution domain was discretised using a spatial step of  $\Delta x = 0.02$  metres. A wave breaking parameter of  $\gamma = 0.3$  was used and the bottom friction was ignored.

The run-up values recorded by Synolakis tended towards two distinct asymptotic forms depending upon whether the solitary wave had broken or not, given by

$$\frac{R}{d} \approx \alpha \left( \frac{H}{d} \right)^\beta, \quad (5.40)$$

where  $\alpha$  and  $\beta$  are empirical coefficients. The values of these coefficients are  $\alpha = (11.0, 1.12)$  and  $\beta = (1.22, 0.59)$  for the lower and upper asymptotes respectively (Borthwick *et al.*, 2005). The run-up values for both the experiments conducted by Synolakis and the hybrid Boussinesq solver have been compared against the asymptotic forms given in Eq. (5.40) (Fig. 5.7). In general, the numerical results follow the behaviour of the experimental results but the numerical model tended to over-predict the run-up values. This can be seen more clearly by examining the plot of the relative errors between the experimental and numerical run-up values (Fig. 5.8). The relative errors between the predicted values and the experimental values are calculated using

$$R_{err} = \frac{f_{pred} - f_{exp}}{f_{exp}}, \quad (5.41)$$

where  $f_{pred}$  and  $f_{exp}$  are predicted and experimental values respectively.

Fig. 5.8 shows that where the dimensionless wave heights are small, i.e.,  $H/d < 0.1$ , the relative errors range between -0.02 and 0.41 with the majority of the values indicating an over-prediction of the run-up. This shows that the numerical model struggles to accurately model wave run-up for very small waves. This shortfall is not of much concern because small waves and the run-up and overtopping that

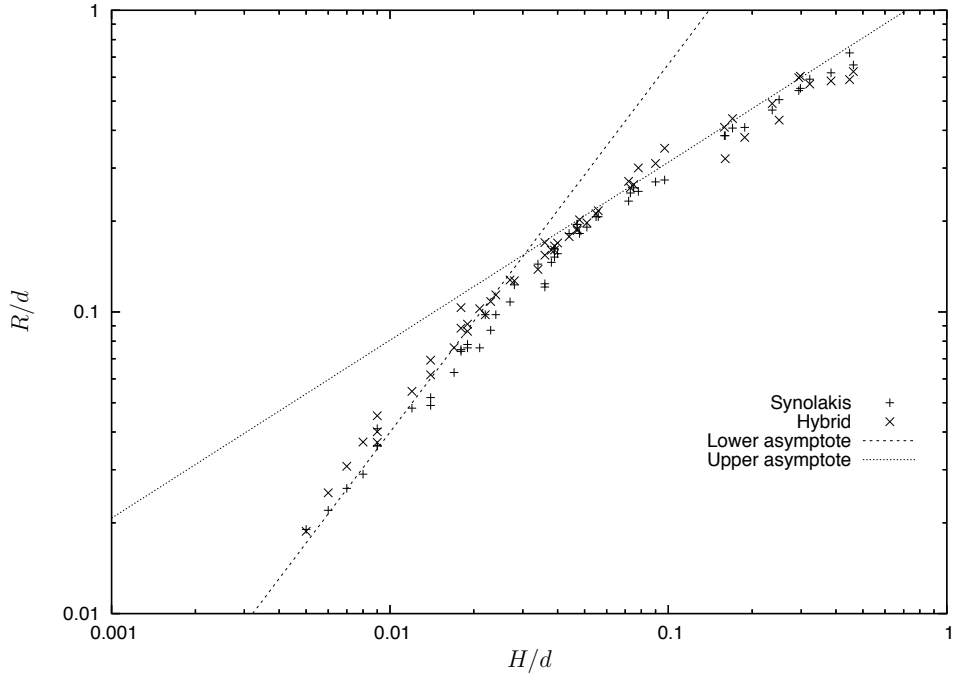


Figure 5.7: Solitary wave run-up on a sloping beach: comparisons between dimensionless run-up values for the results of the experiments of Synolakis (1987) and the hybrid Boussinesq solver.

result from interactions of small waves are considered insignificant from an engineering design standpoint. In addition, it should also be noted that the value of the minimum wet depth parameter,  $\delta$ , would have an influence on the accuracy of the run-up predictions where very small water depths are concerned. This is because for small amplitude waves, the volume contained within the closest ‘wet’ cell to the wet/dry boundary would increase as the value of  $\delta$  increases. If this volume is too large, the computed momentum will cause an over-prediction of the run-up. For larger values of  $H/d$ , the relative error ranges between -0.18 and 0.10 indicating that the hybrid solver can model wave run-up, including where the waves are breaking, to a reasonable degree of accuracy.

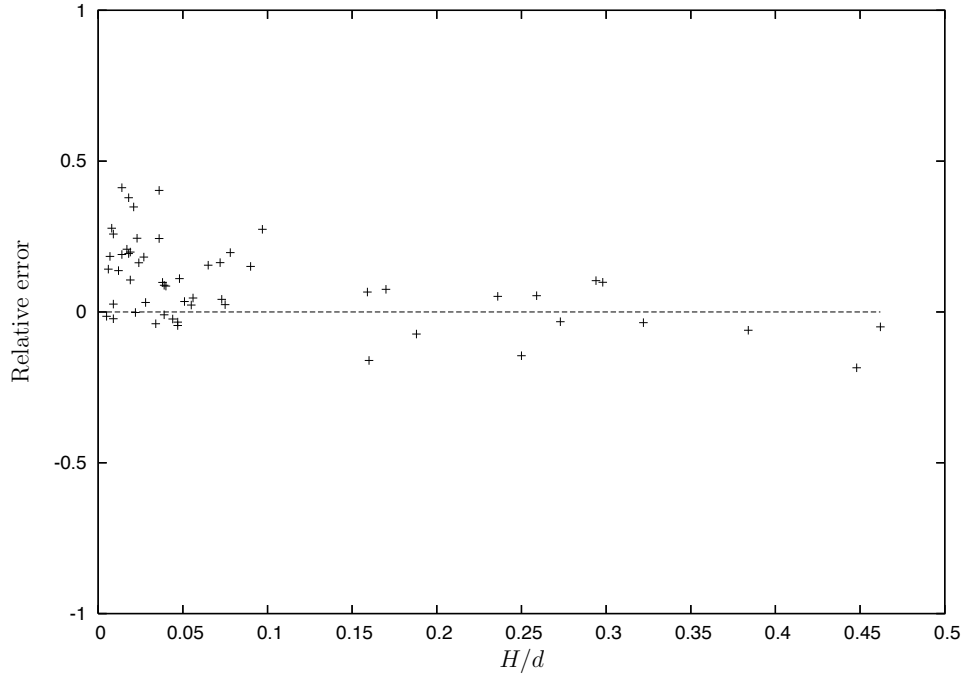


Figure 5.8: Solitary wave run-up on a sloping beach: scatter plot showing the relative errors between  $R/d$  for the experiments of Synolakis (1987) and the hybrid Boussinesq solver.

#### 5.4.4 Numerical simulation of the Edinburgh wave flume experiments

An examination of the applicability of the shallow water equations for modelling overtopping resulting from breaking wave interaction with a near vertical seawall is presented in Chapter 3 and Shiach *et al.* (2004). It was shown that a depth-averaged model could provide good predictions of overtopping for impacting waves where  $h^* \geq 0.075$  (see Section 3.2.2 for the definition of  $h^*$ ). The SWE model, however, was only applied to a region close to the seawall to ensure that the wave conditions within the computational domain are conducive to shallow water (i.e.,  $d/L \leq 1/20$ ). Although only a reduced domain was modelled, the numerical model over-predicted the wave heights due to premature breaking of waves caused by the boundary condition used.

The dispersion properties of the extended Boussinesq equations enable the full Edinburgh wave flume to be modelled and not just the reduced domain used in the SWE based model. Here the hybrid solver has been applied to Madsen and Sørensen's Boussinesq formulation to model the Edinburgh experiments. The waves were internally generated by use of the source function method (see Section 4.5) with the amplitude given by the depth gauge placed at 11.21 metres from

the seawall. A sponge layer was used at the incident boundary to dampen any waves that are reflected from the seawall. Initially, dispersion terms were included in the governing equations throughout the domain except where the bed surface elevation is greater than the water surface elevation ( $d < 0$ ). The use of dispersion terms during the simulation was dependent upon the condition given in Eq. (5.37). Where this condition was violated, the dispersion terms were ignored and the governing equations reverted to the SWE (dispersion terms were also ignored on top of the seawall structure). A simple transient flow boundary condition, Eq. (2.25), was applied to the right-hand boundary. The solution domain was discretised using a uniform mesh with spacing  $\Delta x = 0.02$  metres.

The numerical water surface elevation was recorded at gauges placed at 1.0, 2.0, 3.0, 4.25, 5.5 and 8.0 metres away from the seawall by linearly interpolating between the two closest finite-volume cells. The overtopping volumes ( $\text{m}^3$  per metre of seawall) were calculated using

$$Q = hu\Delta t. \quad (5.42)$$

The water surface elevations for the six depth gauges recorded were compared to the experimental water surface over the intervals  $t = [10, 50]$  and  $t = [50, 100]$  seconds in Fig. 5.9. The numerical surface closely resembles the experimental surface for all six gauges, showing that the hybrid Boussinesq solver along with the source function method can accurately model waves from a given input signal.

The significant wave heights ( $H_s$ ) for the physical experiments and the values recorded from the hybrid solver have been calculated (Tables C.3 and C.5) and directly compared in a scatter plot (Fig. 5.10). Most of the points lie on or close to  $y = x$  indicated; and for all of the depth gauges, the hybrid model has accurately modelled the wave propagation and reflection from the seawall. There are some notable exceptions where a population of points lie under the  $y = x$  line, indicating that the numerical model has under-predicted the wave heights. Closer inspection of the data shows that the runs of the experiments where this under-prediction is occurring are where the incident wave period is less than 1 second (runs 11–15), giving a depth to wavelength ratio of  $d/L > 0.5$  and hence, beyond the range of applicability for the extended Boussinesq equations. The numerical model recorded zero overtopping for all of the 15 runs of the Edinburgh experiments, suggesting that there is a limit to the steepness of the seawall slope when using a fourth-order MUSCL scheme.

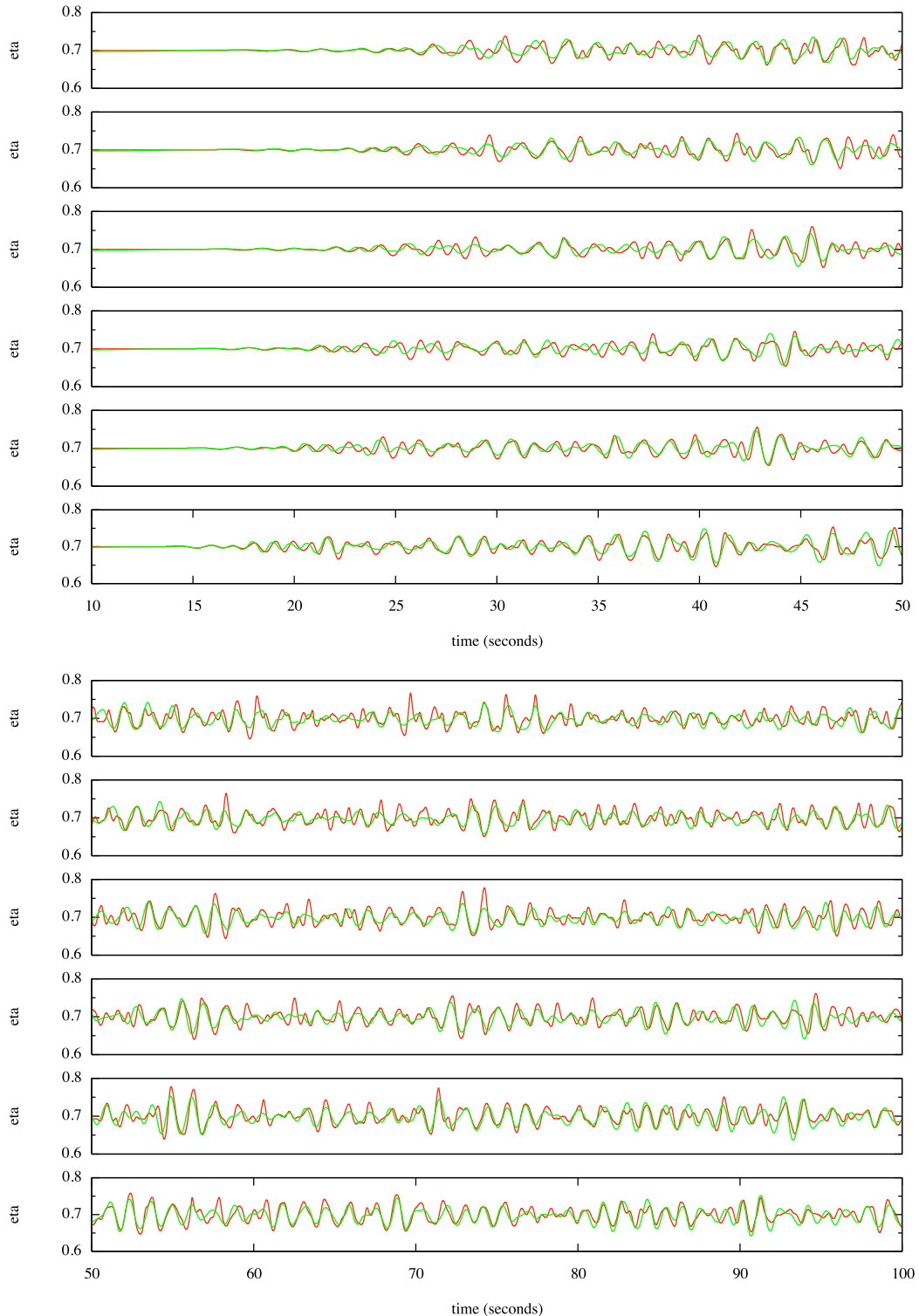


Figure 5.9: Numerical simulation of the Edinburgh wave flume experiments: water surface comparisons between the experimental values (red) and the hybrid solver (green) over the times intervals  $t = [10, 50]$  (top) and  $t = [50, 100]$  (bottom) seconds. Gauges placed (from top to bottom) 1.0, 2.0, 3.0, 4.25, 5.5 and 8.0 metres from the seawall.

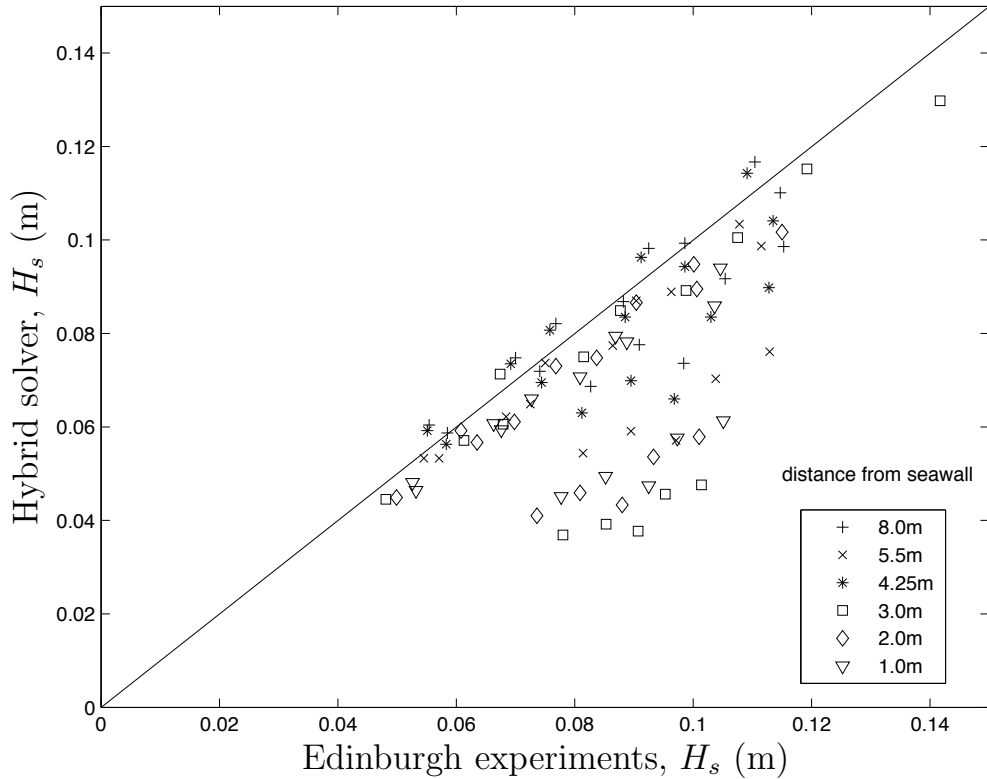


Figure 5.10: Numerical simulation of the Edinburgh wave flume experiments: scatter plot showing the significant wave heights recorded at each depth gauge for the Edinburgh experiments and the hybrid solver.

#### 5.4.5 Random wave overtopping

The final set of experiments that have been modelled using the hybrid Boussinesq solver are experiments that were conducted at Kansai University, Japan. The Kansai experiments observed the volumes of overtopping water resulting from random wave interaction with shallow sloped seawalls. The wave flume used for the Kansai experiments is defined in Fig. 5.11. The bathymetry consisted of a shallow foreshore slope upon which was placed a steeper slope representing a seawall. The position of the seawall slope was dependent upon the water depth,  $d$ , and the depth of the water at the toe of the structure,  $d_{toe}$ . The height of the seawall was given by the crest freeboard,  $R_c$ . The numerical experiment was run for 1200 seconds, with the random waves generated by sampling from the JONSWAP spectrum for a given significant wave height,  $H_s$ . The wave period was set at  $T = 1.0$  seconds for each run of the experiment.

In all, 83 runs were chosen for comparison in this study. The values for the steepness of the foreshore and seawall slopes, the crest freeboard and the significant wave heights are summarised in Table 5.1. The majority of the experiments were

Table 5.1: Random wave overtopping: experimental values

Variable	Values
Foreshore slope	1:30, 1:10
Seawall slope	1:10, 1:7, 1:5, 1:3, 1:4/3
$R_c$	0.005, 0.015, 0.025, 0.035, 0.0625
$H_s$	0.0156, 0.0312, 0.0468, 0.0625, 0.0781

conducted with a foreshore slope of 1:30, with the exception of a 1:10 foreshore slope used where the seawall slope was 1:10. The specific values for each of the 83 runs of the experiment used here for the steepness of the foreshore slope and the seawall slope,  $d$ ,  $d_{toe}$ ,  $R_c$  and  $H_s$  are given in Tables C.7–C.9.

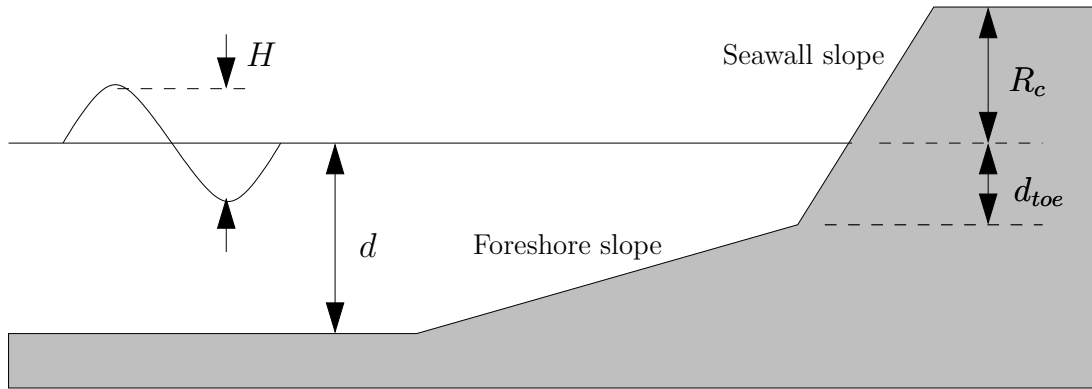


Figure 5.11: Diagram of the Kansai University wave flume.

The overtopping discharge volumes collected by the Kansai experiments have been compared with the empirical models of Owen (1980), van der Meer and Janssen (1995) and Hedges and Reis (1998) and the SWE based numerical model of Hu *et al.* (2000) in Reis *et al.* (2005) for a range of different seawall slope configurations. It was found that, in general, the empirical models over-predicted the dimensionless discharges with Hedges and Reis' semi-empirical H&R model providing better overtopping predictions. The numerical model used by Hu *et al.* (2000) was the same as that presented in Chapter 2 for the inviscid SWE, with the treatment of the source terms achieved by using a simple first-order implicit Euler method combined with the Hancock scheme by use of operator splitting. The incident wave boundary was located approximately one wavelength seaward from the toe of the seawall slope. A non-uniform grid was used with a finer mesh applied near the seawall slope.

The hybrid Boussinesq solver has been used to model the Kansai overtopping

experiments. The solution domain consisted of a wave flume 14 metres long with the wave generating source function located 10 metres seaward from the toe of the foreshore slope. The solution domain was discretised using a uniform mesh with mesh spacing  $\Delta x = 0.02$  metres. A sponge layer was used at the incident boundary to absorb any waves reflected back from the seawall past the source function. The right-hand boundary was the simple transient flow boundary used in the modelling of the Edinburgh experiments. The random waves were generated by the source function method for the required values of  $H_s$  using the JONSWAP spectrum with a peak enhancement parameter of 0.3. As with the modelling of the Edinburgh experiments, the use of the dispersion terms within the governing equations was determined by the condition given in Eq. 5.37, with a wave breaking parameter of  $\gamma = 0.3$  used.

The dimensionless values of the freeboard and discharge volumes are compared for each value of the steepness of the seawall slope in Figs. 5.12–5.14. The general trend shows that although the hybrid scheme over-predicts the overtopping volumes, the steeper the seawall slope the better the numerical predictions. There is an exception to this conclusion when the seawall slope is very shallow (i.e., 1:10). In this case, the numerical results under-predict the overtopping volumes. It should be noted that the slope of the foreshore in this case was the same as that for the seawall and the absence of the bend in the bathymetry may influence the wave breaking and run-up on the seawall slope and therefore the overtopping. More research on using the hybrid Boussinesq solver for overtopping on bathymetry of this type is required.

The absolute relative error between the dimensionless discharges of the physical experiments and the numerical model are plotted against the corresponding dimensionless freeboard,  $R^*$ , in Fig. 5.15. The majority of the values show that the numerical model predicts the overtopping to within an absolute relative error of 1, which is well within the accepted accuracy for empirical overtopping formulae noted in Besley (1999).

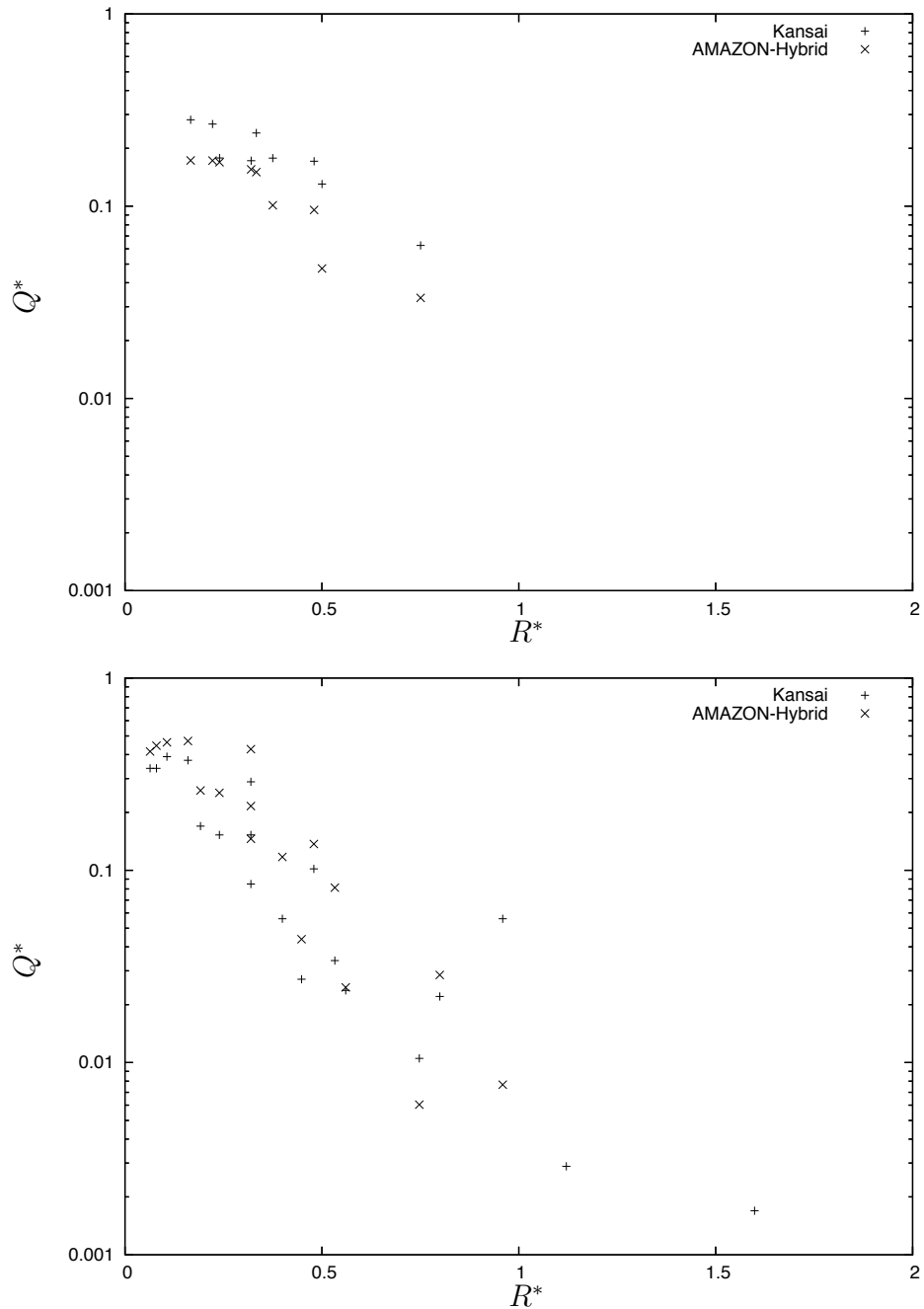


Figure 5.12: Random wave overtopping: comparisons of the dimensionless overtopping discharges ( $Q^*$ ) of the Kansai data and the hybrid Boussinesq solver against the dimensionless freeboard ( $R^*$ ) for seawall slopes 1:10 (top) and 1:7 (bottom).

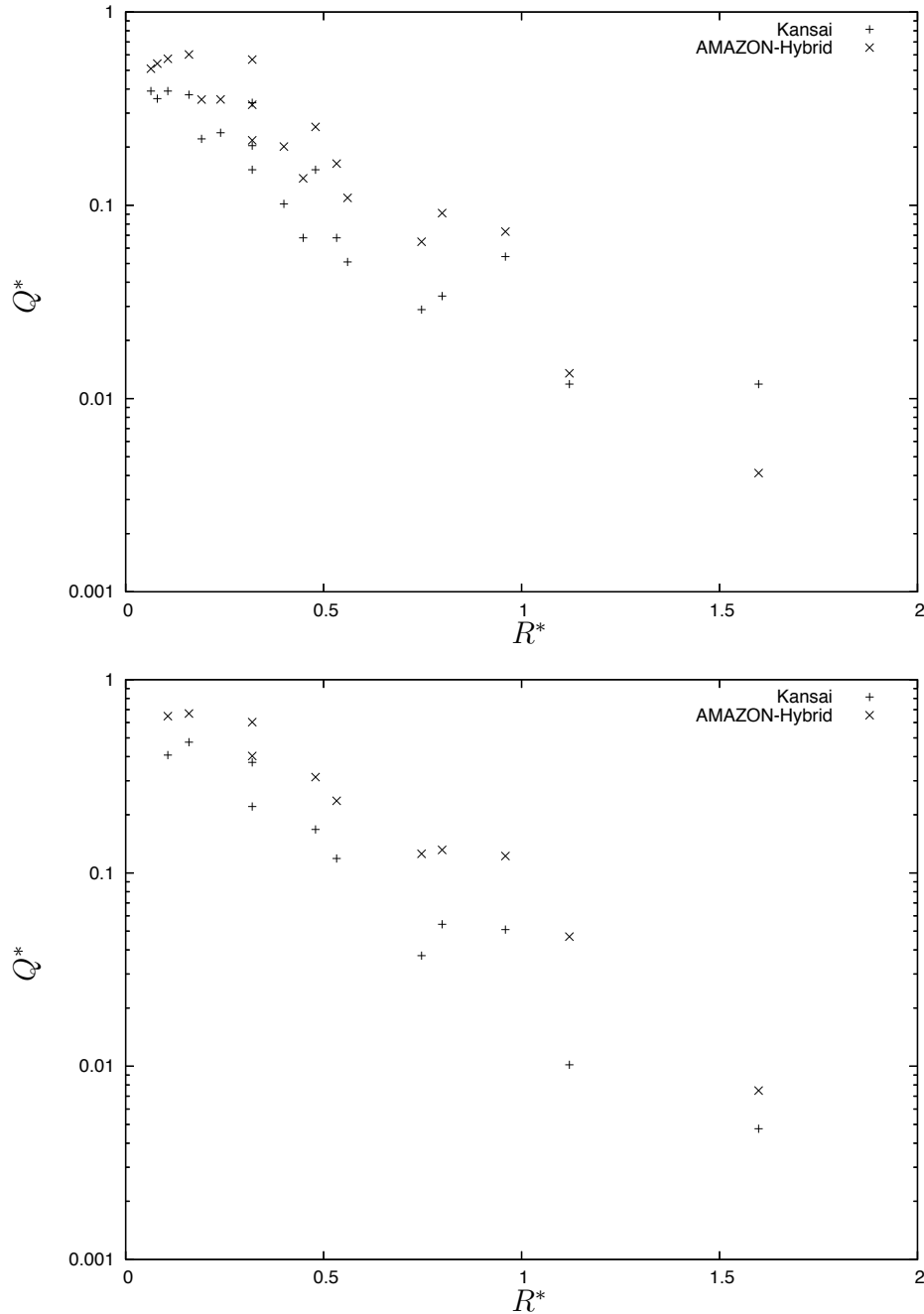


Figure 5.13: Random wave overtopping: comparisons of the dimensionless overtopping discharges ( $Q^*$ ) of the Kansai data and the hybrid Boussinesq solver against the dimensionless freeboard ( $R^*$ ) for seawall slopes 1:5 (top) and 1:3 (bottom).

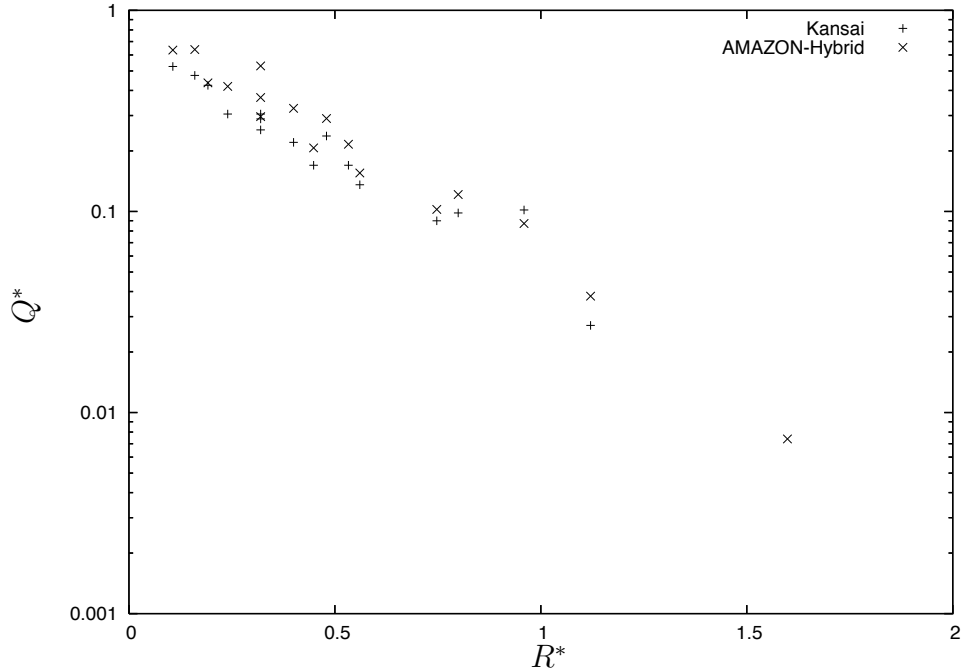


Figure 5.14: Random wave overtopping: comparisons of the dimensionless overtopping discharges ( $Q^*$ ) of the Kansai data and the hybrid Boussinesq solver against the dimensionless freeboard ( $R^*$ ) for seawall slope 1:4/3.

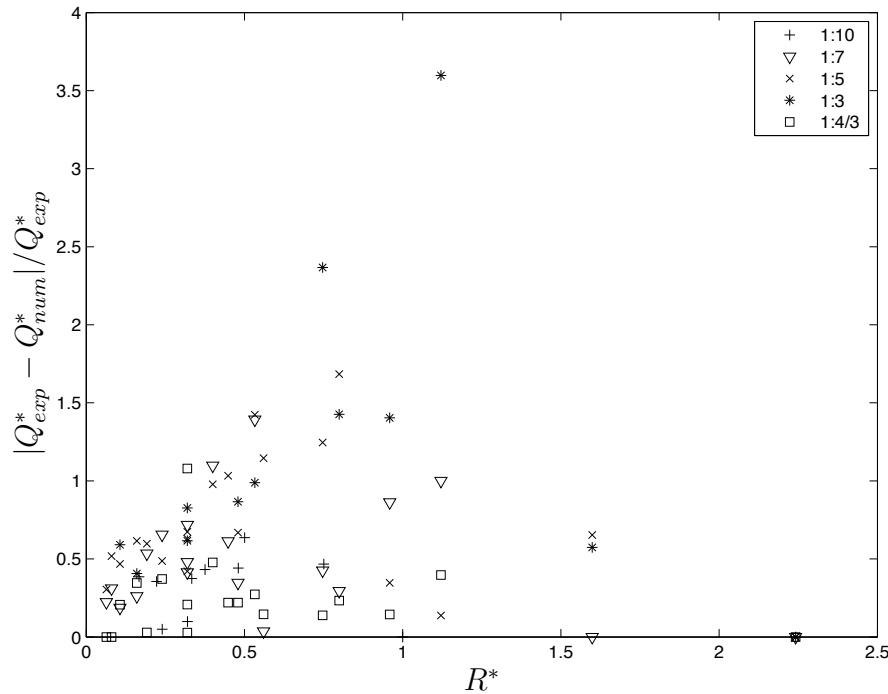


Figure 5.15: Random wave overtopping: scatter plot showing the absolute relative errors between the dimensionless discharges of the Kansai data ( $Q_{exp}^*$ ) and the hybrid Boussinesq solver ( $Q_{num}^*$ ) for a range of seawall slopes.

## 5.5 Chapter Summary

A hybrid finite-volume/finite-difference numerical solver for the extended Boussinesq equations was presented in this chapter. The numerical solver described in Chapter 4 was based on a finite-difference implementation and therefore the solution domain was limited to a uniform Cartesian mesh. The hybrid scheme was originally developed by Erduran *et al.* (2005), where the extended Boussinesq formulation of Madsen and Sørensen (1992) was rewritten so that it is in the form of the shallow water equations plus additional terms that model dispersion. This scheme has been applied to the extended Boussinesq formulation of Nwogu (1993) here. The governing equations were rewritten so that local water depth is a solution variable replacing the water surface elevation. This is made possible by assuming the bed surface elevation does not change significantly over time and the equations are rewritten using simple algebra.

The hybrid solver consists of the finite-volume method that is presented in Chapter 2 to solve the SWE terms within the rewritten form of the extended Boussinesq equations. The values of the conserved variables at each cell interface are calculated using a fourth-order MUSCL reconstruction method. The source and dispersion terms within the governing equations are modelled using central difference formulae where fourth-order accurate differences are used for the first- and third-order derivatives. The use of the fourth-order MUSCL scheme and central differences ensures that the higher-order Boussinesq terms are retained as noted by Wei and Kirby (1995). The governing equations are integrated through time using the third-order Adams-Basforth, fourth-order Adams-Moulton predictor/corrector method used in the finite-difference solver in Chapter 4.

The hybrid Boussinesq solver was validated over a range of standard test cases. The extended Boussinesq equations of Nwogu were used to calculate the solutions for the solitary wave propagation test used previously to validate the finite-difference solver. Both the Nwogu, and Madsen and Sørensen extended Boussinesq equations were used to model the regular wave propagation over a submerged bar test case. The Madsen and Sørensen formulation was then selected to examine wave run-up and overtopping in three different sets of experiments: solitary wave run-up, violent wave run-up and overtopping, and random wave run-up and overtopping. To the author's knowledge this is the first time that an extended Boussinesq-type model has been used to examine non-solitary wave run-up and overtopping.

# Chapter 6

## Conclusions

The aim of this study was to examine numerical modelling of water flow in near shore coastal regions. Traditionally, the design of structures that help prevent damage to property and transport infrastructure have been improved by conducting physical experiments in a wave flume where the sea conditions are replicated, and measuring devices record the waves and overtopping volumes. Conducting these experiments is not a trivial matter due to the time and expense of setting up the wave flume, calibrating the measuring devices and running the experiments. Numerical models can represent a significant saving in the times and costs associated with conducting physical experiments. Validation of these numerical models is achieved by comparing the values calculated by the numerical model against observed values from the physical experiments.

In order to make numerical models a feasible alternative to physical experiments, the computational power required should not exceed the hardware capabilities of computers that are currently available on the market. It is for this reason that only depth-averaged flow models were chosen in this study, whereas numerical models based on the full Navier-Stokes equations are not suitable considering current computing technology. The depth-averaging process applied to the Navier-Stokes equations results in the shallow water equations (SWE), a set of governing equations that can model water flow where the water is considered shallow and the vertical velocity negligible. The definition of shallow water is where the ratio of water depth to wavelength is in the range  $d/L \leq 1/20$ . The SWE are hyperbolic in nature which means that discontinuities can be admitted into the solution so that breaking waves can be modelled as a discontinuity.

AMAZON, an existing numerical model based on the SWE was presented in Chapter 2 (Mingham and Causon, 1998). This model uses a high-resolution finite-volume method to solve the SWE. Spatial discretisation is achieved by dividing

---

the solution domain into finite-volume cells, where the solution variables are calculated at the centre of each cell by integrating around the perimeter. The advantage of using a finite-volume discretisation is that the solution domain is not limited to orthogonal boundaries. The integration of the governing equations through time is calculated using the Hancock scheme, a Godunov-type second-order accurate predictor/corrector scheme. Godunov-type solvers require the values of the conserved variables at the cell interfaces which are calculated here using a Monotonic Upwind Schemes for Conservation Laws (MUSCL) approach. The gradients of the conserved variables across each cell are limited to ensure that there are no under- or over-shoots at the cell interfaces that can cause oscillations in the solution by use of a slope limited function. The corrector stage of the Hancock scheme requires the solution of local Riemann problems at each cell interface caused by the slope limiting process. The Riemann solver developed by Harten, Lax, and van Leer (1983) (HLL) was used to solve the local Riemann problems. The AMAZON numerical model was validated against a one-dimensional dam break problem. This is a standard test case for solvers of hyperbolic equations as a bore wave forms that tests the numerical scheme's ability to treat discontinuities. The solutions using three different slope limiting functions were compared against the analytical solutions for both the wet bed and dry bed case. Of the three slope limiters, it was found that the van Leer limiter provided the best solution and for this reason was chosen for all subsequent calculations using this numerical model.

The treatment of the source terms that model the bed topography was achieved using the Surface Gradient Method (SGM) (Zhou *et al.*, 2001). The SGM is a novel method where the water surface elevation as opposed to the water depth is used as a basis for the MUSCL reconstruction process. This means that the differences between the spatial discretisation of the conserved variables and the bed surface do not affect the solution. The implementation of the SGM to the AMAZON solver requires little alteration to the existing code and the additional computational effort is negligible. The SGM is fully conservative as long as a centred difference is applied to the bed surface. The SGM solver was validated against a number of test cases examining tidal wave flow over regular and irregular bed surfaces; subcritical, supercritical and transcritical flow over a bump in the bed topography; a quasi-stationary case examining the SGMs ability to model small perturbations in the water surface and a surge wave crossing a discontinuity in the bed surface.

The AMAZON-SGM solver was used to model a series of wave flume experiments conducted at Edinburgh University in Chapter 3. These experiments were

designed to reproduce violent overtopping events at a seawall where breaking waves dominate at the structure. Due to the limit of applicability of the SWE, a reduced solution domain of 2.0 metres from the seawall was modelled. This corresponds to a typical depth to wavelength ratio of  $d/L \approx 0.15$ . The waves were generated at the incident wave boundary by explicitly stating the water surface recorded by the corresponding depth gauge from the experiments. The value of the velocity at the incident wave boundary was assumed to be that of the first computational node in from this boundary. A previous study has shown that this treatment provides values for the water surface and velocity which are 99% and 85% accurate, respectively. A comparison of the wave surface elevation recorded at the gauge placed 1.0 metre from the seawall showed that the SWE based model tended to over-predict the wave heights. This is due to the fact that for part of the solution domain, the shallow water condition is violated, causing the waves to shoal and break prematurely. Analysis of the overtopping discharge volumes showed the the shallow water model can predict violent overtopping events to within a relative error value of 20% where the waves are not severely impacting at the structure ( $h^* > 0.075$ ). This research has been published in *Coastal Engineering* (Shiach *et al.*, 2004).

The main disadvantage of a SWE based model as evident in the work discussed in Chapter 3, is that only near shore wave propagation can be modelled or where the shallow water condition is retained, e.g., tsunami wave modelling. For a depth-averaged model to be used as a tool for coastal engineers, it needs to model wave propagation in deeper water. Another system of depth-averaged equations that include dispersion terms enabling deeper water to be modelled is the class of extended Boussinesq equations. Chapter 4 presented the extended Boussinesq equations derived by Nwogu (1993). The derivation of the Nwogu formulation assumes that the horizontal velocity follows a quadratic profile in the vertical direction. This leads to a system of equations where the velocity can be calculated at an arbitrary depth depending upon a free parameter  $\alpha$ . The value of  $\alpha$  therefore influences the dispersion properties and Nwogu suggested an optimal value of  $\alpha = -0.390$  by comparing the linear dispersion properties of the system with the linear dispersion relation. The extended Boussinesq equations of Nwogu are applicable in the range  $d/L < 0.35$ .

The solution method chosen to solve Nwogu's Boussinesq equations was one that was first suggested by Wei and Kirby (1995). This was a finite-difference scheme that uses second- and fourth-order difference stencils for the second- and first-order spatial derivatives respectively. This ensures that the truncation errors

---

of the finite-difference method do not cancel out the dispersion terms present in the governing equations. Time integration was achieved using a third-order Adams-Bashforth predictor and a fourth-order Adams-Moulton corrector. The second-order treatment of the spatial derivatives leads to a tri-diagonal system that is solved at each time step for the calculation of the horizontal velocities. Wei and Kirby suggested inverting the coefficient matrix before the solution routines are called. However, it was found that the use of an efficient tri-diagonal solution routine significantly improved the computational speed of the solver, despite the need to calculate the solution at every time the predictor/corrector stages are invoked. Wave generation was achieved using a source function method applied to a range of computational nodes, as opposed to a single node, as this would cause instabilities in the solution domain because a non-staggered mesh is being used. The treatment of transient flow and solid wall boundary conditions is discussed, where the former requires the application of sponge layers that gradually remove energy from the system to prevent reflected waves from propagating back into the solution domain.

Solitary wave propagation was chosen to validate the numerical solver and demonstrate the dispersion properties of the governing equations. Solitary waves maintain their shape and velocity due to an exact balance between the non-linear terms that cause the wave to steepen, and the dispersion terms that cause the wave to spread out. The solution of the solitary wave propagation test showed that the finite-difference scheme accurately solved Nwogu's Boussinesq equations and the dispersion was retained. There were high frequency oscillations evident behind the wave train but these were too small to cause significant concerns with the solver. The source function method for generating waves, the application of the sponge layers for transient flow boundary conditions and the solid wall boundary conditions were tested using single and multiple period monochromatic wave tests. The source function method was shown to produce the required wave forms appropriate for the limit of applicability of the governing equations. The width of the source function was half the wavelength of the wave generated, as suggested by Wei *et al.* (1999). Although a narrow source function is desirable, it was found that using a narrower source function caused oscillations in the solution. The sponge layers absorbed all energy into the transient flow boundary condition, as shown by the quasi-stationary behaviour of the monochromatic wave test. The solid wall boundary condition reflected all energy and caused standing waves to form at double the height of the incident waves generated by the source function.

The final test performed with the finite-difference solver was to model a series

of experiments conducted by Beji and Battjes (1993) and used by Dingemans (1994) to compare various Boussinesq models. The experiment consists of regular wave propagation over a submerged trapezoidal bar where the waves shoal as they travel up the front facing slope and separate into multiple component waves as the backward slope is encountered. This is a good test for Boussinesq models because the disintegration of the wave train occurs due to dispersion. Comparisons between the experimental and numerical water surface elevations showed that the finite-difference Boussinesq solver could accurately model the wave steepening and the separation and propagation of the component waves. The finite-difference solver, whilst being able to accurately solve the extended Boussinesq equations, does not have the advantage that a finite-volume solver has in that non-orthogonal solution domains can be modelled.

One of the aims of this study was to develop a numerical model that can be integrated into the existing AMAZON suite of flow solvers, in particular the Cartesian cut-cell method used for modelling irregular boundaries in the solution domain. Therefore, a finite-volume based Boussinesq solver would be preferable as opposed to a finite-difference solver. A hybrid finite-volume/finite-difference solver is presented in Chapter 5.

Erduran *et al.* (2005) developed a numerical solver for the extended Boussinesq formulation of Madsen and Sørensen (1992). The governing equations were re-written so that the water depth replaced the water surface elevation as a solution variable. The re-written form of Madsen and Sørensen's Boussinesq equations are essentially the SWE plus some additional dispersion terms. Therefore, the finite-volume solver presented in Chapter 2 was applied to solve the SWE terms and the fourth-order finite-difference stencils used in the finite-difference solver presented in Chapter 4 was used to discretise the additional dispersion terms. The calculation of the variables at the cell interfaces for use in the finite-volume solver was achieved using a fourth-order MUSCL reconstruction. Time integration was achieved using the same Adams third-order predictor, fourth-order corrector method suggested by Wei and Kirby.

This approach was used to solve Nwogu's extended Boussinesq formulation in Chapter 5 which has not previously been examined. The hybrid model used the solitary wave test to compare the solutions using the van Leer and minmod slope limiting functions. It was found that the hybrid scheme could accurately resolve the solitary wave profile when using the van Leer limiter. The use of the minmod limiter in the hybrid solver did not retain the dispersion in the governing equations which was noted in Erduran *et al.* (2005). It was also found that the

hybrid solver presented an improvement over the finite-difference solver where the high frequency oscillations behind the solitary wave were no longer present due to the non-oscillatory feature of MUSCL schemes. The hybrid scheme was also applied to the monotonic wave propagation over a submerged bar test case used to test the finite-difference solver. The extended Boussinesq equations of Nwogu and Madsen and Sørensen were compared with the experimental water surface elevations. The Madsen and Sørensen extended Boussinesq equations provided marginally better results than the Nwogu formulation. However, neither formulation could accurately resolve the break-up of the wave train after the submerged bar for configuration (c) where spilling breakers were observed.

The Madsen and Sørensen formulation was then chosen to model wave run-up and overtopping experiments. The reason for this choice was that the additional dispersion terms can be removed from the solution where the need arises, for example, where wave breaking is likely to occur or the bed surface elevation is greater than the wave surface giving a negative water depth. In programming terms, the removal of the dispersion terms can, in theory, be achieved with the Nwogu formulation. However, as the horizontal velocity is assumed to be at an arbitrary depth and not a depth-averaged velocity, high-frequency oscillations occurred where the additional terms were removed.

The first set of experiments modelled with the hybrid solver applied to the Madsen and Sørensen Boussinesq equations was solitary wave run-up on a sloping beach. Solitary wave run-up was the focus of an extensive study by Synolakis (1987) where a range of non-breaking and breaking solitary waves were generated and the maximum run-up was recorded. It was found that the run-up values followed two asymptotic forms depending upon whether the wave had broken or not. The hybrid Boussinesq solver accurately predicted the run-up values where the solitary wave height to depth ratio was larger than 0.1. Where smaller waves were generated, the numerical model tended to over-predict the run-up values to a relative error in the range  $-0.05 \leq R \leq 0.45$ . This is assumed to be because the height of the waves modelled is close to the minimum wet depth parameter used by the numerical solver.

The violent wave overtopping experiments conducted at Edinburgh University and used for a modelling test case for the SWE solver in Chapter 2, were used to test the hybrid Boussinesq solver for modelling overtopping of near vertical seawalls. The solution domain modelled the whole flume from the depth gauge closest to the wave paddle, which was used as the incident wave boundary, to beyond the seawall. A comparison of the water surface profiles for all 6 depth

gauges showed that the hybrid scheme accurately modelled wave propagation with the numerical water surface closely resembling the experimental water surface. An analysis of the significant wave heights showed that for cases where the extended Boussinesq equations are applicable, the numerical model produced the expected values. It is clear from this analysis that the source function method applied to generate waves from a given input function is valid as long as the approximate wavelength is known. Therefore random waves can also be generated using this method.

The hybrid model produced zero overtopping for all 15 runs of the Edinburgh experiments. This is a concern as it suggests that the hybrid scheme cannot model near vertical sloping structures as well as the SWE based model. There are three possible reasons for the absence of overtopping when using the hybrid model suggested here by the author:

- (i) the dispersion terms in the governing equations were not removed from the calculations at the right moment to best model breaking wave interaction with the seawall;
- (ii) there were an insufficient number of computational cells used for modelling flow on the seawall slope;
- (iii) there is a limit to the slope angle for which the fourth-order solver can accurately model run-up and overtopping.

The suggestion made in (i) would result in a propagating wave not breaking soon enough and therefore the interaction with the seawall not producing as large an overtopping event as it should. Performing repeated runs of the experiments with different values of the wave breaking parameter  $\gamma$  would show whether this was the case. If there was an insufficient number of computational cells placed on the seawall slope, as suggested in (ii), then the fourth-order MUSCL reconstruction that requires values from cells  $i - 2$  to  $i + 3$  for the calculation of the conserved variables at cell interface  $i + 1/2$  could prevent any flow past the top of the seawall where the bed topography abruptly changes direction. It should be noted that the second-order MUSCL reconstruction used in the SWE model did not experience this problem (Shiach *et al.*, 2004). The final suggestion, given in (iii), causes the value of the gradient across the last ‘wet’ cell to be very large. The slope limiting process will then reduce this gradient significantly to prevent oscillations and therefore alter the mass and momentum of the leading ‘wet’ cell. The limit to the steepness of the slope for which a MUSCL based AMAZON scheme can be

applied to model run-up is not presently known. Due to the constraints of time, none of the three suggestions given above were examined here and are left as the focus of a future study.

The final set of experiments that were modelled using the hybrid Boussinesq solver was based upon a series of experiments conducted at Kansai University, Japan, studying random wave run-up and overtopping of various sloping structures. The data from the experiments was used in a study by Reis *et al.* (2005) to compare various empirical, semi-empirical formulae and a SWE based numerical model. 83 runs of the experiments were modelled each consisting of 1200 seconds of simulated random waves. The solution domain consisted of a one-dimensional channel with the wave generating source function located 10 metres from the toe of the seawall. The seawall slopes modelled had steepness ratios of 1:10, 1:7, 1:5, 1:3 and 1:4/3. The waves generated were sampled from the JONSWAP spectrum for significant wave height values of  $H_s = 0.0152, 0.0312, 0.0468, 0.0625$  and  $0.0781$  metres. An analysis of the dimensionless values for the crest freeboard and the discharge volume was conducted for each of the different slope configurations. It was found that the steeper the seawall, the better the numerical overtopping predictions. This suggests that the numerical model did not accurately model the wave run-up on the shallower sloping structures resulting in a large over-prediction of the overtopping.

## 6.1 Further Work

This section contains details of further work that has been suggested by the research conducted in this study which due to time constraints has not been included here.

### Boussinesq modelling of overtopping

In this study, the hybrid Boussinesq solver was used to model wave run-up and overtopping of seawalls of steepnesses in the range 1:10 to 1:4/3 (Chapter 5). It was found that, in general, as the seawall slope steepness increased, the overtopping volumes that were predicted by the numerical model more closely resembled the overtopping volumes observed in the physical experiment. However, it was also found that when modelling an extreme seawall slope no overtopping was observed in the numerical model. There is a need to test the AMAZON-Hybrid model over the range of seawall slopes not covered in this study ([1:1 – 5:1] for example) to

provide guidance on the limitations of the numerical model.

### Modelling of wave run-up and overtopping using Nwogu's Boussinesq formulation

Although the hybrid solver discussed in Chapter 5 can be used to solve Nwogu's extended Boussinesq equations, only the Madsen and Sørensen Boussinesq formulation was used to examine wave run-up and overtopping here. This decision was made because the removal of the dispersion terms in the Madsen and Sørensen formulation requires no special treatment, whereas oscillations form when using Nwogu's formulation. These oscillations occur because of the abrupt change from using the horizontal velocity at an arbitrary depth to using the depth averaged velocity of the SWE.

One method of using the finite-volume based hybrid scheme for the solution of the Nwogu's Boussinesq formulation, in particular for modelling wave run-up and overtopping, would entail introducing a wave breaking model instead of reverting to the SWE. Lynett *et al.* (2002) presented a finite-difference based model of run-up and overtopping where additional terms were introduced to Nwogu's formulation to model wave breaking. To overcome the problem that occurs at the wet/dry boundary, Lynett *et al.* used linear interpolation of the solution variables (water surface elevation  $\eta$  and horizontal velocity  $u_\alpha$ ) to ensure that no special treatment needs to be applied to the fourth-order spatial derivatives calculated for the wet cells close to the wet/dry boundary. The application of a finite-volume based solver will present an improvement over the basic fourth-order finite-difference solver (Wei and Kirby, 1995) used by Lynett *et al.* because of the non-oscillatory feature of MUSCL reconstruction techniques.

A further advantage to using depth-averaged governing equations where there is an assumed velocity profile (for example Nwogu's Boussinesq formulation), is that the range of applicability can be extended to deeper water by utilising a layered approach. Lynett and Liu (2002, 2004b) derived a two-layer Boussinesq formulation which was later extended to an  $N$ -layered formulation (Lynett and Liu, 2004a) where Euler's equation is vertically integrated over each layer assuming a quadratic vertical velocity profile within each layer. The free parameters present in the formulation are determined by comparing the linear dispersion properties for the phase and group velocity with the linear dispersion relation similar to the approach used by Nwogu (1993). It was found that a four layer Boussinesq-type model derived using this approach is applicable up to  $d/L \leq 25$  which when

compared to Nwogu's one-layered system (that is applicable up to  $d/L \leq 0.35$ ) represents a significant improvement and allows for wave propagation in deep water to be modelled.

### Two-dimensional Boussinesq modelling

The numerical models examined in this study have focused on one-dimensional cases only. The numerical schemes presented in this thesis are all extendable to enable modelling of water flow in two-dimensions. The extension of a numerical model to a two-dimensional mesh has several obvious advantages over a one-dimensional model. The one-dimensional model is limited to wave run-up and overtopping where the direction of the incident waves are perpendicular to the shoreline. This is not the case in the real world where oblique wave attack is the norm.

Causon *et al.* (2000) developed a Cartesian cut cell method which can be implemented into a finite-volume based numerical scheme for arbitrary non-orthogonal geographies. The Cartesian cut cell method discretises the two-dimensional solution domain using a uniform Cartesian mesh. Where arbitrary topographies are required, the solid regions are simple 'cut out' of the Cartesian mesh. This approach produces three different types of cells: flow cells where no special treatment is required; solid cells where no flow occurs and which are removed from the calculations; and cut cells where part of the cell has been cut. Cut cells require a special treatment. The advantages that this method has over boundary fitting methods are that no special mesh generation routines are required, and only the cells that have been cut require an alteration of the numerical scheme. Therefore, any loss of accuracy resulting from the special treatment is kept to a minimum. The Cartesian cut cell method has since been extended to deal with moving boundaries (Causon *et al.*, 2001) allowing for the modelling of moving solid objects within the flow region, for example a ship's hull. Richardson (2002) implemented the SGM into the cut cell method and used it to model tsunami generation, propagation and run-up.

Application of the Cartesian cut cell method for the treatment of a two-dimensional AMAZON-Hybrid model would not be as straightforward as in the SWE case. The Hybrid scheme developed by Erduran *et al.* (2005) required a fourth-order MUSCL reconstruction of the variables at each cell interface. This does not present a problem where the additional dispersion terms have been removed, i.e., in shallow water where a second-order reconstruction can be applied.

However, for the case where cut cells occur in intermediate depth water, a fourth-order treatment of the solid wall boundary condition is required for the cell interface where the ‘cut’ has been applied. A crude solution could entail removing the dispersion terms from the governing equations for the cells close to the cut cells.

# Bibliography

- Abbot, M., Dansgaard, A., and Rodenhuis, G. (1973). SYSTEM 21, ‘jupiter’ (a design system for two dimensional nearly horizontal flows). *Journal of Hydraulic Research*, **11**, 1–28.
- Abbot, M. B., Petersen, H. M., and Skovgaard, O. (1978). On the numerical modelling of short waves in shallow water. *Journal of Hydraulic Research*, **16**(3), 173–203.
- Alcrudo, F. and Benkhaldoun, F. (2001). Exact solutions to the Riemann problem of the shallow water equations with a bottom step. *Computers & Fluids*, **30**(6), 643–671.
- Alcrudo, F. and García-Navarro, P. (1993). A high-resolution Godunov-type scheme in finite volumes for the 2D shallow-water equations. *Int. J. Numer. Methods Fluids*, **16**(6), 489–505.
- Allsop, N. W. H., Besley, P., and Madurini, L. (1995). Overtopping performance of vertical walls and composite breakwaters, seawalls and low reflection alternatives. Technical report, Paper 4.7 in MCS Final Report, University of Hanover.
- Ames, W. F. (1977). *Numerical Methods for Partial Differential Equations, Second Edition*. Academic Press, New York.
- Anderson, J. D. (1997). *A History of Aerodynamics*. Cambridge University Press.
- Barber, R. W. (1992). Solving the shallow water equations using a non-orthogonal curvilinear coordinate system. In *Proceedings of the Second International Conference on Hydraulic and Environment Modelling of Coastal, Estuarine and River Waters*, volume 1, pages 469–480, Bradford, England.
- Battjes, J. A. and Groenendijk, H. W. (2000). Wave height distributions on shallow foreshores. *Coastal Engineering*, **40**(3), 161–182.
- Beji, S. and Battjes, J. A. (1993). Experimental investigations of wave propagation over a bar. *Coastal Engineering*, **19**(1–2), 151–162.
- Bermudez, A. and Vázquez-Cendón, M. E. (1994). Upwind methods for hyperbolic conservation laws with source terms. *Computers and Fluids*, **23**, 1049–1071.

- Bernoulli, D. (1738). *Hydrodynamica, sive de viribus et motibus fluidorum commentarii*. Johann Reinhold Dulsseker, Strasbourg.
- Besley, P. (1999). Overtopping of seawalls - design and assessment manual. R&D Technical Report W178. Technical report, HR Wallingford.
- Besley, P., Stewart, T., and Allsop, N. W. H. (1998). Overtopping of vertical structures: new methods to account for shallow water conditions. In N. W. H. Allsop, editor, *Coastlines, Structures and Breakwaters*, pages 46–57. Thomas Telford.
- Billingham, J. and King, A. C. (2000). *Wave Motion*. Cambridge University Press.
- Borthwick, A. G. and Kaar, E. T. (1993). Shallow flow modelling using curvilinear depth-averaged stream function and vorticity transport equations. *Int. J. for Num. Methods in Fluids*, **17**, 417–445.
- Borthwick, A. G. L., Ford, M., Taylor, P. H., Weston, B. P., and Stansby, P. K. (2005). Prediction of solitary wave run-up at an arbitrary plane beach. In *Waves '05*. Fifth International Symposium on Ocean Wave Measurement and Analysis.
- Bruce, G. H., Peaceman, D. W., Rachford, H. H., and Rice, J. D. (1953). Calculations of unsteady-state gas flow through porous media. *Petrol. Trans. AIME*, **198**, 79–92.
- Castro, M. J., García-Rodríguez, J. A., González-Vida, J. M., Macías, J., Parés, C., and Vázquez-Cendón, M. E. (2004). Numerical simulation of two-layer shallow water flows through channels with irregular geometry. *J. Comput. Phys.*, **195**(1), 202–235.
- Causon, D. M., Ingram, D. M., Mingham, C. G., Yang, G., and Pearson, R. V. (2000). Calculation of shallow water flows using a Cartesian cut cell approach. *Advances in Water Resources*, **23**, 545–562.
- Causon, D. M., Ingram, D. M., and Mingham, C. G. (2001). A Cartesian cut cell method for shallow water flows with moving boundaries. *Advances in Water Resources*, **24**(8), 899–911.
- Chow, V. T. (1959). *Open-channel Hydraulics*. McGraw Hill, Kogakusha.
- Clarke, S. and Damgaard, J. (2002). Applications of a numerical model of swash zone flow on gravel beaches. In B. L. Edge, editor, *Proceedings of the 28th International Conference on Coastal Engineering*, volume 1, pages 1028–1036, Cardiff.
- Courant, R., Friedrichs, K. O., and Lewy, H. (1928). Über die partiellen Differenzengleichungen der mathematischen Physik. *Mathematische Annalen*, **100**(1), 32–74.

- Courant, R., Friedrichs, K. O., and Lewy, H. (1967). On the partial difference equations of mathematical physics. *IBM Journal*, pages 215–234. Originally appeared in *Mathematische Annalen* 100, 32–74 (1928).
- Cunge, J. A. (1987). Numerical Hydraulics Modelling: Late '80s context and cross-roads. In J. A. Cunge and P. Ackers, editors, *Proceedings of XXII IAHR Congress: Hydraulic Modelling*, volume B, pages 17–30.
- Dean, R. G. and Dalrymple, R. A. (1991). *Coastal Processes with Engineering Applications*. Cambridge University Press.
- Dingemans, M. W. (1987). Verification of numerical wave propagation models with laboratory measurements. Report H228 Part 1, 400pp, Delft Hydraulics.
- Dingemans, M. W. (1994). Comparison of computations with Boussinesq-like models and laboratory measurements. Technical Report Report H1684.12, Delft Hydraulics.
- Dodd, N. (1998). A numerical model of wave run-up, overtopping and regeneration. In *Proceedings ASCE Journal of Waterways, Port and Coastal Engineering*, volume 124, pages 73–81. ASCE New York.
- Erduran, K. S. (2007). Further application of hybrid solution to another form of Boussinesq equations and comparisons. *Int. J. Numer. Meth. Fluids*, **53**, 827–849.
- Erduran, K. S., Ilic, S., and Kutija, V. (2005). Hybrid finite-volume finite-difference scheme for the solution of Boussinesq equations. *Int. J. Numer. Meth. Fluids*, **49**, 1213–1232.
- Fagherazzi, S., Rasetarinera, P., Hussaini, Y., and Furbish, D. J. (2004). Numerical solution of the dam-break problem with a discontinuous Galerkin method. *J. Hydraul Eng. ASCE*, **130**(6).
- Falconer, R. A. (1976). *Mathematical Modelling of Jet-forced Circulation in Reservoirs and Harbours*. Ph.D. thesis, Imperial College, London.
- Fraccarollo, L. and Toro, E. F. (1995). Experimental and numerical assessment of the shallow water model for two dimensional dam-break type problems. *J. Hydr. Res.*, **33**, 843–864.
- Franco, L., do Gerloni, M., and van der Meer, J. (1994). Wave overtopping on vertical and composite breakwaters. In B. L. Edge, editor, *Proceedings from 24th International Conference on Coastal Engineering*, Kobe, Japan.
- Galvin, C. J. j. (1964). Wave-height prediction for wave generators in shallow water. Technical Report AB0440880, Coastal Engineering Research Center Vicksburg MS.

- García-Navarro, P. and Vázquez-Cendón, M. E. (2000). On numerical treatment of the source terms in the shallow water equations. *Comput. Fluids*, **29**, 951–979.
- Gobbi, M. F. and Kirby, J. T. (1999). Wave evolution over submerged sills: tests of a high-order Boussinesq model. *Coastal Engineering*, **37**, 57–96.
- Godar, Y. (1988). Statistical variability of sea state parameter as a function of wave spectrum. *Coastal Engineering in Japan JSCE*, **31**(2), 39–52.
- Godar, Y. (2000). *Random Seas and Design of Maritime Structures*, volume 15 of *Advance Series on Ocean Engineering*. World Scientific.
- Godar, Y. and Kudaka, M. (2005). Dispersing the myth of spectral width parameter in control of wave height distribution. In *Waves '05*. Fifth International Symposium on Ocean Wave Measurement and Analysis.
- Godar, Y., Kishira, Y., and Kamiyama, Y. (1975). Laboratory investigation on the overtopping rates of sea walls by irregular waves. *Ports and Harbour Research Institute*, **14**, 3–44.
- Godunov, S. K. (1959). A finite difference method for the computation of discontinuous solutions of the equations of fluid dynamics. *Math. Sbornik.*, **47**, 271–306.
- Goutal, N. and Maurel, F. (1997). In N. Goutal and F. Maurel, editors, *Proceedings of the 2nd workshop on dam-break wave simulation*, number HE-43/97/016/B. Département Laboratoire National d'Hydraulique, Groupe Hydraulique Fluviale Electricité de France.
- Green, A. E. and Naghdi, P. M. (1976). A derivation of equations for wave propagation in water of variable depth. *J. Fluid Mech.*, **78**, 237–246.
- Harten, A., Lax, P., and van Leer, B. (1983). On upstream differencing and Godunov-type schemes for hyperbolic conservation laws. *SIAM Rev.*, **25**, 35–61.
- Hasselmann, K., Barnett, T. P., Bouws, E., Carlson, H., Cartwright, D. E., Enke, K., Ewing, J. A., Gienapp, H., Hasselmann, D. E., Kruseman, P., Meerburg, A., Miller, P., Olbers, D. J., Richter, K., Sell, W., and H., W. (1973). Measurements of wind-wave growth and swell decay during the joint north sea wave project (JONSWAP). *Ergnzungsheft zur Deutschen Hydrographischen Zeitschrift Reihe A*, **8**, 8–95.
- Hedges, T. S. and Reis, M. T. (1998). Random wave overtopping of simple seawalls: a new regression model. *Water, Maritime and Energy Journal*, **130**(1), 1–10.
- Hibberd, S. and Peregrine, D. H. (1979). Surf and run-up on a beach: a uniform bore. *J. Fluid Mech.*, **95**(2).

- Hirsch, C. (1988). *Numerical Computation of External and Internal Flows*. John Wiley & Sons Ltd.
- Hu, K. (2000). *High-Resolution Finite Volume Methods for Hydraulic Flow Modelling*. Ph.D. thesis, Manchester Metropolitan University.
- Hu, K., Mingham, C. G., and Causon, D. M. (1998). A bore-capturing finite volume method for open-channel flows. *Int. J. Numer. Meth. Fluids*, **28**, 1241–1261.
- Hu, K., Mingham, C. G., and Causon, D. M. (2000). Numerical simulation of wave overtopping of coastal structures using the non-linear shallow water equations. *Coastal Engineering*, **41**, 433–465.
- Hubbard, M. E. and Dodd, M. (2002). A 2D numerical model of wave run-up and overtopping. *Coastal Engineering*, **47**, 1–26.
- Hughes, S. A. (1993). *Physical Models and Laboratory Techniques in Coastal Engineering*, chapter 7, pages 333–365. World Scientific.
- Ilic, S., Erduran, K. S., and Kutija, V. (2005). A hybrid scheme for the solution of the Boussinesq equations. In J. M. Smith, editor, *29th International Conference on Coastal Engineering*, Lisbon, Portugal. National Civil Engineering Laboratory.
- Johnson, B. H. and Thompson, J. F. (1978). A discussion of boundary-fitted coordinate systems and their applicability to the numerical modelling of hydraulic problems. Technical report, Army Engineer Waterways Experiment Station, Vicksburg, Mississippi.
- Kobayashi, N. and Wurjanto, A. (1989). Wave overtopping on coastal structures. *J. Waterway, Port, Coastal, and Ocean Engineering, ASCE*, **115**, 235–251.
- Kobayashi, N., Otta, A. K., and Roy, I. (1987). Wave reflection and run-up on rough slopes. *J. Waterway, Port, Coastal, and Ocean Engineering, ASCE*, **113**(3), 282–298.
- Koutitas, C. G. (1988). *Mathematical Models in Coastal Engineering*. Pentech Press Ltd.
- Krogstad, H. E. and Arnsten, O. A. (2000). Linear wave theory: Part A. Technical report, Norwegian University of Science and Technology, Trondheim, Norway.
- Lamb, H. (1945). *Hydrodynamics*. Dover Publications, 1st edition.
- Larsen, J. and Dancy, H. (1983). Open boundaries in short-wave simulation: a new approach. *Coastal Engineering*, **7**, 285–297.
- Lee, C., Yong-Sik, C., and Kidai, Y. (2001). Internal generation of waves for extended Boussinesq equations. *Coastal Engineering*, **42**(2), 155–162.

- Leendertse, J. J. (1967). Aspects of a computational model for long-period water-wave propagation. Technical report, The Rand Corporation, Santa Monica, California.
- Leveque, R. J. (1998). Balancing source terms and flux gradients in high-resolution Godunov methods: The quasi steady wave propagation algorithm. *J. Comput. Phys.*, **146**, 346–365.
- Liepmann, H. (1918). Die angenaherte ermittebung harmonischer funtionen and konformer abbildungen. *Bayer. Akad. Wiss., Math.-phys. Klasse, Sitz.*
- Liu, P. L. F. (1994). *Model equations for wave propagation from deep to shallow water*, volume 1 of *Advances in Coastal Engineering*, pages 125–157. World Scientific Publishing, Singapore.
- Longuet-Higgins, M. S. (1952). On the statistical distributions of heights of sea waves. *J. Mar. Res.*, **11**, 245–266.
- Longuet-Higgins, M. S. (1997). Progress toward understanding how waves break. In *Twenty-First Symposium on Naval Hydrodynamics*. National Academic Press, Washington.
- Luth, H. R., Klopman, G., and Kitou, N. (1994). Kinematics of waves breaking partially on an offshore bar; LDV measurements of waves with and with a net onshore current. Technical Report Report H-1573, 40pp, Delft Hydraulics.
- Lynett, P. J. and Liu, P. L. F. (2002). A two-dimensional, depth-integrated model for internal wave propagation over variable bathymetry. *Wave Motion*, **36**, 221–240.
- Lynett, P. J. and Liu, P. L. F. (2004a). Linear analysis of the multi-layer model. *Coastal Engineering*, **51**, 439–454.
- Lynett, P. J. and Liu, P. L. F. (2004b). A two-layer approach to wave modelling. *Proc. R. Soc. Lond.*, **460**, 2637–2669.
- Lynett, P. J., Wu, T., and Liu, P. L. F. (2002). Modeling wave runup with depth-integrated equations. *Coastal Engineering*, **46**, 98–107.
- Madsen, P. A. and Sørensen, O. R. (1992). A new form of the Boussinesq equations with improved linear dispersion characteristics. Part 2. A slowly-varying bathymetry. *Coastal Engineering*, **18**, 183–204.
- Madsen, P. A., Murray, R., and Sørensen, O. R. (1991). A new form of the Boussinesq equations with improved linear dispersion characteristics. Part 1. *Coastal Engineering*, **15**, 371–388.
- Madsen, P. A., Sørensen, O. R., and Schäffer, H. A. (1997a). Surf zone dynamics simulated by a Boussinesq type model. Part I. Model description and cross-shore motion of regular waves. *Coastal Engineering*, **32**, 255–287.

- Madsen, P. A., Sørensen, O. R., and Schäffer, H. A. (1997b). Surf zone dynamics simulated by a Boussinesq type model. Part II: Surf beat and swash oscillations for wave groups and irregular waves. *Coastal Engineering*, **32**, 289–319.
- Mase, H., Hedges, T. S., Shareef, M., and Nagahashi, S. (2003). Wave overtopping formula for gentle slopes incorporating runup. In *Proceedings of Coastal Engineering (in Japanese)*, volume 50, pages 636–640. JSCE.
- McCowan, J. (1894). On the highest wave of permanent type. *Philos. Mag. J. Sci.*, **38**.
- Mingham, C. G. and Causon, D. M. (1998). High-resolution finite-volume method for the shallow water equations. *Journal of Hydraulic Engineering*, **124**(6), 605–614.
- Morton, K. W. and Mayers, D. F. (1994). *Numerical solution of partial differential equations*. Cambridge University Press.
- Murray, R. J. (1989). Short wave modelling using new equations of Boussinesq type. In *Proceedings 9th Australasian Conference on Coastal and Ocean Engineering*, pages 331–336, Institution of Engineers, Adelaide, Australia.
- Niemeyer, H. D., Schulz, D. S., Kaiser, R. an Möller, J., Schüttrumpf, Pullen, T., and van Gent, M. (2002). Validation of mathematical modelling of wave overtopping on dykes. In J. M. Smith, editor, *Proceedings of the 28th International Conference on Coastal Engineering*, volume 1, pages 664–675, Cardiff, U.K.
- Nwogu, O. (1993). An alternative form of the Boussinesq equations for nearshore wave propagation. *Journal of Waterway, Port, Coastal, and Ocean Engineering*, **119**(6), 618–638.
- O'Connor, J. J. and Robertson, E. F. (2000). Claude Louis Marie Henri Navier. *St. Andrews University*.
- Owen, M. (1980). Design of seawalls allowing for wave overtopping,. Technical Report EX924, HR Wallingford.
- Owen, M. (1982). Overtopping of sea defences. In *Proc. Conf. Hydraulic Modelling of Civil Engineering Structures*, pages 469–480, Coventry. BHRA.
- Pearson, J., Bruce, T., and Allsop, N. W. H. (2001). Prediction of wave overtopping at steep seawalls – variabilities and uncertainties. In *Proceedings Waves '01*, San Francisco. ASCE.
- Peregrine, D. H. (1967). Long waves on a beach. *Journal of Fluid Mechanics*, **27**(4), 815–827.
- Peregrine, D. H. (2003). Water wave impacts on walls. *Annual Review of Fluid Mechanics*, **35**, 23–43.

- Reis, M. T., Hu, K., and Hedges, T. S. (2005). Empirical, semi-empirical and numerical overtopping models: a comparison. In *Waves '05*. Fifth International Symposium on Ocean Wave Measurement and Analysis.
- Richardson, L. F. (1910). The approximate arithmetical solution by finite differences of physical problems involving differential equations, with an application to the stresses in a masonry dam. *Transactions of the Royal Society of London*.
- Richardson, S. R. (2002). *Numerical Simulation of Impulsive Wave Overtopping Events Resulting from Landslides*. Ph.D. thesis, Manchester Metropolitan University.
- Richardson, S. R., Ingram, D. M., Mingham, C. G., and Causon, D. M. (2001). On the validity of the shallow water equations for violent overtopping. In B. L. Edge and J. M. Hemsley, editors, *Ocean Wave Measurement and Analysis*, volume 2, pages 1112–1124. Waves 2001, ASCE.
- Richardson, S. R., Pullen, T., and Clarke, S. (2002). Jet velocities of overtopping waves on sloping structures: measurements and computation. In J. M. Smith, editor, *Proceedings of the 28th International Conference on Coastal Engineering*, volume 2, pages 2239–2250, Cardiff, U.K.
- Roache, P. J. (1972). *Computational Fluid Dynamics*. Hermosa Publishers, Albuquerque.
- Roe, P. L. (1981). Approximate Riemann solvers, parameter vectors, and difference schemes. *J. Comput. Phys.*, **43**, 357–372.
- Shiach, J. B., Mingham, C. G., Ingram, D. M., and Bruce, T. (2004). The applicability of the shallow water equations for modelling violent wave overtopping. *Coastal Engineering*, **51**(1), 1–15.
- Shiach, J. B., Mingham, C. G., Ingram, D. M., Causon, D. M., Bruce, T., Pearson, J., and Allsop, N. W. H. (2005). Extended shallow water prediction of overtopping. In J. M. Smith, editor, *29th International Conference on Coastal Engineering*, volume 4, pages 4443–4455, Lisbon, Portugal. National Civil Engineering Laboratory.
- Silvester, R. (1974). *Coastal Engineering, 1: Developments in Geotechnical Engineering*, volume 4A. Elsevier Scientific Publishing Company.
- Sørensen, O. R., Schäffer, H. A., and Madsen, P. A. (1998). Surface zone dynamics simulated by a Boussinesq type model. Part III. Wave-induced horizontal nearshore circulations. *Coastal Engineering*, **33**(2), 155–176.
- Sørensen, R. M. (1993). *Basic Wave Mechanics: For Coastal Engineers*. John Wiley & Sons.

- Stelling, G. S. (1984). *On the Construction of Computational Methods for Shallow Water Flow Problems*. Ph.D. thesis, Delft University of Technology, The Netherlands.
- Stewart, R. H. (2004). *Introduction to Physical Oceanography*. Texas A & M University.
- Sverdrup, H. U. (1947). Wind-driven currents in a baroclinic ocean: with application to the equatorial currents of the eastern Pacific. In *Proceedings of the National Academy of Sciences*, pages 318–326.
- Synolakis, C. E. (1987). The runup of solitary waves. *Journal of Fluid Mechanics*, **185**, 532–545.
- Thomas, L. H. (1949). Elliptic problems in linear difference equations over a network. Technical report, Columbia University, New York.
- Toro, E. F. (1989). A weighted average flux method for hyperbolic conservation laws. In *Proc. Roy. Soc. London, Ser. A*, volume 423, pages 401–418.
- Toro, E. F. (1992). Riemann problems and the WAF method for solving two-dimensional shallow water equations. *Philosophical Transactions: Physical Sciences and Engineering*, **338**(1649), 43–68.
- Toro, E. F. (1997). *Riemann solvers and numerical methods for fluid dynamics*. Springer-Verlag.
- van der Meer, J. W. and Janssen, J. P. F. M. (1995). Wave run-up and wave overtopping at dikes. In N. Kobayashi and Z. Demirbilek, editors, *Wave Forces on Inclined and Vertical Wall Structures*, pages 1–27. ASCE, New York.
- van Gent, M. R. A. (1994). Modelling of wave action on and in coastal structures. *Coastal Engineering*, **22**, 311–339.
- van Gent, M. R. A. (1995). *Wave interaction with permeable coastal structures*. Ph.D. thesis, Delft University.
- van Leer, B. (1985). On the relation between the upwind-differencing schemes of Godunov, Engquist-Osher and Roe. *SIAM Journal of Scientific and Statistical Computing*, **5**, 1.
- Vázquez-Cendón, M. E. (1999). Improved treatment of source terms in upwind schemes for the shallow water equations in channels with irregular geometry. *Journal of Computational Physics*, **148**, 497–526.
- Walkley, M. and Berzins, M. (2002). A finite element method for the two-dimensional extended Boussinesq equations. *International Journal for Numerical Methods in Fluids*, **39**, 865–885.

- Walkley, M. A. and Berzins, M. (1999a). A finite element method for the one-dimensional extended Boussinesq equations. *International Journal for Numerical Methods in Fluids*, **29**, 143–157.
- Walkley, M. A. and Berzins, M. (1999b). *A numerical model for extended Boussinesq shallow-water wave equations*. Ph.D. thesis, The University of Leeds.
- Watts, P., Ioualalen, M., Grilli, S., Shi, F., and Kirby, J. T. (2005). Numerical simulation of the December 26, 2004 Indian Ocean tsunami using a higher-order Boussinesq model. In *Waves '05*. Fifth International Symposium on Ocean Wave Measurement and Analysis.
- Weare, T. J. (1976). Instability in tidal flow computational schemes. *Journal of the Hydraulics Division, ASCE*, **102**(5), 569–580.
- Wedge, D. C. (2006). *Wave Overtopping Prediction Using Global-Local Artificial Neural Networks*. Ph.D. thesis, Manchester Metropolitan University.
- Wei, G. and Kirby, J. T. (1995). Time-dependent numerical code for extended Boussinesq equations. *Journal of Waterway, Port, Coastal, and Ocean Engineering*, **121**(5), 251–261.
- Wei, G., Kirby, J. T., and Sinha, A. (1999). Generation of waves in Boussinesq models using a source function method. *Coastal Engineering*, **36**, 271–299.
- Weisstein, E. W. (2007). *Froude Number*. Wolfram Research, <http://scienceworld.wolfram.com/physics/FroudeNumber.html>.
- Witting, J. M. (1984). A unified model for the evolution of non-linear water waves. *J. Comput. Phys.*, **56**, 203–236.
- Wu, C., Huang, G. F., and Zheng, Y. H. (1999). Theoretical solution of dam-break shock wave. *Journal of Hydraulic Engineering, ASCE*, **125**(11), 1210 – 5.
- Yamamoto, S., Kano, S., and Daiguji, H. (1998). An efficient CFD approach for simulating unsteady hypersonic shock-shock interference flows. *Computers and Fluids*, **27**(5–6), 571–580.
- Zhao, D. H., Shen, H. W., Tabios, G. Q., Lai, J. S., and Tan, W. Y. (1994). Finite-volume two-dimensional unsteady-flow model for river basins. *Journal of Hydraulic Engineering*, **120**(7), 863–883.
- Zhao, D. H., Shen, H. W., Tabios, G. Q., and Lai, J. S. (1996). Approximate Riemann solvers in FVM for 2D hydraulic shock wave modelling. *Journal of Hydraulic Engineering*, **122**(12), 692–702.
- Zhou, J. G., Causon, D. M., Mingham, C. G., and Ingram, D. M. (2001). The surface gradient method for the treatment of source terms in the shallow water equations. *J. Comput. Phys.*, **168**, 1–25.

## Appendix A

### Validation of the Hyperbolic Nature of the SWE

A formal validation of the hyperbolic nature of the SWE is given here. This follows the validation given in Hirsch (1988). The one-dimensional form of the time-dependent SWE can be written as

$$\frac{\partial h}{\partial t} + u \frac{\partial h}{\partial x} + h \frac{\partial u}{\partial x} = 0, \quad (\text{A.1})$$

$$\frac{\partial u}{\partial t} + u \frac{\partial u}{\partial x} + g \frac{\partial h}{\partial x} = 0. \quad (\text{A.2})$$

In matrix form, Eqs. (A.1) and (A.2) can be written as

$$\frac{\partial}{\partial t} \begin{pmatrix} h \\ u \end{pmatrix} + \begin{pmatrix} u & h \\ g & u \end{pmatrix} \frac{\partial}{\partial x} \begin{pmatrix} h \\ u \end{pmatrix} = 0. \quad (\text{A.3})$$

The two characteristic velocities,  $a_{1,2}$ , are obtained from the solution of the eigenvalue problem

$$\begin{vmatrix} -a + u & h \\ g & -a + u \end{vmatrix} = 0 \quad (\text{A.4})$$

which yields

$$a_{1,2} = u \pm \sqrt{gh}. \quad (\text{A.5})$$

Since these eigenvalues are always real, the system is always hyperbolic in  $(x, t)$ .

## Appendix B

# Derivation of difference formulae

Consider the Taylor series expansions of a function  $f(x)$  for  $x \pm \Delta x$

$$f_{i+1} = f_i + \Delta x f'_i + \frac{\Delta x^2}{2!} f''_i + \frac{\Delta x^3}{3!} f^{(3)}_i + \dots + \frac{\Delta x^n}{n!} f^n_i, \quad (\text{B.1})$$

$$f_{i-1} = f_i - \Delta x f'_i + \frac{\Delta x^2}{2!} f''_i - \frac{\Delta x^3}{3!} f^{(3)}_i + \dots + (-1^n) \frac{\Delta x^n}{n!} f^n_i. \quad (\text{B.2})$$

By truncating the series after the first-order derivative and rearranging, the following finite difference approximations of the first-order derivative can be derived

$$f'_i = \frac{f_{i+1} - f_i}{\Delta x} + \mathcal{O}(\Delta x), \quad (\text{B.3})$$

$$f'_i = \frac{f_i - f_{i-1}}{\Delta x} + \mathcal{O}(\Delta x). \quad (\text{B.4})$$

Eqs. (B.3) and (B.4) are the forward and backward difference approximations of  $f'(x)$  respectively. These finite differences are first-order accurate, where  $\mathcal{O}(\Delta x)$  is the order of accuracy for the finite difference, and not the truncation error of the series. A second-order accurate finite difference can be derived by considering the central difference approximation. Subtracting Eq. (B.2) from Eq. (B.1) and rearranging gives

$$f'_i = \frac{f_{i+1} - f_{i-1}}{2\Delta x} + \mathcal{O}(\Delta x^2). \quad (\text{B.5})$$

This central difference is second-order accurate, and therefore is a more accurate approximation of  $f'(x)$  than the first-order accurate forward or backwards differences given above. It is desirable to use higher-order accurate differences when approximating derivatives although, in general, the higher the order of accuracy, the more solution nodes are required in the approximation. The central difference approximation of the second derivative can be derived by adding Eq. (B.2) to

Eq. (B.1) and rearranging to give

$$f_i'' = \frac{f_{i+1} - 2f_i + f_{i-1}}{\Delta x^2} + \mathcal{O}(\Delta x^2). \quad (\text{B.6})$$

Higher order finite differences are derived by the method of undetermined coefficients in Appendix B.1.

## B.1 Derivation of Fourth- Order Finite Difference Schemes

The derivation of the finite difference stencils used in Section 4.3 can be achieved *via* the method of undetermined coefficients. The derivation of the fourth-order central difference approximation of the first order derivative is shown here. All of the other finite difference approximations used can be derived using a similar method.

Consider a five point finite difference stencil

$$f_i^{(1)} = \frac{\alpha_1 f_{i-2} + \alpha_2 f_{i-1} + \alpha_3 f_i + \alpha_4 f_{i+1} + \alpha_5 f_{i+2}}{h}, \quad (\text{B.7})$$

where  $f_i^{(n)}$  denotes the  $n^{\text{th}}$  derivative of the variable  $f$ ,  $\alpha_i \{i = 1, 2, \dots, 5\}$  are coefficients, the values of which are to be determined; the values of  $f_k$  where  $k = i - 2, i - 1, \dots, i + 2$  are the values of the variable at the solution nodes; and  $h$  is the spatial step, i.e.,  $\Delta x$  or  $\Delta y$ . By approximating the values of  $f$  using the Taylor series truncated to fourth order accuracy, the values of  $\alpha$  can be determined.

The fourth order Taylor series expansions of  $f_{i-2}$ ,  $f_{i-1}$ ,  $f_i$ ,  $f_{i+1}$  and  $f_{i+2}$  are:

$$f_{i-2} = f_i - 2hf_i^{(1)} + 2h^2 f_i^{(2)} - \frac{4}{3}h^3 f_i^{(3)} + \frac{2}{3}h^4 f_i^{(4)} + \mathcal{O}(h^5), \quad (\text{B.8})$$

$$f_{i-1} = f_i - hf_i^{(1)} + \frac{h^2}{2} f_i^{(2)} - \frac{h^3}{6} f_i^{(3)} + \frac{h^4}{24} f_i^{(4)} + \mathcal{O}(h^5), \quad (\text{B.9})$$

$$f_i = f_i, \quad (\text{B.10})$$

$$f_{i+1} = f_i + hf_i^{(1)} + \frac{h^2}{2} f_i^{(2)} + \frac{h^3}{6} f_i^{(3)} + \frac{h^4}{24} f_i^{(4)} + \mathcal{O}(h^5), \quad (\text{B.11})$$

$$f_{i+2} = f_i + 2hf_i^{(1)} + 2h^2 f_i^{(2)} + \frac{4}{3}h^3 f_i^{(3)} + \frac{2}{3}h^4 f_i^{(4)} + \mathcal{O}(h^5). \quad (\text{B.12})$$

Substituting Eqs. (B.8)–(B.12) into Eq. (B.7) gives

$$\begin{aligned} f_i^{(1)} = & \frac{\alpha_1}{h} \left( f_i - 2hf_i^{(1)} + 2h^2f_i^{(2)} - \frac{4}{3}h^3f_i^{(3)} + \frac{2}{3}h^4f_i^{(4)} \right) \\ & + \frac{\alpha_2}{h} \left( f_i - hf_i^{(1)} + \frac{h^2}{2}f_i^{(2)} - \frac{h^3}{6}f_i^{(3)} + \frac{h^4}{24}f_i^{(4)} \right) \\ & + \frac{\alpha_3}{h}f_i + \frac{\alpha_4}{h} \left( f_i + hf_i^{(1)} + \frac{h^2}{2}f_i^{(2)} + \frac{h^3}{6}f_i^{(3)} + \frac{h^4}{24}f_i^{(4)} \right) \\ & + \frac{\alpha_5}{h} \left( f_i + 2hf_i^{(1)} + 2h^2f_i^{(2)} + \frac{4}{3}h^3f_i^{(3)} + \frac{2}{3}h^4f_i^{(4)} \right) + \mathcal{O}(h^4) \end{aligned} \quad (\text{B.13})$$

which can be rearranged to give

$$\begin{aligned} f_i^{(1)} = & (\alpha_1 + \alpha_2 + \alpha_3 + \alpha_4 + \alpha_5) \frac{f_i}{h} + (-2\alpha_1 - \alpha_2 + \alpha_4 + 2\alpha_5) f_i^{(1)} \\ & + \left( 2\alpha_1 + \frac{1}{2}\alpha_2 + \frac{1}{2}\alpha_4 + 2\alpha_5 \right) hf_i^{(2)} + \left( -\frac{4}{3}\alpha_1 - \frac{1}{6}\alpha_2 + \frac{1}{6}\alpha_4 + \frac{4}{3}\alpha_5 \right) h^2f_i^{(3)} \\ & + \left( \frac{2}{3}\alpha_1 + \frac{1}{24}\alpha_2 + \frac{1}{24}\alpha_4 + \frac{2}{3}\alpha_5 \right) h^4f_i^{(4)} + \mathcal{O}(h^4). \end{aligned} \quad (\text{B.14})$$

Writing Eq. (B.14) in the form of a matrix equation gives

$$\begin{pmatrix} 1 & 1 & 1 & 1 & 1 \\ -2 & -1 & 0 & 1 & 2 \\ 2 & 1/2 & 0 & 1/2 & 2 \\ -4/3 & -1/6 & 0 & 1/6 & 4/3 \\ 2/3 & 1/24 & 0 & 1/24 & 2/3 \end{pmatrix} \begin{pmatrix} \alpha_1 \\ \alpha_2 \\ \alpha_3 \\ \alpha_4 \\ \alpha_5 \end{pmatrix} = \begin{pmatrix} f_i/h \\ f_i^{(1)} \\ hf_i^{(2)} \\ h^2f_i^{(3)} \\ h^3f_i^{(4)} \end{pmatrix}, \quad (\text{B.15})$$

which can be solved by matrix inversion. We require the approximation of the first order derivative,  $f_i^{(1)}$ , therefore

$$\begin{pmatrix} \alpha_1 \\ \alpha_2 \\ \alpha_3 \\ \alpha_4 \\ \alpha_5 \end{pmatrix} = \begin{pmatrix} 0 & 1/12 & -1/12 & -1/2 & 1 \\ 0 & -2/3 & 4/3 & 1 & -4 \\ 1 & 0 & -5/2 & 0 & 6 \\ 0 & 2/3 & 4/3 & -1 & -4 \\ 0 & -1/12 & -1/12 & 1/2 & 1 \end{pmatrix} \begin{pmatrix} 0 \\ 1 \\ 0 \\ 0 \\ 0 \end{pmatrix}. \quad (\text{B.16})$$

Evaluation of the matrix equation in Eq. (B.16) leads to the following values for the  $\alpha$  coefficients

$$\alpha_1 = \frac{1}{12}, \quad \alpha_2 = -\frac{2}{3}, \quad \alpha_3 = 0, \quad \alpha_4 = \frac{2}{3}, \quad \alpha_5 = -\frac{1}{12}. \quad (\text{B.17})$$

Therefore the fourth-order central difference approximation of a first order derivative can be found by substituting the values of  $\alpha$  into Eq. (B.7)

$$f_i^{(1)} = \frac{f_{i-2} - 8f_{i-1} + 8f_{i+1} - f_{i+2}}{12h}. \quad (\text{B.18})$$

which is of the same form that is stated in Eq (4.27).

# Appendix C

## Wave Statistics, Run-up and Overtopping Tables

The values recorded from the experiments modelled in the main body of the text have been included here for completeness. For details of these experiments, the reader is directed to the relevant sections in the text.

### C.1 Solitary Wave Run-up on a Sloping Beach

The details of the solitary wave run-up experiments conducted by Synolakis (1987), and modelled using the hybrid scheme in Section 5.4.3, are given in Tables C.1 and C.2. The dimensionless parameters,  $H/d$  and  $R/d$ , used in Fig. 5.7 have been calculated and included here for completeness. The height of the solitary waves,  $H$ , can be calculated from  $d$  and  $H/d$ , should the reader wish to reproduce the experiments.

### C.2 Edinburgh Wave Flume Experiments: wave statistics

The significant wave heights,  $H_s$ , and the corresponding significant wave periods,  $T_m$ , for the six depth gauges recorded for the hybrid Boussinesq model described in Section 5.4.4 are presented here. The wave statistics have also been calculated for the depth gauge data from the physical experiments for direct comparison. Note that the wave statistics given in Table 3.1 are recorded at the toe of the seawall. They therefore do not provide a good description of the wave conditions due to non-linear effects of shoaling. The values of  $H_s$  and  $T_m$ , given in metres

and seconds respectively, calculated from the physical experiments are shown in Tables C.3 and C.4 respectively. The values of  $H_s$  and  $T_m$  calculated from the hybrid Boussinesq model are shown in Tables C.5 and C.6 respectively.

### C.3 Random Wave Overtopping Results

The details of the random wave overtopping experiments described in Section 5.4.5 are presented in Tables C.7 – C.9. The columns show (from left to right): the foreshore slope; the seawall slope; the water depth,  $d$ , measured from the bottom of the wave flume; the water depth at the toe of the seawall,  $d_{toe}$ ; the crest freeboard,  $R_c$ ; and the significant wave height,  $H_s$ . The overtopping values for the Kansai University experiments and the hybrid Solver model are presented in Tables C.10–C.12. The columns show (from left to right): the dimensionless freeboard,  $R^*$ ; the discharge volumes,  $Q$ ; and the dimensionless discharges,  $Q^*$ , for the Kansai data and the Hybrid Boussinesq solver respectively. All dimensions are in metres with the exception of the discharge volumes,  $Q$ , which are in cubic centimetres, the dimensionless values for the freeboard,  $R^*$ , and the overtopping volumes,  $Q^*$ . The values of  $R^*$  and  $Q^*$  are calculated using the following:

$$R^* = \frac{R_c}{H_s}, \quad (C.1)$$

$$Q^* = \frac{Q}{\sqrt{gH_s^3}}, \quad (C.2)$$

where  $Q$  is the discharge volume in cubic metres and  $g = 9.81 \text{ ms}^{-2}$  is the acceleration due to gravity.

Table C.1: Solitary wave run-up on a sloping beach: comparisons of run-up values.

$d$ (m)	$H/d$	Synolakis		Hybrid	
		$R$ (m)	$R/d$	$R$ (m)	$R/d$
0.0625	0.2500	0.0316	0.5060	0.0270	0.4326
0.0625	0.0720	0.0146	0.2330	0.0169	0.2711
0.0801	0.4480	0.0579	0.7230	0.0472	0.5893
0.0979	0.0780	0.0246	0.2510	0.0294	0.3004
0.0979	0.3840	0.0608	0.6210	0.0571	0.5834
0.0981	0.0970	0.0269	0.2740	0.0342	0.3491
0.0984	0.4620	0.0648	0.6590	0.0616	0.6265
0.0989	0.2360	0.0462	0.4670	0.0486	0.4911
0.1567	0.0900	0.0423	0.2700	0.0487	0.3107
0.1572	0.2590	0.0816	0.5190	0.0860	0.5469
0.1562	0.2980	0.0861	0.5510	0.0945	0.6052
0.1565	0.3220	0.0925	0.5910	0.0892	0.5699
0.1569	0.1700	0.0639	0.4070	0.0686	0.4375
0.1670	0.2730	0.0813	0.4870	0.0787	0.4712
0.2085	0.0360	0.0259	0.1240	0.0322	0.1542
0.2092	0.1880	0.0856	0.4090	0.0793	0.3791
0.2101	0.1590	0.0807	0.3840	0.0860	0.4094
0.2144	0.1600	0.0823	0.3840	0.0691	0.3222
0.2208	0.0360	0.0267	0.1210	0.0375	0.1698
0.2400	0.0480	0.0437	0.1820	0.0485	0.2021
0.2843	0.0390	0.0432	0.1520	0.0470	0.1655
0.2855	0.0400	0.0445	0.1560	0.0484	0.1694
0.2914	0.0210	0.0221	0.0760	0.0299	0.1025
0.2934	0.0140	0.0144	0.0490	0.0203	0.0692
0.2935	0.0510	0.0561	0.1910	0.0580	0.1976
0.2940	0.0750	0.0759	0.2580	0.0777	0.2643
0.2954	0.0730	0.0733	0.2480	0.0763	0.2583
0.2962	0.0650	0.0675	0.2280	0.0780	0.2633

Table C.2: Solitary wave run-up on a sloping beach: comparisons of run-up values.

$d$ (m)	$H/d$	Synolakis		Hybrid	
		$R$ (m)	$R/d$	$R$ (m)	$R/d$
0.2963	0.0550	0.0613	0.2070	0.0627	0.2118
0.2972	0.0560	0.0615	0.2070	0.0644	0.2166
0.2973	0.0340	0.0428	0.1440	0.0411	0.1384
0.2975	0.0180	0.0220	0.0740	0.0263	0.0883
0.2977	0.0090	0.0107	0.0360	0.0135	0.0453
0.9800	0.0180	0.0735	0.0750	0.1013	0.1034
0.2983	0.0270	0.0322	0.1080	0.0381	0.1276
0.2986	0.0380	0.0436	0.1460	0.0479	0.1603
0.3000	0.0470	0.0585	0.1950	0.0565	0.1884
0.3048	0.0470	0.0594	0.1950	0.0568	0.1862
0.3097	0.0190	0.0242	0.0780	0.0267	0.0863
0.3106	0.0190	0.0236	0.0760	0.0283	0.0911
0.3331	0.0090	0.0137	0.0410	0.0133	0.0401
0.3352	0.0050	0.0064	0.0190	0.0063	0.0187
0.3355	0.0060	0.0074	0.0220	0.0084	0.0251
0.3361	0.0070	0.0087	0.0260	0.0103	0.0308
0.3365	0.0280	0.0414	0.1230	0.0427	0.1269
0.3365	0.0080	0.0098	0.0290	0.0125	0.0370
0.3376	0.0230	0.0294	0.0870	0.0366	0.1083
0.3384	0.0170	0.0213	0.0630	0.0258	0.0761
0.3404	0.0240	0.0334	0.0980	0.0388	0.1140
0.3452	0.0120	0.0166	0.0480	0.0188	0.0546
0.3429	0.0140	0.0178	0.0520	0.0212	0.0619
0.3439	0.0090	0.0124	0.0360	0.0127	0.0369
0.3797	0.0440	0.0691	0.1820	0.0675	0.1778
0.3799	0.0220	0.0372	0.0980	0.0372	0.0978
0.3832	0.0390	0.0621	0.1620	0.0615	0.1604

Table C.3: Edinburgh wave flume experiments: experimental  $H_s$ 

Run	Distance of gauge from seawall (m)					
	8.00	5.50	4.25	3.00	2.00	1.00
1	0.0768	0.0750	0.0758	0.0679	0.0698	0.0727
2	0.1104	0.1078	0.1091	0.0988	0.1006	0.1046
3	0.0925	0.0904	0.0912	0.0815	0.0837	0.0869
4	0.0554	0.0545	0.0551	0.0481	0.0499	0.0526
5	0.0700	0.0684	0.0692	0.0613	0.0635	0.0663
6	0.0882	0.0864	0.0885	0.1075	0.0904	0.0809
7	0.1147	0.1115	0.1135	0.1417	0.1150	0.1036
8	0.0741	0.0725	0.0744	0.0877	0.0768	0.0676
9	0.0585	0.0571	0.0583	0.0674	0.0608	0.0532
10	0.0986	0.0963	0.0986	0.1192	0.1001	0.0888
11	0.0909	0.0895	0.0895	0.0853	0.0809	0.0852
12	0.0827	0.0814	0.0812	0.0780	0.0736	0.0777
13	0.1054	0.1038	0.1030	0.0953	0.0933	0.0973
14	0.1153	0.1129	0.1128	0.1014	0.1010	0.1051
15	0.0984	0.0971	0.0968	0.0907	0.0880	0.0925

Table C.4: Edinburgh wave flume experiments: experimental  $T_m$ 

Run	Distance of gauge from seawall (m)					
	8.00	5.50	4.25	3.00	2.00	1.00
1	1.2446	1.2364	1.2245	1.2302	1.2343	1.2391
2	1.2499	1.2578	1.2593	1.3042	1.2727	1.2694
3	1.2426	1.2371	1.2376	1.2422	1.2607	1.2364
4	1.2338	1.2322	1.2129	1.1725	1.2142	1.2222
5	1.2390	1.2304	1.2207	1.2004	1.2241	1.2238
6	1.4456	1.4658	1.4554	1.5475	1.4787	1.3990
7	1.4859	1.5075	1.4833	1.5620	1.5017	1.4491
8	1.4412	1.4350	1.4343	1.5628	1.4691	1.3836
9	1.4584	1.4191	1.4330	1.5635	1.4717	1.3706
10	1.4653	1.4841	1.4682	1.5657	1.4842	1.4110
11	0.9738	0.9738	0.9715	0.9625	0.9911	0.9717
12	0.9574	0.9696	0.9708	0.9566	0.9756	0.9649
13	0.9772	0.9925	0.9912	0.9799	1.0107	0.9971
14	0.9866	0.9982	0.9975	0.9889	1.0164	1.0083
15	0.9755	0.9844	0.9817	0.9703	1.0055	0.9858

Table C.5: Edinburgh wave flume experiments: Hybrid  $H_s$ 

Run	Distance of gauge from seawall (m)					
	8.00	5.50	4.25	3.00	2.00	1.00
1	0.0821	0.0737	0.0807	0.0606	0.0611	0.0660
2	0.1167	0.1034	0.1143	0.0892	0.0895	0.0940
3	0.0982	0.0870	0.0963	0.0750	0.0748	0.0794
4	0.0604	0.0533	0.0592	0.0445	0.0449	0.0481
5	0.0748	0.0662	0.0735	0.0571	0.0567	0.0607
6	0.0868	0.0774	0.0835	0.1005	0.0866	0.0707
7	0.1101	0.0987	0.1041	0.1298	0.1017	0.0859
8	0.0719	0.0649	0.0695	0.0849	0.0730	0.0594
9	0.0587	0.0533	0.0563	0.0713	0.0592	0.0464
10	0.0993	0.0889	0.0943	0.1152	0.0948	0.0782
11	0.0776	0.0591	0.0699	0.0392	0.0459	0.0494
12	0.0687	0.0544	0.0630	0.0369	0.0410	0.0451
13	0.0917	0.0703	0.0835	0.0456	0.0536	0.0576
14	0.0986	0.0761	0.0898	0.0476	0.0579	0.0613
15	0.0736	0.0571	0.0660	0.0377	0.0433	0.0474

Table C.6: Edinburgh wave flume experiments: Hybrid  $T_m$ 

Run	Distance of gauge from seawall (m)					
	8.00	5.50	4.25	3.00	2.00	1.00
1	1.2995	1.3416	1.3181	1.6316	1.5673	1.4411
2	1.3044	1.3211	1.3405	1.5418	1.4431	1.3806
3	1.3303	1.3549	1.3177	1.5877	1.4757	1.4031
4	1.3230	1.3737	1.3097	1.5123	1.5658	1.4359
5	1.3198	1.3489	1.3018	1.4967	1.4828	1.3983
6	1.5194	1.6509	1.6219	1.6831	1.6511	1.6482
7	1.5429	1.6326	1.4877	1.6790	1.6539	1.5247
8	1.5471	1.6856	1.6858	1.6799	1.6154	1.7125
9	1.5381	1.5684	1.5529	1.6614	1.6039	1.5911
10	1.5167	1.5626	1.5352	1.6645	1.6140	1.5374
11	1.0407	1.0836	1.0832	1.2812	1.1977	1.1638
12	1.0540	1.1692	1.1225	1.8693	1.3440	1.2638
13	1.0536	1.0843	1.0763	1.3165	1.1620	1.1384
14	1.0588	1.0910	1.0797	1.2422	1.1460	1.1416
15	1.0325	1.1394	1.0797	1.6975	1.3127	1.2162

Table C.7: Random wave overtopping: experimental setup.

Run Number	Foreshore	Seawall	$d$	$d_{toe}$	$R_c$	$H_s$
1	1:10	1:10	0.32	0.0000	0.0625	0.0625
2	1:10	1:10	0.30	0.0000	0.0625	0.0625
3	1:10	1:10	0.31	0.0000	0.0150	0.0200
4	1:10	1:10	0.31	0.0000	0.0150	0.0300
5	1:10	1:10	0.31	0.0000	0.0150	0.0312
6	1:10	1:10	0.31	0.0000	0.0150	0.0400
7	1:10	1:10	0.31	0.0000	0.0150	0.0450
8	1:10	1:10	0.31	0.0000	0.0150	0.0468
9	1:10	1:10	0.31	0.0000	0.0150	0.0625
10	1:10	1:10	0.31	0.0000	0.0150	0.0674
11	1:10	1:10	0.31	0.0000	0.0150	0.0899
12	1:30	1:7	0.40	0.3326	0.0050	0.0156
13	1:30	1:7	0.40	0.3326	0.0050	0.0312
14	1:30	1:7	0.40	0.3326	0.0050	0.0468
15	1:30	1:7	0.40	0.3326	0.0050	0.0625
16	1:30	1:7	0.40	0.3326	0.0050	0.0781
17	1:30	1:7	0.37	0.3029	0.0350	0.0156
18	1:30	1:7	0.37	0.3029	0.0350	0.0312
19	1:30	1:7	0.37	0.3029	0.0350	0.0468
20	1:30	1:7	0.37	0.3029	0.0350	0.0625
21	1:30	1:7	0.37	0.3029	0.0350	0.0781
22	1:30	1:7	0.39	0.3232	0.0150	0.0156
23	1:30	1:7	0.39	0.3232	0.0150	0.0312
24	1:30	1:7	0.39	0.3232	0.0150	0.0468
25	1:30	1:7	0.39	0.3232	0.0150	0.0625
26	1:30	1:7	0.39	0.3232	0.0150	0.0781
27	1:30	1:7	0.38	0.3138	0.0250	0.0156
28	1:30	1:7	0.38	0.3138	0.0250	0.0312
29	1:30	1:7	0.38	0.3138	0.0250	0.0468
30	1:30	1:7	0.38	0.3138	0.0250	0.0625
31	1:30	1:7	0.38	0.3138	0.0250	0.0781

Table C.8: Random wave overtopping: experimental setup.

Run Number	Foreshore	Seawall	$d$	$d_{toe}$	$R_c$	$H_s$
32	1:30	1:5	0.40	0.3326	0.0050	0.0156
33	1:30	1:5	0.40	0.3326	0.0050	0.0312
34	1:30	1:5	0.40	0.3326	0.0050	0.0468
35	1:30	1:5	0.40	0.3326	0.0050	0.0625
36	1:30	1:5	0.40	0.3326	0.0050	0.0781
37	1:30	1:5	0.37	0.3029	0.0350	0.0156
38	1:30	1:5	0.37	0.3029	0.0350	0.0312
39	1:30	1:5	0.37	0.3029	0.0350	0.0468
40	1:30	1:5	0.37	0.3029	0.0350	0.0625
41	1:30	1:5	0.37	0.3029	0.0350	0.0781
42	1:30	1:5	0.39	0.3232	0.0150	0.0156
43	1:30	1:5	0.39	0.3232	0.0150	0.0312
44	1:30	1:5	0.39	0.3232	0.0150	0.0468
45	1:30	1:5	0.39	0.3232	0.0150	0.0625
46	1:30	1:5	0.39	0.3232	0.0150	0.0781
47	1:30	1:5	0.38	0.3138	0.0250	0.0156
48	1:30	1:5	0.38	0.3138	0.0250	0.0312
49	1:30	1:5	0.38	0.3138	0.0250	0.0468
50	1:30	1:5	0.38	0.3138	0.0250	0.0625
51	1:30	1:5	0.38	0.3138	0.0250	0.0781
52	1:30	1:3	0.40	0.3326	0.0050	0.0156
53	1:30	1:3	0.40	0.3326	0.0050	0.0312
54	1:30	1:3	0.40	0.3326	0.0050	0.0468
55	1:30	1:3	0.37	0.3029	0.0350	0.0156
56	1:30	1:3	0.37	0.3029	0.0350	0.0312
57	1:30	1:3	0.37	0.3029	0.0350	0.0468
58	1:30	1:3	0.39	0.3232	0.0150	0.0156
59	1:30	1:3	0.39	0.3232	0.0150	0.0312
60	1:30	1:3	0.39	0.3232	0.0150	0.0468
61	1:30	1:3	0.38	0.3138	0.0250	0.0156
62	1:30	1:3	0.38	0.3138	0.0250	0.0312
63	1:30	1:3	0.38	0.3138	0.0250	0.0468

Table C.9: Random wave overtopping: experimental setup.

Run Number	Foreshore	Seawall	$d$	$d_{toe}$	$R_c$	$H_s$
64	1:30	1:4/3	0.40	0.3326	0.0050	0.0156
65	1:30	1:4/3	0.40	0.3326	0.0050	0.0312
66	1:30	1:4/3	0.40	0.3326	0.0050	0.0468
67	1:30	1:4/3	0.40	0.3326	0.0050	0.0625
68	1:30	1:4/3	0.40	0.3326	0.0050	0.0781
69	1:30	1:4/3	0.37	0.3029	0.0350	0.0156
70	1:30	1:4/3	0.37	0.3029	0.0350	0.0312
71	1:30	1:4/3	0.37	0.3029	0.0350	0.0468
72	1:30	1:4/3	0.37	0.3029	0.0350	0.0625
73	1:30	1:4/3	0.37	0.3029	0.0350	0.0781
74	1:30	1:4/3	0.39	0.3232	0.0150	0.0156
75	1:30	1:4/3	0.39	0.3232	0.0150	0.0312
76	1:30	1:4/3	0.39	0.3232	0.0150	0.0468
77	1:30	1:4/3	0.39	0.3232	0.0150	0.0625
78	1:30	1:4/3	0.39	0.3232	0.0150	0.0781
79	1:30	1:4/3	0.38	0.3138	0.0250	0.0156
80	1:30	1:4/3	0.38	0.3138	0.0250	0.0312
81	1:30	1:4/3	0.38	0.3138	0.0250	0.0468
82	1:30	1:4/3	0.38	0.3138	0.0250	0.0625
83	1:30	1:4/3	0.38	0.3138	0.0250	0.0781

Table C.10: Random wave overtopping: overtopping values.

Run number	$R^*$	Kansai		Hybrid Solver	
		$Q$	$Q^*$	$Q$	$Q^*$
1	1.0000	41.46	0.0008	0.00	0.0000
2	1.0000	8.29	0.0002	0.00	0.0000
3	0.7506	553.04	0.0625	294.92	0.0333
4	0.5004	2119.85	0.1304	771.08	0.0474
5	0.4804	2958.72	0.1712	1653.33	0.0957
6	0.3753	4451.61	0.1779	2530.25	0.1011
7	0.3336	7175.73	0.2403	4492.20	0.1504
8	0.3202	5471.88	0.1723	4930.88	0.1553
9	0.2402	8708.11	0.1781	8275.60	0.1693
10	0.2224	14680.15	0.2676	9466.39	0.1725
11	0.1668	23777.47	0.2815	14600.76	0.1729
12	0.3197	1761.94	0.2884	2606.93	0.4266
13	0.1599	6449.27	0.3732	8133.23	0.4706
14	0.1066	12386.62	0.3901	14701.92	0.4630
15	0.0799	16583.00	0.3392	21731.32	0.4446
16	0.0639	23175.44	0.3392	28350.39	0.4150
17	2.2417	0.00	0.0000	0.00	0.0000
18	1.1209	49.84	0.0029	0.00	0.0000
19	0.7472	333.90	0.0105	191.88	0.0060
20	0.5604	1160.81	0.0237	1202.18	0.0246
21	0.4483	1854.04	0.0271	2990.97	0.0438
22	0.9592	342.02	0.0560	46.90	0.0077
23	0.4796	1758.89	0.1018	2368.68	0.1371
24	0.3197	4846.94	0.1527	6851.69	0.2158
25	0.2398	7462.35	0.1527	12353.62	0.2527
26	0.1918	11587.72	0.1696	17777.09	0.2602
27	1.5987	10.36	0.0017	0.00	0.0000
28	0.7993	381.09	0.0221	493.00	0.0285
29	0.5329	1077.10	0.0339	2577.42	0.0812
30	0.3997	2736.19	0.0560	5739.66	0.1174
31	0.3197	5793.86	0.0848	9953.26	0.1457

Table C.11: Random wave overtopping: overtopping values.

Run number	Kansai			Hybrid Solver	
	$R^*$	$Q$	$Q^*$	$Q$	$Q^*$
32	0.3197	2072.87	0.3392	3468.09	0.5676
33	0.1599	6449.27	0.3732	10419.65	0.6029
34	0.1066	12386.62	0.3901	18184.64	0.5727
35	0.0799	17412.14	0.3562	26430.36	0.5407
36	0.0639	26651.76	0.3901	34759.84	0.5088
37	2.2417	0.00	0.0000	0.00	0.0000
38	1.1209	205.20	0.0119	233.44	0.0135
39	0.7472	915.53	0.0288	2056.32	0.0648
40	0.5604	2487.45	0.0509	5337.73	0.1092
41	0.4483	4635.09	0.0678	9421.95	0.1379
42	0.9592	331.66	0.0543	446.68	0.0731
43	0.4796	2638.34	0.1527	4401.41	0.2547
44	0.3197	6462.58	0.2035	10524.43	0.3315
45	0.2398	11608.10	0.2375	17256.57	0.3530
46	0.1918	15064.04	0.2205	24070.08	0.3523
47	1.5987	72.55	0.0119	25.15	0.0041
48	0.7993	586.30	0.0339	1573.86	0.0911
49	0.5329	2154.19	0.0678	5220.38	0.1644
50	0.3997	4974.90	0.1018	9842.39	0.2013
51	0.3197	10428.95	0.1527	14810.81	0.2168
52	0.3197	2280.16	0.3732	3685.61	0.6032
53	0.1599	8208.16	0.4749	11548.08	0.6682
54	0.1066	12925.17	0.4071	20556.86	0.6475
55	2.2417	0.00	0.0000	0.00	0.0000
56	1.1209	175.89	0.0102	808.67	0.0468
57	0.7472	1184.81	0.0373	3988.87	0.1256
58	0.9592	310.93	0.0509	747.55	0.1223
59	0.4796	2902.17	0.1679	5416.47	0.3134
60	0.3197	7001.13	0.2205	12787.50	0.4028
61	1.5987	29.02	0.0047	45.69	0.0075
62	0.7993	938.08	0.0543	2276.26	0.1317
63	0.5329	3769.84	0.1187	7495.27	0.2361

Table C.12: Random wave overtopping: overtopping values.

Run number	$R^*$	Kansai		Hybrid Solver	
		$Q$	$Q^*$	$Q$	$Q^*$
64	0.3197	1554.66	0.2544	3232.68	0.5290
65	0.1599	8208.16	0.4749	11043.91	0.6390
66	0.1066	16695.01	0.5258	20153.69	0.6348
67	0.0799	0.00	0.0000	0.00	0.0000
68	0.0639	0.00	0.0000	0.00	0.0000
69	2.2417	4.15	0.0007	0.00	0.0000
70	1.1209	469.04	0.0271	655.18	0.0379
71	0.7472	2854.31	0.0899	3250.32	0.1024
72	0.5604	6633.20	0.1357	7596.56	0.1554
73	0.4483	11587.72	0.1696	14139.44	0.2070
74	0.9592	621.86	0.1018	532.16	0.0871
75	0.4796	4104.08	0.2375	5008.02	0.2898
76	0.3197	9693.87	0.3053	11706.81	0.3687
77	0.2398	14924.70	0.3053	20473.63	0.4188
78	0.1918	28969.30	0.4240	29804.98	0.4363
79	1.5987	5.49	0.0009	45.12	0.0074
80	0.7993	1700.26	0.0984	2097.25	0.1213
81	0.5329	5385.49	0.1696	6856.24	0.2159
82	0.3997	10778.95	0.2205	15920.26	0.3257
83	0.3197	19699.12	0.2884	20256.20	0.2965

# Appendix D

## Published Papers

During the completion of this study two refereed papers were produced and are included here.

1. Shiach, J., Mingham, C., Ingram, D., and Bruce, T. (2004). The applicability of the shallow water equations for modelling violent wave overtopping. *Coastal Engineering*, **51**, 1–15.
2. Shiach, J., Mingham, C., Ingram, D., Causon, D., Bruce, T., Pearson, J., and Allsop, N. (2005). Extended shallow water prediction of overtopping. In J. Smith, editor, *29th International Conference on Coastal Engineering*, Lisbon, Portugal. National Civil Engineering Laboratory.



Available online at [www.sciencedirect.com](http://www.sciencedirect.com)



Coastal Engineering 51 (2004) 1–15

## Coastal Engineering

An International Journal for Coastal,  
Harbour and Offshore Engineers

[www.elsevier.com/locate/coastaleng](http://www.elsevier.com/locate/coastaleng)

# The applicability of the shallow water equations for modelling violent wave overtopping

J.B. Shiach<sup>a,\*</sup>, C.G. Mingham<sup>a</sup>, D.M. Ingram<sup>a</sup>, T. Bruce<sup>b</sup>

<sup>a</sup>Centre for Mathematical Modelling and Flow Analysis, Manchester Metropolitan University, Chester Street, Manchester M1 5GD, UK  
<sup>b</sup>School of Engineering and Electronics, The University of Edinburgh, Kings Buildings, Mayfield Road, Edinburgh EH9 3JL, UK

Received 26 March 2003; received in revised form 1 October 2003; accepted 4 November 2003

## Abstract

The shallow water equations (SWE) have been used to model a series of experiments examining violent wave overtopping of a near-vertical sloping structure with impacting wave conditions. A finite volume scheme was used to solve the shallow water equations. A monotonic reconstruction method was applied to eliminate spurious oscillations and ensure proper treatment of bed slope terms. Both the numerical results and physical observations of the water surface closely followed the relevant Rayleigh probability distributions. However, the numerical model overestimated the wave heights and suffered from the lack of dispersion within the shallow water equations. Comparisons made on dimensionless parameters for the overtopping discharge and percentage of waves overtopping between the numerical model and the experimental observations indicated that for the lesser impacting waves, the shallow water equations perform satisfactorily and provide a good alternative to computationally more expensive methods.

© 2004 Elsevier B.V. All rights reserved.

**Keywords:** Violent wave overtopping; Shallow water equations; Finite volume method; Surface gradient method

## 1. Introduction

Violent wave overtopping occurs when waves break against sea walls, throwing water up and over the top. Of the hundreds of kilometres of coastal defences in Britain, a significant proportion have roads, railways and footpaths running alongside. Violent overtopping events have been known to wash

people, cars and trains into the sea and represent a threat to human life and property.

Wave overtopping has been studied extensively over the past 30 years. Goda et al. (1975), Owen (1982) and Franco et al. (1994) all present data and guidance on overtopping volumes for a variety of sloping and vertical structures. Owen and Franco et al. focus primarily upon cases where waves do not break (pulsating or nonimpulsive conditions). While Goda's data includes violent or impulsive conditions, these are not treated separately. Besley et al. (1998) and Pearson et al. (2001) have used observations from either physical models or field data to gain a greater understanding of violent, impulsive overtopping.

\* Corresponding author. Tel.: +44-161-247-1515; fax: +44-161-247-1483.

E-mail address: [j.shiach@mmu.ac.uk](mailto:j.shiach@mmu.ac.uk) (J.B. Shiach).

Guidance on mean and wave-on-wave overtopping volumes under violent conditions is now established, but for simple structures and standard sea spectra only.

Violent overtopping events are difficult to model using current numerical methods. Ideally, the use of the well-known Navier–Stokes equations would provide a good model of the overtopping events. However, numerical solvers for these equations require extensive computational resources, and until computers are developed that can allow for a model based on the Navier–Stokes equations to be practical, an alternative method is required.

A depth-averaged formulation of the Navier–Stokes equations exists in the shallow water equations (SWE). As the SWE are depth averaged, any vertical velocity is neglected. Thus, these equations, in theory, may not be suitable as a basis for a numerical model for violent wave overtopping where vertical velocities are a major feature. However, SWE models are easy to implement and computationally efficient. Therefore, before discarding them altogether, an analysis of the limitations of the SWE model is required.

Existing models that make use of the SWE to model wave runup and overtopping include ODI-FLOCS (van Gent, 1994, 1995) and ANEMONE (Dodd, 1998). These models have been used to give predictions of wave runup and overtopping of sea dikes where wave conditions are less impacting and violent overtopping is less likely to occur.

This paper examines the validity of a numerical model based on the SWE to model violent wave overtopping of sea walls.

## 2. Numerical model

The shallow water equations (SWE) in one dimension can be expressed as

$$\frac{\partial}{\partial t} \mathbf{U} + \frac{\partial}{\partial x} \mathbf{F}(\mathbf{U}) = \mathbf{S} \quad (1)$$

where

$$\mathbf{U} = \begin{pmatrix} \phi \\ \phi u \end{pmatrix}, \quad \mathbf{F}(\mathbf{U}) = \begin{pmatrix} \phi u \\ \phi u^2 + \frac{1}{2} \phi^2 \end{pmatrix},$$

$$\mathbf{S} = \begin{pmatrix} 0 \\ g\phi \partial H/\partial x \end{pmatrix}, \quad (2)$$

and  $\phi = gh$  is the geopotential;  $h$  is the water depth;  $g = 9.81 \text{ m s}^{-2}$  is the acceleration due to gravity;  $u$  is the depth average velocity in the  $x$ -direction, and  $H$  is the distance between a fixed reference level and the bed surface elevation (see Fig. 1). In this form,  $\mathbf{U}$  represents the vector of conserved variables,  $\mathbf{F}(\mathbf{U})$  the flux vector function, and  $\mathbf{S}$  is the vector of source terms.

The SWE are a hyperbolic system of partial differential equations that can admit discontinuities into the solution. These can be difficult to model as spurious oscillations created by the numerical scheme around the area of the discontinuity tend to contaminate the solution and eventually render any results worthless. Therefore, for a scheme to be considered applicable when solving the SWE, it must be able to satisfactorily deal with discontinuous behaviour. The

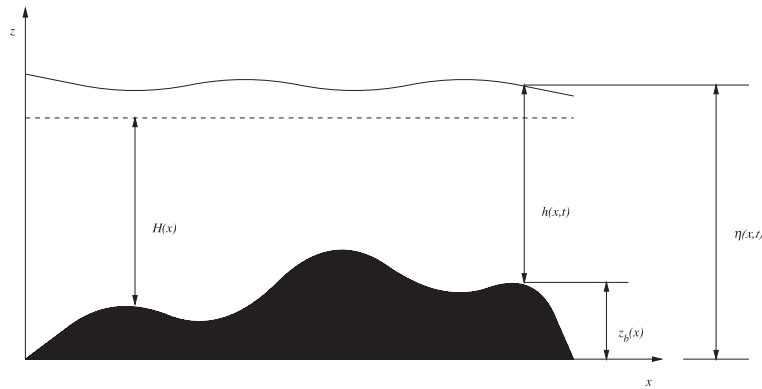


Fig. 1. Definition sketch for bed topography.

MUSCL–Hancock finite volume scheme (van Leer, 1985) has been chosen by the authors as it has been extensively tested over a range of demanding test cases (Mingham and Causon, 1998; Hu et al. 2000) and performed admirably in all. The scheme is a high-resolution Godunov-type scheme incorporating the HLL Riemann solver (Harten et al. 1983) to provide solutions to the local Riemann problems at the cell interfaces.

### 2.1. The MUSCL–Hancock scheme

The MUSCL–Hancock scheme is a two-stage predictor–corrector method. The predictor stage is given as

$$\mathbf{U}_{ij}^{n+1/2} = \mathbf{U}_{ij}^n - \frac{\Delta t}{2A} \left( \sum_{m=1}^M \mathbf{F}(\mathbf{U}_m) \cdot \mathbf{L}_m - A\mathbf{S}_{ij}^n \right), \quad (3)$$

where  $n$  is the time step counter;  $ij$  is the cell index;  $\Delta t$  is the step;  $A$  is the cell area;  $\mathbf{L}_m$  is the cell side vector defined as the cell side multiplied by the outward pointing unit normal vector;  $M$  is the number of sides of the cell  $ij$ . The fluxes at the cell interfaces  $m$  ( $\mathbf{F}(\mathbf{U}_m)$ ) are calculated using slope limited gradients based upon neighbouring cell data (Section 2.1.1).

The corrector stage provides a fully conservative solution over one time step and is given as

$$\mathbf{U}_{ij}^{n+1} = \mathbf{U}_{ij}^n - \frac{\Delta t}{A} \left( \sum_{m=1}^M \mathbf{F}(\mathbf{U}_m^L, \mathbf{U}_m^R)^{n+1/2} \cdot \mathbf{L}_m - A\mathbf{S}_{ij}^{n+1/2} \right), \quad (4)$$

where the flux vector  $\mathbf{F}(\mathbf{U}_m^L, \mathbf{U}_m^R)$  are the solutions to the local Riemann problems at each time step calculated using the HLL approximate Riemann solver (see Section 2.1.2).  $\mathbf{U}_m^L$  and  $\mathbf{U}_m^R$  are the conserved variables at the left and right side of each cell interface, respectively.

A full description and extensive validation of the MUSCL–Hancock scheme can be found in Mingham and Causon (1998).

#### 2.1.1. MUSCL reconstruction

MUSCL (Monotonic Upwind Schemes for Conservation Laws) schemes use the values of the con-

served variables at the cells immediately adjacent to the cell  $i$  to calculate a slope-limited gradient which ensures that there is no over/undershoots at the cell interfaces,  $(i \pm 1/2)$  (Toro, 1997). Here, the authors have used the well-known van Leer slope limiter function which is given in Hirsch (1998).

The values of the conserved variables  $\phi$  and  $\phi u$  can be found at the cell interfaces by using linear interpolation. For example, the values of the geo-potential at the left- and right-hand side of the cell interface  $(i - 1/2)$  are

$$\begin{aligned} \phi_{i-1/2}^L &= \phi_{i-1} + \frac{1}{2} \Delta x_{i-1} \delta\phi_{i-1}, \\ \phi_{i-1/2}^R &= \phi_i - \frac{1}{2} \Delta x_i \delta\phi_i, \end{aligned} \quad (5)$$

where  $\delta\phi_i$  are the slope limited gradients of  $\phi_i$  and

$$\Delta x_i = x_{i+1/2} - x_{i-1/2}. \quad (6)$$

#### 2.1.2. HLL approximate Riemann solver

The corrector stage of the Hancock scheme requires the solution to a local Riemann problem at every cell interface. The Riemann solver used here was developed by Harten et al. (1983) (HLL) and has shown to be accurate and robust in practice (Mingham and Causon, 1998) and considerably less computationally expensive than an exact Riemann solver. The wave speed calculations used here can be found in Davis (1988) for a wet bed and Fraccarollo and Toro (1995) for a dry bed.

#### 2.1.3. Time step calculation

To ensure that the time marching scheme remains stable, a maximum allowable time step calculation based upon the stability condition developed by Courant, Friedrichs and Lewy (CFL) is applied (Morton and Mayers, 1994). The time step  $\Delta t$  is given by

$$\Delta t = v \min_i \left( \frac{\Delta x_i}{|u_i| + \sqrt{\phi_i}} \right), \quad (7)$$

where  $v$  is the Courant number ( $0 < v \leq 1$ ). For all numerical solutions presented here, a Courant number

of  $\nu=0.65$  was used throughout to ensure scheme stability.

## 2.2. The surface gradient method

The numerical scheme presented in Section 2.1 solves the homogeneous form of the SWE where applications are mainly limited to flat-bed shock and bore wave propagation problems. However, the inclusion of the source terms that model bed topography ensure more realistic formulations applicable to problems such as wave runup and overtopping on a sloping beach and tidal flows in coastal water regions. It has been found that for a conservative scheme a naïve numerical treatment of source terms may lead to nonphysical behaviour of the fluid (Leveque, 1998).

The numerical treatment of source terms has received particular attention in the last few years with a variety of different methods proposed. Garcia-Navarro and Vázquez-Cendón (2000) proposed an upwind scheme which uses an extension of the formulation of Roe's scheme. Another approach was proposed by Hu et al. (2000), in which the authors used the MUSCL–Hancock scheme to solve the inviscid SWE along with an ODE solver (Euler) for the treatment of the source terms. Both of the methods described above performed well on standard test cases. However, they did suffer from being overly complicated. Zhou et al. (2001) developed a Surface Gradient Method (SGM) to deal with the treatment of the source terms that requires very few alterations to the MUSCL–Hancock scheme. The SGM was shown to give excellent agreement with known solutions to standard test cases chosen to examine the scheme's ability to model both transcritical flow and steady-state problems.

Traditional MUSCL schemes use the conserved variables  $\phi$  and  $\phi u$  to approximate the fluxes at the cell interfaces such as

$$\begin{aligned}\phi_{i\pm 1/2} &= \phi_i \pm \frac{1}{2} \Delta x_i \delta \phi_i, \\ (\phi u)_{i\pm 1/2} &= (\phi u)_i \pm \frac{1}{2} \Delta x_i \delta(\phi u)_i,\end{aligned}\quad (8)$$

where  $i \pm 1/2$  are the cell interfaces;  $\Delta x$  is the cell width and  $\delta \phi_i$  and  $\delta(\phi u)_i$  are the slope-limited gradients across cell  $i$ . The SGM approach uses the water

surface elevation as the basis for the MUSCL reconstruction instead of the geopotential. The water surface elevation,  $\eta_i$ , is defined by

$$\eta_i = h_i + z_{bi}, \quad (9)$$

where  $h_i$  and  $z_{bi}$  are the water height and bed surface elevation, respectively (Fig. 1). The reconstruction process is then applied by using

$$\phi_{i\pm 1/2} = g \left( \eta_i \pm \frac{1}{2} \Delta x_i \delta \eta_i - z_{bi \pm 1/2} \right) \quad (10)$$

This approach ensures that any errors that are caused by the difference between the gradient of the water height,  $h(x,t)$ , and the gradient of the bed slope,  $z_b(x)$ , do not affect the solution. The SGM is fully conservative so long as a centred discretisation of the source terms is used. When using the SGM, the bed surface elevation,  $z_{bi}$  is calculated by averaging the bed elevation at the cell interfaces.

A full description of the SGM together with a formal proof of the conservative properties and validation can be found in Zhou et al. (2001).

## 3. Violent wave overtopping

The more violent impact of water waves on sea walls cause velocities and pressures much larger than those associated with the wave's propagation under gravity (Peregrine, 2002), and it is under these conditions that violent wave overtopping can occur. A study into violent wave overtopping was the focus of the VOWS (Violent Overtopping by Waves at Sea walls) project funded by the EPSRC (Engineering and Physical Sciences Research Council). As part of the VOWS project, physical model tests of violent wave overtopping were carried out in a wave channel at the University of Edinburgh.

Allsop et al. (1995) developed a parameter ( $h^*$ ) that measures the type of wave interaction (and therefore, the type of overtopping) with vertical walls. The  $h^*$  parameter is given as

$$h^* = \frac{h}{H_s} \left( \frac{2\pi h}{g T_m^2} \right), \quad (11)$$

where  $h$  is the wave height at the toe of the structure;  $H_s = H_{1/3}$  (the mean of the top one-third

wave heights) is the significant wave height,  $g = 9.81 \text{ m s}^{-2}$  is the acceleration due to gravity and  $T_m$  is the mean wave period. When  $h^* > 0.3$ , the waves reflect from the vertical structure, and any overtopping is likely to be gentle ‘green water’ overtopping. When  $h^* \leq 0.3$ , impacting waves begin to prevail and ultimately dominate, resulting in violent wave overtopping.

### 3.1. The Edinburgh wave flume experiments

The wave flume that was used to carry out the physical modelling is approximately 20 m in length by 0.4 m wide with an absorbing flap-type wave generator located at one end (Fig. 2). The operating water depth is 0.7 m (intermediate depth at the wave generator). The basic bathymetry of the wave flume consists of a 1:10 sloping beach on which is placed a 10:1 battered wall. The battered wall is placed so that the water depth at the toe of the structure,  $h$ , is 0.09 m. Eight wave gauges that record water surface elevation are placed at 1.0, 2.0, 3.0, 4.25, 5.5, 6.75, 8.0 and 11.21 m away from the battered wall and record water depth at a rate of 100 Hz (Fig. 3). The wave generator produced 1024-second sequences of waves from the JONSWAP spectrum with  $\gamma = 3.3$ , representing sequences consisting of  $\sim 1000$  waves. In all, 15 runs of the experiment were carried out using this configuration that produced  $h^*$  values ranging from 0.03 to 0.1.

Table 1 contains the significant wave height ( $H_s$ ) measured at the toe of the battered wall, the mean wave period ( $T_m$ ), the  $h^*$  parameter and the dimensionless freeboard  $R_h$  (see Section 3.4) for the 15 runs of the experiment.

### 3.2. Numerical model of the Edinburgh wave flume experiments

For the numerical modelling of the Edinburgh wave flume experiments, a reduced solution domain starting at 2.0 m away from the battered wall was used to minimise the energy loss that may occur as the waves propagate up the flume. The total length of the numerical flume was 2.1 m which was discretised into 100 computational cells ( $\Delta x = 0.021 \text{ m}$ ). The water surface elevation recorded at the gauge placed 2.0 m away from the battered wall serves as the boundary condition for the water depth at the left-hand boundary, whilst the velocity was assumed to be the same as that of the first computational cell in from the left-hand boundary. This boundary condition takes into account both incident waves and reflecting waves from the structure. A study carried out by Richardson et al. (2001) showed that this boundary condition provides values of the water surface and velocity that are 99% and 85% accurate, respectively, when compared to a moving boundary model. A transmissive boundary condition was used at the right-hand boundary to allow water to pass out of the solution domain.

Data were collected from two points within the solution domain. At  $x = 1.0 \text{ m}$ , the water surface elevation was recorded which corresponds with the gauge placed 1.0 m from the battered wall. At  $x = 2.03 \text{ m}$ , the overtopping discharge,  $q$ , was calculated from the water depth and positive velocity by using the equation

$$q = hu\Delta t. \quad (12)$$

An overtopping event is considered to have occurred if a positive water depth is recorded at the gauge

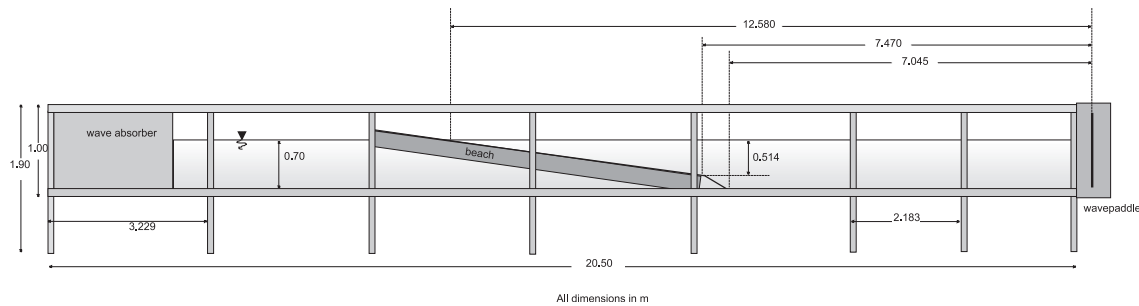


Fig. 2. Edinburgh wave flume: side elevation.

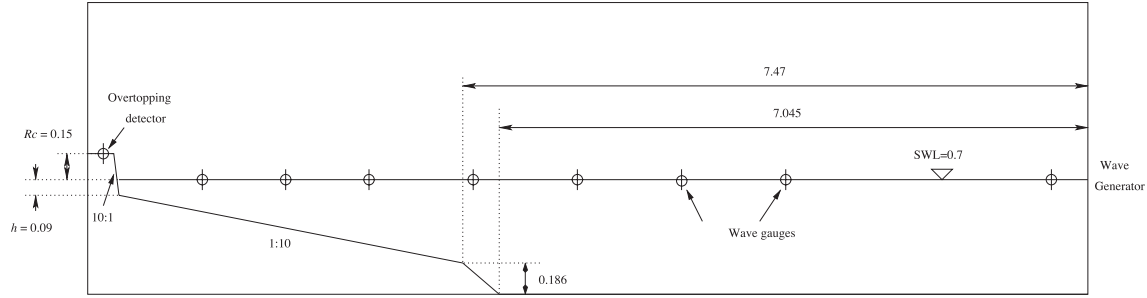


Fig. 3. Edinburgh wave flume: experimental setup.

placed at the top of the battered wall and the velocity recorded at the same gauge is landward.

### 3.3. Results

A plot of the numerical and experimental water surface at the gauge placed 1.0 m away from the battered wall over two separate time intervals can be seen in Fig. 4. A comparison between the water surface elevation for the physical model and the numerical model suggests that the numerical surface over-predicts the wave heights at the gauge placed 1.0 m away from the battered wall. The crests of the numerical waves occur at the same time as the physical waves. The lack of dispersion within the SWE is responsible for this shortfall in the numerical

model as the energy loss observed in the physical model is not replicated.

Plots showing the overtopping discharge,  $q$ , over time 0–1200 s for all 15 runs of the numerical model and the physical model can be seen in Figs. 5 and 6. An overtopping event can be identified in Figs. 5 and 6 to be a steep upward turn in the discharge plot. Runs 3, 13 and 14, in particular, show excellent agreement between the numerical and physical discharge. However, runs 7, 9 and 10 show that the agreement is poor for these cases. A quantitative analysis of the discharges has been performed in Section 3.4.

### 3.4. Wave and overtopping statistics

In order to compare the numerical model of the wave flume and the physical experiment, a number of statistics have been calculated that analyse the water surface elevations and the overtopping discharges. To compare the water surface elevations recorded by the depth gauges placed 1.0 m away from the battered wall, the probability density functions (PDFs) for numerical and physical models have been calculated and compared with the Rayleigh distributions. Analysis of the overtopping discharges has been achieved by calculating values of dimensionless parameters and comparing results against empirical formulae.

#### 3.4.1. Rayleigh wave height distribution

Longuet-Higgins (1952) showed that based upon the linear model of waves with a narrow energy spectrum, wave heights in deep water should follow the Rayleigh distribution (Battjes and Groenendijk,

Table 1  
Edinburgh wave flume experiment parameters

Run	$H_s^\dagger$	$T_m^\dagger$	$h^*$	$R_h$
1	0.063	1.23	0.0544	0.1296
2	0.074	1.27	0.0435	0.0881
3	0.069	1.25	0.0481	0.1046
4	0.059	1.25	0.0563	0.1431
5	0.062	1.25	0.0536	0.1296
6	0.071	1.50	0.0325	0.0686
7	0.078	1.48	0.0304	0.0584
8	0.063	1.52	0.0356	0.0849
9	0.050	1.52	0.0449	0.1347
10	0.075	1.50	0.0307	0.0615
11	0.062	0.97	0.0889	0.2152
12	0.059	0.95	0.0974	0.2477
13	0.066	0.98	0.0818	0.1860
14	0.068	1.00	0.0763	0.1683
15	0.064	0.98	0.0844	0.1978

<sup>†</sup> Measured at the toe of the battered wall.

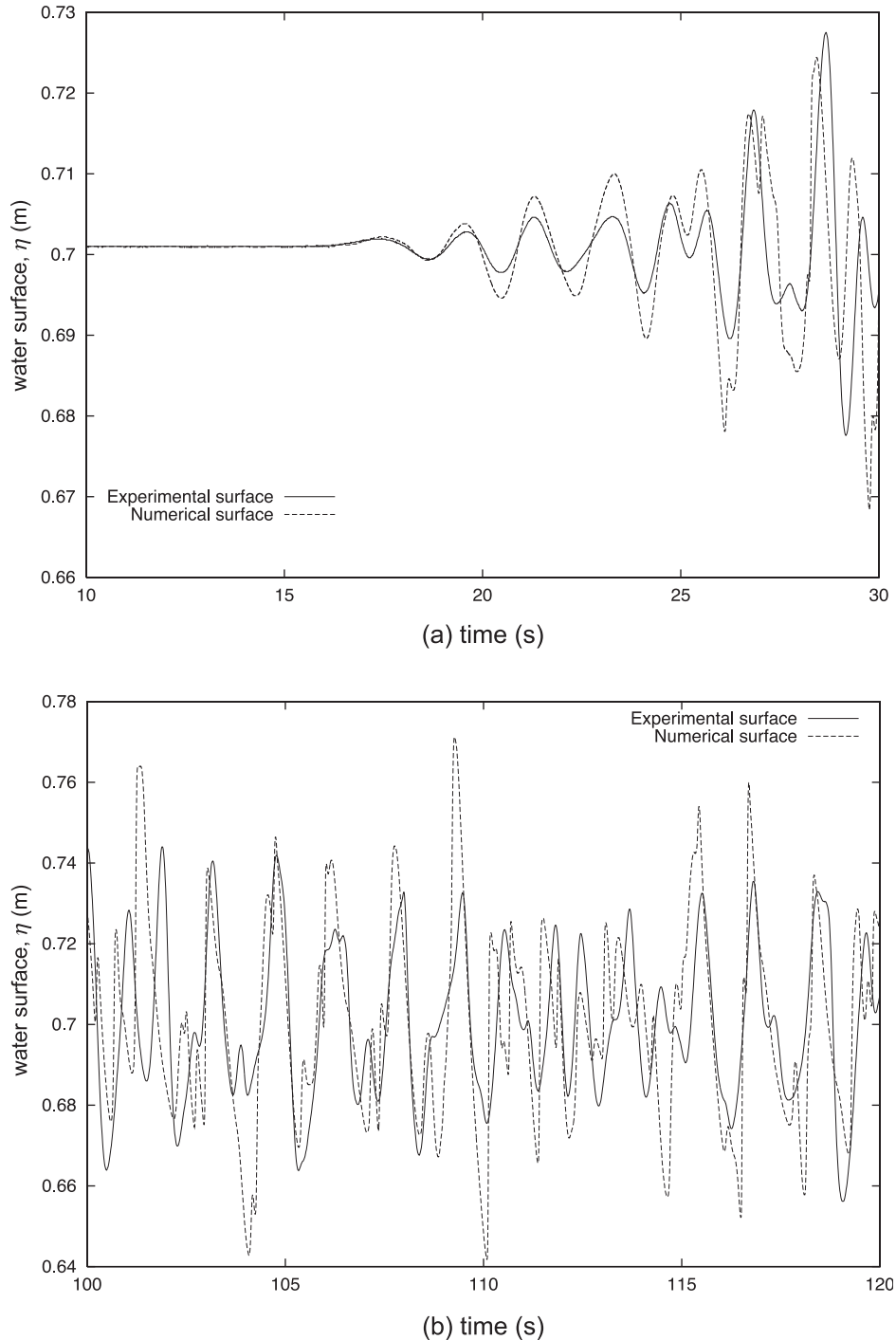


Fig. 4. Numerical simulation of the Edinburgh wave flume experiments: comparison of the experimental (solid line) and the numerical (dotted line) water surface at gauge placed 1.0 m from the battered wall over time intervals of  $t=[10,30]$  (a) and  $t=[100,120]$  (b).

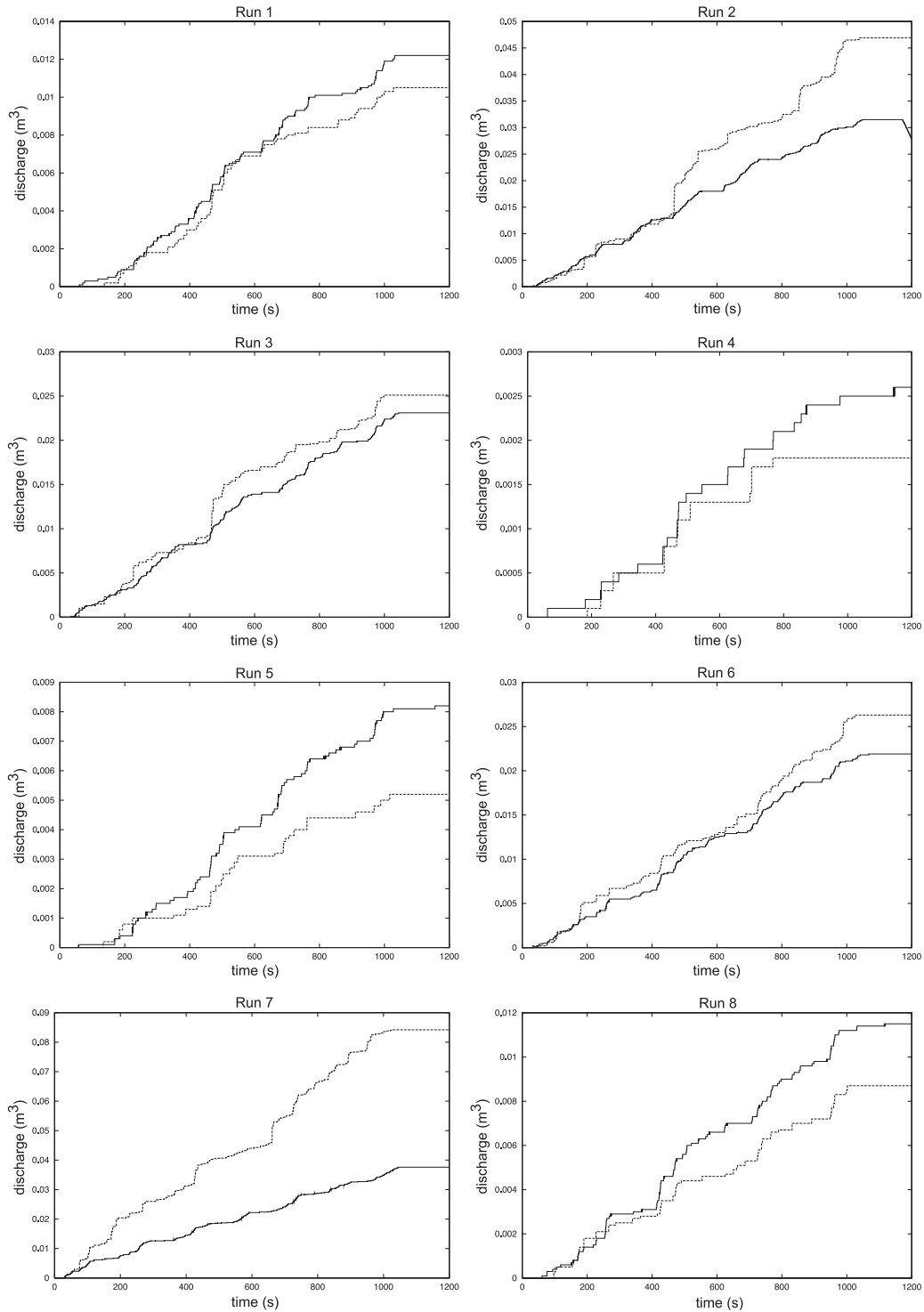


Fig. 5. Comparison of the numerical discharge (dotted line) against the experimental discharge (solid line) for runs 1–8.

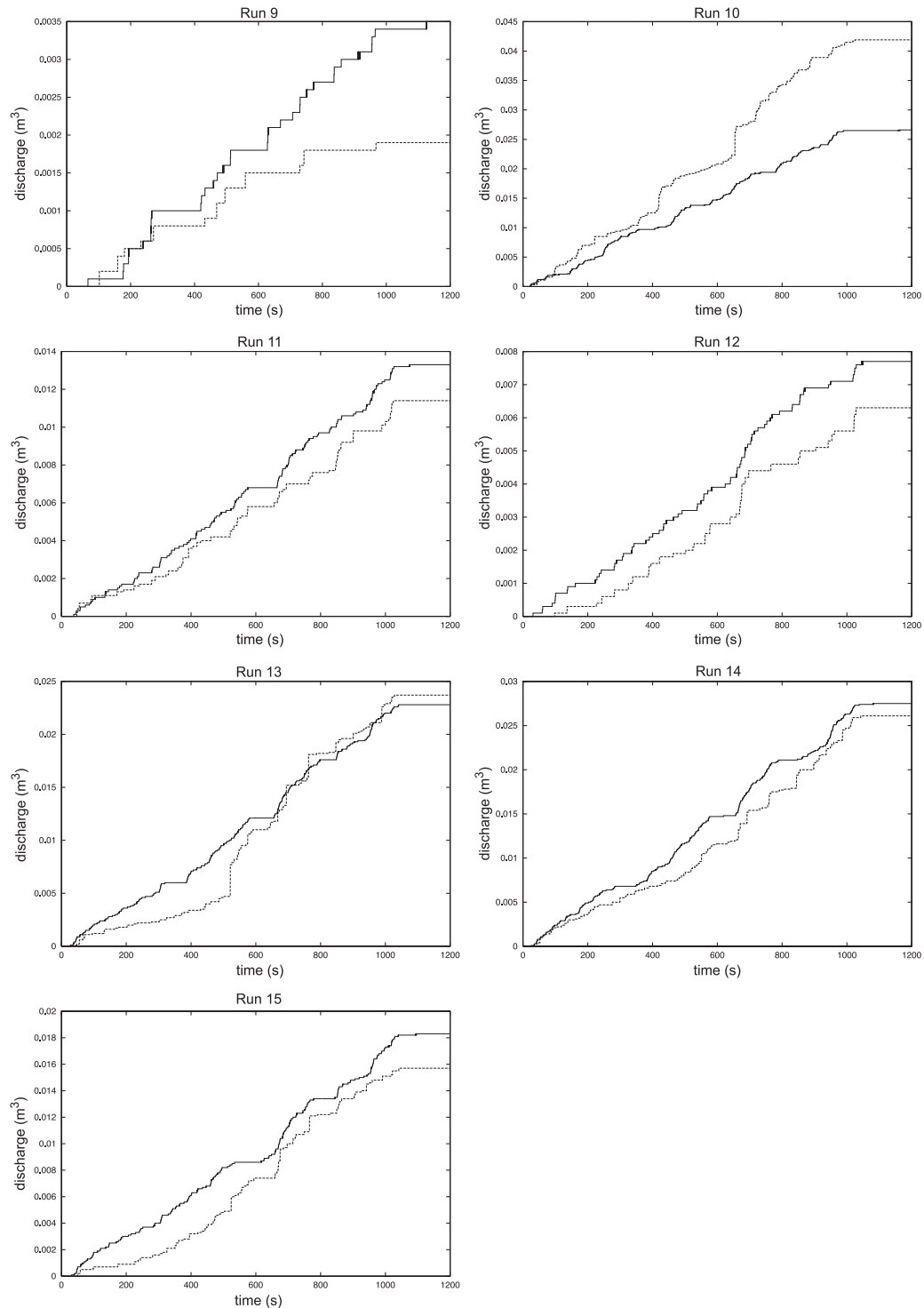


Fig. 6. Comparison of the numerical discharge (dotted line) against the experimental discharge (solid line) for runs 9–15.

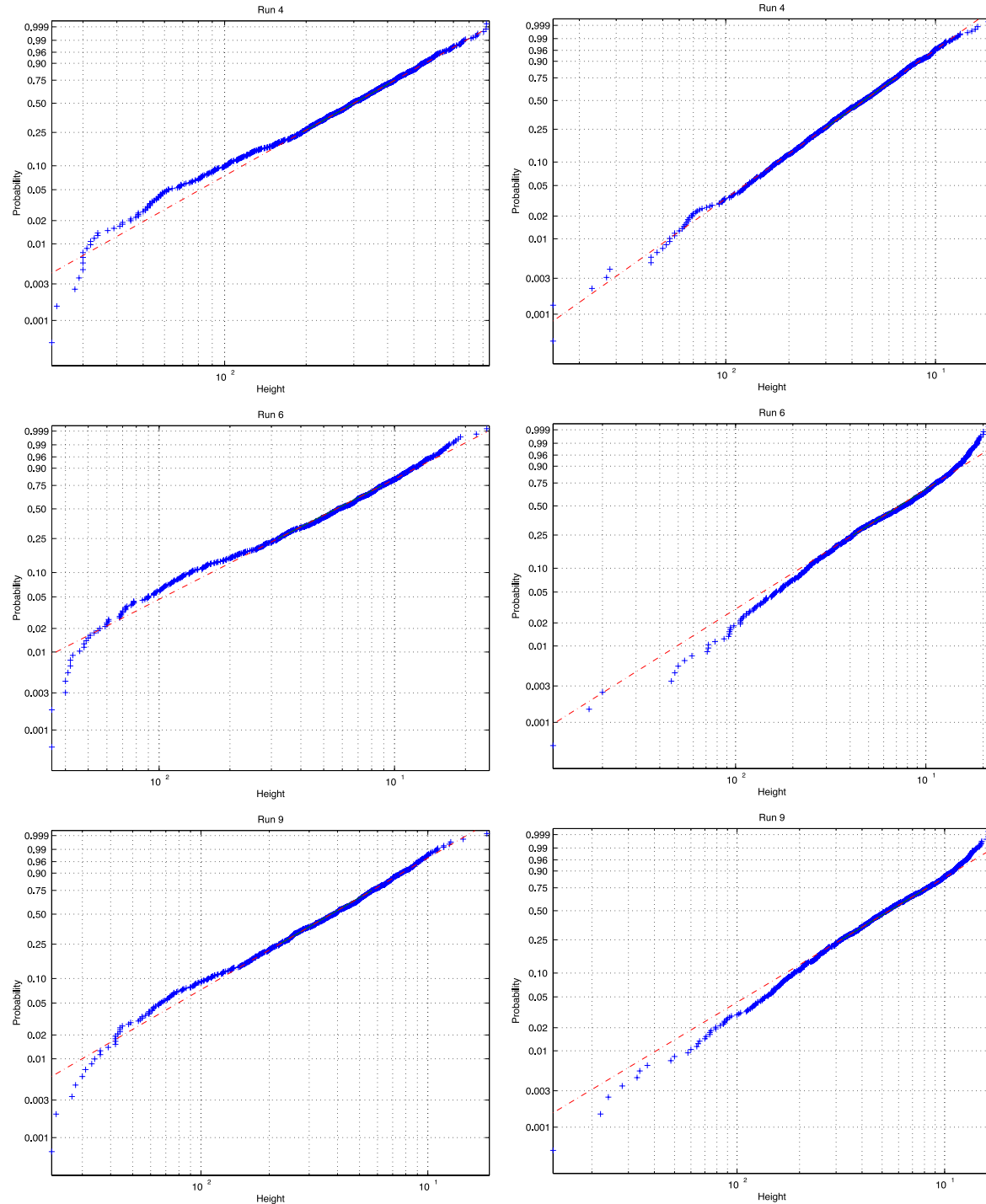


Fig. 7. Comparison of the experimental (left) and numerical (right) PDFs against their corresponding Rayleigh distributions (dashed line) for runs 4, 6 and 9.

2000). The probability that waves have a height less than  $H$  is then

$$P(\underline{H} < H) = 1 - \exp \left[ - \left( \frac{H}{H_{\text{rms}}} \right)^2 \right], \quad (13)$$

where  $\underline{H}$  is a random variable;  $H_{\text{rms}} = H_{1/3}/1.416$  is the root mean square (rms) of the wave heights, and  $H_{1/3}$  is the mean of the top 1/3 wave heights.

The observed probability distribution for the wave heights is given as

$$P(\underline{H} < H) = 1 - \frac{i}{N - 1}, \quad (14)$$

where  $i$  is the  $i$ th largest recorded wave height and  $N$  is the number of waves recorded. Plots of the observed and Rayleigh probability functions for runs 4, 6 and 9 are compared in Fig. 7.

The observed probability functions for both the physical experiment and the numerical model closely follow the Rayleigh distribution when the observed wave heights are greater than the median value. For smaller wave heights, there is a degree of scatter away from the Rayleigh probability distribution. However, as noted earlier (Fig. 4), the numerical model produces greater wave heights.

### 3.4.2. Overtopping statistics

In order to compare overtopping discharges between different experimental set-ups, dimensionless

parameters for the volume of discharge and freeboard have been calculated. For  $h^*$  values of less than 0.3, these are given as (Besley, 1999)

$$Q_h = \left( \frac{Q}{\sqrt{gH_s^3}} \right) / h^{*2}, \quad (15)$$

and

$$R_h = \left( \frac{R_c}{H_s} \right) h^*, \quad (16)$$

where  $H_s$  is the significant wave height at the toe of the battered wall,  $Q_h$  is the dimensionless discharge and  $R_h$  is the dimensionless freeboard;  $Q$  is the mean overtopping discharge rate per metre of sea wall ( $q/t$  where  $t$  denotes the total amount of time the experiments was run for, in this case  $t=1200$  s), and  $R_c$  is the crest freeboard (Fig. 2). Besley et al. (1998) performed an extensive range of measurements for mean overtopping discharge on vertical walls, and the line of best fit using these measurements can be described by the following equation

$$Q_h = 0.000137 R_h^{-3.24}. \quad (17)$$

Besley also developed an equation describing the proportion of waves that overtop a vertical wall given

Table 2  
Overtopping statistics

Run	$h^*$	Physical model					Numerical model				
		$Q$	$Q_h$	$N_{\text{ow}}$	$N_w$	$N_{\text{ow}}/N_w$ (%)	$Q$	$Q_h$	$N_{\text{ow}}$	$N_w$	$N_{\text{ow}}/N_w$ (%)
1	0.063	1.26E–05	0.0502	175	863	20	1.09E–05	0.0436	84	1037	8
2	0.074	3.25E–05	0.2033	479	888	54	5.02E–05	0.3142	290	967	30
3	0.069	2.38E–05	0.1216	299	900	33	2.70E–05	0.1379	196	1017	19
4	0.059	2.68E–06	0.0100	39	850	5	1.24E–06	0.0046	13	1038	1
5	0.062	8.45E–06	0.0349	132	898	15	6.19E–06	0.0255	44	1042	4
6	0.071	2.26E–05	0.2531	329	719	46	2.40E–05	0.2693	203	854	24
7	0.078	3.88E–05	0.4971	535	712	75	8.83E–05	1.1317	541	847	64
8	0.063	1.19E–05	0.1104	173	682	25	9.49E–06	0.0883	61	861	7
9	0.050	3.61E–06	0.0212	76	658	12	2.17E–06	0.0127	14	849	2
10	0.075	2.74E–05	0.3431	410	719	57	4.87E–05	0.6088	292	864	34
11	0.062	1.37E–05	0.0205	204	1000	20	1.11E–05	0.0167	89	1252	7
12	0.059	7.94E–06	0.0099	125	1017	12	6.91E–06	0.0086	47	1239	4
13	0.066	2.35E–05	0.0415	394	985	30	2.61E–05	0.0460	150	1233	12
14	0.068	2.84E–05	0.0576	357	1000	36	2.63E–05	0.0534	214	1225	17
15	0.064	1.89E–05	0.0313	278	985	28	1.63E–05	0.0270	121	1239	10

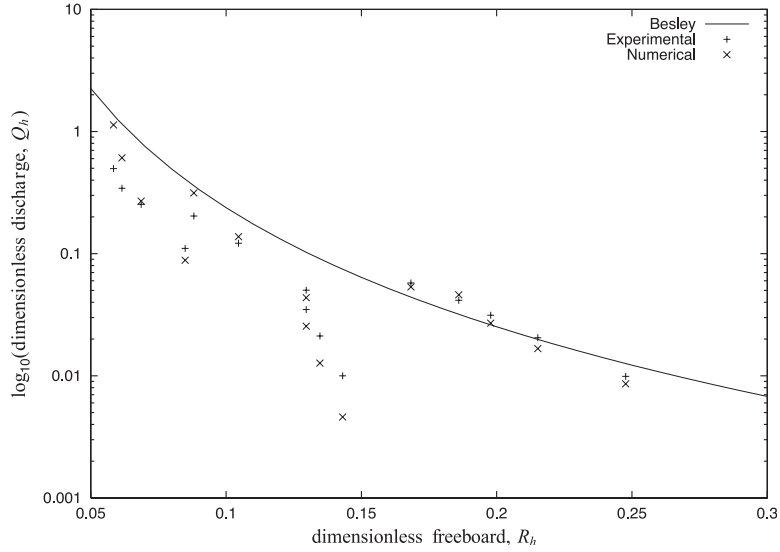


Fig. 8. Dimensionless discharge ( $Q_h$ ) plotted against dimensionless freeboard ( $R_h$ ) for the physical model and the numerical model.

the dimensionless freeboard parameter. For  $h^* \leq 0.3$ , this is

$$N_{ow}/N_w = 0.031R_h^{-0.99}, \quad (18)$$

where  $N_{ow}$  is the number of overtopping waves, and  $N_w$  is the number of waves in the sequence.

**Table 2** contains the overtopping statistics calculated for both the physical and numerical models. The dimensionless discharges are plotted against the dimensionless freeboards in Fig. 8 which also shows Besley's relationship. The percentages of waves overtopping in the numerical and physical models are shown in Fig. 9, along with the empirical Besley curve.

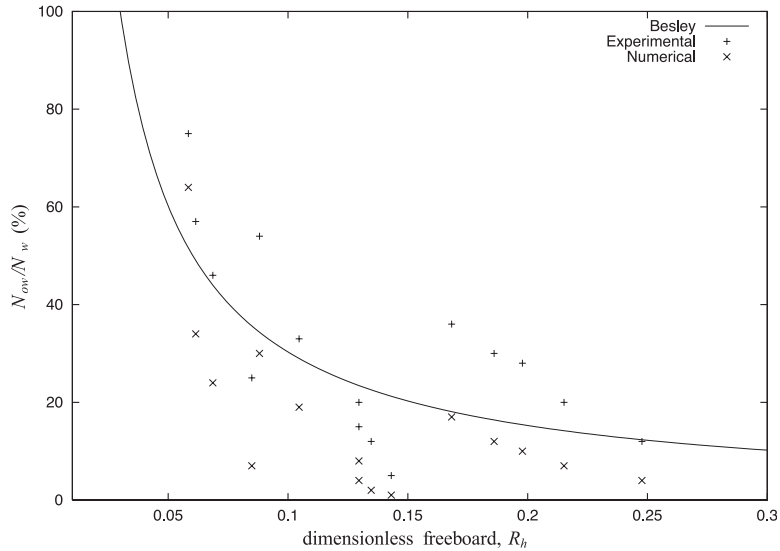


Fig. 9. Percentage of waves overtopping the 10:1 battered wall.

For dimensionless freeboard values of 0.16 and greater, there is excellent agreement both between the numerical and experimental dimensionless discharges and with the Besley curve (Fig. 8). At the lower values of  $R_h$  ( $R_h \leq 0.1$ ), there is not so good agreement between the two data sets and the Besley curve. However, the general trend is still maintained. For  $R_h$  between 0.12 and 0.15, there is a marked decrease in the accuracy of the Besley curve when compared to the calculated dimensionless discharges.

The percentage of waves overtopping in the numerical model is significantly less than was recorded from the physical model (Fig. 9). This is due to the fact that breaking waves are represented by bore waves in the depth averaged SWE. The physical processes that occur to create violent overtopping events cannot be modelled properly in this manner, hence, the wave-by-wave overtopping predictions. However, as a comparison of the discharge volume shows, the SWE give good predictions of mean overtopping discharge. In keeping with the findings from Fig. 8, where the  $R_h$  values are greater than 0.16, the numerical model shows slightly better agreement with the Besley curve than at lower values of  $R_h$  where the data points are more scattered.

The absolute percentage difference between the numerical and the physical models has been calculat-

ed for both the dimensionless discharge and the significant wave height 1.0 m from the battered wall (Fig. 10). Fig. 10 shows that there are two distinct populations of data points, the runs where the  $h^*$  values are 0.075–0.1 and the runs where the  $h^*$  values are less than 0.06. For runs where the  $h^*$  parameter is 0.075–0.1 (runs 11–15), the percentage errors for both the dimensionless discharge ( $Q_h$ ) and the significant wave heights ( $H_s$ ) are less than 20%. For the runs where the  $h^*$  parameter is less than 0.06 (runs 1–10), the absolute percentage error for the significant wave height is typically 35–40%, and the percentage error for the dimensionless discharge is also spread around the 35–40% area, with two outliers that have a percentage error of 79% and 127% where the value of  $h^*$  is the lowest of all of the runs at 0.03.

#### 4. Conclusions

AMAZON, a numerical model based upon the shallow water equations was described. The numerical scheme used is the MUSCL–Hancock scheme which is a high-resolution Godunov-type scheme that uses MUSCL reconstruction to prevent spurious oscillations. The surface gradient method, a modern method for dealing with the treatment of source terms within

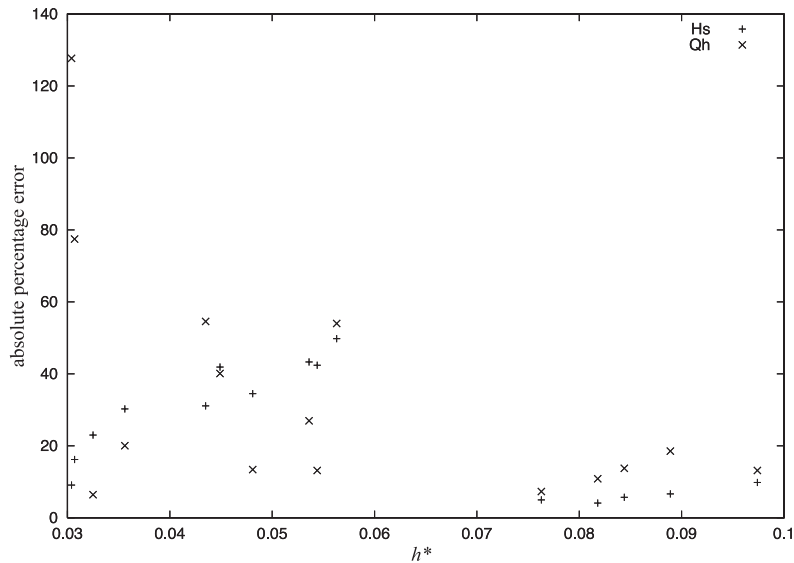


Fig. 10. Percentage error between the physical model and the numerical model for the observed significant wave height ( $H_s$ ) and the dimensionless discharge ( $Q_h$ ).

the shallow water equations, was discussed and implemented. The numerical model was used to simulate a physical experiment carried out in a wave flume as part of the VOWS project.

Comparisons between water surface elevations of the physical and numerical models show that although the waves occur at the same time, the numerical surface over-predicts the heights of each wave. This can be attributed to the lack of dispersion within the shallow water equations that are being used in non-shallow water. The probability density functions for non-exceedence were calculated for both the physical and numerical models and compared against the expected Rayleigh distributions. Both models showed good agreement with the expected Rayleigh distributions, but again showed that the numerical model over-predicts the wave heights.

Dimensionless statistics were calculated to compare overtopping discharges. These were then compared to empirical formulae that showed that for higher  $h^*$  values, there was better agreement between the numerical model, the physical model and the empirical formulae. An analysis of the percentage of overtopping waves showed that the numerical model significantly underestimated the number of overtopping events in the sequence, but it was noted that for higher values of  $R_h$  (and therefore,  $h^*$ ) the numerical model provided a better fit to the empirical formulae than for lower values of  $h^*$ . Finally, a comparison was made between the absolute percentage error between the numerical and physical model that showed that for  $h^*$  values 0.075–0.1, the shallow water equations produce results to within 20% of the physical model for both the significant wave height and the dimensionless discharge. For values of  $h^*$  below 0.06, the analysis showed that the percentage errors ranged from a typical 40% to a couple of outliers at 79% and 127% for small values of  $h^*$  where waves are mostly impacting.

It is concluded that the shallow water equations provide a useful alternative to more computationally expensive models for violent wave overtopping provided the  $h^*$  parameter does not fall below 0.075 and that the seaward boundary condition is sufficiently close to the structure. This model provides a useful engineering design tool with 1000 wave simulations taking less than two minutes to run on a moderately fast PC. Further work to extend the model to include

dispersive terms, helping to eliminate differences between the physical and numerical wave heights, will allow the seaward boundary to be located further offshore.

## Acknowledgements

The authors would like to thank Dr. Jonathan Pearson and Prof. William Allsop for their invaluable contribution to the VOWS project and for providing the experimental data. The VOWS project was funded by the EPSRC under two linked grants, numbers GR/M 42312 and GR/M 42428. The authors also wish to acknowledge the helpful discussions on wave overtopping that have taken place within the EU-funded Framework-V project CLASH, contract number EVK3-CT-2001-00058.

## References

- Allsop, N.W.H., Besley, P., Madurini, L., 1995. Overtopping performance of vertical walls and composite breakwaters, sea walls and low reflection alternatives. Tech. rep., Paper 4.7 in MCS Final Report, University of Hanover.
- Battjes, J.A., Groenendijk, H.W., 2000. Wave height distributions on shallow foreshores. *Coastal Engineering* 40, 161–182.
- Besley, P., 1999. Overtopping of Sea walls—design and assessment manual. R&D Technical Report W178. Tech. rep., Environment Agency, Bristol.
- Besley, P., Stewart, T., Allsop, N.W.H., 1998. Overtopping of vertical structures: new methods to account for shallow water conditions. Proceedings of International Conference on Coastlines, Structures and Breakwaters '98, Institution of Civil Engineers, London, pp. 46–57.
- Davis, S.F., 1988. Simplified second-order Godunov-type methods. *SIAM Journal of Statistical and Scientific Computing* 9, 445–473.
- Dodd, N., 1998. A numerical model of wave runup, overtopping and regeneration. *Proc. ASCE Journal of Waterways, Port and Coastal Engineering* 124 (2), 73–81.
- Fraccarollo, L., Toro, E.F., 1995. Experimental and numerical assessment of the shallow water model for two dimensional dam-break type problems. *Journal of Hydraulic Research* 33, 843–864.
- Franco, L., de Gerloni, M., van der Meer, J., 1994. Wave overtopping on vertical and composite breakwaters. Proceedings from 24th International Conference on Coastal Engineering, Kobe, ASCE, New York.
- Garcia-Navarro, P., Vázquez-Cendón, M.E., 2000. On numerical treatment of the source terms in the shallow water equations. *Computers and Fluids* 29, 951–979.

- Godá, Y., Kishira, Y., Kamiyama, Y., 1975. Laboratory investigation on the overtopping rates of sea walls by irregular waves. Ports and Harbour Research Institute, Yokosuka 14, 3–44.
- Harten, A., Lax, P., van Leer, B., 1983. On upstream differencing and Godunov-type schemes for hyperbolic conservation laws. SIAM Review 25, 35–61.
- Hirsch, C., 1998. Numerical Computation of External and Internal Flows, vol. 1. Wiley, Chichester, UK.
- Hu, K., Mingham, C.G., Causon, D.M., 2000. Numerical simulation of wave overtopping of coastal structures using the non-linear shallow water equations. Journal of Coastal Engineering 41, 433–465.
- Leveque, R.J., 1998. Balancing source terms and flux gradients in high-resolution Godunov methods: the quasi steady wave propagation algorithm. Journal of Computational Physics 146, 346–365.
- Longuet-Higgins, M.S., 1952. On the statistical distributions of heights of sea waves. Journal of Marine Research 11, 245–266.
- Mingham, C.G., Causon, D.M., 1998. High-resolution finite-volume method for shallow water flows. Journal of Hydraulic Engineering 124, 605–614.
- Morton, K.W., Mayers, D.F., 1994. Numerical Solution of Partial Differential Equations. Cambridge Univ. Press, Cambridge, UK.
- Owen, M., 1982. Overtopping of sea defences. Proceedings from Conference Hydraulic Modelling of Civil Engineering Structures, BHRA, University of Warwick, Coventry, pp. 469–480.
- Pearson, J., Bruce, T., Allsop, N.W.H., 2001. Prediction of wave overtopping at steep sea walls—variabilities and uncertainties. Proceedings Waves'01. ASCE, San Francisco, pp. 1797–1808.
- Peregrine, D.H., 2002. Water wave impact on walls. Annual Reviews of Fluid Mechanics 35, 23–43 (in press).
- Richardson, S.R., Ingram, D.M., Mingham, C.G., Causon, D.M., 2001. On the validity of the shallow water equations for violent overtopping. Ocean Wave Measurement and Analysis, Proceedings Waves'01, vol. 2. ASCE, Reston VA, pp. 1112–1125.
- Toro, E.F., 1997. Riemann Solvers and Numerical Methods for Fluid Dynamics. Springer-Verlag, Berlin.
- van Gent, M., 1994. Modelling of wave action on and in coastal structures. Coastal Engineering 22.
- van Gent, M., 1995. Wave interaction with permeable coastal structures. PhD thesis, Delft University, pp. 311–339.
- van Leer, B., 1985. On the relation between the upwind-differencing schemes of Godunov, Engquist–Osher and Roe. SIAM Journal of Scientific and Statistical Computing 5, 1.
- Zhou, J.G., Causon, D.M., Mingham, C.G., Ingram, D.M., 2001. The surface gradient method for the treatment of source terms in the shallow water equations. Journal of Computational Physics 168, 1–25.

## **EXTENDED SHALLOW WATER PREDICTION OF OVERTOPPING**

J. SHIACH, C.G. MINGHAM, D.M. INGRAM AND D.M. CAUSON

*Centre for Mathematical Modelling and Flow Analysis,  
Manchester Metropolitan University, Chester Street, Manchester, M1 5GD, UK.*

T. BRUCE AND J. PEARSON

*School of Engineering and Electronics,  
The University of Edinburgh, Kings Buildings, Mayfield Road, Edinburgh EH9  
3JL, UK.*

N.W.H. ALLSOP

*HR Wallingford,  
Howbery Park, Wallingford, Oxfordshire, OX10 8BA, UK.*

An existing numerical model of wave run-up and overtopping based on the shallow water equations (SWE) has been extended to model waves in deeper water using Nwogu's formulation of the Boussinesq equations. This hybrid model uses a high resolution finite volume method to solve the SWE whilst a fourth-order accurate finite difference method is used to solve the Boussinesq equations. The numerical model has been used to predict wave heights and overtopping discharges of a series of experiments that focus on violent wave overtopping. The numerical model provided good predictions for the wave heights throughout the domain with a tendency to slightly under-predict the wave heights near the boundary of the two models. The overtopping discharge volumes calculated by the model over-predict those of the physical experiment.

### **1. Introduction**

Overtopping of coastal structures by waves represent a hazard to buildings, cars and, most importantly, people. As a result, overtopping has been extensively studied in the last 30 years in order to provide guidance for the construction of sea defences based upon field observations and physical models. In particular, violent overtopping of seawalls was the focus of the VOWS project (Violent Overtopping by Waves at Seawalls). Violent wave overtopping occurs when waves impact against seawalls throwing water up

and over the top (Fig. 1) causing the water to overtop at speeds much larger than normal pulsating overtopping.

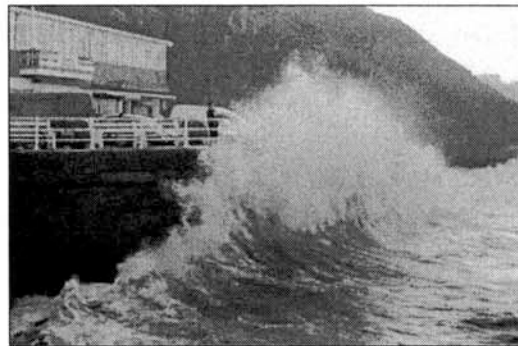


Figure 1. Violent wave overtopping event: Whitby, N. Yorks, U.K.

Previous studies include those by Franco *et al.* (1994) and Owen (1982) where data for overtopping volumes for non-breaking waves (pulsating or non-impulsive conditions) on sloping and vertical structures are presented. Goda *et al.* (1975) included violent (or impacting) conditions as well as pulsating conditions but these were not compared directly. More recently, Besley *et al.* (1998) and Pearson *et al.* (2001) have provided guidance on mean and wave-on-wave overtopping volumes under violent conditions based upon field observations and physical models.

## 2. Numerical Model

The use of computers has allowed the numerical solution of equations that describe fluid flow to provide engineers with an alternative to small scale physical models. These numerical models can provide coastal engineers with wave run-up and overtopping predictions without the time and cost associated with physical experiments and field observations. Ideally the full Navier-Stokes equations would provide a good choice of governing equations on which to base such a model. However, present numerical models based upon the full Navier-Stokes equations require extensive computational resources. A simplified form of the Navier-Stokes equations are the shallow water equations (SWE). Use of the SWE can drastically reduce the computation time required for a numerical model wave run-up and overtopping and therefore may represent a usable alternative to the Navier-Stokes equa-

tions.

Existing numerical models of overtopping based on the shallow water equations include HR Wallingford's ANENOME model developed by Dodd (1998) and ODIFLOCS developed by van Gent (1994) at Delft Hydraulics. ANENOME and ODIFLOCS have been used to model run-up and overtopping on shallow sloping structures (Richardson *et al.* 2002 , Clarke and Damgaard, 2002 ) but so far neither model has been used to model overtopping of near vertical structures. Another model based upon the SWE is AMAZON developed at the Manchester Metropolitan University (Mingham and Causon 1998 , Hu *et al.* 2000 ). AMAZON has been used to model overtopping of both shallow sloping structures (Hu *et al.*, 2000 , Causon *et al.* 2000 ) and violent overtopping of near vertical structures (Shiach *et al.* 2004 , Richardson *et al.* 2001 ). Despite shallow water models providing good predictions of overtopping discharges for particular cases, due to the absence of terms that model dispersion, they provide poor predictions of wave propagation where the relative depth ratio ( $h/L$ , where  $h$  is the water depth and  $L$  is the wavelength) is larger than 0.05. This has been overcome previously by reducing the computational domain so that only the area immediately seaward of the structures is modelled.

To overcome this shortcoming in shallow water models, an extended form of the Boussinesq equations has been used to model wave propagation in intermediate depth water ( $0.05 < h/L < 0.5$ ) allowing the seaward boundary of the numerical model to extended out further and therefore increase the applicability of the model. This new hybrid model has been used to provide wave run-up and overtopping discharge comparisons to the VOWS experiments performed at Edinburgh University.

The numerical model used here is a hybrid of the non-linear shallow water equations (SWE) and Nwogu's Boussinesq equations. The SWE are only applicable for a relative depth of  $h/L < 0.05$  whereas Nwogu's Boussinesq equations have been shown to have a range of applicability of  $0 < h/L < 0.5$  (Nwogu, 1993). However, the SWE are quicker and easier to solve than the Boussinesq equations and do not require any special treatment for the case where the bed topography is above the still water level. Therefore the numerical model uses the Boussinesq equations to model wave propagation in intermediate depth water and the SWE to model wave run-up and overtopping, i.e.,

$$\text{Numerical model} = \begin{cases} \text{Boussinesq} & \text{where } h/L > 0.05 \\ \text{SWE} & \text{elsewhere} \end{cases} . \quad (1)$$

### 2.1. The Shallow Water Equations

The SWE are a depth-averaged form of the Navier-Stokes equations that can model breaking waves as a discontinuity in height. The SWE written in vector form are:

$$\frac{\partial}{\partial t} \mathbf{U} + \frac{\partial}{\partial x} \mathbf{F}(\mathbf{U}) + \frac{\partial}{\partial y} \mathbf{G}(\mathbf{U}) = \boldsymbol{\Omega} \quad (2)$$

where  $\mathbf{U}$  is the vector of conserved variables,  $\mathbf{F}(\mathbf{U})$  and  $\mathbf{G}(\mathbf{U})$  are flux vector functions and  $\boldsymbol{\Omega}$  is the vector of source terms that are used to model bed topography, friction and bed shear stresses. Here the terms that only model bed topography are used. The conserved, flux and source term vectors are

$$\mathbf{U} = \begin{pmatrix} \phi \\ \phi u \\ \phi v \end{pmatrix}, \quad \mathbf{F}(\mathbf{U}) = \begin{pmatrix} \phi u \\ \phi u^2 + \frac{1}{2}\phi^2 \\ \phi uv \end{pmatrix}, \quad (3)$$

$$\mathbf{G}(\mathbf{U}) = \begin{pmatrix} \phi u \\ \phi uv \\ \phi v^2 + \frac{1}{2}\phi^2 \end{pmatrix}, \quad \boldsymbol{\Omega} = \begin{pmatrix} 0 \\ g\phi \frac{\partial H}{\partial x} \\ g\phi \frac{\partial H}{\partial y} \end{pmatrix}. \quad (4)$$

where  $\phi = gh$  is the geopotential,  $g = 9.81\text{ms}^{-2}$  is the acceleration due to gravity,  $h$  is the local water depth,  $u$  and  $v$  are depth-averaged horizontal velocities in the  $x$  and  $y$  directions respectively and  $H$  is the distance between the bed surface and a fixed arbitrary datum measured downwards.

### 2.2. Shallow water equations solver – AMAZON

The SWE given in Eqs. (2)–(4) are solved using a high-resolution finite volume method that is second-order in time and space. The MUSCL-Hancock scheme is a Godunov-type method that uses a monotonic reconstruction of the conserved variables to obtain values at cell interfaces that prevent spurious oscillations in the solution. Solutions to local Riemann problems that are required for the corrector stage are calculated using the HLL approximate Riemann solver (Harten *et al.* 1983). A full description of the SWE numerical scheme including applications to well known test cases can be found in Mingham and Causon (1998).

Previous versions of the AMAZON solver used an operator splitting technique for the treatment of the source terms. The MUSCL-Hancock scheme described above was used to solve the advection terms on the left-hand side of Eq. (2) whilst a first-order implicit Euler method was used

for the source terms. Zhou *et al.* (2001) developed a surface gradient method (SGM) for the treatment of bed source terms in the SWE that uses the water surface elevation instead of the geopotential as the basis for the linear reconstruction in the mass transport equation. This approach insures that any differences in the solution to the geopotential and the bed source terms do not have an adverse affect on the solution. The implementation of the SGM for the MUSCL-Hancock requires very little alteration to the existing scheme and the additional computational cost is negligible. A full description of the SGM and proof of its conservative properties can be found in Zhou *et al.* (2001).

### 2.3. Nwogu's Boussinesq Equations

Nwogu (1993) derived a new form of Boussinesq equation that uses the horizontal velocity at an arbitrary depth as the dependent variable. This derivation leads to a system of equations that, by altering a free parameter  $\alpha$ , can change the dispersive properties of the system. Nwogu's Boussinesq equations are given as:

$$\eta_t + \nabla \cdot [(h + \eta)\mathbf{u}_\alpha] + \nabla \cdot \left\{ \left( \frac{z_\alpha^2}{2} - \frac{h^2}{6} \right) h \nabla(\nabla \cdot \mathbf{u}_\alpha) + \left( z_\alpha + \frac{h}{2} \right) h \nabla[\nabla \cdot (h \mathbf{u}_\alpha)] \right\} = 0 \quad (5)$$

$$\mathbf{u}_{\alpha t} + g \nabla \eta + (\mathbf{u}_\alpha \cdot \nabla) \mathbf{u}_\alpha + z_\alpha \left\{ \frac{z_\alpha}{2} \nabla(\nabla \cdot \mathbf{u}_{\alpha t}) + \nabla[\nabla \cdot (h \mathbf{u}_{\alpha t})] \right\} = 0 \quad (6)$$

where  $\eta$  is the water surface elevation above the still water level (SWL),  $\mathbf{u}_\alpha = (u_\alpha, v_\alpha)$  is the horizontal velocity at an arbitrary depth  $z_\alpha$ ,  $h$  is the distance between the SWL and the bed surface,  $\nabla = (\partial/\partial x, \partial/\partial y)$  is the horizontal gradient operator and  $g = 9.81 \text{ ms}^{-2}$  is the acceleration due to gravity.

The value of the free parameter  $\alpha$  gives the depth  $z_\alpha$  at which the horizontal velocities are calculated (using the SWL as the basis for the coordinate system), and also determines the dispersive properties of the system. The free parameter can take a value in the range  $-1/2 \leq \alpha \leq 0$  where  $\alpha = -1/2$  corresponds to the velocities at the bed surface and  $\alpha = 0$  corresponds to velocities at the free surface (a value of  $\alpha = -1/3$  gives the standard form of the Boussinesq equations derived by Peregrine, 1967). Nwogu (1993) obtained a value of  $\alpha = -0.390$  (corresponding to a depth of  $z_\alpha = -0.531h$ ) by minimising the error between the dispersion properties of the linearised system and linear dispersion theory.

#### **2.4. Boussinesq Equations Solver**

Nwogu's Boussinesq equations are solved using a fourth-order accurate finite-difference method described by Wei and Kirby (1995). Integration through time is achieved by a third-order Adams-Basforth predictor and fourth-order Adams-Moulton corrector method. All first-order derivatives are discretised using a fourth-order stencil insuring that the order of the truncation error in the numerical scheme is less than that of the order of the error in the derivation of the governing equations. The momentum equation is written so that all terms including time derivatives are collected together resulting in a tri-diagonal system that requires solving at each time step.

#### **2.5. Wave Generation**

Wave generation within the Boussinesq domain is achieved by use of an internal source function method. Larsen and Dancy (1983) first used the method where mass is added to the continuity equation at single point in the solution domain. The method works well when a staggered mesh is used, but applying this method to a scheme that uses a collocated mesh causes the scheme to become unstable. To overcome this, Wei *et al.* (1999) used a Gaussian shape function to add the mass over a range of mesh points so that the scheme remains stable.

Mass is added to Eq. (5) in the form of a source function defined by

$$f(x, t) = g(x)s(t) \quad (7)$$

where  $s(t)$  is the input time series and  $g(x)$  is the Gaussian shape function given as

$$g(x) = \exp [-\beta(x - x_s)^2] \quad (8)$$

where  $x_s$  is the centre of the source function and  $\beta$  is a parameter that determines the width of the source function. It is beneficial to use a narrow source function when generating waves within the Boussinesq domain as addition nodes are required for the source function. Here the authors have chosen a source function width that is half the wavelength of a typical wave,  $L$ , determined by the peak wave period. This leads to the following definition of  $\beta$

$$\beta = \frac{80}{L^2}. \quad (9)$$

The amplitude of the Gaussian shape function is given as

$$D = \frac{2a(\omega^2 - \alpha_1 g k^4 h^3)}{\omega k I [1 - \alpha(kh)^2]} \quad (10)$$

where  $a$  is the amplitude of the input signal,  $\omega$  is the peak frequency,  $\alpha_1 = \alpha + 1/3$ ,  $k$  is the wavenumber,  $h$  is the water depth and  $I$  is given by

$$I = \sqrt{\frac{\pi}{\beta}} \exp\left(\frac{-k^2}{4\beta}\right). \quad (11)$$

### 2.6. Boundary Conditions

There are three types of boundary condition used in the hybrid numerical model: absorbing boundary for the Boussinesq domain, incident wave boundary condition for the SWE domain and transient boundary condition for the SWE domain. A sponge layer analogy is used to provide absorbing boundaries for the Boussinesq domain. The boundary conditions for the SWE domain are described in Shiach *et al.* (2004).

## 3. Results

The numerical model described in Section 2 has been used to model physical experiments carried out at Edinburgh University's wave flume facility. The experiments were carried out as part of the EPSRC funded VOWS project whose aim was the study of violent wave overtopping (Allsop *et al.* 2005). The experiment consisted of an 11.21 metre wave flume with a still water level (SWL) of 0.7 metres (Fig. 2). The bathymetry for the experiment modelled here consists of a 1:10 sloping beach on which a near vertical 10:1 battered wall is located so that the water height at the toe of the wall is 0.09 metres. The crest freeboard is 0.15 metres. Gauges are placed at 1.0, 2.0, 3.0, 4.25, 5.5, 6.75, 8.0 and 11.21 metres from the battered wall recording water depth, an overtopping detector is placed on top of the wall to record overtopping events and a tank connected to a load cell is placed behind the battered wall to calculate discharge volume. An absorbing flap-type wave generator is used to generate waves from the JONSWAP spectrum with a peak enhancement parameter of  $\gamma = 3.3$ . As the waves propagate towards the battered wall, the sloping beach causes them to shoal and break upon the structure therefore causing violent overtopping to occur.

Comparisons of the water surface elevation for the seven depth gauges are given in Fig. 3. The water surface height generated by the numerical

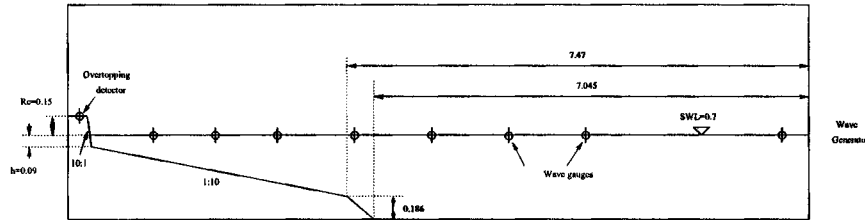


Figure 2. Sketch of the Edinburgh wave flume.

model shows good agreement with the physical water surface for the gauges close to the wave generator. For the gauges placed 4.25 and 3.0 metres from the battered wall, the numerical model tends to under-predict the wave heights. This is probably due to the absence of flow from the SWE domain into the Boussinesq domain. The depth gauges placed within the SWE domain give good agreement with the physical experiment.

The significant wave heights ( $H_s$  = mean of the top 1/3 wave heights) for the Edinburgh experiments and the numerical model are contained in Tables 1 and 2 respectively. This data can also be seen in the form of a scatter plot in Fig. 4 where the experimental values of  $H_s$  are plotted against the numerical predictions of  $H_s$ . The numerical model provides wave height predictions to within 10% of the experimental wave heights, although they tend to under-predict them. This is probably due to the fact that waves are not reflected back into the Boussinesq domain.

Table 1. Significant wave heights (m) for each of the depth gauges over runs 16 – 21 of the Edinburgh experiments.

Run	Gauge distance from wall in metres						
	8.0	6.75	5.5	4.25	3.0	2.0	1.0
16	0.069	0.070	0.072	0.072	0.066	0.064	0.060
17	0.086	0.086	0.088	0.089	0.082	0.082	0.076
18	0.078	0.078	0.081	0.079	0.072	0.082	0.096
19	0.102	0.102	0.105	0.102	0.094	0.096	0.125
20	0.085	0.084	0.084	0.080	0.080	0.075	0.078
21	0.099	0.088	0.096	0.097	0.095	0.089	0.087

The mean overtopping discharges ( $q = l/s \text{ m}$ ) for runs 16 – 21 can be seen in Table 3. For all of the runs of the experiments compared here, the numerical model over-predicts the volume of water overtopping the seawall. In order to compare the overtopping discharges for the different experimental set-ups, dimensionless parameters for the volume of discharge

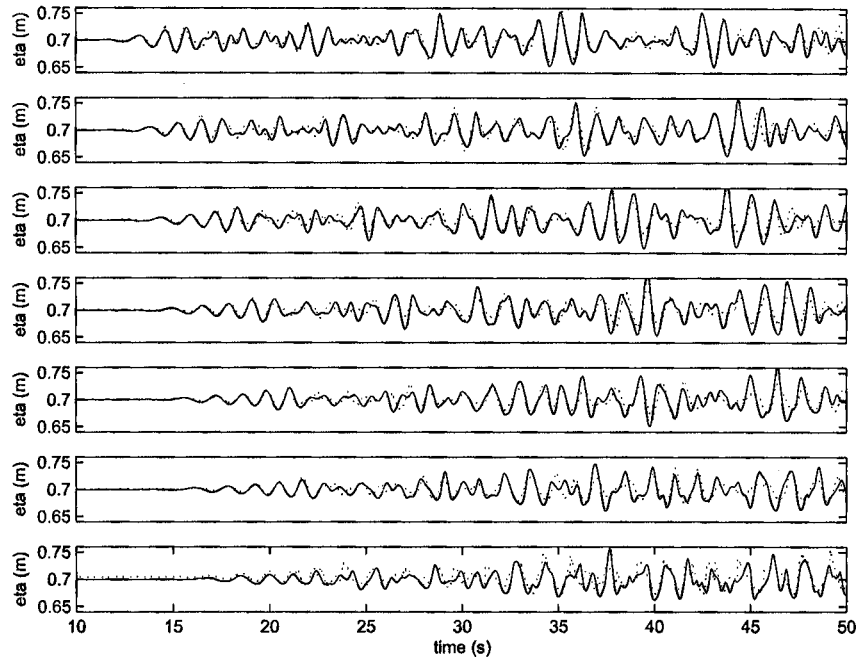


Figure 3. Comparison between the experimental water surface (solid line) and the numerical water surface (dotted line) for the gauges placed (from top to bottom) 8.0, 6.75, 5.5, 4.25, 3.0, 2.0 and 1.0 metres from the seawall.

Table 2. Significant wave heights (m) for each of the depth gauges over runs 16 – 21 of the numerical model.

Run	Gauge distance from wall in metres						
	8.0	6.75	5.5	4.25	3.0	2.0	1.0
16	0.071	0.067	0.063	0.058	0.055	0.056	0.062
17	0.089	0.084	0.079	0.073	0.072	0.072	0.077
18	0.076	0.071	0.067	0.063	0.060	0.059	0.086
19	0.097	0.093	0.086	0.081	0.080	0.080	0.108
20	0.092	0.089	0.087	0.075	0.073	0.070	0.065
21	0.110	0.105	0.101	0.089	0.087	0.085	0.076

and freeboard have been calculated (Besley, 1999). These are compared with the empirical formula for the dimensionless overtopping discharge for vertical structures derived by Besley in Fig. 3. Where  $0.05 < R_h < 0.1$  the numerical model provides good agreement with the Besley curve, but

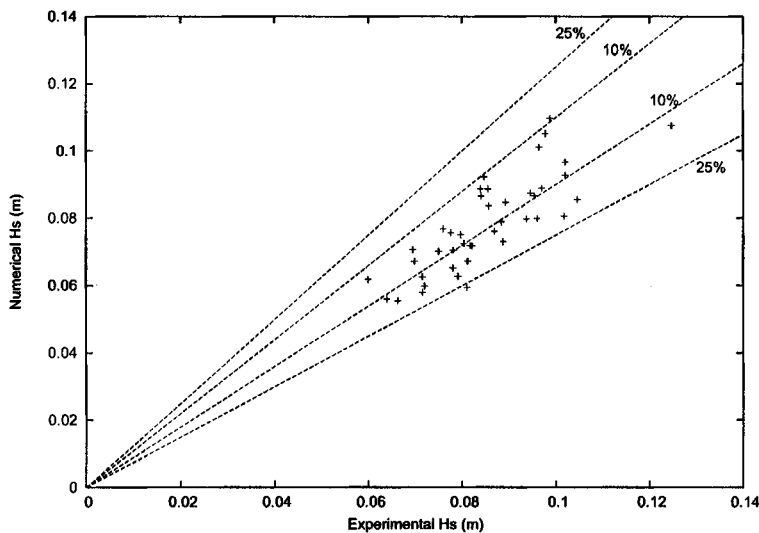


Figure 4. Significant wave heights: Comparison between the VOWS experiments and the numerical model.

where the dimensionless freeboard increases to approximately 0.2 there is a notable difference between the discharge values from the numerical model and both the Besley curve and the experimental values.

Table 3. Mean overtopping volumes  
( $g = 1/\text{s m}$ ).

Run	Experiment	Numerical Model
16	0.0056	0.0356
17	0.0275	0.0338
18	0.0213	0.0525
19	0.0481	0.0725
20	0.0119	0.0069
21	0.0219	0.0725

#### 4. Conclusions

A hybrid numerical model based on the shallow water equations and Nwogu's extended Boussinesq equations has been presented. A second-order finite-volume method was used to solve the shallow water equations incorporating the Surface Gradient Method for the treatment of source

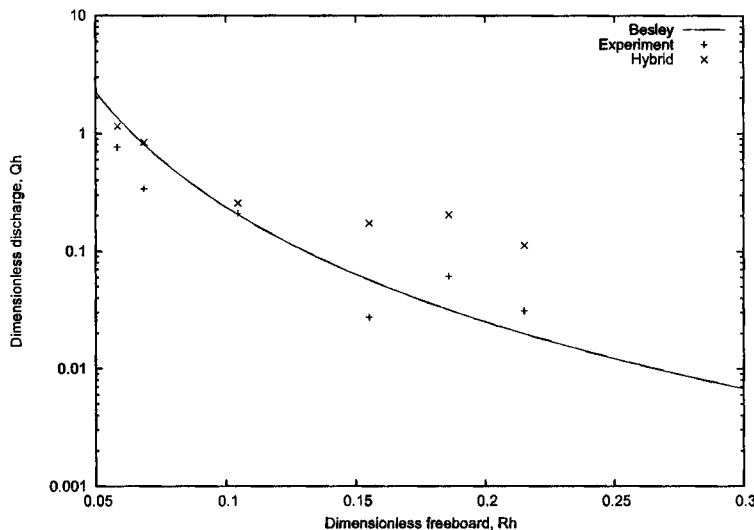


Figure 5. Dimensionless discharge ( $Q_h$ ) plotted against dimensionless freeboard ( $R_h$ ) for the physical model and the numerical model.

terms. The extended Boussinesq equations were solved using a fourth-order finite-difference method where the truncation error in the numerical scheme is less than that of the governing equations, thus ensuring that the dispersive properties of the governing equations are fully retained in the model. Wave generation was achieved by using an internal source function method within the Boussinesq domain using wave heights from the physical experiments.

The numerical model was used to give comparisons of water surface elevation and mean overtopping discharge to a series of experiments carried out to model violent wave overtopping of a near vertical seawall. The numerical model provided good predictions of the water surface elevation for locations throughout the flume. The significant wave heights were calculated for comparison and, whilst most values were accurate to within 10%, there was a general trend for the numerical model to under-predict the wave heights. The mean overtopping discharge volume was over-predicted by the numerical model in all 6 runs modelled here. It is suspected that the under-prediction of the wave heights for the gauges located near the boundary between the Boussinesq domain and the shallow water domain is a result of the absence of reflective waves entering the Boussinesq domain. Further work to rectify this problem is being undertaken.

### Acknowledgments

The authors are grateful for the funding provided for the VOWS and CLASH projects. The VOWS project was funded by the EPSRC under two linked grants, numbers GR/M 42312 and GR/M 42428. The CLASH project was funded by the EU, contract number EVK3-CT-2001-00058.

### References

1. N.W.H. Allsop, T. Bruce, J. Pearson, and P. Besley. Wave overtopping at vertical and steep seawalls. *ICE Water, Maritime and Engineering Journal*, In Press.
2. P. Besley. Overtopping of seawalls - design and assessment manual. R&D Technical Report W178. Technical Report 1 85705 069 X, Environmental Agency, Bristol, 1999.
3. P. Besley, T. Stewart, and N.W.H. Allsop. Overtopping of vertical structures: new methods to account for shallow water conditions. In *Proceedings of International Conference on Coastlines, Structures and Breakwaters '98*, pages 46–57. Institution of Civil Engineers, 1998.
4. D.M. Causon, D.M. Ingram, C.G. Mingham, J. Zang, K. Hu, and J. Zhou. Numerically simulating seawall overtopping. In Billy L. Edge, editor, *Coastal Engineering 2000*, volume 3. ICCE, ASCE, 2000.
5. S. Clarke and J. Damgaard. Applications of a numerical model of swash zone flow on gravel beaches. In Billy L. Edge, editor, *Coastal Engineering 2002*, volume 1, pages 1028–1036, Cardiff, 2002.
6. N. Dodd. A numerical model of wave run-up, overtopping and regeneration. In *Proceedings ASCE Journal of Waterways, Port and Coastal Engineering*, volume 124, pages 73–81. ASCE New York, 1998.
7. L. Franco, M. de Gerloni, and J. van der Meer. Wave overtopping on vertical and composite breakwaters. In *Proceedings from 24th International Conference on Coastal Engineering*, Kobe, 1994.
8. Y. Goda, Y. Kishira, and Y. Kamiyama. Laboratory investigation on the overtopping rates of sea walls by irregular waves. *Ports and Harbour Research Institute*, 14:3–44, 1975.
9. K. Hu, C.G. Mingham, and D.M. Causon. Numerical simulation of wave overtopping of coastal structures using the non-linear shallow water equations. *Coastal Engineering*, 41:433–465, 2000.
10. J. Larsen and H. Dancy. Open boundaries in short wave simulation. *Coastal Engineering*, 7:285–297, 1983.
11. C.G. Mingham and D.M. Causon. High-resolution finite-volume method for shallow water flows. *Journal of Hydraulic Engineering*, 124:605–614, 1998.
12. O. Nwogu. An alternative form of the Boussinesq equations for nearshore wave propagation. *Journal of Waterway, Port, Coastal, and Ocean Engineering*, 119(6):618–638, 1993.
13. M. Owen. Overtopping of sea defences. In *Proceedings from Conference Hy-*

- draulic Modelling of Civil Engineering Structures*, pages 469–480, Coventry, 1982. BHRA.
- 14. J. Pearson, T. Bruce, and N.W.H. Allsop. Prediction of wave overtopping at steep seawalls – variabilities and uncertainties. In *Proceedings Waves '01*, San Francisco, 2001. ASCE.
  - 15. D.H. Peregrine. Long waves on a beach. *Journal of Fluid Mechanics*, 27(4):815–827, 1967.
  - 16. S.R. Richardson, D.M. Ingram, C.G. Mingham, and D.M. Causon. On the validity of the shallow water equations for violent overtopping. In Billy L. Edge and J. Michael Hemsley, editors, *Ocean Wave Measurement and Analysis*, volume 2, pages 1112–1124. Waves 2001, ASCE, 2001.
  - 17. S.R. Richardson, T. Pullen, and S. Clarke. Jet velocities of overtopping waves on sloping structures: measurements and computation. In Billy L. Edge, editor, *ICCE 2002*, volume 2, pages 2239–2250, Cardiff, 2002.
  - 18. J.B. Shiach, C.G. Mingham, D.M. Ingram, and T. Bruce. The applicability of the shallow water equations for modelling violent wave overtopping. *Coastal Engineering*, 51:1–15, 2004.
  - 19. M.R.A. van Gent. Modelling of wave action on and in coastal structures. *Coastal Engineering*, 22, 1994.
  - 20. G. Wei and J.T. Kirby. Time-dependent numerical code for extended Boussinesq equations. *Journal of Waterway, Port, Coastal, and Ocean Engineering*, 121(5):251–261, 1995.
  - 21. G. Wei, J.T. Kirby, and A. Sinha. Generation of waves in Boussinesq models using a source function method. *Coastal Engineering*, 36:271–299, 1999.
  - 22. J.G. Zhou, D.M. Causon, C.G. Mingham, and D.M. Ingram. The surface gradient method for the treatment of source terms in the shallow water equations. *Journal of Computational Physics*, 168:1–25, 2001.